INTERNATIONAL JOURNAL OF
MODERN PHYSICS A

Volume 24, Number 5
February 20, 2009

SPECIAL ISSUE

PROCEEDINGS OF THE 15TH INTERNATIONAL WORKSHOP ON BEAM DYNAMICS AND OPTIMIZATION (BDO 2008)

St. Petersberg, Florida, USA, July 10–12, 2008

Editors

Dimitri Ovsyannikov
Martin Berz
Pavel Snopok

World Scientific

NEW JERSEY • LONDON • SINGAPORE • BEIJING • SHANGHAI • HONG KONG • TAIPEI • CHENNAI

INTERNATIONAL JOURNAL OF MODERN PHYSICS A
Vol. 24, No. 5 (20 February 2009)

SPECIAL ISSUE

Proceedings of the 15th International Workshop on Beam Dynamics and Optimization (BDO 2008)
St. Petersburg, Florida, USA, July 10–12, 2008
Editors: Dmitri Ovsyannikov, Martin Berz and Pavel Snopok

CONTENTS

(*Continued*)

Cited in Science Citation Index®, Science Citation Index Expanded(TM), Current Contents®/Physical, Chemical & Earth Sciences

Vol. 24, No. 5 (20 February 2009) pp. 799–1067

PREFACE

This special issue of IJMPA contains papers presented at the Fifteenth International Workshop on Beam Dynamics and Optimization (BDO 2008), which was held on July 10–12, 2008 in St. Petersburg, Florida, USA.

The series of workshops on Beam Dynamics and Optimization began in 1994 in Saint Petersburg, Russia. Since then, fourteen workshops were held in Russia: in Saint Petersburg, Saratov, and in Dubna. In the years 2004 and 2005, the BDO workshops were included as separate sections into the 8th International Computational Accelerator Physics Conference (ICAP 2004), and the International Conference on Stability and Control Processes (SCP 2005), respectively. The year 2008 marks the first time the workshop was held outside the borders of Russia, although the name of the location was instantly familiar to earlier participants: BDO 2008 took place in St. Petersburg, Florida, USA.

Traditionally, the objective of the Workshop is to bring together mathematicians, physicists and engineers to present and discuss recent developments in the area of mathematical control methods, modeling and optimization and theory and design of charged particle beams and plasma, parallel and distributed computing in accelerator physics. Over thirty talks and poster reports were presented.

During the workshop three online sessions were organized between St. Petersburg, Florida and DESY (Germany), Moscow Engineering Physics Institute (Russia) and Saint Petersburg State University (Russia).

Finally, the completion of the proceedings would not have been possible without the careful refereeing efforts to which many individuals contributed invaluable time and effort. The organizers are indebted and thankful to the efforts of referees from Fermi National Accelerator Laboratory (USA), Argonne National Laboratory (USA), Brookhaven National Laboratory (USA), D. V. Efremov Scientific Research Institute (NIIEFA, Russia), TRIUMF (Canada), the Joint Institute for Nuclear Research (Russia), Lawrence Berkeley National Laboratory (USA), National Synchrotron Radiation Laboratory (China), General Atomics (USA), Cinvestav (Mexico), Institute for High Energy Physics (Protvino, Russia), Petersburg Nuclear Physics Institute (Russia), Michigan State University (USA), University

of Maryland (USA), Saint Petersburg State University (Russia), Saint Petersburg State Polytechnical University (Russia), University of Frankfurt (Germany) and Technical University Kaiserslautern (Germany).

We hope this special issue on beam dynamics and optimization will be useful for many researchers in beam physics and related fields.

Dmitri Ovsyannikov, Martin Berz and Pavel Snopok
Editors

ORGANIZATION

BDO 2008

The 15th International Workshop on Beam Dynamics and Optimization

Organized by

Saint Petersburg State University, Saint Petersburg, Russia
Michigan State University, East Lansing, MI, USA
University of California, Riverside, CA, USA

Chairs:

Dmitri A Ovsyannikov (Russia)
Martin Berz (USA)
Pavel Snopok (USA/Russia)

Organizing Committee:
S. N. Andrianov (Russia)
Yu. A. Budanov (Russia)
A. N. Dovbnya (Ukraine)
N. V. Egorov (Russia)
V. P. Gorbachev (Russia)
G. Hanson (USA)
R. Jameson (USA)
C. Johnstone (USA)
A. B. Kurzhanskiy (Russia)
A. Poklonskiy (Russia)
Yu. Senichev (Germany)
M. F. Vorogushin (Russia)
I. P. Yudin (Russia)
D. V. Zhukov (Russia)

Scientific Committee:
S. Kawata (Japan)
E. D. Kotina (Russia)
E. S. Masunov (Russia)
K. Makino (USA)
F. Meot (France)
D. Neuffer (USA)
A. D. Ovsyannikov (Russia)
R. Ryne (USA)
Yu. A. Svistunov (Russia)
A. Todd (USA)
E. I. Veremey (Russia)
A. P. Zhabko (Russia)
W. Wan (USA)

FLORIDA
ST PETERSBURG
BDO 2008
USA

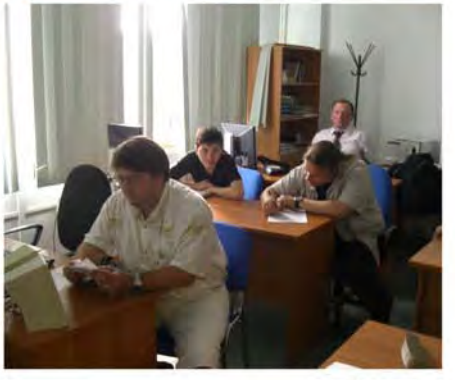

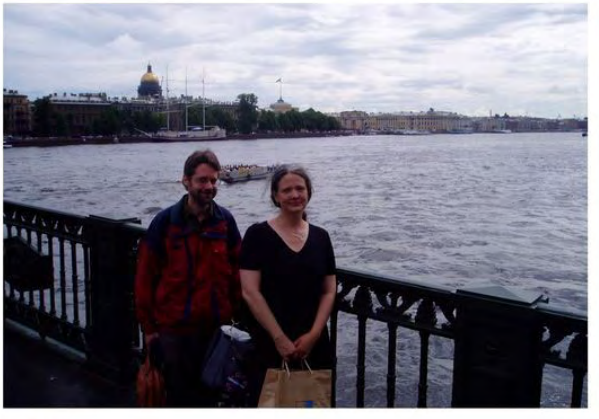








International Journal of Modern Physics A
Vol. 24, No. 5 (2009) 799–815

World Scientific
www.worldscientific.com

SOME PROBLEMS OF NANOPROBE MODELING

SERGE N. ANDRIANOV,* NIKOLAY S. EDAMENKO† and YURY V. TERESHONKOV‡

Faculty of Applied Mathematics and Control Processes, Saint Petersburg State University, 35 Universitetskii pr., Peterhof, Saint Petersburg, 198504, Russia

*sandrianov@yandex.ru

†nse47@yandex.ru

‡yury.tereshonkov@gmail.com

We treat here the process of simulation of ion micro- and nanoprobes in detail using the matrix formalism for Lie algebraic tools. Similar approach allows realizing necessary analytical and numerical modeling procedures.

Nowadays ion micro- and nanoprobes are extensively applied in different branches of science and industry. It is known that similar facilities are very sensitive to certain of steering parameters of the systems. In other words, similar beam lines are high precision systems, requiring preliminary modeling for thorough analysis of possible optimal working regimes. In this paper we consider analytical and numerical models, which allow one to study effect of various aberrations on basic beam characteristics. Research process performs from linear to nonlinear model with step by step including nonlinear effects of different nature.

Previous papers of the authors consider some aspects of nonlinear models. The present paper deals with full conception of modeling process, generalizing most essential aberrations and providing adequate solution methods.

Keywords: Nanoprobe; matrix formalism; nonlinear model.

PACS numbers: 41.85.p, 29.27.a, 41.85.Ja

1. Introduction

Nanoprobes are high-precision systems because of their purposes. Interest in such focusing systems has been increasing during last years. Usually parameters of the nanoprobes are calculated for the specific needs in particular cases. Many people want to obtain high-volume output of nanoprobes, because such systems are very needed for many fields of application. However there are many parasitic effects in nanoprobes which could prevent their high-volume output. In the present paper we consider a number of undesirable effects in nanoprobes and give some recommendations how to increase the system quality.

Beam lines are usually simulated using piecewise constant model of steering fields. In many papers there were considered various models of steering fields and found field distribution along beam axis. However there is no consistent investigation of influence of fringe field form and length. Due to the lack of information about

fringe fields distribution along the reference axis, it is a quite complicated problem of choosing necessary model functions. Several papers[1,2] are devoted to various models for fringe field simulation, e.g. trigonometric and polynomial functions,[3] exponential functions (e. g. Enge function[1]). Such set of modeling functions could be appended using classes of smoothness functions and necessary conditions on fringe fields.[3] Several examples of similar functions can be found below. The problem of choice of convenient functions is quite essential due to the lack of information about the influence of some classes of modeling functions on beam characteristics. With the aid of the paper[4] it is possible to find analytical solutions for some classes of the model functions. It is necessary to investigate influence of different model functions and their parts on basic characteristics of focusing systems.

As the basic nanoprobe, structure we consider the well known "Russian quadruplet"[5,6] which consists of four quadrupole lenses and has power supply symmetry. However one can use the methodology which described in the present paper almost for any structure of focusing system with different magnet elements.

2. The Logic Scheme of a Modeling Process

Because of a complexity of beam lines and bundle of parameters and quality criterions, it is useful to consider scheme of modeling process. This process starts with the simplest steering field model (the piecewise constant) with ignorance of the nonlinear effects. Then the process performs with step by step including of tolerances, nonlinear effects and fringe fields effects. On the last step one should investigate the most complicated model of steering fields with many effects. Scheme of the modeling process is following:

- the piecewise constant model for steering fields and the corresponding solution in linear case;
- the piecewise constant model for steering fields, solution in linear case and holding tolerances;
- the piecewise constant model for steering fields and solution in nonlinear case (aberrations could be considered up to second, third, fifth or even more order);
- the piecewise constant model for steering fields, solution in nonlinear case and holding tolerances;
- fringe fields effects and the corresponding solution in linear case;
- fringe fields effects and the solution in nonlinear case;
- fringe fields effects, solution in nonlinear case and holding tolerances;
- the previous step items and the correction of parasitic nonlinear effects.

It is required to introduce a working point. The working point is an optimal (in a manner) point, which could be used for providing essential system characteristics. Each stage of modeling process finishes with obtaining a set of optimal solutions (working points), which are convenient for practice and satisfied necessary requirements for basis beam and system characteristics. In order to drop too

sensitive points it is necessary to include holding tolerances in the model. Also one can use correction procedure for getting better beam characteristics using matrix formalism.[7,8,9]

The main contribution of nonlinear aberrations of third order leads to increasing of the beam size and changes the circular symmetry. One of the most essential parasitic nonlinear effects are spherical and geometrical aberrations, but their influence could be decreased using special correctors. As the correction elements one could choose sextupole and octupole lenses, which help to reduce size of beam spot and may also improve circular symmetry.[9]

The fringe fields effects lead to displacement of working points from optimal in the sense of model on previous stage. It is necessary to move working points in order to keep optimal final beam characteristics. It is required to obtain the set of optimal working points with taking into account of fringe field effects, nonlinear effects and tolerances.

We should consider beam dynamics and solution of motion equations before introducing several requirements for nanoprobe focusing system.

3. The Mathematical Model

Let us describe the modeling process and give the necessary mathematical information.

3.1. *Beam dynamics*

It is known that motion equations for a particle beam in focusing systems can be represented in the following general form

$$\frac{d\mathbf{X}(s)}{ds} = \mathbf{F}\big(\mathbf{X}, s\big), \tag{1}$$

where $\mathbf{X}$ is a phase vector, $\mathbf{F}\,(\mathbf{X}, s)$ is an evolution operator which can be obtained using the transition from the Newton–Lorentz equation to a special coordinate system refereed to an optical (reference) axis of the beam line.

3.1.1. *Solution of linear motion equations*

For the linear approximation, one can write down the motion equations for a system with drifts and quadrupole lenses in the form

$$\begin{cases} x'' + k(s)x = 0, & x' = dx/ds, \\ y'' - k(s)y = 0, & y' = dy/ds, \end{cases} \tag{2}$$

where $k(s)$ is a function describing field distribution along the reference axis. Solution of (2) can be represented with the aid of matrizant[10,11]

$$\mathbf{X}(s) = \mathbb{R}(s|s_0)\mathbf{X}_0, \tag{3}$$

where $\mathbf{X}_0 = \mathbf{X}(s_0)$ is the initial phase vector. A set of diaphragms form an initial phase manifold $\mathfrak{M}_0$, $\mathbf{X}(s_0) \in \mathfrak{M}_0$. The parameters of the diaphragms system can be varied with the aim of increasing of the beam emittance. A total matrizant $\mathbb{R}(s_N|s_0)$ for the nanoprobe can be presented using the group property as a product of partial matrizants corresponding to individual intervals on the references axis:

$$\mathbb{R}(s_N|s_0) = \prod_{k=1}^{N} \mathbb{R}(s_k|s_{k-1}), \tag{4}$$

where s_0 and s_N stand for initial and final values of the variable s, measured along some trajectory. Eq. (4) is the exact presentation for any N and does not depend on types of fragmentation and satisfies an initial value problem.

3.1.2. *Solution of nonlinear motion equations*

For the nonlinear approximation, solution of motion equation (1) can be written as following[12]

$$\frac{d\mathbf{X}(s)}{ds} = \sum_{k=1}^{\infty} \mathbb{P}^{1k}\mathbf{X}^{[k]}, \tag{5}$$

where $\mathbf{X}^{[k]}$ is the Kronecker k-th power for the phase vector $\mathbf{X}$. Here $\mathbb{P}^{1k}(s)$ are the $(n \times d[n,k])$ matrices with $d[n,k] = \binom{n+k-1}{k}$ and with the entries equal to k-th derivative of the components of vector function $\mathbf{F}(\mathbf{X}, s)$. It is known[12] that $\mathbb{P}^{kj}(t) \equiv 0$ when $k > j$ and

$$\mathbb{P}^{kj} = \mathbb{P}^{1\,(j-k+1)} \oplus \mathbb{P}^{(k-1)\,(j-1)}, \quad j \geq k, \tag{6}$$

Eq. (5) can also be represented in the following form

$$\frac{d\mathbf{X}^{\infty}}{dt} = \mathbb{P}^{\infty}(t)\mathbf{X}^{\infty},$$

where $\mathbb{P}^{\infty}(t)$ has an upper triangular block representation:

$$\mathbb{P}^{\infty} = \begin{pmatrix} \mathbb{P}^{11} & \mathbb{P}^{12} & \dots & \mathbb{P}^{1k} & \dots \\ \mathbb{O} & \mathbb{P}^{22} & \dots & \mathbb{P}^{2k} & \dots \\ \vdots & \vdots & \ddots & \vdots & \ddots \\ \mathbb{O} & \mathbb{O} & \dots & \mathbb{P}^{2k} & \dots \\ \vdots & \vdots & \ddots & \vdots & \ddots \end{pmatrix},$$

where block matrices $\mathbb{O}$ are zero matrices and $\mathbb{P}^{kj}$ can be evaluated using (6).

3.1.3. *Description of the beam initial manifold*

Eqs. (1) and (4) describe motion for a single particle—a so-called one-particle approximation. As a matter of fact, the particles beam is presented as a manifold occupied by phase points, so the problem is to describe the behaviour of the whole manifold. This can be done with the help of the following representations:

- Pointwise description.
  A set of phase vectors $\mathbb{M}_0^N = \{\mathbf{X}_0^1, \dots \mathbf{X}_0^N\}^*$, where $\mathbf{X}_0^i$ represents the phase vector of the i-th particle and operation * means transposition. In other words, we transfer from one particle description $\mathbf{X}_0$ to the set of particle description $\mathbb{M}_0^N$. Solution (3) should be replaced with

$$\mathbb{M}(s) = \mathbb{R}(s|s_0)\mathbb{M}_0^N, \tag{7}$$

  where $\mathbb{M}(s)$ is a final set of phase vectors corresponding to the particles on the target.
- Description in terms of a beam envelope matrix $\mathbb{S}$.
  We will treat two variants of this matrix. For the first variant, the corresponding elements σ_{ik}^{env} are defined as follows

$$\sigma_{ik}^{\text{env}} = x_i(k - \max(\mathfrak{M}))\, x_k(i - \max(\mathfrak{M})),$$

  where $x_i(k - \max(\mathfrak{M}))$ is the i-th component of the phase vector $\mathbf{X}$ with the maximal k-th component on the beam transverse manifold $\mathfrak{M}$. It is required to consider the restriction of components of the phase vector

$$x^2 = \sup_j \sup_{\mathfrak{M}_{(s)}} x_j^2 \le a^2,$$

  where a is an aperture radius.
  For the second variant, the σ-matrix is taken to be the well known rms-envelope matrix

$$\mathbb{S}^{\text{rms}}(s) = \int\limits_{\mathfrak{M}_{(s)}} f(\mathbf{X}, s)\mathbf{X}\mathbf{X}^* d\mathbf{X}, \tag{8}$$

  where $f(\mathbf{X}, s)$ denotes distribution function.
  For the linear beam line model, the propagation of σ-matrix is described by following equation (valid for both $\mathbb{S}^{\text{env}}$ and $\mathbb{S}^{\text{rms}}$)

$$\mathbb{S}(s) = \mathbb{R}(s|s_0)\mathbb{S}(s_0)\mathbb{R}^*(s|s_0), \tag{9}$$

  For the nonlinear case, we can use the nonlinear version[9] of the equality (9):

$$\mathbb{S}^{11}(s) = \sum_{i=1,k=1}^{\infty} \mathbb{R}^{1,i}(s|s_0)\mathbb{S}^{ik}(s_0) \left(\mathbb{R}^{1k}(s|s_0)\right)^*, \tag{10}$$

  where "nonlinear components" $\mathbb{S}^{ik}$, $i, k \le 1$ of the σ-matrix in (10) can be evaluated using the analogue of the equality (8)

$$\mathbb{S}^{ik}(s) = \int\limits_{\mathfrak{M}_{(s)}} f(\mathbf{X}, s)\mathbf{X}^{[i]} \left(\mathbf{X}^{[k]}\right)^* d\mathbf{X}, \tag{11}$$

  where $X^{[i]}, X^{[k]}$ are the Kronecker powers of the phase vector X of the corresponding orders.

- Description in terms of a distribution function $f_0(\mathbf{X}_0, s)$.
  Let us consider the distribution function as the function of quadratic form $\varkappa_0^2 = \mathbf{X}_0^* \mathbb{A}_0 \mathbf{X}_0$,

$$f_0(\mathbf{X}_0, 0) = \varphi_0(\varkappa_0^2) = \sum_{k=0}^{\infty} a_k^0 \varkappa_0^{2k},$$

  where a_k^0 are scalar coefficients, describing the form of distribution function on ellipsoid, bounded the beam initial manifold. Using the Lie algebraic tools,[13,14] one can write down the following equation

$$f(\mathbf{X}, s) = f_0(\mathcal{M}^{-1}(s|s_0; \mathcal{V}) \circ \mathbf{X}),$$

  where $\mathcal{M}(s|s_0; \mathcal{V})$ is an evolution operator, generated by the beam line and $\mathcal{V}(\mathbf{X}, s)$ is the Lie operator $\mathcal{V}(\mathbf{X}, s) = \mathbf{F}^*(\mathbf{X}, s)\, \partial/\partial \mathbf{X}$.
  For instance, one can use the following distribution functions:

$$f(\mathbf{X}, s) = f_n \exp\left(-\frac{\mathbf{X}^* \mathbb{S}^{-1} \mathbf{X}}{2}\right),$$

$$f(\mathbf{X}, s) = P_n(\varkappa_0^2) \exp\left(-\frac{Q_m(\varkappa_0^2)}{2}\right) \Theta(1 - \varkappa_0^2),$$

  where f_n is a normalizing factor, $\varkappa_0^2 = \mathbf{X}_0^* \mathbb{S}_0^{-1} \mathbf{X}_0$, while P_n and Q_m denote the polynomials of corresponding degrees, and Θ stands for the Heaviside function.

3.2. *Fringe Fields Modeling*

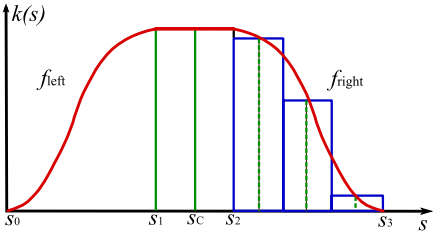

Fig. 1. A piecewise continuous approximation of the fringe field.

Fringe fields are intrinsic effects in any type of beam forming and focusing systems. Usually every kind of beam lines has a lot of control elements, so it is necessary to take into account a superposition of fringe fields for nearby magnets. The present paper deals with ordinary sum of fringe fields functions without investigation of induced fields in nearby elements. We consider symmetrical fringe fields relatively the center $s_c = (s_2 - s_1)/2$ of each element according to an experimental data (see Fig. 1). Also L_{eff} is supposed to be a constant. Assuming fringe field as a piecewise function, we can write down

$$f(s) = f_0 \begin{cases} f_{\text{l}}(s), & s \in [s_0, s_1), \\ 1, & s \in [s_1, s_2], \\ f_{\text{r}}(s), & s \in (s_2, s_3], \end{cases} \tag{12}$$

where $f_l(s)$ and $f_r(s)$ are the left (input) and right (output) parts of fringe field modeling function, f_0 is a maximum focusing strength ($k_{\max}$). In order to make $f(s)$ smooth in joints, it is necessary to imply several additional restrictions

$$\begin{aligned} f_{\rm l}(s_0) = f_{\rm r}(s_3) = 0, \quad f_{\rm l}(s_1) = f_{\rm r}(s_2) = f_0, \\ \frac{{\rm d}f_{\rm l}(s_0)}{{\rm d}s} = \frac{{\rm d}f_{\rm l}(s_1)}{{\rm d}s} = \frac{{\rm d}f_{\rm r}(s_2)}{{\rm d}s} = \frac{{\rm d}f_{\rm r}(s_3)}{{\rm d}s} = 0. \end{aligned} \tag{13}$$

In order to consider a broader class of modeling functions for fringe fields one can also use asymptotic conditions instead of (13), using, for instance, the Enge function[1])

$$\begin{aligned} \lim_{s\to+s_0} f_{\rm l}(s) &= 0, & \lim_{s\to-s_1} f_{\rm l}(s) &= f_0, \\ \lim_{s\to+s_0} \frac{{\rm d}f_{\rm l}(s)}{{\rm d}s} &= 0, & \lim_{s\to-s_1} \frac{{\rm d}f_{\rm l}(s)}{{\rm d}s} &= 0, \\ \lim_{s\to+s_2} f_{\rm r}(s) &= 0, & \lim_{s\to-s_3} f_{\rm r}(s) &= f_0, \\ \lim_{s\to+s_2} \frac{{\rm d}f_{\rm r}(s)}{{\rm d}s} &= 0, & \lim_{s\to-s_3} \frac{{\rm d}f_{\rm r}(s)}{{\rm d}s} &= 0. \end{aligned} \tag{14}$$

With the aid of conditions (13) or (14), we can construct smooth approximation of a quadrupole gradient distribution along the optical axis. This approach (see Fig. 2) is used in the special software for fringe field modeling. In the present paper we consider superposition of fringe fields as the direct sum of each fringe field.

Fringe fields of neighbour magnet lenses can be described as:

$$f^1(s) = f_0^1 \begin{cases} f_{\rm l}^1(s), & s \in [s_1, s_2), \\ 1, & s \in [s_2, s_3), \\ f_{\rm r}^1(s), & s \in [s_3, s_5], \end{cases} \quad f^2(s) = f_0^2 \begin{cases} f_{\rm l}^2(s), & s \in [s_4, s_6), \\ 1, & s \in [s_6, s_7), \\ f_{\rm r}^2(s), & s \in [s_7, s_8]. \end{cases} \tag{15}$$

The resulting fringe field of the two neighbour lenses takes the form

$$f(s) = \begin{cases} f^1(s), & s \in [s_0, s_4), \\ f_{sup}(s), & s \in [s_4, s_5), \\ f^2(s), & s \in [s_5, s_8], \end{cases} \tag{16}$$

where $f_{sup}(s) = f_{\rm r}^1(s) + f_{\rm l}^2(s)$.

As above mentioned, fragmentation of the whole system Fig. 1 could be done using representation of the field along the beam axis. The solution of motion equations with fringe field effects could be obtained using Eq. (4), where s_0 is an initial point and s_N is the final point (target).

Other points s_i can be selected, for instance, in the beginning and in the end of a drift, between the start and the end points of fringe field of each magnet lens.

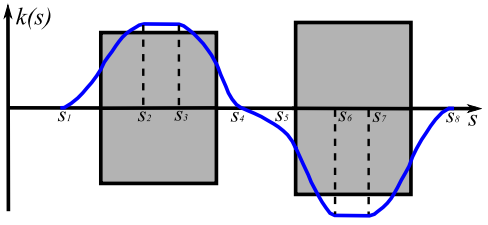

Fig. 2. An example of the fringe field superposition.

Although the segmentation of the fringe field can be performed arbitrary, one should take care of the accuracy of the approximation of the fringe field (see Fig. 1). In order to get necessary precision of the solution it is required to check the exact and the approximate matrizants.

Efficiency of function approximation could be estimated using two equivalent norms (see Fig. 1):

$$\|f-g\|_C = \sup_{s\in[s_0,s_3]} |f(s)-g(s)|, \quad \|f-g\|_{L_2} = \int_{s_0}^{s_3} \Big(f(s)-g(s)\Big)^2 \mathrm{d}s. \tag{17}$$

In order to estimate number of intervals for splitting of beam line (or its part), one can also use the following equation

$$\frac{\|\mathbb{R}_n(s_t|s_0) - \mathbb{R}_m(s_t|s_0)\|}{\|\mathbb{R}_n(s_t|s_0)\| + \|\mathbb{R}_m(s_t|s_0)\|} < \varepsilon, \quad \forall n,m > N(\varepsilon), \tag{18}$$

where s_0 is an initial point, s_t is a final point, $\{m,n,N\} \subset \mathbb{N}$ are the number of intervals. It is possible to use N or more intervals for unsure the necessary accuracy ε. It is more convenient to use estimation for matrizant because this parameter could be determined in practice.

Here we use a piecewise approximation of a fringe field (see Fig. 1) for necessary evaluations of the matrizant. This approach allows one to exploit the analytical formula for matrizant for any model of the fringe field. Usually in practice L_{eff} is used instead of the actual magnet length. This effective length could is introduced as

$$L_{\text{eff}} = \frac{1}{k_{\max}} \int_{s_0}^{s_3} k(s)ds = \gamma L_{\text{iron}},$$

where $k_{\max}$ is the maximum focusing strength of the field, γ is the experimental parameter for some type of magnet lens and L_{iron} is a real ("in iron") corresponding length of a magnet element.

Also fringe fields could be approximated with piecewise linear functions. Because of such approach real magnet field of steering elements is approximated with a set of trapezes. It is known that such representation is better than piecewise constant model. Using piecewise linear model, partial matrizants could be found in Airy[15] functions. For example, the following equations

$$\begin{cases} x'' + (ms+a)x = 0, & x' = dx/ds, \\ y'' - (ms+b)y = 0, & y' = dy/ds, \end{cases}$$

where m, a, b are constants have solutions in the form

$$\begin{cases} x(s) = C_1 A_i\left(-\dfrac{ms+a}{m^{2/3}}\right) + C_2 B_i\left(-\dfrac{ms+a}{m^{2/3}}\right), \\ y(s) = C_1 A_i\left(\dfrac{ms+a}{-m^{2/3}}\right) + C_2 B_i\left(\dfrac{ms+a}{-m^{2/3}}\right), \end{cases}$$

where C_1, C_2 are constants, A_i and B_i are the Airy special functions. For numerical calculations, series of Airy functions could be restricted by necessary number of terms (e. g. 6–8 terms). Because of the polynomial structure of Airy functions series it is easy to integrate, e. g. first 6–8 terms of the series analytically. Usually it is enough to keep 6–8 terms for necessary accuracy. Moreover, analytic formulas could be saved in data bases for using in computations. With the such base of integrated analytic functions and group property of matrizant, one can calculate full matrizant almost the same as for piecewise constant approximation. Also it is possible to use numerical methods for calculation of integrals, but using the analytical formulas is better because of its accuracy.

The fringe fields could be approximated with curvilinear trapezoids as well. However when it is necessary to approximate them even with second-order parabolic curves partial matrizants could be expressed with hypergeometric functions. Such matrizants are more complicated for calculations than matrizants for piecewise constant or piecewise linear model.

Using the experimental data and restrictions (13), we can approximate left-hand side (right-hand side could be found after mirroring left part relative to s_c) of real fringe fields for example with some approximation functions below:

- $f_{\mathrm{l}}(s) = A\sin(\nu s + \psi) + B$ is a trigonometric one,
- $f_{\mathrm{l}}(s) = As^3 + Bs^2 + Cs + D$ is a polynomial one.
  We also consider more complex approximation functions satisfying (14)
- $f_{\mathrm{l}}(s) = 1/\left[1 + \exp\left(1/P_5(s)\right)\right]$, where $P_5(s)$ is a five degree polynomial $As^5 + Bs^4 + Cs^3 + Ds^2 + Es + F$.

Also fringe field modeling function could be composite e. g. it may consist two or more parts. Some examples of such functions are following. One can obtain analytical solution for each such function,[4] so it is convenient to approximate real fringe field with them because of decreasing of calculating expenditure. Let us consider strictly increasing function $F(s)$ defined on (s_1, s_2). It is growing from zero (or neighborhood of zero) to its maximum value. Usually it is convenient to consider normalized function, when the maximum value is equal to 1. It is helpful to use reflection and sewing together transformations. One can reflect $F(s)$ using $F_{\mathrm{r}}(s) = F(-s + s_1 + s_2)$ transformation or sewing together two functions $F_1(s)$ and

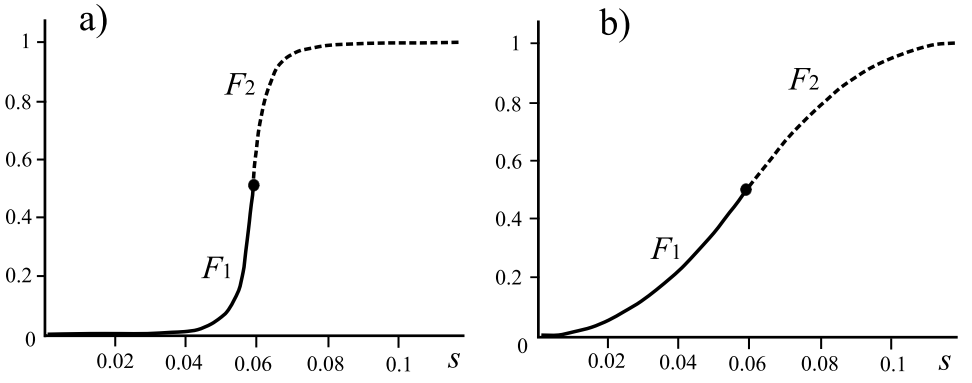

Fig. 3. Examples of piecewise-smooth functions which satisfied (13). Part a) represents model function (20) and part b)—model function (21).

$F_2(s)$. They could be found using the following equations

$$F_1(s) = \frac{F(2s)}{2}, \quad F_2(s) = -\frac{F\big(2(-s+s_2-s_1)\big)}{2} + F(s_2). \tag{19}$$

There are some classes of functions for fringe field modeling for which it is known the analytical matrizants. As an example it is possible to use the following function

$$F(s) = \frac{1}{2}\frac{1}{(a+bs)^4}. \tag{20}$$

The approximation plot for (20) is presented on Fig. 3a). After reflection the parameters for (20) could be e. g. $a = 1$, $b = 10$. For Fig. 3b) the model function $F(s)$ is following

$$F(s) = \frac{1+2n-s^2+(e^{2s^2})}{[H_n(s)]^4}, \quad F_m(s) = 72.4s^2 + \frac{72.4(e^{2s^2})}{(16s^4-48s^2+12)^4}, \tag{21}$$

where $H_n(s)$ is a Hermitian polynomial of degree n, $F_m(s)$ is an example of model function (see Fig. 3b)). Hereinafter we will use $F(s)$ for a class of functions and $F_m(s)$ for a model function from the corresponding class with specified parameters. Also $F_1(s)$ and $F_2(s)$ could be obtained from $F_m(s)$ using (19).

Fig. 4a) represents the plot for the following model function $F(s)$

$$F(s) = \alpha^2\left(1/2 - \cos^2\alpha s + 3/4\tan^2\alpha s\right), \quad \alpha = 10,\ F_m(s) = (-F+50)/523, \tag{22}$$

where $F_m(s)$ is an example of model function with $\alpha = 10$ (see Fig. 4a)). The following model function is corresponding to Fig. 4b)

$$F(s) = -\Big(\frac{n(n-1)}{s^2} + m^2 s^{2m-2} + m(m+2n-1)s^{m-2}\Big), \tag{23}$$

where $n = 1,\ m = 5,\ F_m(s) = 20.37F$. The plot of the following model function

$$F(s) = -\alpha^2\big[n - n(n-1)\,\mathrm{tg}^2\,\alpha t\big],\ \alpha = 10,\ F_m(s) = (-F+200)/1168. \tag{24}$$

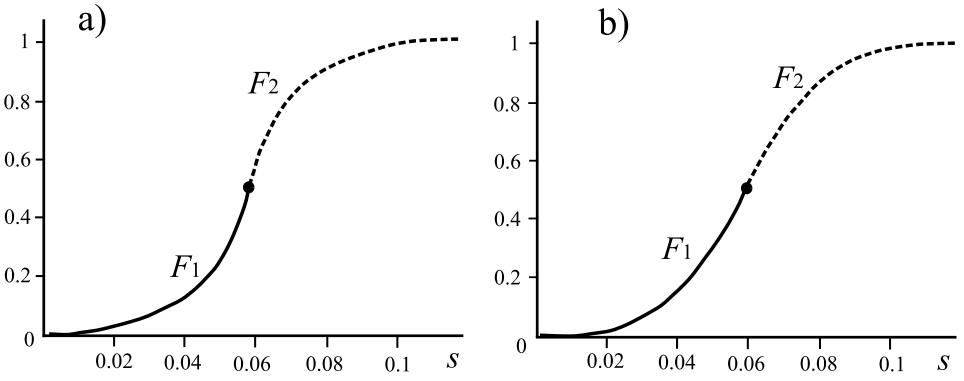

Fig. 4. Examples of piecewise-smooth functions satisfying (14). Part a) represents model function (22) and part b)—model function (23).

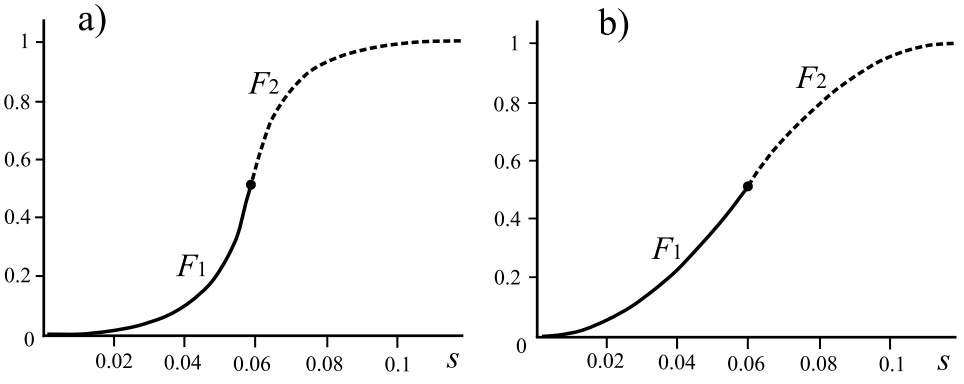

Fig. 5. Piecewise-smooth functions satisfying (14). Part a) represents model function (24) and part b)—model function (25).

is given on Fig. 5a). Finally, Fig. 5b) represents the following model function

$$F(s) = \frac{n(2m+1-s^2)}{4s^2} - n(n-1)\left(t - 2m\frac{H_{m-1}(s)}{H_m(s)}\right)^2, \qquad (25)$$

where $n = 1,\ m = 1,\ F_m(s) = 72(3 - F(s))$.

All the above described functions are symmetric, but one can create custom composite function, which can consist of two or more parts. For example it is possible to construct the modeling function of fringe field like on Fig. 6 by variation of the corresponding parameters. Using the experimental data, reflection and sewing together transformations for functions that have analytical solutions (e. g. some above mentioned) one can build necessary modeling functions. These functions help investigating real steer-

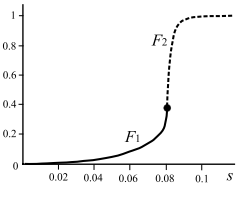

Fig. 6. An example of the fringe field modeling function.

ing fields with fringe fields effects. Also it is possible to use functions which do not have analytical solution, one can use the described above approaches of functions approximation using piecewise constant, piecewise linear model, second-order parabolic curves or even more smooth.

4. Nanoprobe Requirements

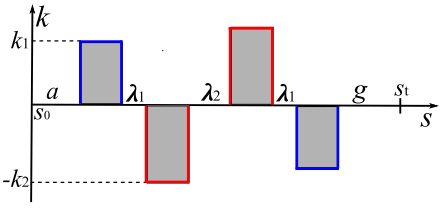

Fig. 7. A "russian quadruplet" focusing system.

As above mentioned as the basic system for nanoprobe we use "Russian quadruplet" (RQ). In the present paper we consider RQ with the same length of magnet lenses L_{eff} and with drift length λ_1 between first and second, and third and fourth lenses. Between couples of lenses drift length is λ_2. A drift gap ("pre-distance") has the length a, a focusing component—"objective" (has the length $s_t - s_0$), a drift gap with the length g—"working distance". Control system of quadrupoles satisfies "symmetry on power supply" condition, which can be written in the form of the following equality

$$k(s) = -k(s_t - s), \quad s \in [s_0, s_t], \tag{26}$$

where s is a length parameter measured along with optical axis of the system, s_0 is an initial point, s_t is an end point (see Fig. 7), $k(s)$ is a distribution function of gradient along the optical axis of the system. The matrizant $\mathbb{R}(s|s_0)$ (see eq. (3)) is the corresponding matrix propagator of the system, which can be presented as follows

$$\mathbb{R}(s_t|s_0) = \mathbb{R}_g \mathbb{M}(s_1|s_0)\mathbb{R}_a, \tag{27}$$

where partial propagators have a block-diagonal structure. Condition (26) is imposed on objective leads to contract between elements m_{ik} of the transfer matrix $\mathbb{M}$ in the following form:

$$\begin{aligned} m_{11} &= m_{44}, \ m_{12} = m_{34}, \\ m_{21} &= m_{43}, \ m_{22} = m_{33}. \end{aligned} \tag{28}$$

It is obviously that if the condition

$$m_{11} = m_{22}, \tag{29}$$

is correct, then we can get identical equality between transfer matrices in both planes $\{x, x'\}$, $\{y, y'\}$ from (28). It is also evidently that if the condition (29) is correct, full-length propagators will be equal in mentioned planes. Let us formulate requirements for nanoprobe:

- Demagnification requirements: $|r_{11}| = \gamma$, where γ is a desired demagnification parameter. Usually for nanoprobes it is less than 0.01 e. g. 0.001.

- Restrictions on working distance: $g \geq g_{\text{techn}} > 0$, where g_{techn} is a technological restriction on the working distance (other values of the length parameters should be also more than some technological restrictions).
- "Round to round beam condition": find control gradients of magnets, their lengths, lengths of drift gaps for ensure condition (29) in order to get round beam;
- "Point to point" condition: $r_{12} = r_{34} = 0$, it could be obtained from (29).

5. Computer Modeling

Because of requirements of nanoprobe high precision it is necessary to consider a lot of effects, find the most essential of them (one can compare an influence of various effects) and simulate the real focusing system. It is required to perform preliminary modeling of nanoprobe in order to save time and money. Let us illustrate an influence of fringe fields on the examples of load curves distortion and degradation of particle beam characteristics.

5.1. *Load curves distortion induced by fringe fields effects*

The load curves definition was introduced in A. D. Dymnikov and S. Ya. Yavor paper,[5] then it was used in papers of A. D. Dymnikov and S. N. Andrianov. These curves describe additional restrictions, which imposed on beam characteristics. The restrictions are associated with the same beam demagnification in both $\{x, s\}$ and $\{y, s\}$ planes. In some cases the restrictions could be more complicated and lead to load surfaces, which could describe particles distribution in the beam. The load curves concept demonstrated its efficiency, because it allows investigating geometrical properties of the corresponding curves and make conclusion about beam characteristics. In the present paper "load curves distortion" means a modification of

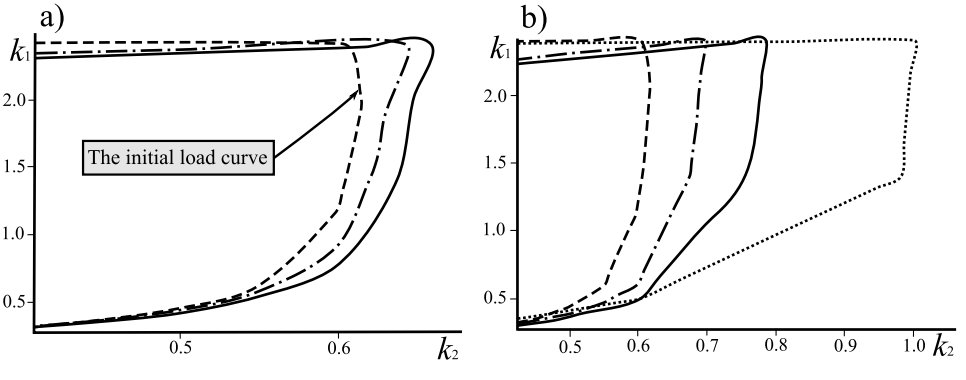

Fig. 8. The load curves distortion for fringe field parts are equal to $\frac{1}{32}$ (dash-dot curve) and $\frac{1}{16}$ (ordinary curve) for plot a) and $\frac{1}{8}$ (dash-dot curve), $\frac{1}{4}$ (ordinary curve) and $\frac{1}{2}$ (dash curve) for plot b).

the load curves from the initial stage (when fringe field length are equal to zero) to curves, which were created with taking into account of fringe fields. The fringe fields induced significant load curves transformation, so authors use the term "distortion" in order to emphasize of fringe field influence.

The fringe field modeling function could be built with different parameters, also length of fringe field could be varied. For example, in the present paper authors used $f_{\text{left}} = A\sin(\nu s + \psi) + B$ for left part of fringe field modeling function (see Fig. 1), where A, ν, ψ, B are parameters. The right part of fringe field could be easily obtained by reflecting over the center point s_c (see Fig. 1). Using (13) one can get $A = -k_{max}/2$, $B = k_{max}/2$ (where k_{max} is the maximum focusing strength of the field) and

$$\nu = \frac{\pi}{L_{fr}}, \quad \psi = \frac{\pi(3L_{fr} - 2s_c + L_0)}{2L_{fr}},$$

where $L_{fr} = s_1 - s_0$ is the fringe field length, $L_0 = L_{eff} - 2L_{fr}$ is the length of constant field part, $s_c = s_0 + L_{fr} + L_0/2$ is the center point coordinate (see Fig. 1).

The load curves could be constructed with taking into account of fringe fields effects. One can easily change fringe field length L_{fr} then recalculate modeling function for this length, approximate modeling function with e.g. piecewise constant model, calculate necessary matrizant for objective (see Eqs. (27)–(29)) and construct the load curves (see algorithm[3]).

The fringe field presentation and the corresponding beam line segmentation are presented on Fig. 1. One can split the beam line on several parts. Each quadrupole (for RQ system in the present paper) could be split like on Fig. 1. Using (4) full matrizant can be presented as a production of all partial matrizants. In the present paper we exploit well-known matrizant presentation for a piecewise constant model. Height of each rectangle is defined by value of modeling fringe field function in the middle of correspondent interval. Using model functions of fringe fields one can include experimental data into model, it is better than recalculation of matrizant for the whole system because it is easier to add some correction in fringe field model from real experimental data than recalculate all matrizants. This approach gives a necessary flexibility for researcher as opposed to full recalculation using only experimental data.

5.2. *Demagnification with fringe fields effects*

Fringe fields effects are intrinsic and could heavily impact on beam characteristics. One can find a set of optimal working points with different sensitivity using described above scheme of modeling process. For example if fringe field length L_{fr} increase from zero to 0.001 part of L_{eff} beam spot size could increase tenfold. In the Fig. 9 one can see L_{fr}, which means fringe field length, r_{11} and r_{33} are total matrizant elements, which describes demagnification in $\{x, s\}$ and $\{y, s\}$ planes correspondingly.

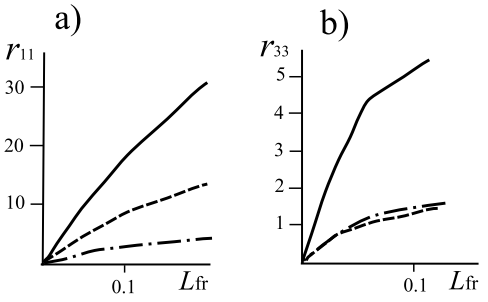

Fig. 9. The curves are corresponding to demagnification in $\{x, s\}$ and $\{y, s\}$ for three working points with different initial demagnification value: $r_{11}^0 = 0.0039$ is an ordinary curve, $r_{11}^0 = 0.0057$ is a dash curve and $r_{11}^0 = 0.046$ is a dash-dot curve.

5.3. *A working point movement*

It is necessary to move working point in order to improve beam characteristics with fringe fields effects. If all system parameters are constant with taking into account of fringe fields effects beam characteristics will be significantly worse than in piecewise constant model of the steering field.

If we put effective length of each lens $L_{\text{eff}} = 1$ and get some parameters from paper about Kiev's nanoprobe,[16] it is easy to calculate other parameters $a = 135.5625$, $\lambda_1 = 3.3$, $\lambda_2 = 5.5$. All lengths of magnet lenses are parameterized using $L_{\text{eff}} = 1$, so they become nondimensional parameters.

One can calculate working distance g using $r_{12} = 0$ equation, where r_{ij} are the elements of total matrizant of the system. Selection of working point could be illustrated on Fig. 10. If we choose $\varkappa_1 = 1.415$ and $\varkappa_2 = 0.608$ it it easy to calculate that $g = 0.47$, demagnification in $\{x, s\}$ plane $\text{DM}_x = 0.0042$ and demagnification in $\{y, s\}$ plane $\text{DM}_y = 0.0042$. Even through fringe field length of each lens is $L_{\text{fr}} = 1/32 L_{\text{eff}}$ demagnification parameters are $\text{DM}_x = 7.603$ and $\text{DM}_y = 1.49$ for $\{x, s\}$ and $\{y, s\}$ planes correspondingly. One can construct the load curve for $0 \le L_{fr} \le 0.5 L_{\text{eff}}$ using algorithm.[3] Fig. 10 represents load curves for $L_{\text{fr}} = 0$ and $L_{\text{fr}} = 1/32 L_{\text{eff}}$. It is required to move working point e.ġ. to $\varkappa_1 = 1.415$ and $\varkappa_2 = 0.63$ then one can obtain $\text{DM}_x = 0.0082$ and $\text{DM}_y = 0.0083$. In other words system parameters could be corrected in order to get more optimal beam characteristics, on Fig. 10 one should use the working point on the load curve which is corresponding to $L_{\text{fr}} = 1/32 L_{\text{eff}}$.

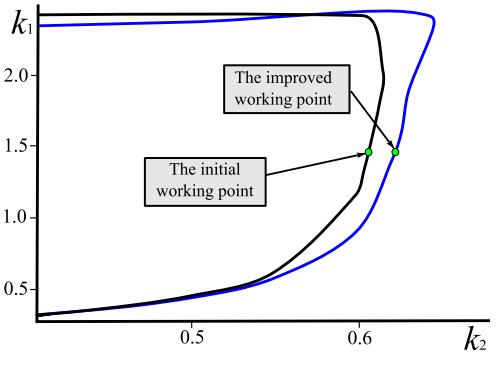

Fig. 10. The example of initial and improved working points.

6. Conclusion

There are a lot of models for fringe field presentation. One can select some of them, which better approximate real fringe fields using e.g. functional norms. Also researcher can construct his own modeling function and using the described above methodology evaluate fringe field influence. Beam lines constructors (after the investigation of fringe field influence) can modify magnet lens or lens arrangement in order to improve beam characteristics. The working point could be moved from the initial load curve to load curves with taking into account of fringe fields by continuity. If fringe field length a little grow so the working point a little move, but it should be on the other load curves (including fringe fields in calculations). In most cases the optimal working point means the point with the better demagnification values. The following list is summarizing the most essential ideas:

- After obtaining a set of optimal solutions it is required to drop too sensitive points.
- The fringe fields effects should be considered because they could heavily impact on beam characteristics.
- It is required to move working point from initial load curve to other load curve which was constructed with taking into account fringe fields effects in order to improve nanoprobe characteristics.
- Nonlinear effects and aberrations influence could be decreased using correction procedure with multipoles.
- It is necessary to realize comparative analysis of many effects in nanoprobe and struggle against the most essential parasitic effects.

References

1. Martin Berz, Béla Erdélyi and Kyoko Makino, Fringe Field Effects in Small Rings of Large Acceptance, in *Phys. Rev. ST Accel. Beams*, (Volume 3, 124001, 2000), 11 P.
2. Yu. L. Martirosyan, Investigation of Fringe Magnetic Fields Effects in Storage Rings, in *Journal of Technical Physics*, (Volume 73, Issue 10, 2003), P. 113–115. (in Russian)
3. Yu. Tereshonkov and S. Andrianov, Load Curves Distortion Induced by Fringe Fields Effects in the Ion Nanoprobe, in *Proc. European Particle Accelerator Conference*, (Italy, Genova, 2008), P. 1514–1516.
4. T. A. Antone and A. A. AL-Maaitah, Analytical solutions to classes of linear oscillator equations with time varying frequencies, in *Journal of Mathematical Physics*, (Volume 33, Issue 10, October 1992), P. 3330–3339.
5. A. D. Dymnikov, S. Ya. Yavor *J. of Techn. Phys.*, Vol. 33, Issue 7, P. 851-858, (1963).
6. S. N. Andrianov, A. D. Dymnikov and G.M. Osetinsky, Forming system for proton microbeams, *Instr. and Exper. Techn.*, Vol. 1, P. 39–42 (1978) (in Russian).
7. S. N. Andrianov, Some Problems of Nonlinear Aberration Correction *AIP Conf. Proc.* (N405. N.-Y., 1997), P. 103–116.
8. S. Andrianov, A. Chechenin, The High Order Aberration Correction, in *Proc. European Particle Accelerator Conference*, (Edinburgh, Scotland, 2006), P. 2125–2127.
9. S. Andrianov, N. Edamenko and Yu. Tereshonkov, Synthesis of optimal nanoprobe

(Nonlinear approximation), in *Proc. European Particle Accelerator Conference*, (Italy, Genova, 2008), P. 2972–2974.
10. F. R. Gantmacher, *The Theory of Matrices*, (Chelsea Publishing Company, New York, 1984).
11. S. Andrianov, N. Edamenko, A. Chernyshev and Yu. Tereshonkov, Synthesis of Optimal Nanoprobe (Linear Approximation), in *Proc. European Particle Accelerator Conference*, (Italy, Genova, 2008), P. 2969–2971.
12. S. N. Andrianov, *Dynamical Modeling of Beam Particle Control Systems*, (St. Petersburg State University, St. Petersburg, 2004) (in Russian).
13. A. J. Dragt, Lectures on Nonlinear Orbit Dynamics, in *AIP Conf. Proc.*, (No 87. NY, 1982), P. 147–313.
14. S. N. Andrianov, A Matrix Representation of the Lie Algebraic Methods for Design of Nonlinear Beam Lines *AIP Conf. Proc.* (N391. N.-Y., 1997), P. 355–360.
15. M. Abramowitz, I. A. Stegun (eds.), *Handbook of Mathematical Functions with Formulas, Graphs, and Mathematical Tables*, (U.S. Department of Commerce, New York, 2002).
16. S. A. Lebed, Double-mode probe forming system for modern ion nanoprobe, *J. of Applied Physics*, Vol. 72, 2002. P. 92–95 (in Russian).

International Journal of Modern Physics A
Vol. 24, No. 5 (2009) 816–842

World Scientific
www.worldscientific.com

SELF-CONSISTENT DISTRIBUTIONS FOR CHARGED PARTICLE BEAM IN MAGNETIC FIELD

OLEG I. DRIVOTIN* and DMITRI A. OVSYANNIKOV†

Applied Mathematics and Control Processes Department, Saint Petersburg State University, Saint Petersburg, Russia

** drivotin@ya.ru*

† dovs45@mail.ru

The problem of constructing self-consistent stationary particle distributions in four-dimensional phase space is considered for an azimuthally symmetric charged particle beam in a longitudinal magnetic field. In the general case of a longitudinally nonuniform beam, it is assumed that the magnetic field and the radius of the beam cross-section can slowly vary in the axial direction. The simplest case of a longitudinally uniform beam is studied in more detail. The approach applied here is to analyze the particle density in the space of integrals of motion. The relations between this density, the phase density, and the density in the configuration space are obtained. The set of admissible values of integrals of motion for a radially confined beam is examined. The construction of new self-consistent distributions consists in the specifying of some function defined on this set. Wide classes of new distributions are found. In particular cases, some of these distributions are identical to those known before, for example, the Kapchinsky-Vladimirsky distribution.

Keywords: Charged particle beam; Vlasov equation; self-consistent distributions; phase density.

PACS numbers: 41.75.-i, 52.27.Jt, 52.65.Ff

1. Introduction

The problem of constructing self-consistent distributions for a charged particle beam arises at high particle densities where the particle interaction essentially affects their dynamics. In this case, it is assumed that the distribution density of particles in the phase space evolves according to the Vlasov equation, which corresponds to the concept of self-consistent field; meaning that the force acting on a particle is determined as the mean force of the whole ensemble of particles. On the other hand, it is assumed that the particle density is small enough to neglect the particle interaction at close ranges by non-Coulomb forces, which can be allowed for by introducing the collision integral into the Vlasov equation.

The problem of finding stationary solutions to the Vlasov equation for the beam propagating through a longitudinal magnetic field was discussed in many works.[1–18]

The most known solution is the Kapchinsky-Vladimirsky (KV) distribution,[1] where the particles are evenly distributed across the beam and have the same energy of the transverse motion, so that their phase space distribution is described by the delta-function, and the dimension of the support of the distribution density function in the four-dimensional phase space of the transverse motion is equal to three. The simplest, and also well-known, case is the Brillouin flow,[3] where all particles rotate around the beam axis with the same angular velocity. In the latter case, the dimension of the support of the distribution density function is equal to two. Another known distribution is the water-bag distribution.[1,6,15] Its phase density is constant in that region of the phase space of the transverse motion where the energy of the transverse motion of a particle H is less than some given value of H_0, and equal to zero for $H > H_0$. A wide class of distributions can be obtained by making use of the density inversion theorem,[15] where one can find the relevant phase density of particles for a given density in the configuration space. This theorem also applies to the distributions characterized, as the water-bag distribution, by the fact that the phase density of particles is equal to zero for those regions of the phase space where the energy of the transverse motion of particles is greater than a given value of H_0, $H > H_0$, and it is not constant at the values smaller than H_0, $H < H_0$, as for the water-bag distributions, but varies so that it depends only on H and is independent of the angular momentum of particles, M.

The distributions were also investigated[2,15] for which the phase density depends on the linear combination $H + kM$, where k is some constant instead of H (so-called rigid rotor distributions). Thus, the analog of the KV distribution is the distribution for which all particles have the same value of $H + kM$. The density inversion theorem is also extended to this case and applies to the distribution for which the phase density depends only on the combination $H + kM$, and is equal to zero when $H + kM$ is greater than some limiting value.

Furthermore, the distributions have been investigated for the beam propagating through a periodic focusing magnetic field, and new distributions that are similar to the KV distribution and rigid rotor distributions have been found.[11,12,14,15,17]

In this paper we consider stationary self-consistent distributions for the axially symmetric beam propagating through a longitudinal magnetic field. Our approach is based on the analysis of the distribution density in the space of integrals of motion. Actually, the construction of new self-consistent distributions consists in specifying of some function defined on this set. We apply this approach to a longitudinally uniform beam and a beam in a longitudinally nonuniform field with the variable radius of the beam cross-section.

In the first case, under some conditions formulated below, the distribution density in the space of integrals of motion specifies a radially confined distribution of particles in the phase space. For the radially confined beam, the sets of admissible values for the integrals of motion and for the transverse components of the particle velocity are considered. The relations between the density in the space of integrals of motion, the phase density, and the density in the configuration space

are obtained. Making use of these relations, we may study a large class of distributions for which the phase density is a polynomial in the integrals of motion. In this case, substitution of the expression for the density in the configuration space into Poisson's equation reduces the problem of constructing self-consistent distributions to the boundary problem for the second-order ordinary differential equation. As an example of application of this technique, the uniform density distribution in the admissible region of the phase space is considered. This distribution differs from the known water-bag distribution in that the upper limit of the energy of the transverse motion of particles H depends on the angular momentum M, so that H can be greater than the value of H_0 for which the beam with the water-bag distribution has the same radius of the beam cross-section.

The solutions of the relevant boundary problem for various values of the beam parameters are found numerically. In addition, some properties of the solutions are given, specifically, the properties of the solutions for the beam current approaching the limiting value that is equal to the current of the Brillouin flow for the beam with the given radius of the cross-section. The proofs of these properties are not included in this paper. In particular, it follows from these properties that, as the beam current approaching the current of the Brillouin flow, the region of admissible values for the integrals of motion shrinks to the point which corresponds to the values of these integrals for the Brillouin flow, and the particle density in the configuration space tends to the density of the Brillouin flow. It is conceivable that the limit behavior of the other distributions for a radially confined beam is the same. Thus, although this distribution has been found not analytically but numerically, it helps in the investigation of some analytical properties of particle distributions. On the other hand, the solutions of the above-mentioned boundary problem can be considered as special functions, so that the particle density and the potential can be treated as analytical solutions.

Stationary axially symmetric self-consistent distributions with the uniform charge density across the beam are also studied in some detail. We have found broad classes of such distributions. The Kapchinsky-Vladimirsky distribution is a special case of these distributions. For such distributions, the region of admissible values for the integrals of motion has a simpler form. For the known KV distribution and similar distributions with the nonzero mean angular momentum, it is shown that the supports of their distribution density functions in the space of integrals of motion are straight-line segments. The linear combinations of such distributions are also analyzed. In this case, the density in the space of integrals of motion depends on an arbitrary integrable function with the given value of its integral. The particular case where this function is constant is considered as an illustration.

Furthermore, the integral equation is obtained for the particle distribution density in the space of integrals of motion. It is shown how broad classes of their solutions can be found. An example is provided where the solution is constructed as a third-degree polynomial.

Finally, we considered a longitudinally nonuniform beam with the uniform distribution of particles across the beam that is propagating through a longitudinal magnetic field slowly changing along the beam axis, which is not necessarily periodical. In this case, the equation of a particle radial motion and the envelope equation form the Ermakov system of simultaneous equations. The known integral of the Ermakov system is taken as one of the integrals of motion. A similar integral, also known as Courant-Snyder invariant, is used in the analysis of the transverse beam dynamics in the fields that are periodically linear in transverse coordinates. Making use of this integral instead of the energy of the transverse motion H, we have shown that the results for the beam with the constant radius and uniform charge density across the beam can all be generalized as the case of the longitudinally nonuniform beam.

2. Problem Formulation

We shall consider the stationary charged particle beam that is azimuthally symmetric and uniform along its axis and propagates through a uniform longitudinal magnetic field that is independent of the longitudinal position. In this case, the Vlasov equation for the phase density $n(\mathbf{x}, \mathbf{v})$ can be written as

$$\mathbf{v}\frac{\partial n}{\partial \mathbf{x}} + \frac{1}{m_0\gamma}\left(-\frac{e}{\gamma^2}\frac{\partial U}{\partial \mathbf{x}} + e[\mathbf{v}, \mathbf{B}]\right)\frac{\partial n}{\partial \mathbf{v}} = 0. \tag{1}$$

Here $\mathbf{x}$ is the transverse position of a particle, $\mathbf{v}$ is the vector of the transverse velocity (the transverse motion is regarded as nonrelativistic), e and m_0 are the charge and the rest mass of a particle, γ is the reduced particle energy, $\gamma = (1 - \beta^2)^{-1/2}$, $\beta = \dot{z}/c$ is the reduced longitudinal velocity that is assumed to be the same for all particles of a given cross-section and independent of the longitudinal position under the assumption of longitudinal uniformity. Further, $\mathbf{B}$ is the flux density of the applied magnetic field, U is the potential of the self-electric field of the beam satisfying Poisson's equation

$$\Delta U = -e\rho/\varepsilon_0, \tag{2}$$

ρ is the particle density in the configuration space,

$$\rho = \int n(x, v)\, dv,$$

ε_0 is the electric constant. The phase density n is assumed to be normalized according to

$$\int n(x, v)\, dv\, dx = J/(e\beta c), \tag{3}$$

where J is the beam current.

We shall assume that the potential $U(r)$ satisfies the boundary conditions

$$U(0) = 0, \qquad dU/dr|_{r=0} = 0. \tag{4}$$

The second condition can be interpreted as the condition for the absence of the particles with the zero radial velocity along the beam axis. The first condition specifies the potential on the beam axis. Strictly speaking, the potential should be set on some surface surrounding the beam. We shall assume that the beam propagates through a region surrounded by the perfectly conducting coaxial cylindrical wall located at a radius that is greater than the radius of the beam cross-section. Then, because of the longitudinal uniformity of the beam, the difference of the potentials at the axis and at the boundary is constant, and we can therefore set the potential on the axis. Furthermore, our model is applicable not only for the beam inside the cylindrical pipe, but also for the radially nonconfined beam. A similar model can be used for the beam propagating through the uniformly charged neutralizing background.

The problem is to find phase density n and potential U which satisfy the equations and the conditions (1)–(4).

Using the standard approach of the theory of partial differential equations, one can find that the characteristic lines of the Vlasov equation (1) are described by the ordinary differential equations

$$\frac{d\mathbf{x}}{dt} = \mathbf{v}, \qquad \frac{d\mathbf{v}}{dt} = \frac{1}{m_0\gamma}\left(-\frac{e}{\gamma^2}\frac{\partial U}{\partial \mathbf{x}} + e[\mathbf{v},\mathbf{B}]\right),$$

which are the particle orbit equations, and that the phase density conserves along the characteristic lines.[1] Integrating the system of the particle orbit equations, one can obtain the following first integrals[1]

$$r^2(\dot{\varphi} + \omega_0) = M, \tag{5}$$

$$\dot{r}^2 + \omega_0^2 r^2 + M^2/r^2 + 4\varepsilon U(r) = H. \tag{6}$$

Here r, φ, z are the cylindrical coordinates of a particle, $\omega_0 = eB_z/2m_0\gamma$, $\varepsilon = e/2m_0\gamma^3$, B_z is the component of $\mathbf{B}$ along z-axis (the transverse components of $\mathbf{B}$ are assumed to be equal to zero), dot means differentiation with respect to t. The right-hand sides of the equalities (5) and (6) contain some constants, M and H, that can be regarded as the integrals (or constants) of motion. The constant H, i.e. the energy of the transverse motion of a particle, and the constant M, i.e. its angular momentum, are multiplied in both cases by some constant coefficient. Note that the first integral (5) is also the first integral for the longitudinally nonuniform beam according to Bush's theorem.

The integral M characterizes the azimuthal motion: making use of Eq. (5) one can determine the azimuthal velocity $\dot{\varphi}$. The integral H characterizes the radial motion. Given M and H, the radial velocity $\dot{r}$ can be uniquely determined from Eq. (6). Then some trajectory in the phase space of the radial motion can be defined.

We shall formulate the sufficient condition, where for each admissible pair of values of the integrals M and H there is a well-defined trajectory in the phase space of radial motion. Let us consider the function

$$V_0(r) = \omega_0^2 r^2 + 4\varepsilon U(r) \tag{7}$$

and assume that $V_0(r)$ is a strictly convex function. Because $dV_0/dr|_{r=0} = 0$, the function $V_0(r)$ increases without bound as r increases. Therefore, the equation

$$H = V_0(r)$$

has exactly one root for $H \geq 0$ and has no roots otherwise. Let us denote this root by $r_{\max}(0, H)$, and set $r_{\min}(0, H) = 0$. We shall also consider the function $V_M(r) = V_0(r) + M^2/r^2$ at $M \neq 0$. This function is convex as a sum of two convex functions and has the unique minimum, because $V_M(r) \to \infty$, $dV_M/dr \to -\infty$ as $r \to 0$, and $V_M(r) \to -\infty$, $dV_M/dr > 0$ as $r \to \infty$. And then, for the H greater than this minimal value, the equation

$$H = V_M(r) \tag{8}$$

has exactly two roots. When H is equal to the minimum value of $V_M(r)$ Eq. (8) has one root. When H is less than this minimum, Eq. (8) has no roots. Denote the roots of Eq. (8) by $r_{min}(M, H)$ and $r_{max}(M, H)$, $r_{min}(M, H) < r_{max}(M, H)$. According to Eq. (6), the motion with the given M and H is possible only for the values of r belonging to the interval $[r_{min}(M, H),\ r_{max}(M, H)]$, because only in this interval the value of $\dot{r}$ can be determined. The functions $V_0(r)$ and $V_M(r)$ are plotted in Fig. 1.

If $M \neq 0$, and $r_{min}(M, H) \neq r_{max}(M, H)$, then $r_{min}(M, H)$ and $r_{max}(M, H)$ are the turning points of a particle with respect to the r coordinate. At these points, $\dot{r} = 0$. Furthermore, from Eq. (6) we have

$$\ddot{r} = -\omega_0^2 + M^2/r^3 - 2\varepsilon dU/dr = -0.5\, dV_M(r)/dr.$$

Since the function dV_M/dr is strictly increasing, we have $\ddot{r} < 0$ at $r = r_{max}(M, H)$, and $\ddot{r} > 0$ at $r = r_{min}(M, H)$.

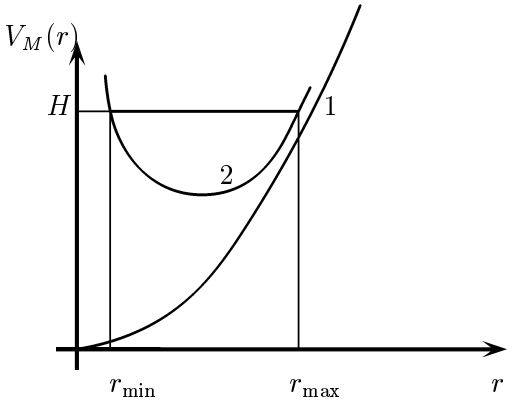

Fig. 1. The curves 1 and 2 represent the plots of the functions $V_0(r) = \omega_0^2 r^2$ and $V_M(r) = M^2/r^2 + \omega_0^2 r^2, M \neq 0$, respectively. The motion of a particle with the given M and H is possible only within the interval $[r_{min}(M, H), r_{max}(M, H)]$.

Therefore, the transverse motion of a particle can be described as follows: the radial coordinate r of a particle increases from the value $r = r_{min}(M, H)$ to the value $r = r_{max}(M, H)$. As this takes place, the particle rotates around the beam axis through the angle $\delta\varphi$, which can be found by making use of Eq. (5). Then r again decreases to the value $r = r_{min}(M, H)$, and the particle rotates through the same angle $\delta\varphi$, etc. If, however, $r_{min}(M, H) = r_{max}(M, H)$, then $\dot{r} = 0$, $\ddot{r} = 0$, and the trajectory of a particle is a circumference. When $M = 0$, the pattern of motion remains as before, except that $\dot{r} \neq 0$ at $r = r_{min}(0, H)$.

Since the coordinate φ is not included in (5) and (6), rotating the trajectory of a particle corresponding to the given M and H through any angle around the beam axis yields the trajectory corresponding to the same M and H. Therefore, if the function $U(r)$ is such that $V_0(r)$ is a strictly convex function, then the particle trajectories are radially confined, and for each pair of the values of M and H (from the region of admissible values that will be discussed below) there is a set of trajectories that are reciprocally transferable through rotation around the beam axis.

3. Particle Distribution in the Space of Integrals of Motion

We shall consider some stationary axially symmetric distribution of beam particles in the four-dimensional phase space of the transverse motion. This distribution can be described by the density of particles in the phase space $n(\mathbf{x}, \mathbf{v})$. We also introduce the distribution density $f(M, H)$ of the beam particles in the space of the integrals of motion M and H. Three conditions shall be imposed on the distribution. First, we require that the self electric potential be such that the function $V_0(r)$ defined in the previous section is strictly convex. As we have seen, under this condition, each admissible pair of H and M yields a set of radially confined trajectories, which can be conversely transferred through rotation around the beam axis. Second, we require that the particles corresponding to each admissible pair of M and H be uniformly distributed over all trajectories of this set. The second condition ensures the axial symmetry of the distribution as a whole. Finally, we also require that for each trajectory, the particles be uniformly distributed over the phases of the trajectory. In other words, this condition can be formulated as follows: the segments of the trajectories corresponding to equal time intervals must contain equal numbers of the particles. The last condition ensures the stationarity of the distribution.

Under these three conditions, each function $f(M, H)$ defined for the admissible values of M, H corresponds to some stationary distribution that is axially symmetric and uniform along the axis.

Let us establish the relation between the density $f(M, H)$ for the stationary axially symmetric beam and the phase density $n(\mathbf{x}, \mathbf{v})$. The phase density as the fourth-degree differential form has different components in different systems of coordinates. For the sake of convenience, we introduce the following notation: let the density of the particle distribution over the variables $a, b, \ldots$ be $\frac{DN}{D(a, b, \ldots)}$. This

means that the quantity $\frac{DN}{D(a,b,\ldots)}\,da\,db\ldots$ gives the average number of particles in the infinitely small volume $da\,db\ldots$.

We shall consider the component of the phase density in coordinates $x, y, \dot{x}, \dot{y}$, which can be written in terms of our notations as $\frac{DN}{D(x,y,\dot{x},\dot{y})}$. Since for the same admissible value of H there are two values of the radial velocity (when $\dot{r}^2 > 0$) differing in sign, the phase density as a function of M and H has two branches: one branch corresponding to the particles moving away from the axis, and the other corresponding to the particles approaching the axis. In view of the fact that $\dot{\varphi} = (x\dot{y} - \dot{x}y)/r^2$, $\dot{r} = (x\dot{x} + y\dot{y})/r$, we then have

$$\frac{DN}{D(x,y,\dot{x},\dot{y})} = \frac{1}{2}\frac{DN}{D(x,y,M,H)}\det\left|\left(\frac{\partial(M,H)}{\partial(\dot{x},\dot{y})}\right)\right| = r|\dot{r}|\frac{DN}{D(x,y,M,H)}. \quad (9)$$

As for the particles for which $\dot{r} \equiv 0$ (i.e. the particles moving along the circular trajectories), we assume that they do not contribute to the phase density. These particles occupy a region with zero volume in the four-dimensional phase space of transverse motion.

Because for each pair M, H the particles are uniformly distributed over the angles and phases of trajectories, the value of $\frac{DN}{\partial(x,y,M,H)}$ is independent of the azimuthal coordinate φ and the radial coordinate r within the interval $[r_{min}(M,H), r_{max}(M,H)]$. Then

$$\frac{DN}{D(M,H)} = \int_0^{2\pi}\int_{r_{min}(M,H)}^{r_{max}(M,H)} \frac{DN}{D(x,y,M,H)}\,r\,dr\,d\varphi = 2\pi\frac{DN}{D(x,y,\dot{x},\dot{y})}P(M,H), \quad (10)$$

where $P(M,H)$ denotes the integral

$$P(M,H) = \int_{r_{min}(M,H)}^{r_{max}(M,H)} \frac{dr}{|\dot{r}|} = \int_{r_{min}(M,H)}^{r_{max}(M,H)} \frac{dr}{\sqrt{H - \omega_0^2 r^2 - M^2/r^2 - 4\varepsilon U(r)}}. \quad (11)$$

Note that the expression under the square root in (11) is always positive in accordance with the above assumption.

The equality (10) can be written as

$$n(\mathbf{x},\mathbf{v}) = \frac{f(M(\mathbf{x},\mathbf{v}),H(\mathbf{x},\mathbf{v}))}{2\pi P(M(\mathbf{x},\mathbf{v}),H(\mathbf{x},\mathbf{v}))}. \quad (12)$$

This equality establishes the relation between the phase density $n(\mathbf{x},\mathbf{v})$, given in the phase space of the transverse motion and the density $f(M,H)$, that is, the particle density in the space, where the integrals of motion M, and H are the phase variables, and this space will be called the space of the integrals of motion. Recall that the equality (12) is meaningful for a stationary axially symmetric beam when the above three conditions are fulfilled.

Making use of the relation (9), we may express the particle density in the configuration space

$$\rho(r) = \int\limits_{\Omega(r)} \frac{DN}{D(x,y,M,H)}\, dM\, dH = \frac{1}{2\pi r} \int\limits_{\Omega(r)} \frac{DN}{D(x,y,\dot{x},\dot{y})} \frac{dM\, dH}{|\dot{r}|}.$$

Here $\Omega(r)$ is the set of admissible values of M and H, that will be considered below. Substituting here the expression for the phase density (12), we obtain

$$\rho(r) = \frac{1}{2\pi r} \int\limits_{\Omega(r)} \frac{f(M,H)\, dM\, dH}{P(M,H)(H - M^2/r^2 - \omega_0^2 r^2 - 4\varepsilon U(r))^{1/2}}. \tag{13}$$

Substituting the expression (13) into Poisson's equation written in cylindrical coordinates and taking into account the fact that derivatives with respect to φ and z are equal to zero due to the symmetry of the distribution, we obtain integro-differential equation for the potential $U(r)$:

$$\frac{d}{dr} r \frac{dU}{dr} = -\frac{e}{2\pi\varepsilon_0} \int\limits_{\Omega(r)} \frac{f(M,H)\, dM\, dH}{P(M,H)(H - M^2/r^2 - \omega_0^2 r^2 - 4\varepsilon U(r))^{1/2}}. \tag{14}$$

So, the problem of constructing stationary self-consistent distributions that are azimuthally symmetric and axially uniform reduces to the solution of the boundary problem (14), (4) with the additional condition of strict convexity for the function (7).

In what follows we shall consider only the radially confined beam: $r \le R$ where R is the beam radius. In this section, and in the following two sections, we shall assume that R is independent of the coordinate z. Let us determine the set of admissible values for M and H. Denote this set by Ω_R. It follows from Eq. (6) that

$$H \le M^2/R^2 + \omega_0^2 R^2 + 4\varepsilon U(R). \tag{15}$$

On the other hand, $H > H_{\min} = \min\limits_r V_M(r)$, or

$$H > V_M(r_0(M)) \tag{16}$$

where $r_0(M)$ is the value of r corresponding to the minimum of the function $V_M(r)$.

The set Ω_R defined by the inequalities (15) and (16) is presented in Fig. 2.

We shall also consider the set $\Omega(r)$ of all admissible values of the integrals of motion H and M for the particles whose trajectories pass through a point with the radial coordinate r. It is clear that this set is given by the inequalities (15) and

$$H > V_M(r). \tag{17}$$

The maximum value of $|M|$ is determined from the condition of simultaneous solvability of the inequalities (15) and (17), which has the form

$$|M| \le rR\left[\omega_0^2 + 4\varepsilon \frac{U(R) - U(r)}{R^2 - r^2}\right]^{1/2}.$$

The set $\Omega(r)$ is presented in Fig. 2.

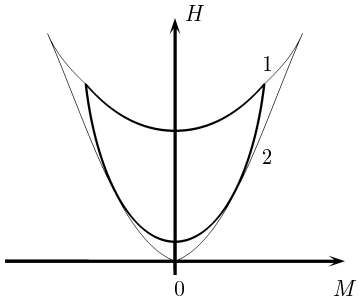

Fig. 2. The sets Ω_R and $\Omega(r)$. Thin lines represent the boundaries of the set Ω_R : 1 – $H = \omega_0^2 R^2 + M^2/R^2 + 4\varepsilon U(R)$; 2 – $H = \min_r V_M(r)$. The boundaries of the set $\Omega(r)$ are depicted by thick lines.

In the four-dimensional phase space with coordinates $r, \varphi, v_r = \dot{r}, v_\perp = r(\dot{\varphi} + \omega_0)$, the set

$$\frac{v_r^2}{1 - r^2/R^2} + v_\perp^2 \le \omega_0^2 R^2 + 4\varepsilon R^2 \frac{U(R) - U(r)}{R^2 - r^2} \tag{18}$$

is the set of all admissible values of the phase variables and corresponds to the closure of the set Ω_R. When φ and r in (18) are fixed, $r \in [0, R]$, we obtain the section of the specified set by the surfaces $r = const$, $\varphi = const$, that are the ellipses centered at the point $v_r = 0$, $v_\perp = 0$ with semiaxes $\{\omega_0^2(R^2 - r^2) + 4\varepsilon(U(R) - U(r))\}^{1/2}$, $\{\omega_0^2 R^2 + 4\varepsilon R^2(U(R) - U(r))/(R^2 - r^2)\}^{1/2}$ directed along the axes v_r and $v_\perp$, respectively. These sections at various r are shown in Fig. 3 (the dependence on φ is lacking due to axial symmetry). Thin lines depict the boundaries of the set of admissible values $v_r, v_\perp$ for four values of $r : 0, r_1, r_2, R \quad (0 < r_1 < r_2 < R)$. All points within the boundaries are admissible, but the support of the actual distribution density function may not be identical to the entire region within the boundaries; it must only be included in this region.

As an example, the support of the distribution density function for KV distribution,[1] for which all particles have the same value of the integral of motion $H : H = \omega_0^2 R^2 + 4\varepsilon(U(R) - U(r))$, is shown in Fig. 3. This support is represented by the circumferences $v_r^2 + v_\perp^2 = \omega_0^2(R^2 - r^2) + 4\varepsilon(U(R) - U(r))$ (the thick lines in Fig. 3). The KV distribution will be considered below in more detail. The bold dot at the origin represents the Brillouin flow, where all particles rotate as a whole around the z-axis with the angular velocity $-\omega_0$.[3]

4. Distribution with Uniform Phase Density

Finding the self-consistent distribution for the arbitrary density $f(M, H)$ is a very difficult problem, because the right-hand side of Eq.(14) contains the unknown function $P(M, H)$ in the integrand, depending on the potential $U(r)$. Furthermore, the domain of integration in Eq. (14) also depends on $U(r)$. To simplify the problem,

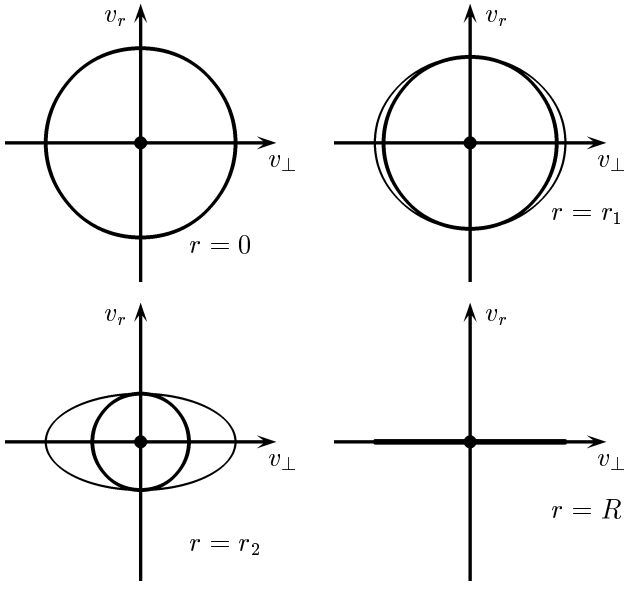

Fig. 3. The sets of admissible values of transverse velocities at various values of r.

one can find the solution not for the given density $f(M,H)$, but for the given ratio $f(M,H)/2\pi P(M,H)$. This value represents the right-hand side in the relation (11), which expresses the phase density in terms of the density $f(M,H)$. Therefore, to specify this ratio is to specify the phase density for the corresponding values of the phase variables. When this ratio is a polynomial in M,H, we may obtain a finite expression for the density $\rho(r)$ making use of Eq. (13).

Introducing new integration variables into the expression (13):

$$\theta = atan\frac{rR\sqrt{H-\omega_0^2r^2-M^2/r^2-4\varepsilon U(r)}}{M(R^2-r^2)^{1/2}}, \quad v=\sqrt{\frac{H-\omega_0^2r^2-M^2/R^2-4\varepsilon U(r)}{R^2-r^2}}$$

and making use of the relation (12) we may obtain

$$\rho(r) = 2R^2\sqrt{R^2-r^2}\int\limits_0^\pi d\theta \int\limits_0^{\sqrt{\omega_0^2+4\varepsilon(U(R)-U(r))/(R^2-r^2)}} \tilde{f}(v^2(R^2-r^2\sin^2\theta)+V_0(r), vrR\cos\theta)v\,dv. \quad (19)$$

Here $\tilde{f}(M,H) = f(M,H)/2\pi P(M,H)$, so that $n(\mathbf{x},\mathbf{v}) = \tilde{f}(M(\mathbf{x},\mathbf{v}),H(\mathbf{x},\mathbf{v}))$. The integrand in Eq. (19) is the polynomial in v, $\cos\theta$, and integrable in terms of elementary functions.

For example, consider the first-degree polynomial:

$$\tilde{f}(M,H) = n_0 + \alpha_1 H + \alpha_2 M$$

where n_0, α_1, α_2 are the arbitrary constants bounded only by the condition $\tilde{f}(M,H) \geq 0$. Integrating the expression (19) gives

$$\rho(r) = \pi R(R^2 - r^2)^{1/2}\left[\omega_0^2 + 4\varepsilon\frac{U(R) - U(r)}{R^2 - r^2}\right]\{n_0 + \alpha_1[\omega^2 r^2 + 4\varepsilon U(r)]\}$$

$$+\pi\alpha_1\frac{R(R^2 - r^2)^{1/4}}{2}(R^2 - \frac{r^2}{2})\left[\omega_0^2 + 4\varepsilon\frac{U(R) - U(r)}{R^2 - r^2}\right]^2. \tag{20}$$

In the simplest case of the zeroth polynomial, where the phase density is constant at all admissible values of the integrals of motion M and H, Poisson's equation takes the form

$$\frac{1}{y}\frac{d}{dy}y\frac{d\Phi}{dy} = -\lambda\left[(1 - y^2)^{1/2} - \frac{\Phi(y)}{(1 - y^2)^{1/2}}\right] \tag{21}$$

where $y = r/R$, $\Phi(y) = 4\varepsilon(U(yR) - U(R))/\omega_0^2 R^2$, $\lambda = 4\pi e n_0 \varepsilon R^2/\varepsilon_0 > 0$. According to the conditions (4), the boundary conditions for Φ are

$$\Phi(1) = 0, \qquad \left.\frac{d\Phi}{dy}\right|_{y=0} = 0. \tag{22}$$

A similar (but not identical) distribution, known as the water-bag distribution was investigated earlier (see [1, 6, 15]).

For the water-bag distribution, particles fill the region between the line $H = H_0$, where $H_0 = \omega_0^2 R^2 + 4\varepsilon U(R)$, and the lower boundary of the set Ω_R defined by the inequality (16). For the distribution under consideration, the upper boundary for H is not H_0, but is given by the inequality (15).

The boundary problem (21), (22) has a unique solution for each positive value of the parameter λ.

We may prove that $d^2\Phi/dy^2 > -2$. It follows from this inequality that the foregoing condition for the strict convexity of the function $V_0(r) = \omega_0^2 R^2(y^2 + \Phi(y)) + 4\varepsilon U(R)$ is satisfied.

We may also prove that

$$0 \leq \lambda\left[(1 - y^2)^{1/2} - \frac{\Phi(y)}{(1 - y^2)^{1/2}}\right] \leq 4, \tag{23}$$

and

$$\lim_{\lambda\to\infty} \lambda\left[(1 - y^2)^{1/2} - \frac{\Phi(y)}{(1 - y^2)^{1/2}}\right] = 4. \tag{24}$$

The left-hand side inequality in (23) implies that the particle density is positive, so that the solution $\Phi(y)$ is physically feasible.

Note that the particle density is equal to

$$\frac{\omega_0^2\varepsilon_0}{4e\varepsilon} = \lambda\left[(1 - y^2)^{1/2} - \frac{\Phi(y)}{(1 - y^2)^{1/2}}\right]\frac{\rho_B}{4}$$

according to (21) where $\rho_B = \varepsilon_0 B_z^2 \gamma / 2m_0$ is the density of the Brillouin flow. Therefore, the right-hand side inequality in (23) implies that the particle density at any point does not exceed the density of the Brillouin flow. Finally, the property (24) implies that the limiting value of the density is the density of the Brillouin flow.

We shall now consider how the set Ω_R varies with the parameter λ. The relation (24) gives

$$\Phi(y) = 1 - y^2 - \frac{4}{\lambda}\left(1 - y^2\right)^{1/2} + o\left(\frac{1}{\lambda}\right).$$

Then

$$V_M(r) = \frac{M^2}{r^2} + \omega_0^2 R^2 - \frac{2\omega_0^2 R(R^2 - r^2)^{1/2}}{\lambda} + 4\varepsilon U(R) + o\left(\frac{1}{\lambda}\right).$$

Therefore, the admissible values of M are of an order of $O(\lambda^{-1/2})$. The admissible values of H belong to the segment $[H_{\max}, H_{\max} - \Delta H]$, where $H_{\max} = M^2/R^2 + \omega_0^2 R^2 + 4\varepsilon U(R)$,

$$\Delta H = H_{\max} - \frac{M^2}{r_0^2} - \omega_0^2 r_0^2 - 2\varepsilon U(r_0) = \frac{M^2}{R^2} - \frac{M^2}{r_0^2} + O\left(\frac{1}{\lambda}\right) = O\left(\frac{1}{\lambda}\right),$$

and the r_0 value is the minimum of the function $V_M(r)$. So, the limit distribution for the distributions under consideration is the Brillouin flow for which the particle density is constant: $\rho_0 = \rho_B$, and the electric current is $J = e\beta cL = \pi R^2 \rho_0 e\beta c = \pi e\varepsilon_0 R^2 B^2 \gamma \beta c / 2m_0$.

The phase density is equal to $n_0 = \lambda\varepsilon_0 / 4\pi e R^2 \varepsilon$, so that $n_0 \to \infty$ as $\lambda \to \infty$.

The boundary problem (21), (22) at various values of the parameter λ was solved numerically making use of the Runge-Kutta method. The results of the numerical solution for various values of the parameter are presented in Fig. 4.

5. Distributions with Uniform Charge Density in Beam Cross-Section

This section focuses on the particle distributions for which the particle density in the configuration space $\rho(r)$ is the step-function of the radial coordinate r, being

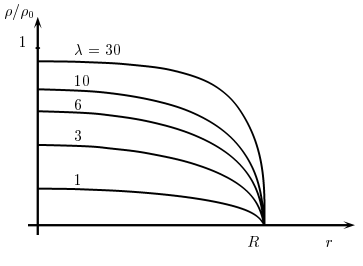

Fig. 4. Radial profiles of beam density at various λ.

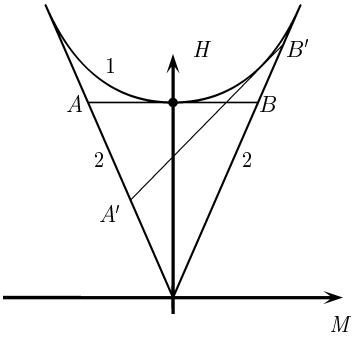

Fig. 5. The set Ω_R for the uniform beam. The curve 1 represents the upper boundary of the set Ω_R : $H = M^2/R^2 + \omega^2 R^2$. The segments 2 represent the lower boundary of the set Ω_R : $H = 2\omega|M|$.

constant inside the beam cross-section and zero outside:

$$\rho(r) = \begin{cases} \rho_0, & r \le R, \\ 0, & r > R. \end{cases} \tag{25}$$

Making use of Poisson's equation, we then obtain $U(r) = -\rho_0 r^2/4\varepsilon_0$. Introducing the variable ω :

$$\omega^2 = \omega_0^2 - \rho_0\varepsilon/\varepsilon_0 \tag{26}$$

($\omega^2 > 0$ for the radially confined beam), we obtain $P(M,H) = \pi/2\omega$, and the expression (13) takes the form

$$\rho(r) = \frac{\omega}{\pi^2 r} \int\limits_{\Omega(r)} \frac{f(M,H)\,dM\,dH}{(H - M^2/r^2 - \omega^2 r^2)^{1/2}}. \tag{27}$$

The sets of admissible values of M and H are determined by the inequalities (15), (16), (17), which in this case take the form

$$2\omega|M| < H \le M^2/R^2 + \omega^2 R^2, \quad \omega^2 r^2 + M^2/r^2 < H \le M^2/R^2 + \omega^2 R^2 \tag{28}$$

for Ω_R and $\Omega(r)$, respectively. The set Ω_R is shown in Fig. 5.

The simplest known distribution is the Brillouin flow. For this, all particles have the same values of integrals M and H : $M = 0$, $H = \omega^2 R^2$. It is depicted in Fig. 5 by the bold dot.

We assume that

$$f(M,H) = f_0\delta(H - H_0 - kM), \quad f_0 > 0, \quad (M,H) \in \Omega_R \tag{29}$$

where $\delta(H - H(M))$ denotes the simple layer on the surface $H = H(M)$ whose density relative to the variable H is equal to 1. This means that for some set Ω

$$\int\limits_{\Omega} F(M,H)\delta(H - H(M))\,dM\,dH = \int\limits_{S} F(M,H(M))\,dM$$

for an arbitrary integrable function $F(M, H)$. Here, S is the intersection of the surface $H = H(M)$ with the set Ω.

For the distribution (29), the density of particles in the configuration space $\rho(r)$ is independent of r (at $r \le R$). Indeed,

$$\rho(r) = \frac{\omega f_0}{\pi^2 r} \int\limits_{\Omega(r)} \frac{\delta(H - H_0 - kM)\, dM\, dH}{(H - M^2/r^2 - \omega^2 r^2)^{1/2}} =$$

$$\frac{\omega f_0}{\pi^2 r} \int\limits_{M_1}^{M_2} \frac{dM}{(H_0 + kM - M^2/r^2 - \omega^2 r^2)^{1/2}} = \frac{\omega f_0}{\pi} = \rho_0.$$

Here M_1 and M_2 are the roots of denominator in the integrand:

$$M_{1,2} = kr^2/2 \pm (k^2 r^4/4 + H_0 r^2 - \omega^2 r^4)^{1/2}.$$

The maximum value of the coordinate r which satisfies the condition $k^2 r^4/4 + H_0 r^2 - \omega^2 r^4 \ge 0$ is equal to $[H_0/(\omega^2 - k^2/4)]^{1/2}$. On the other hand, this value is equal to R. Hence, we have $H_0 = R^2(\omega^2 - k^2/4)$.

It can be readily seen that M_1 and M_2 are the abscissas of the points of intersection of the straight line $H = H_0 + kM$ with the boundaries of the set Ω_R : $H = 2\omega M$ and $H = -2\omega M$, because these boundaries are also determined by the condition that the above-mentioned integrand denominator is equal to zero. Obviously, $H_0 > 0$ and $k^2 < 4\omega^2$.

It can be shown that the straight line $H = H_0 + kM$ is tangent to the parabola $H = M^2/R^2 + \omega^2 R^2$, that is the upper boundary of H belonging to Ω_R. Thus, the support of the distribution density function (29) is the segment of the straight line that is tangent to the upper boundary of Ω_R and included in Ω_R (the segment $A'B'$ in Fig. 5). The extreme positions of the segment are the straight-line parts of the boundary of the set Ω_R.

The distributions (29) are well known. In the works [2, 4, 15] they are considered as the simplest example of what is known as the rigid rotor distribution. In the general case, the rigid rotor distribution is a distribution such that the phase density depends only on the combination $H + kM$, but not on M and H separately. To find the density in the configuration space for the rigid rotor distribution, which is generally not uniform, the density inversion theorem can be used (e.g., see [15]). The KV distribution is the particular case corresponding to $k = 0$ (the segment AB in Fig. 5).

The mean angular momentum for the distributions (29) is not equal to zero, except for the KV distribution. This can be seen from Fig. 5 where the parts of the segment $A'B'$ lying on the left and on the right of the axis H are not equal. Therefore, these distributions, with the exception of the KV distribution, are not good models, because a real beam is launched with the zero mean angular momentum.

Note that the values of f_0 can be arbitrary large. Indeed, substituting the expression for ρ_0 into (26) and solving with respect to ω, we obtain

$$\omega = -\frac{\varepsilon f_0}{2\pi\varepsilon_0} + \left[\frac{\varepsilon^2 f_0^2}{4\pi^2\varepsilon_0^2} + \omega_0^2\right]^{1/2}.$$

If $f_0 \to \infty$, the main term of the last expression is equal to $\pi\varepsilon_0\omega_0^2(\varepsilon f_0)^{-1}$. Therefore $\rho_0 \to \varepsilon_0\omega_0^2/\varepsilon = \rho_B$. The set Ω_R shrinks to the point $(0,0)$ because the size of the set Ω_R is determined by ω, and $\omega \to 0$. Thus, the limit distribution as $f_0 \to \infty$ is the Brillouin flow.

It is easy to understand that by taking arbitrary linear combinations of the distributions (29) we shall obtain the beam cross-section uniform distributions. For example, consider the linear combination of a finite number of distributions (29):

$$f(M,H) = \sum_{k\in K} f_k\delta(H - H_0(k) - kM), \quad f_k > 0 \tag{30}$$

where $H_0(k) = R^2(\omega^2 - k^2/4) > 0$ and K is a finite set of real numbers, $K \subset (-2\omega, 2\omega)$. Substituting (30) into (27) we have

$$\rho_0 = \frac{\omega}{\pi}\sum_{k\in K} f_k.$$

Similarly, it is not difficult to show that the values of f_k can be arbitrary large. If $f_k \to \infty$ for any $k \in K$ then $\rho_0 \to \varepsilon_0\omega_0^2/\varepsilon$, and the limit distribution is also the Brillouin flow.

In general,

$$f(M,H) = \int_{-2\omega}^{2\omega} f(k)\delta(H - H_0(k) - kM)\,dk, \quad f(k) > 0. \tag{31}$$

Let us find k corresponding to the given values of M and H in Eq. (31). From the equation $H = (\omega^2 - k^2/4)R^2 + kM$ we have

$$k_{1,2} = \frac{2}{R^2}\left[M \pm (M^2 - HR^2 + \omega^2R^4)^{1/2}\right]. \tag{32}$$

It follows from (32) that $dk = dH(M - kR^2/2)^{-1}$. Then (31) can be written as

$$f(M,H) = \int_{2\omega|M|}^{M^2/R^2+\omega^2R^2} \sum_{i=1}^{2} \frac{f(k_i)\delta(H - R^2(\omega^2 - k_i^2/4 - k_iM))\,dH}{|M - k_iR^2/2|} =$$

$$\frac{f(k_1) + f(k_2)}{(M^2 - HR^2 + \omega^2R^4)^{1/2}}.$$

Substituting (31) into (27), we may obtain

$$\rho_0 = \frac{\omega}{\pi^2 r}\int_{-2\omega}^{2\omega} f(k)\,dk \int_{\Omega(r)} \frac{\delta(H - H_0(k) - kM)dM\,dH}{(H - M^2/r^2 - \omega^2r^2)^{1/2}} =$$

$$\frac{\omega}{\pi^2 r}\int\limits_{-2\omega}^{2\omega} f(k)\,dk \int\limits_{\Omega(r)} \frac{dM}{(H_0 + kM - M^2/r^2 - \omega^2 r^2)^{1/2}} = \frac{\omega}{\pi}\int\limits_{-2\omega}^{2\omega} f(k)\,dk.$$

As before, it can be shown that any finite values of $f(k)$ are admissible.

Obviously, the first two distributions (29) and (30) that we have discussed are the particular cases of the distribution (31).

The distributions (30) and (31) cannot be found on the basis of the approach applied in the works [15, 16] where each distribution is described making use of its own effective potential, and, therefore, two of them cannot be readily combined.

The simplest case which cannot be reduced to the previous cases is the distribution with $f(k) = F_0, \quad F_0 = \pi\rho/(4\omega^2)$. In this case,

$$f(M,H) = \frac{\pi\rho_0}{2\omega^2(M^2 - HR^2 + \omega^2 R^4)^{1/2}}. \tag{33}$$

The four-dimensional volume of the support of this distribution density function is not equal to zero. The phase density is given by the expression

$$n = \frac{\rho_0}{2\pi\omega\sqrt{R^2 - r^2}} \cdot \frac{1}{\sqrt{\omega^2 R^2 - v_r^2/(1 - r^2/R^2) - v_\perp^2}},$$

as it follows from (12). Here $v_\perp = r(\dot\varphi + \omega_0)$.

6. Integral Equation for Uniform Charge Distributions

More general results can be obtained by considering the expression (27) for density $\rho(r)$ as the integral equation. Substituting the expression (25) into the left-hand side of (27) and taking into account the fact that the integration domain is determined by the inequalities (28), we obtain the integral equation for the function $f(M,H)$:

$$\rho_0 = \frac{\omega}{\pi^2 r}\int\limits_{-rR\omega}^{rR\omega} dM \int\limits_{M^2/r^2+\omega^2 r^2}^{M^2/R^2+\omega^2 R^2} (H - \omega^2 r^2 - M^2/r^2)^{-1/2} f(M,H)\,dH, \quad r \le R.$$

Here, the left-hand side is independent of r $(r \le R)$, but the integrand and integration limits on the right-hand side are dependent on r. The problem is to find a function $f(M,H)$ such that the result of integration is also independent of r.

Let us introduce new integration variables y, α :

$$H = M^2/R^2 - \omega^2(R^2 - r^2)y^2 \sin^2\alpha + \omega^2 R^2, \quad M = rR\omega y\cos\alpha,$$

and the function

$$F(k_1,k_2) = f(M,H)(M^2 - HR^2 + \omega^2 R^4)^{1/2}.$$

Here $k_{1,2}$ are the slopes of the straight lines passing through the point (M,H) and being tangent to the curve $H = M^2/R^2 + \omega^2 R^2$, that is a part of the boundary of

the set Ω_R, as determined by the relation (32). Expressing $k_{1,2}$ in terms of y, α, we have

$$k_1 = 2y\cos(\alpha-\theta), \quad k_2 = 2y\cos(\alpha+\theta) \quad \text{where} \quad \theta = \arccos r/R.$$

Obviously, $k_i \in (-1,1), \quad i=1,2$. It follows from $\alpha \in [0,\pi]$ that $k_1 \geq k_2$. Therefore, $F(k_1,k_2)$ is defined in the triangle $-2\omega < k_2 \leq k_1 < 2\omega$. We assume that in the triangle $-2\omega < k_1 < k_2 < 2\omega$, the function $F(k_1,k_2)$ is defined by the equality

$$F(k_1,k_2) = F(k_2,k_1). \tag{34}$$

Then the integral equation under consideration can be written as

$$\rho_0 = \frac{1}{\pi^2}\int_0^{2\pi}\int_0^1 \frac{F(2y\cos(\alpha-\theta), 2y\cos(\alpha+\theta))}{(1-y^2)^{1/2}} y\,dy\,d\alpha. \tag{35}$$

It is easy to see that the function $F(k_1,k_2) = f_1(k_1) + f_2(k_2)$ satisfies this equation. Taking into account the condition (34), we find that $f_2(x) = f_1(x) + c$ (c is a constant). Without loss of generality, we may assume that $c = 0$. Then

$$f(M,H) = \frac{f_1(k_1) + f_1(k_2)}{(M^2 - HR^2 + \omega^2R^4)^{1/2}}. \tag{36}$$

So, we have the same result as for the integral representation (31).

Moreover, analyzing the equation (35), we can obtain other density functions $f(M,H)$ for which the particle distribution is uniform in the beam cross-section. The solution of Eq. (35) can be sought for as a series

$$F(x,z) = \sum_{m=0}^{\infty}\sum_{n=0}^{\infty} c_{mn}x^m z^n.$$

It can be seen that the coefficients c_{m0} are arbitrary, in which case the convergence of the series

$$\sum_{m=0}^{\infty} c_{m0}x^m$$

at $x \in (-2\omega, 2\omega)$ must be ensured, and $c_{0m} = c_{m0}$. Furthermore, it follows from (34) that $c_{mn} = c_{nm}, m,n > 0$. The condition of nonnegativity for the function $f(M,H)$ can be satisfied for the bounded function $F(x,z), x,z \in (-2\omega, 2\omega)$ by adding some positive constant F_0 to $F(x,z)$.

Instead of the remaining series

$$\sum_{m=1}^{\infty}\sum_{n=1}^{\infty} c_{mn}x^m z^n,$$

we shall consider a polynomial in x,z. Substituting it into (35), we may obtain its coefficients.

For example, in the case of the third-degree polynomial $F(x,z) = c_1xz + c_2x^2z^2 + c_3(xz^3 + x^3z)$, we may obtain two equalities: $5c_1 + 6c_3\omega^2 = 0$ and $c_2 = 0$ from (35). Therefore,

$$F(k_1,k_2) = ck_1k_2[24\omega^2 - 5(k_1^2 + k_2^2)].$$

Hence, the function

$$f(M,H) = \frac{-c(H - \omega^2R^2)(10M^2 - 5HR^2 + 2\omega^2R^4) + F_0}{(M^2 - HR^2 + \omega^2R^4)^{1/2}}$$

gives the beam cross-section uniform distribution. The constants c and F_0 in this expression should be such that the values of $f(M,H)$ be positive at any admissible values of M, H.

The values of the function $F(k_1,k_2)$ can be arbitrary large. Here the equality (26) implies that the density ρ_0 is bounded above by the Brillouin flow density $\rho_B = \varepsilon_0\omega_0^2/\varepsilon$.

7. Distributions for a Beam with Non-Constant Radius

This section focuses on particle distributions for the stationary azimuthally symmetric beam in the longitudinal magnetic field that is, as before, uniform in the beam cross-section, but a more general case is investigated. Suppose that the radius of the beam cross-section and the magnetic field vary in the longitudinal direction. As in Section 5, the particle density in the configuration space $\rho(r,z)$ is assumed to be a step-function of the radial coordinate r :

$$\rho(r,z) = \begin{cases} \rho_0(z), r \le R(z), \\ 0, \qquad r > R(z). \end{cases}$$

We assume that the radius of the cross-section R significantly varies only at the distances that are much greater than R. Then Poisson's equation for the potential of the self electric field of the beam $U(r,z)$ can be written as

$$\frac{1}{r}\frac{\partial}{\partial r}r\frac{\partial U}{\partial r} = \frac{e\rho_0(z)}{\varepsilon_0}.$$

According to (3), $\rho_0(z) = J/(\pi R^2 e\dot{z}) = \lambda/R^2$ where $\lambda = J/(\pi e\dot{z})$, J is the beam current, and $\dot{z}$ is the longitudinal velocity of a particle assumed to be equal for all particles. We also assume that the longitudinal velocity can slowly vary in the axial direction. The longitudinal component of the magnetic field vector potential satisfies a similar equation. Then the equation of the radial motion of particles is given by

$$\ddot{r} = -\omega^2 r + M^2/r^3 \tag{37}$$

where $\omega^2 = \omega_0^2 - \lambda/R^2$. Here M is the same integral as before, but in this case the variable H given by (6) is not an integral. Let us formulate the conditions under which another integral of the equation (37) exists.

We assume that the beam envelope $R(z)$ can be defined as the envelope only for particles with $M = 0$. We shall see at a later time that this assumption holds for the distributions under consideration. For the particles with $M = 0$, the equation of the radial motion is linear:

$$\dot{X} = AX \tag{38}$$

where

$$X = \begin{pmatrix} r \\ \dot{r} \end{pmatrix}, \ A = \begin{pmatrix} 0 & 1 \\ -\omega^2 & 0 \end{pmatrix}.$$

We assume that at the initial instant of time $t = t_0$ the particles fill the ellipse

$$X_0^* B_0 X_0 \leq 1, \ B_0 = \begin{pmatrix} a_0^{-2} & 0 \\ 0 & c_0^{-2} \end{pmatrix}.$$

Then, at $t \geq t_0$, they will fill the ellipses

$$X^* B X \leq 1$$

where $B = F^{*-1} B_0 F^{-1}$, and F is the matrizant of the system (38). It can be readily shown that R^2 is the first diagonal element of the matrix B^{-1} :

$$R^2 = (B^{-1})_{11} = a_0^2 F_{11}^2 + c_0^2 F_{12}^2.$$

The matrix elements $F : F_{11}$ and F_{12} satisfy the equations

$$\ddot{F}_{11} = -\omega^2 F_{11}, \ \ddot{F}_{12} = -\omega^2 F_{12}.$$

Introducing the variable $\theta : a_0 F_{11} = R\cos\theta$, so that $c_0 F_{12} = R\sin\theta$, we pass to the following equations

$$\ddot{R} - R\dot{\theta}^2 = -\omega^2 R, \tag{39}$$

$$2\dot{R}\dot{\theta} + R\ddot{\theta} = 0. \tag{40}$$

Note that, in our case, the t-dependence of R is given by the relation $R = R(z(t))$. In view of the fact that $F(t_0)$ is the identity matrix, we have $R(t_0) = a_0$, $\dot{R}(t_0) = 0$, $\theta(t_0) = 0$, $\dot{\theta}(t_0) = c_0/a_0$.

Integrating the equation (40), we obtain $\dot{\theta} = a_0 c_0 / R^2$. Then the equation (39) for the beam envelope takes the form

$$\ddot{R} = -\omega^2 R + \frac{a_0^2 c_0^2}{R^3} \tag{41}$$

or

$$\ddot{R} = -\omega_0^2 R + \frac{\lambda}{R} + \frac{a_0^2 c_0^2}{R^3}. \tag{42}$$

The system of equations (37) and (41) can be reduced to the known Ermakov system[19,20] if the variable ω which depends on t and R is regarded as a function of t.

Using the known expression for the integral of the Ermakov system,[20] we may have that the value

$$I = (R\dot{r} - r\dot{R})^2 + \frac{M^2R^2}{r^2} + \frac{a_0^2c_0^2r^2}{R^2} = \left(\frac{dq}{d\tau}\right)^2 + \frac{M^2}{q^2} + a_0^2c_0^2q^2 \tag{43}$$

is the integral of motion. Here $q = r/R$, $d\tau = dt/R^2$. Another integral of the motion M can be written as

$$M = q^2\left(\frac{d\varphi}{d\tau} + R^2\omega_0\right). \tag{44}$$

Note that, when $M = 0$, and $\omega = \omega(t)$, the integral (43) is identical to the well-known Courant-Snyder invariant.[21]

Let us find a set $\tilde{\Omega}_1$ in the space of variables M, I such that the condition $q \le 1, \forall t \ge t_0$ holds for all particles.

It follows from (43) that

$$I \le M^2 + a_0^2c_0^2. \tag{45}$$

Furthermore,

$$I \ge \min_q\left(\frac{M^2}{q^2} + a_0^2c_0^2q^2\right) = 2a_0c_0|M|.$$

Excluding the particles corresponding to the lower boundary of the set Ω_1, we obtain

$$I > 2|M|a_0c_0. \tag{46}$$

The set $\tilde{\Omega}_1$ defined by the conditions (45),(46) is shown in Fig. 6. A similar set Ω_R for the longitudinally uniform beam was considered in Sections 3 and 5. Comparing Figs. 5 and 6, one can see that the shapes of the sets Ω_R and $\tilde{\Omega}_1$ are identical, but the vertical axes are different: axis H in Fig. 5 and axis I in Fig. 6.

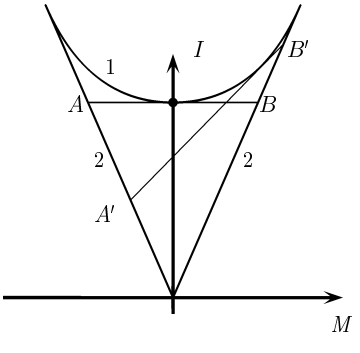

Fig. 6. The set $\tilde{\Omega}_1$. The curve 1 represents the upper boundary of the set $\tilde{\Omega}_1 : I = M^2 + a_0^2c_0^2$. The segments 2 represent the lower boundary of the set $\tilde{\Omega}_1 : I = 2a_0c_0|M|$.

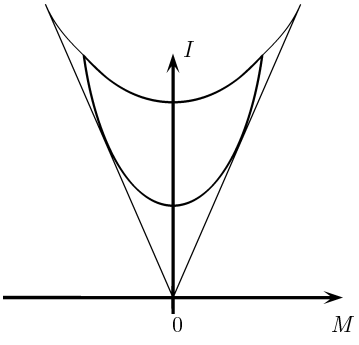

Fig. 7. The set $\tilde{\Omega}(q)$. The boundaries of $\tilde{\Omega}(q)$ are depicted by thick lines, with the thin lines representing the boundaries of the set $\tilde{\Omega}_1$.

If the beam particles fill the set $\tilde{\Omega}_1$, the assumption that the beam envelope can be determined only by the particles with $M = 0$ will represent the facts. This follows from the condition $q \leq 1$, or $r \leq R$, which determines the set $\tilde{\Omega}_1$.

We shall also consider a set $\tilde{\Omega}(q)$ of M and I such that the particles possessing these M and I pass through a point corresponding to the given q. First, note that

$$I \geq \frac{M^2}{q^2} + a_0^2 c_0^2 q^2. \tag{47}$$

If the inequality (47) is satisfied, then $I - M^2/q^2 - a_0^2 c_0^2 q^2 \geq 0$, and the particle can move at a point corresponding to this q. Furthermore, we have the inequality (45) bounding the value of the integral I for the given value of the integral M. Therefore, the set $\tilde{\Omega}(q)$ is defined by (47), (45) (see Fig. 7).

The set $\tilde{\Omega}(q)$ in Fig. 7 appears as the set $\Omega(r)$ in the Fig. 2, but here the differences are the same as those between Fig. 5 and Fig. 6.

We shall consider the particular case $R = const$, $\lambda = const$, $\omega_0 = const$. Here, as it follows from Eq. (42), the beam radius is equal to $R = (\lambda + \sqrt{\lambda^2 + 4\omega_0^2 a_0^2 c_0^2})/(2\omega_0^2)$. Expressing c_0^2 from this equality, we find that $c_0^2 = \omega^2 R^2$. Then $I = HR^2$. So, for the beam with constant radius the integrals I, H are the same, if the factor R^2 is not taken into account.

In what follows we shall consider the phase distribution of the particles of some infinitely thin layer moving along the axis z with the velocity $\dot{z}$. We assume that this layer is bounded by two parallel infinitely close planes moving along the axis z with the same velocity. Making use of the notation introduced in Section 3, we shall consider the density in the four-dimensional phase space of transverse positions and velocities $n = DN/D(x, y, \dot{x}, \dot{y})$ (here x, y are transverse Cartesian coordinates).

We assume that the phase density n depends only on M and I :

$$n = n(M(r, \dot{\varphi}), I(r, \dot{r}, \dot{\varphi}))$$

where $n(M, I)$ denotes some function of M and I. Our goal is to find those functions $n(M, I)$ which correspond to the uniform distribution of particles across the

beam. The mapping $(r, \dot{r}, \varphi, \dot{\varphi}) \mapsto (M, I)$ has rank 2. This means that we drop two variables on which the phase density can depend. The independence from the variable φ implies the axial symmetry of the beam. The independence from the third variable r among the remaining three variables r, M, I narrows the class of admissible distributions, but significantly simplifies the further analysis because in this case the conservation of the phase density along particle trajectories implies the conservation of $n(M, I)$ along the z-axis.

Then we have

$$\frac{DN}{D(q, M, I)} = \int_0^{2\pi} d\varphi \frac{DN}{D(q, \varphi, M, I)} = 4\pi \frac{DN}{D(q, \varphi, q', \varphi')} |det \frac{\partial(q', \varphi')}{\partial(M, I)}| =$$

$$\frac{2\pi}{q^2|q'|} \frac{DN}{D(q, \varphi, q', \varphi')} = \frac{2\pi}{q^2|q'|} \frac{1}{R^4} \frac{DN}{D(q, \varphi, \dot{q}, \dot{\varphi})} =$$

$$\frac{2\pi}{q^2|q'|} \frac{1}{R^4} \frac{DN}{D(x, y, \dot{x}, \dot{y})} |\det \frac{\partial(x, y, \dot{x}, \dot{y})}{\partial(q, \varphi, \dot{q}, \dot{\varphi})}| = \frac{2\pi}{|q'|} n(M, I) \tag{48}$$

(stroke denotes differentiation with respect to the variable τ).

Let us introduce the density of the particle distribution in the space of the integrals M and I : $f(M, I)$. It follows from Eq. (48) that

$$f(M, I) = \int_{q_{min}(M,I)}^{q_{max}(M,I)} \frac{DN}{D(q, M, I)} \, dq = \pi^2 n(M, I)/a_0 c_0 \tag{49}$$

because

$$\int_{q_{min}(M,I)}^{q_{max}(M,I)} dq/|q'| = \pi/2a_0 c_0.$$

Expressing the particle density in the configuration space $\rho(r)$ in terms of $f(M, I)$, we obtain

$$\rho(r) = \frac{1}{2\pi r} \int_{\Omega_q} \frac{DN}{D(r, M, I)} \, dM \, dI = \frac{1}{rR} \int_{\tilde{\Omega}(q)} \frac{n(M, I) \, dM \, dI}{|q'|}. \tag{50}$$

We also introduce the particle density in the space with the coordinates x/R, y/R denoted by $\tilde{\rho}$. From Eq.(49), Eq.(50), in view of Eq.(42), we may obtain

$$\tilde{\rho}(q) = \frac{a_0 c_0}{\pi^2 q} \int_{\tilde{\Omega}(q)} \frac{f(M, I) \, dM \, dI}{(I - M^2/q^2 - a_0^2 c_0^2 q^2)^{1/2}}. \tag{51}$$

In the expression (51) we exclude the particles for which $q' \equiv 0$ in accordance with (46). To allow for these particles shall require an additional term in the expression (51). In particular, it is precisely this term that can describe the distribution analogous to the Brillouin flow for the longitudinally uniform beam. For this distribution, all particles have the same values of the integral of motion $M : M = 0$, and the values of the integral I are such that $dq/d\tau = 0$, namely $I = a_0^2 c_0^2 q^2$. As distinct from the Brillouin flow, all particles can move in the radial direction, but simultaneously, so that their normalized coordinate q remains constant for each particle. If R, λ, ω_0 are constant, this distribution is identical to the Brillouin flow. Therefore, it can be called the generalized Brillouin flow.

The expression (51) is similar to the expression (27) obtained in Section 5 for the beam with the constant radius. The integral of motion I and the constant $a_0 c_0$ correspond to the integral of motion H and the constant ω. Therefore, the results of that section can also be extended to the this case.

Comparing the expressions (27) and (51), we can see they have the same structure, but differ in variables that occur in them: the variable r in (27) is replaced by q in (51), H by I and ω by the product $a_0 c_0$. Therefore, one can expect that for every distribution described in Sections 5 and 6 there exists a similar distribution for a longitudinally nonuniform beam.

First, we shall consider the distributions that are similar to the distributions (29), (30), (31). Let us take $f(M, I)$ as a simple layer with density f_0 in respect of the variable I on the segment belonging to the set Ω_1 in the same sense as in Section 5:

$$f(M, I) = f_0 \delta(I - I_0(k) - kM), \ f_0 > 0, \ (M, I) \in \Omega_1 \tag{52}$$

where $I_0(k) = a_0^2 c_0^2 - k^2/4$.

Substituting (52) into (51) we have

$$\tilde{\rho}(q) = \frac{a_0 c_0 f_0}{\pi^2 q} \int\limits_{\Omega_q} \frac{\delta(I - I_0(k) - kM)\, dM\, dI}{(I - M^2/q^2 - a_0^2 c_0^2 q^2)^{1/2}} =$$

$$\frac{a_0 c_0 f_0}{\pi^2 q} \int\limits_{M_1}^{M_2} \frac{dM}{(I_0 + kM - M^2/q^2 - a_0^2 c_0^2 q^2)^{1/2}} = \frac{a_0 c_0 f_0}{\pi}, \quad q < 1.$$

Here M_1 and M_2 are determined from the condition that the argument of the square root in the integrand becomes zero:

$$M_{1,2} = kq^2 \pm (k^2 q^4/4 + I_0 q^2 - a_0^2 c_0^2 q^4)^{1/2}.$$

Hence, for the distribution (52), the density of particle distribution in the configuration space is constant throughout the beam cross-section, and, therefore, it is the solution of the problem.

In much the same way as for the distribution (29), it can be shown that the support of the distribution density function (52) is a segment of the straight line

that is tangent to the upper boundary of the set $\tilde{\Omega}_1$. The segment is bounded by the lines $I = \pm 2a_0c_0M$ (segment A'B' in Fig. 6). When $k = 0$, this segment is parallel to the axis M (segment AB in Fig. 6). If R, λ, ω_0 are constant, the distribution (52) at $k = 0$ is identical to the KV distribution, and the distribution at $k \neq 0$ is identical to the distribution (29).

Furthermore, each linear combination of the distributions (52) will also be uniform in the beam cross-section:

$$f(M, I) = \sum_{k \in K} \alpha_k \delta_{I = I_0(k) + kM}, \quad \rho = \frac{a_0 c_0}{\pi R^2} \sum_{k \in K} \alpha_k$$

where K is a finite set of real numbers, $K \subset (-2a_0c_0, 2a_0c_0)$, or

$$f(M, I) = \int\limits_{-2a_0c_0}^{2a_0c_0} \alpha(k) \delta_{I = I_0(k) + kM}\, dk, \quad \rho = \frac{a_0 c_0}{\pi R^2} \int\limits_{-2a_0c_0}^{2a_0c_0} \alpha(k)\, dk.$$

Here, α_k in the first case or $\alpha(k)$ in the second one are the functions defined on the discrete set K or on the interval $(-2a_0c_0, 2a_0c_0)$ such that there are respectively

$$\sum_{k \in K} \alpha_k \quad \text{or} \quad \int\limits_{-2a_0c_0}^{2a_0c_0} \alpha(k)\, dk.$$

Another way to seek for the uniform self-consistent distributions is to consider the equality (51) as an integral equation for the density of the distribution.

Introducing new integration variables in much the same way as in the case of the longitudinally uniform beam (Section 6), we obtain the integral equation

$$\frac{a_0^2 c_0^2}{2\pi} \int\limits_0^{2\pi} \int\limits_0^1 \frac{F(y\cos(\alpha - \theta), y\cos(\alpha + \theta))}{(1 - y^2)^{1/2}} y\, dy\, d\alpha = J \tag{53}$$

which is similar to the equation (27). Here

$$F(k_1, k_2) = \begin{cases} f(M, I)(M^2 - I + a_0^2 c_0^2)^{1/2}, k_1 \geq k_2, \\ F(k_2, k_1), k_1 < k_2, \end{cases}$$

$k_{1,2} = 2(M \pm (M^2 - I + a_0^2 c_0^2)^{1/2})$ and $\theta = \arccos q$. This is exactly the integral equation for the function of two arguments $F(k_1, k_2)$. Both arguments depend on q as $q = \cos\vartheta$. The problem is to find a function $F(k_1, k_2)$ such that the result of the integration does not depend on q.

Any nonnegative solution of Eq. (53) satisfying the condition

$$F(k_1, k_2) = F(k_2, k_1) \tag{54}$$

corresponds to some self-consistent particle distribution.

The simplest case is $F(k_1, k_2) = g_0 > 0$ where g_0 is constant. In this case, the density of the distribution in the space of the integrals of motion is

$$f(M, I) = g_0(M^2 - I + a_0^2 c_0^2)^{-1/2}. \tag{55}$$

This distribution does not reduce to any distribution obtained before.

Another simplest case is $F(k_1, k_2) = g_1(k_1) + g_2(k_2)$. Substituting this expression into Eq. (53), we may see that this is exactly the solution. In view of the condition (54), we have $g_1(k) = g_2(k) + g_0$. The term with g_0 corresponds to the previous case (55). Omitting it, we obtain

$$f(M, I) = \frac{g(k_1) + g(k_2)}{(M^2 - I + a_0^2 c_0^2)^{1/2}}, \qquad g(k) \geq 0.$$

Other solutions can be sought for in the form of a series

$$F(x, z) = \sum_{m=0}^{\infty} \sum_{n=0}^{\infty} c_{mn} x^m z^n. \tag{56}$$

or a polynomial, as in Section 6.

For example, seeking for the solution of (53) as a third-degree polynomial, we obtain

$$f(M, I) = \frac{-c\,(I - a_0^2 c_0^2)(10M^2 - 5I + 2a_0^2 c_0^2) + g_0}{(M^2 - I + a_0^2 c_0^2)^{1/2}}. \tag{57}$$

This density (57) gives the self-consistent distribution that is uniform in the beam cross-section. The constant values c and g_0 shall be such that $f(M, I) \geq 0$ for all $(M, I) \in \Omega$. The values of $F(k_1, k_2)$, J, and λ can be arbitrary great. In this case, the radius of the beam cross-section $R(z)$ behaves according to the envelope equation (42) with great values of λ.

8. Conclusion

Within the framework of the approach presented in this paper, the particle density in the space of the integrals of motion M and H for the longitudinally uniform beam and M and I for the longitudinally nonuniform beam is introduced. The sets of admissible values of the integrals under consideration are analyzed.

This approach allows us to specify naturally various self-consistent distributions, both those previously known and new ones. In particular, the known distributions such as KV distribution and some distributions of the rigid rotor type receive very simple interpretation, namely, the supports of the density functions of these distributions are some segments that are easily determined. However, the approach developed here makes it possible to consider also the linear combinations of such distributions that are new distributions and cannot be reduced to the known distributions. The supports of the density functions of such distributions can have a nonzero phase volume. The integral equation presented in this paper also allows to obtain new self-consistent distributions with a nonzero phase volume.

The proposed approach was also applied for the beam nonuniform along its axis, for which wide classes of self-consistent distributions were found. In the particular instance of longitudinal uniformity, they are identical to the distributions for a uniform beam. Therefore, some of them can be regarded as the generalizations of distributions, such as Brillouin flow and KV distribution. The important feature of these distributions is that the beam radius and the magnetic field can vary along the beam axis, though this variation should be sufficiently slow. This means that they are more realistic than many of the previously considered distributions, and can be used for the solution of various problems of modeling and optimization of accelerating and focusing structures with high density beams.

References

1. I. M. Kapchinsky, *Particles Dynamics in Resonant Linear Accelerators* (Atomizdat, Moscow, 1966).
2. R. C. Davidson, *Physics of Nonneutral Plasmas* (Addison-Wesley Publishing Co., Reading, MA, 1990).
3. L. Brillouin, *Phys.Rev.* **67** 260–266 (1945).
4. R. C. Davidson, N. A. Krall, *Phys.Fluids* **13,** 1543–1555 (1970).
5. A. D. Vlasov, *Zh. Tekhn. Fiz. (USSR)* **49,** 1821–1826 (1979).
6. I. Hoffmann, *Transport and Focusing of High Intensity Unneutralised Beams.* In: Applied Charged Particle Optics, ed. by A.Septier (Academic Press, New York, 1983) Part C, pp.49–140.
7. O. I. Drivotin, D. A. Ovsyannikov, *Zh. Vychisl. Mat. Mat. Fiz. (USSR)* **27,** 416–427 (1987).
8. O. I. Drivotin, D. A. Ovsyannikov, *Zh. Vychisl. Mat. Mat. Fiz. (USSR)* **29,** (1989) 1245–1250
9. O. I. Drivotin, D. A. Ovsyannikov, *Dokl. Russ. Acad. Nauk* **334,** 284–287 (1994).
10. O. I. Drivotin, D. A. Ovsyannikov, Proc. of the 1997 Particle Accelerators Conf. (Vancouver, 1997), pp.1943–1945.
11. R. L. Gluckstern, *Phys. Rev. Lett.* **73,** 1247–1250 (1994).
12. R. L. Gluckstern, W.-H. Cheng, H. Ye *Phys. Rev. Lett.* **75,** 2835–2838 (1995).
13. G. P. Saraph, M. Reiser, *Particle Accelerators* **49,** 15–26 (1995).
14. C. Chen, R. Pakter, R. C. Davidson, *Phys. Rev. Lett.* **79,** 225–228 (1997).
15. R. C. Davidson, C. Chen, *Particle Accelerators* **59,** 175–250 (1998).
16. R. C. Davidson, *Phys. Plasmas* **5,** 3459–3468 (1998).
17. R. L. Gluckstern, A. V. Fedotov, S. Kurennoy, R. Ryne, *Phys. Rev. E* **58,** 4977–4990 (1998).
18. O. I. Drivotin, D. A. Ovsyannikov, *Nucl. Instr. Meth. Phys. Res.* **A 558,** 112–118 (2006).
19. V. P. Ermakov, *Univ. Izv. (Kiev)* **20,** 1–25 (1880).
20. J. R. Ray, *Adv. Nonlinear Waves* **1,** 230–233 (1984).
21. E. D. Courant, H. S. Snyder, *Annals of Physics* **3,** 1–48 (1958).

International Journal of Modern Physics A
Vol. 24, No. 5 (2009) 843–856

World Scientific
www.worldscientific.com

INVESTIGATION AND OPTIMIZATION OF LOW-ENERGY HEAVY-ION BEAM DYNAMICS IN PERIODIC AXISYMMETRICAL STRUCTURES WITH DC FOCUSING

VYACHESLAV SERGEEVICH DYUBKOV* and EDUARD SERGEEVICH MASUNOV†

Department of Electrophysical Facilities,
Moscow Engineering Physics Institute (State University),
Kashirskoe shosse 31, Moscow 115409, Russian Federation
**vsdyubkov@mephi.ru*
†*esmasunov@mephi.ru*

It is well-known that nonsynchronous harmonics of a RF field can focus particles. In order to focus ultra-low energy beam particles, a spatially periodic electrostatic field can be used, too. In this case the transverse focusing is provided by a periodic array of electrostatic lenses. This article is dedicated to questions of two high-current low-energy beam focusing types used in an injector-buncher of an ion linear accelerator, an application of a spatially periodic electrostatic focusing being examined for the first time. A two-dimensional nonlinear motion equation is derived in the Hamiltonian form in a smooth approximation. It allows us to study a correlation between the longitudinal and transverse ion beam dynamics at low energies. An investigation of the phase and transverse beam dynamics stability conditions in the initial part of the linac are given consideration. Conditions of the beam dynamics stability are found and analyzed. An approach to the field optimization problem is described. A method of the geometric parameter choice is worked out for a realization of the required field distributions in each structure. To verify the results of the beam dynamics stability analysis and optimized structure parameter choice, numerical simulations of low-energy heavy-ion beams are carried out.

Keywords: Electrostatic focusing; nonlinear beam dynamics; structure parameter optimization.

PACS numbers: 41.85.Ne, 02.60.Cb

1. Introduction

The problem of the effective low-energy linac design is of interest to many fields of science, industry and medicine (e.g. nuclear physics, surface hardening, ion implantation, hadron therapy). The most significant problem for low-energy high-current beams of charged particles is the question of the transverse stability due to the influence of Coulomb's repelling forces. The low-energy heavy-ion beam transport is known to be provided by the periodic array of electrostatic lenses (electrostatic

undulator).[1] The idea is to constructively join a periodic RF cavity and an electrostatic undulator (ESU) in the same device. In order to accelerate low-energy ion beams, one of the following efficient RF focusing types can be used: alternating phase focusing (APF),[2–4] radio frequency quadrupole (RFQ), focusing by means of the nonsynchronous wave field, as well as the undulator RF focusing. The attained threshold proton beam current in a RFQ[5] is about (100 to 150) mA and the further current rise leads to severe difficulties. A particle focusing with the use of the nonsynchronous wave in the two-wave approach was considered.[6] Detailed analysis of the focusing by means of nonsynchronous waves of the RF field shows that the focusing by the fast harmonic of the field in periodic ordinary Wideröe (also called Sloan-Lawrence) type and Alvarez type structures is not effective as the acceleration rate is very small. Increasing the low harmonic amplitude leads to the longitudinal beam instability which quickly disrupts the resonant conditions. The RF focusing by the nonsynchronous harmonics was discussed in detail.[6,7]

Alternatively, the acceleration and focusing can be provided by means of the electromagnetic waves which are nonsynchronous with the beam (the so-called undulator focusing).[8] In this case the acceleration mechanism is similar to that in the inverse free electron laser (IFEL). Systems without the synchronous wave are effective only for light-ion beams. For low-energy heavy-ion beams to be accelerated, it is necessary to have the wave synchronous with the particles.

The purpose of this work is to study and show advantages of the spatially periodic DC (also called electrostatic) focusing for high-intensity low-velocity heavy-ion beams.

2. Low-Energy Beam Motion Equation

The analytical investigation of the beam dynamics in a polyharmonical field is a difficult problem. Rapid longitudinal and transverse oscillations as well as a strong dependence of field components on transverse coordinates do not allow us to use the linear approximation in the paraxial region for a field series. Nevertheless, the analytical beam dynamics investigation can be carried out by means of the averaging method over the rapid oscillations period (the so-called smooth approximation) in the oscillating fields, which was suggested by P. L. Kapitsa[9] for the first time. Let us express the RF field in an axisymmetric periodic resonant structure and the ESU field as the Fourier expansion by the standing wave spatial harmonics, assuming that the structure period is a slowly varying function of the longitudinal coordinate z

$$\begin{aligned} E_z &= \sum_{n=0}^{\infty} E_n I_0\left(k_n r\right) \cos\left(\int k_n \, dz\right) \cos \omega t; \\ E_r &= \sum_{n=0}^{\infty} E_n I_1\left(k_n r\right) \sin\left(\int k_n \, dz\right) \cos \omega t; \end{aligned} \tag{1}$$

$$E_z^{\mathrm{u}} = \sum_{n=0}^{\infty} E_n^{\mathrm{u}} I_0\left(k_n^{\mathrm{u}} r\right) \cos\left(\int k_n^{\mathrm{u}}\, dz\right);$$
$$E_r^{\mathrm{u}} = \sum_{n=0}^{\infty} E_n^{\mathrm{u}} I_1\left(k_n^{\mathrm{u}} r\right) \sin\left(\int k_n^{\mathrm{u}}\, dz\right), \tag{2}$$

where E_n, E_n^{u} are the nth harmonic amplitudes of the RF and ESU fields on the axis; $k_n = (\theta + 2\pi n)/D$ is the propagation wave number for the nth RF field spatial harmonic, $k_n^{\mathrm{u}} = (\theta^{\mathrm{u}} + 2\pi n)/D^{\mathrm{u}}$ is the factor of the nth ESU field harmonic; D, D^{u} are the geometric periods of the resonant structure and ESU; θ, θ^{u} are the gap-to-gap phase differences for the resonant structure and ESU respectively; $\omega = 2\pi c/\lambda$ is the angular frequency, c is the speed of light, λ is the free-space RF wavelength; I_0 and I_1 are the modified Bessel functions of the first kind of orders 0 and 1.

We shall assume the beam velocity (the one-particle approximation) v differs significantly from all of the field harmonic phase velocities except that of the synchronous harmonic of RF field, the gap-to-gap spacing of the RF structure along the beam axis being defined as $D = \beta_s \lambda\,(s + \theta/2\pi)$, where s denotes the synchronous harmonic number, and β_s is the normalized velocity of the synchronous (equilibrium) particle.

It is convenient to introduce nondimensional variables $\widehat{\mathbf{\Omega}} = (\xi; \varrho)$ and τ as

$$\widehat{\mathbf{\Omega}} = 2\pi \mathbf{R}/\lambda \in C^2, \qquad \mathbf{R} = \big(z(t); r(t)\big), \qquad \tau = \omega t \in \mathbb{R}, \tag{3}$$

then one can write the second Newton's law

$$\frac{d^2 \widehat{\mathbf{\Omega}}}{d\,\tau^2} = \widehat{\mathbf{e}}\Big(\tau, \widehat{\mathbf{\Omega}}\Big), \tag{4}$$

where $\widehat{\mathbf{e}} = q\mathbf{E}\lambda/2\pi m c^2$, q and m are charge and mass of the particle.

The particle path in a superposition of the rapidly oscillating fields (1), (2) we seek as a sum of a slowly varying term $\overline{\mathbf{Y}}$ and a rapidly oscillating one, $\widetilde{\mathbf{Y}}$. We assume that the amplitude of the rapid velocity oscillations is much smaller than that of the slowly varying velocity component for the smooth approximation to be employed. Thus, the second-order differential equation of motion can be written as

$$\frac{d^2}{d\,\tau^2}\left(\overline{\mathbf{Y}} + \widetilde{\mathbf{Y}}\right) = \widehat{\mathbf{e}}\Big(\tau, \overline{\mathbf{Y}}\Big) + \widetilde{\mathbf{Y}} \frac{\partial}{\partial \widetilde{\mathbf{Y}}}\, \widehat{\mathbf{e}}\Big(\tau, \widehat{\mathbf{\Omega}}\Big)\Big|_{\widetilde{\mathbf{Y}} = 0}. \tag{5}$$

Finding $\widetilde{\mathbf{Y}}$ (as it was done in Ref. 10) with the aid of averaging over the rapid oscillations, one readily obtains Eq. (5) as follows

$$\ddot{\overline{\mathbf{Y}}} = \underset{\tau}{\mathcal{M}}\Big[\widehat{\mathbf{e}}\Big(\tau, \overline{\mathbf{Y}}\Big)\Big] + \frac{1}{2} \nabla \underset{\tau}{\mathcal{M}}\Big[\widehat{\mathbf{e}}\Big(\tau, \overline{\mathbf{Y}}\Big) \widetilde{\mathbf{Y}}\Big(\tau, \overline{\mathbf{Y}}\Big)\Big], \tag{6}$$

where $\overline{\mathbf{Y}} = \overline{\widehat{\mathbf{\Omega}}}$, $\underset{\tau}{\mathcal{M}}$ is the averaging operator over the explicitly contained variable τ. Now the shortened Eq. (6) can be presented in the form of the Hamilton's autonomous equations, namely

$$\frac{d\,\mathbf{Q}}{d\,\tau} = \frac{\partial\,\mathcal{H}}{\partial\,\mathbf{\mathcal{P}}}; \qquad \frac{d\,\mathbf{\mathcal{P}}}{d\,\tau} = -\frac{\partial\,\mathcal{H}}{\partial\,\mathbf{Q}}, \tag{7}$$

where $\boldsymbol{\mathcal{P}}$ and $\boldsymbol{\mathcal{Q}}$ are the canonically conjugate variables, the canonical coordinates being selected in such a way that the origin in a phase space is an equilibrium point, i.e. $\boldsymbol{\mathcal{Q}} = (\overline{\widehat{\boldsymbol{\Omega}}} - \widehat{\boldsymbol{\Omega}}_s)/\beta_s$ and the beam-wave system Hamiltonian is

$$\mathcal{H}(\boldsymbol{\mathcal{P}}, \boldsymbol{\mathcal{Q}}) = \frac{1}{2}\boldsymbol{\mathcal{P}}^2 + U_{\text{ef}}(\boldsymbol{\mathcal{Q}}). \tag{8}$$

Here $U_{\text{ef}}(\boldsymbol{\mathcal{Q}})$ is the effective potential function (EPF) which describes the low-energy beam interaction with the polyharmonical field of the system. The EPF depends solely on the averaged variable $\boldsymbol{\mathcal{Q}} = (\zeta; \eta)$.

3. Analysis of Effective Potential Function

3.1. *Case of Wideröe Type Structure*

For Wideröe type structure we make $\theta^{\text{u}} = \theta = \pi$ and $D^{\text{u}} = D$, then the EPF can be written as $U_{\text{ef}} = U_0 + U_1 + U_2$, where

$$\begin{aligned}
U_0 &= -\frac{1}{2} e_s \left[I_0(\eta) \sin(\varphi_s + \zeta) - \zeta \cos\varphi_s - \sin\varphi_s \right];\\
U_1 &= \frac{1}{16} \sum_{n\neq s}^{\infty} \frac{e_n^2}{\nu_{n,s}^2} w_{n,s}^{(0)}(\eta) + \frac{1}{16} \sum_{n=0}^{\infty} \frac{e_n^2}{\mu_{n,s}^2} w_{n,s}^{(0)}(\eta) + \frac{1}{4} \sum_{n=0}^{\infty} \frac{e_n^{\text{u}\,2}}{\iota_{n,s}^2} w_{n,s}^{(0)}(\eta);\\
U_2 &= \frac{1}{16} \sum_{\substack{n\neq s\\ k_n + k_p = 2k_s}}^{\infty} \frac{e_n e_p}{\nu_{n,s}^2} \Big[w_{n,s,p}^{(1)}(\eta) \cos(2\zeta + 2\varphi_s) + 2\zeta \sin 2\varphi_s\\
&\quad - \cos 2\varphi_s \Big] + \frac{1}{8} \sum_{\substack{n\neq s\\ k_n - k_p = 2k_s}}^{\infty} \frac{e_n e_p}{\nu_{n,s}^2} \Big[w_{n,s,p}^{(2)}(\eta) \cos(2\zeta + 2\varphi_s)\\
&\quad + 2\zeta \sin 2\varphi_s - \cos 2\varphi_s \Big].
\end{aligned} \tag{9}$$

Here $e_i = \widehat{e}_i/\beta_s$, $\nu_{n,s} = (k_n - k_s)/k_s$, $\mu_{n,s} = (k_n + k_s)/k_s$, $\iota_{n,s} = k_n/k_s$. $n, s, p \in \mathbb{N}_0$, φ_s is the synchronous particle phase and the functions of the dimensionless transverse coordinate are defined as

$$\begin{aligned}
w_{n,s}^{(0)}(\eta) &= I_0^2(\iota_{n,s}\eta) + I_1^2(\iota_{n,s}\eta) - 1;\\
w_{n,s,p}^{(1)}(\eta) &= I_0(\iota_{n,s}\eta) I_0(\iota_{p,s}\eta) - I_1(\iota_{n,s}\eta) I_1(\iota_{p,s}\eta);\\
w_{n,s,p}^{(2)}(\eta) &= I_0(\iota_{n,s}\eta) I_0(\iota_{p,s}\eta) + I_1(\iota_{n,s}\eta) I_1(\iota_{p,s}\eta).
\end{aligned} \tag{10}$$

From these expressions one can see that the term U_0 of the EPF is responsible for both the beam acceleration and its transverse defocusing. The term U_1 influences only the transverse motion, always focusing the particles in the transverse direction. The term U_2 has an influence not only on the longitudinal motion but on the transverse one. The extreme point of U_2 as well as U_0 is a saddle point. Therefore, the necessary condition for the simultaneous transverse and longitudinal focusing is the existence of the EPF total minimum. A typical view of the EPF is shown in Fig. 1. One can see that the term U_1 contains the sum of squares of the

normalized spatial ESU harmonic amplitudes. So, the ultra-low energy heavy-ion beam transverse focusing can be provided by the zero spatial harmonic of ESU. On the other hand, if the ESU is absent (that is $\forall n \in \mathbb{N}_0 \;\; e_n^{\mathrm{u}} = 0$) the second term of the EPF is reduced. In this case the transverse stability is provided by using nonsynchronous harmonics of the RF field only. For the amplitudes of the nonsynchronous harmonics to be increased we have to include additional electrodes (see Sec. 5). Thereby, the use of ESU eliminates the need for the channel geometry complication, enabling higher shunt impedance, if equal and opposite DC potentials are supplied to the same sequential drift tubes which are used to excite the RF field, i.e. we can constructively join the periodic RF system and ESU in the same device.

At first, one should analyze the EPF about the origin. The EPF is expanded in Maclaurin's double series with the remainder in Peano's form

$$U_{\mathrm{ef}} = \frac{1}{2}\Omega_{0\zeta}^2\zeta^2 + \frac{1}{2}\Omega_{0\eta}^2\eta^2 + \frac{1}{2}\varepsilon\zeta\eta^2 + \frac{1}{6}\delta\zeta^3 + o\big(\|\mathfrak{Q}\|_2^3\big), \tag{11}$$

where the expansion coefficients are given by

$$\begin{aligned}
\Omega_{0\zeta}^2 &= \frac{1}{2}e_s\sin\varphi_s - \frac{1}{4}\sum_{\substack{n\neq s\\ k_n+k_p=2k_s}}^{\infty}\frac{e_n e_p}{\nu_{n,s}^2}\cos 2\varphi_s - \frac{1}{2}\sum_{\substack{n\neq s\\ k_n-k_p=2k_s}}^{\infty}\frac{e_n e_p}{\nu_{n,s}^2}\cos 2\varphi_s;\\
\Omega_{0\eta}^2 &= -\frac{1}{4}e_s\sin\varphi_s + \frac{3}{32}\sum_{n\neq s}^{\infty}\frac{e_n^2}{\nu_{n,s}^2}\iota_{n,s}^2 + \frac{3}{32}\sum_{n=0}^{\infty}\frac{e_n^2}{\mu_{n,s}^2}\iota_{n,s}^2 + \frac{3}{8}\sum_{n=0}^{\infty}e_n^{\mathrm{u}\,2}\\
&\quad + \frac{1}{32}\sum_{\substack{n\neq s\\ k_n+k_p=2k_s}}^{\infty}\frac{e_n e_p}{\nu_{n,s}^2}\frac{k_n^2+k_p^2-k_n k_p}{k_s^2}\cos 2\varphi_s\\
&\quad + \frac{1}{16}\sum_{\substack{n\neq s\\ k_n-k_p=2k_s}}^{\infty}\frac{e_n e_p}{\nu_{n,s}^2}\frac{k_n^2+k_p^2+k_n k_p}{k_s^2}\cos 2\varphi_s;\\
\varepsilon &= \partial\,\Omega_{0\eta}^2\Big/\partial\varphi_s;\\
\delta &= \partial\,\Omega_{0\zeta}^2\Big/\partial\varphi_s.
\end{aligned} \tag{12}$$

The expression (11) looks like the generalized Hénon-Heiles potential.[11] It is clear that the parameters of the channel must be chosen in terms of the conditions of positivity of $\Omega_{0\zeta}^2$ and $\Omega_{0\eta}^2$ to insure the transverse and the longitudinal focusing simultaneously. Furthermore, there can appear internal parametric resonances (radial phase oscillation) with the third-order terms in the anharmonic potential. This can destroy the stable beam dynamics due to a beam-wave system energy transfer between the two degrees of freedom. Another important restriction on the choice of the spatial harmonic amplitudes can be obtained from the condition of non-overlapping for different harmonic separatrices in the phase space $(\zeta;\dot{\zeta})$. Firstly,

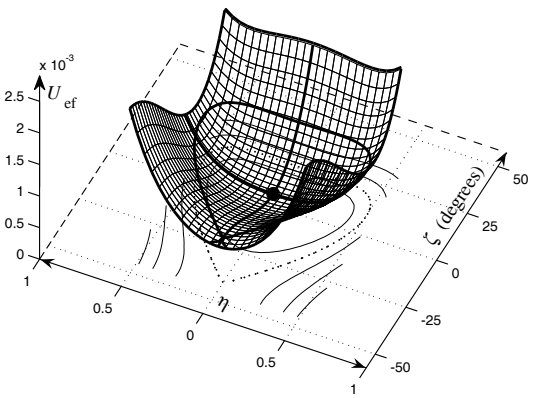

Fig. 1. A typical view of the effective potential function.

this restriction defines limits of the applicability of the averaging method. Secondly, it is the necessary condition of the longitudinal (phase) stability. The effective separatrix (bucket) can be derived analytically in terms of the system Hamiltonian (8). In the slow wave frame of the RF field, the bunch is acted on by a field which is similar to the electrostatic undulator one, i.e. the RF focusing mechanism by the nonsynchronous harmonic and the DC one are the same. It is noticeable that the availability of the terms proportional to $\cos 2\varphi_s$ in the squares of the small oscillation frequencies makes it possible to realize acceleration without the synchronous harmonic, when $45° < \varphi_s \leq 90°$.

3.2. *Case of Alvarez Linac Structure*

The EPF for the Alvarez type structure ($\theta = 0$, $\theta^{\mathrm{u}} = \pi$, $D^{\mathrm{u}} = D$) has a form similar to the Wideröe one, but the most important feature is the appearance of an additional term U_2^{a} in U_2, namely

$$U_2^{\mathrm{a}} = \frac{1}{4} e_0 e_{2s} \left[I_0(2\eta) \cos(2\zeta + 2\varphi_s) + 2\zeta \sin 2\varphi_s - \cos 2\varphi_s \right], \tag{13}$$

where $s \neq 0$ unlike the system considered above. Note that the harmonic amplitude of the RF field for the Alvarez type structure is not equal to the Wideröe type structure. Moreover, in this case the basic harmonic is e_1, and e_0 is the dimensionless average field value. The availability of the additional term (13) leads to the next serious result. The additional term may be comparable with U_0 and essentially increases the acceleration rate as the average field value is large. One can assume that the Alvarez type structure, which is commonly used for acceleration of medium-energy particles, may be used for the low-energy beam acceleration. In this case the transverse stability can be provided by using the ESU in view of the period smallness.

4. Approach to Field Optimization Problem

Hereafter we discuss Wideröe type linac. Numerical simulations of low-velocity beams have shown that particle loss is mainly caused by the longitudinal beam dynamics. It is well-known that the region of stable phase motion is defined by the longitudinal channel acceptance value. At injection into the injector-buncher, particle representation points occupy a certain volume in the six-dimensional phase space. The longitudinal phase "volume" becomes deformed and fills a separatrix area step by step due to the force nonlinearity which provides the phase stability. In terms of the Liouville's theorem for conservative systems the synchronous harmonic amplitude must be chosen so that the channel acceptance is a nondecreasing function of the longitudinal beam coordinate. One can show from Ref. 12 that the current value of the "longitudinal" threshold is proportional to the channel acceptance (the separatrix area). Therefore, taking into account the equation of motion for the equilibrium particle, the law of the synchronous harmonic amplitude variation at a field increasing length (for $s = 0$) can be written as

$$\frac{d\,\widehat{e}_s}{d\,\xi} = \frac{\widehat{e}_s}{\ell}\frac{d\,\ell}{d\,\xi} - \frac{\widehat{e}_s}{\psi}\frac{d\,\psi}{d\,\xi} - \frac{{\widehat{e}_s}^3\cos\varphi_s}{\beta_s(0)\widehat{e}_s(0)\psi(0)}\frac{\psi}{\ell} - \begin{cases} 0 & \text{(i)}; \\ \dfrac{\chi\,{\widehat{e}_s}^{\frac{9}{2}}\sin 2\varphi_s}{8{\beta_s}^8(0)\widehat{e}_s{}^{\frac{3}{2}}(0)\psi^{\frac{3}{2}}(0)}\dfrac{\psi^{\frac{3}{2}}}{\ell^{\frac{3}{2}}} & \text{(ii)}, \end{cases} \tag{14}$$

where (i) and (ii) correspond to the DC focusing and the RF focusing by only the first harmonic respectively; ψ depends on the φ_s value and it is an implicit function of ξ (i.e. $(\psi \circ \varphi_s)(\xi)$); ℓ is a certain function of ξ which can be found by numerical optimization in every given case. $\widehat{e}_s(0)$ defines the initial channel acceptance. On the one hand, the choice of $\widehat{e}_s(0)$ is determined by the requirement to minimize the particle momentum spread which appears due to the phase spread at injection. On the other hand, it should be sufficient to capture particles into the separatrix. χ is the amplitude ratio, that is $\widehat{e}_1/\widehat{e}_s$. In the accelerating parts of the structures, $\widehat{e}_s$ is constant. The nonlinear Eq. (14) can be solved by using one of the numerical methods.

5. Channel Geometry Choice

It was supposed to use an injector-buncher of low charge state lead ions ($\beta = 2.3 \times 10^{-3}$) working at a frequency of 101.28 MHz for NICA project.[13] Evidently, the geometric period D of the Wideröe type structure is about 3.5 mm. It is difficult to fabricate an RF cavity with the focusing by the first nonsynchronous harmonic for this D value. To increase the D value one can decrease the working frequency, but then the transverse cavity size should be increased too. Therefore, one should use the ESU in this case. A cross-section of the structure with the spatial periodic electrostatic focusing is shown in Fig. 2. If an inter-electrode gap width h is equal to $2D/3$ the harmonic with number $n = 1$ (the higher harmonics are smaller) will be suppressed for both the RF and the electrostatic fields and we will

have only two harmonics, i.e. the accelerating e_0 and the focusing e_0^{u} ones. It is worth pointing out that $\chi^{\mathrm{u}} = e_0^{\mathrm{u}}/e_0$ is constant along the channel.

However, the linac period value increases owing to the acceleration. It allows one to use the structure with focusing by the first harmonic of the RF field only. As it was mentioned above, for the amplitude of the nonsynchronous harmonic to be increased over e_0 it is necessary to set three electrodes on the structure period. The implementation of the structure channel for one period of the RF field is shown in Fig. 3. We suppose there are only two harmonics (e_0 and e_1) in the structure, and use boundary conditions at the drift tube apertures to find the dependence of the amplitude ratio χ on the structure geometric parameters. Based on the fact that the field is zero in the centers of the electrodes, the RF field amplitude ratio can be expressed as

$$\chi = -3\frac{c_1 I_0(\alpha\rho) + I_0(\rho)}{c_2 I_0(3\alpha\rho) + I_0(3\rho)}, \tag{15}$$

where $c_1 = \cos(\pi/3 + \pi d/D)$, $c_2 = \cos(\pi + 3\pi d/D)$, $d = D/2\pi\sqrt{3}\chi$ is the displacement value of the drift tubes with the bore radius b, α is the ratio of the bore electrode radii (b/a), $\rho = \pi a/D$. By varying the length, the corner radii (r_1, r_2) as well as the outer radius (R_{o}) of the drift tubes, one can suppress the higher RF harmonics and obtain only two waves in the structure. The ratio of the bore radii b/a versus a/D for different χ values is plotted in Fig. 4. To verify the obtained analytical results we have used the POISSON SUPERFISH solver code[14] (see Fig. 5 and Fig. 6). The analytical results correspond to the POISSON SUPERFISH data up to 2%.

Note, in the case of the spatial periodic electrostatic focusing, we face difficulties which lie in the fact that the desired e_0^{u} value must be held constant along the channel. The question of high-voltage input into the RF cavity should be investigated too.

6. Numerical Simulation Results

A computer simulation of the non-averaged high-intensity lead beam dynamics in the discussed Wideröe type structure with the basic spatial harmonic (e_0) of the RF field was carried out by means of the specialized computer code BEAMDULAC-ARF[8] based on the Cloud-In-Cell method to calculate beam self-space-charge field. In the case of RF focusing only the first nonsynchronous harmonic was taken into account. We examined only the basic spatial harmonic of the ESU (i.e. e_0^{u}), studying the electrostatic focusing. The equilibrium particle phase is linearly reduced from an input value $\varphi_s(0)$ to an output value $\varphi_s(L_{\mathrm{b}})$ at a bunching length L_{b} and it is kept constant further on. The initial phase density distribution is similar to Fermi distribution for completely degenerate gas (also called "water-bag" model). In terms of the Hamilton's equations (7), the analysis of the EPF (9), and taking into account Eq. (14) we have determined optimal parameters of the systems involved which

ensure the high current transmission coefficient and acceleration rate. Simulation parameters are summarized in Table 1 and Table 2 for the injector-buncher with ESU. Simulation parameters corresponding to the structure with the RF focusing are presented in Table 3 and Table 4.

The output beam phase space in the planes $(\zeta; \dot{\zeta})$ and $(\eta; \dot{\eta})$ are shown in Fig. 7 and Fig. 8 respectively for the structure with ESU. The output longitudinal and transverse phase spaces for the structure with the RF focusing are plotted in Fig. 9 and Fig. 10.

The particle loss is observed in the longitudinal direction in both cases. It is the result of the beam interaction with the nonsynchronous harmonic which leads to the increase of the beam amplitude oscillations. The numerical simulation results confirmed similarity between the RF focusing and the electrostatic focusing. As one can see from Table 1 and Table 3 the acceleration rate in the system with the focusing by the periodic array of electrostatic lenses is smaller as compared to

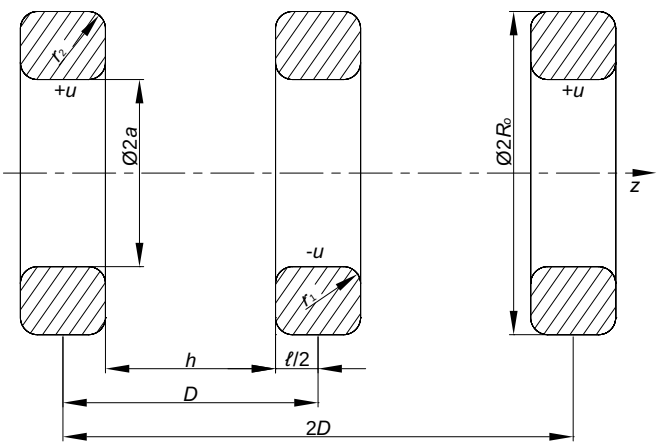

Fig. 2. Structure period for the spatial periodic electrostatic focusing.

Table 1. System parameters with electrostatic focusing only.

Quantity		Value
Particle type	Pb^{25+}	...
Charge to mass ratio	Z/A	0.12
Energy in	W_{in} (keV/u)	2.5
Energy out	W_{out} (keV/u)	125.9
Frequency	f (MHz)	101.28
System length	L (m)	2.5
Field increasing length	L_{f} (m)	0.95
Bunching length	L_{b} (m)	0.95
Input/output phase of the equilibrium particle	φ_s (degrees)	90.0/36.0
Accelerating harmonic maximal value at the axis	$E_{0,\max}$ (kV/cm)	11.95
Ratio of the harmonic amplitudes	χ^{u}	9.5

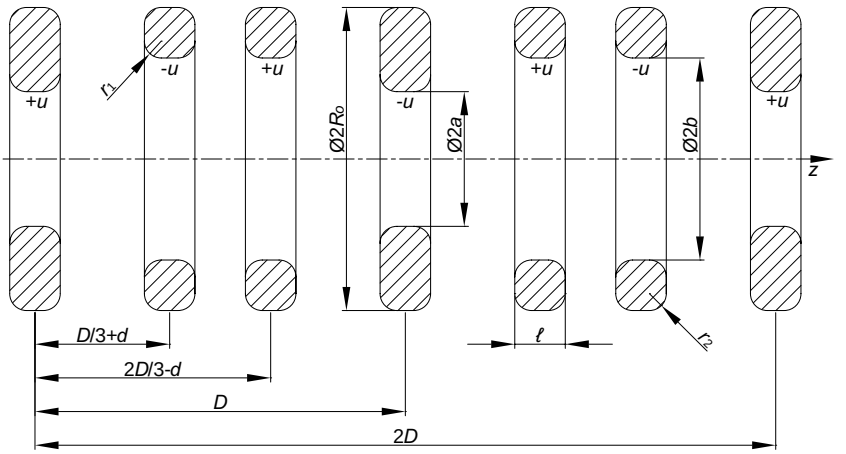

Fig. 3. Structure period for RF focusing by the first harmonic.

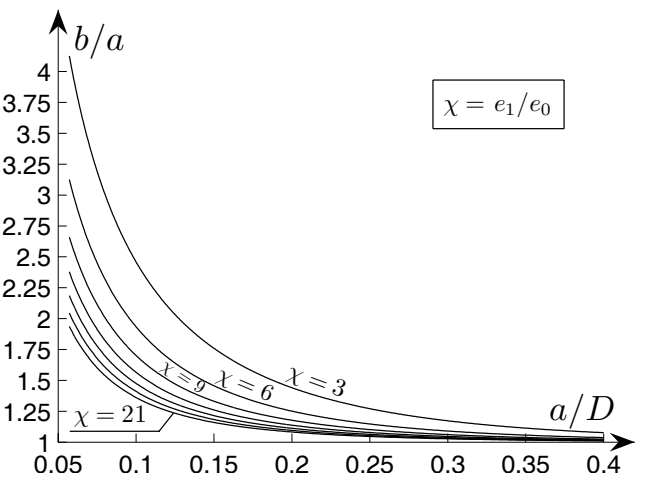

Fig. 4. b/a vs a/D for different χ values.

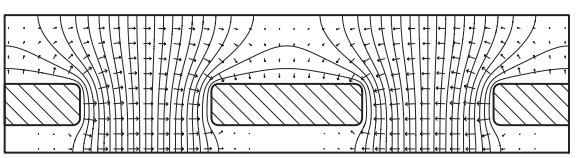

Fig. 5. Equipotential curves in the system with DC focusing calculated by the program SUPERFISH.

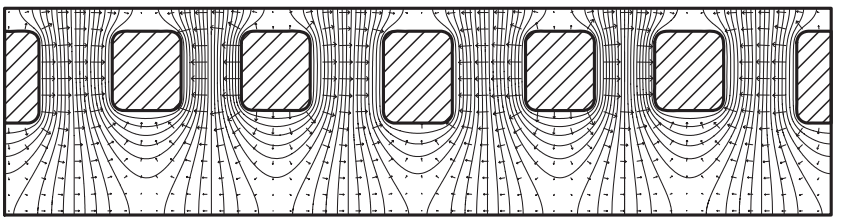

Fig. 6. Potential distribution pattern for the system with RF focusing.

Table 2. Beam parameters for the system with DC focusing.

Quantity		Value
Initial beam current	I (μA)	5.0
Initial beam radius	r_{b} (mm)	0.5
Input/output longitudinal emittance	$\epsilon_{\mathrm{l\!l}}$ (keV·ns/u)	$0.5\pi/34.1\pi$
Input/output longitudinal acceptance	$\mathcal{A}_{\mathrm{l\!l}}$ (keV·ns/u)	$0.62\pi/7.5\pi$
RMS input/output transverse emittance	$\epsilon_{\perp}$ (mm·mrad)	$1.2\pi/35.6\pi$
Input/output transverse acceptance	$\mathcal{A}_{\perp}$ (mm·mrad)	$10.0\pi/91.1\pi$
Current transmission coefficient	K_{c} (%)	86.1
Output relative energy spread	δW (%)	13.5
Output phase spread	$\triangle\varphi$ (degrees)	$\pm$29.5

Table 3. RF system parameters with focusing by the first nonsynchronous harmonic only.

Quantity		Value
Particle type	Pb^{25+}	...
Charge to mass ratio	Z/A	0.12
Energy in	W_{in} (keV/u)	2.5
Energy out	W_{out} (keV/u)	259.8
Frequency	f (MHz)	33.76
System length	L (m)	2.44
Field increasing length	L_{f} (m)	1.75
Bunching length	L_{b} (m)	1.75
Input/output value of the equilibrium particle	φ_s (degrees)	90.0/22.5
Accelerating harmonic maximal value at the axis	$E_{0,\mathrm{max}}$ (kV/cm)	42.67
Ratio of the harmonic amplitudes	χ	4.0

the structure with the RF focusing. However, ESU is the adequate solution for the problem of the ultra-low energy high-intensity heavy-ion beam focusing. All the results obtained in the smooth approximation agree within a few percent with the numerical simulation results.

7. Summary

The spatial periodic electrostatic focusing investigation was carried out by using the smooth approximation. It was shown that the electrostatic undulator focusing of

Table 4. Beam parameters for the system with the RF focusing.

Quantity		Value
Initial beam current	I (μA)	5.0
Initial beam radius	$r_{\rm b}$ (mm)	1.0
Input/output longitudinal emittance	$\epsilon_{\rm ll}$ (keV·ns/u)	$0.5\pi/40.9\pi$
Input/output longitudinal acceptance	$\mathcal{A}_{\rm ll}$ (keV·ns/u)	$3.7\pi/37.7\pi$
RMS input/output transverse emittance	$\epsilon_{\perp}$ (mm·mrad)	$2.3\pi/35.3\pi$
Input/output transverse acceptance	$\mathcal{A}_{\perp}$ (mm·mrad)	$10.0\pi/70.1\pi$
Current transmission coefficient	$K_{\rm c}$ (%)	85.1
Output relative energy spread	δW (%)	16.1
Output phase spread	$\triangle\varphi$ (degrees)	$\pm$25.5

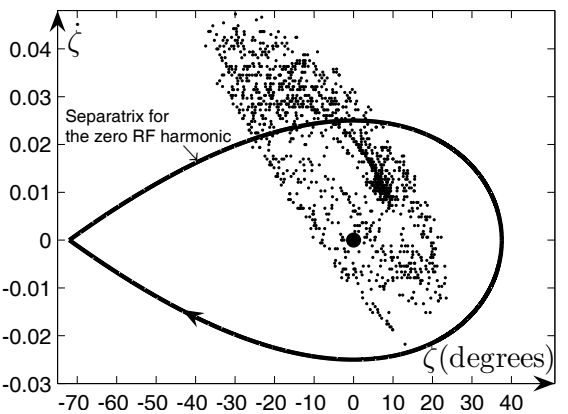

Fig. 7. The longitudinal phase space.

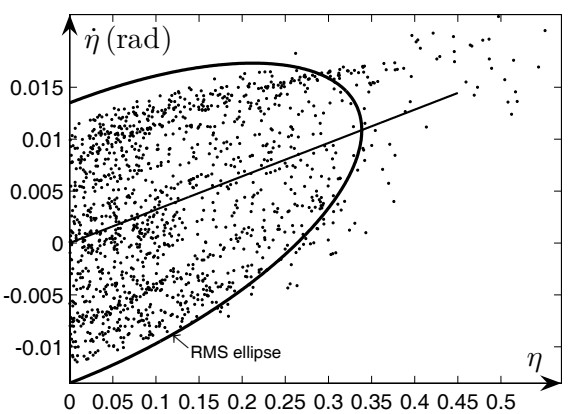

Fig. 8. The trace space.

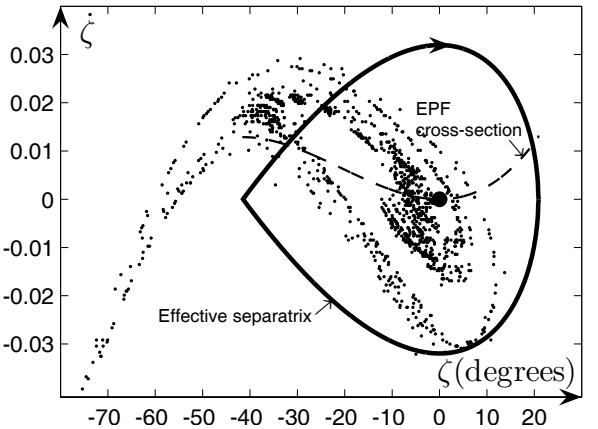

Fig. 9. The longitudinal phase space.

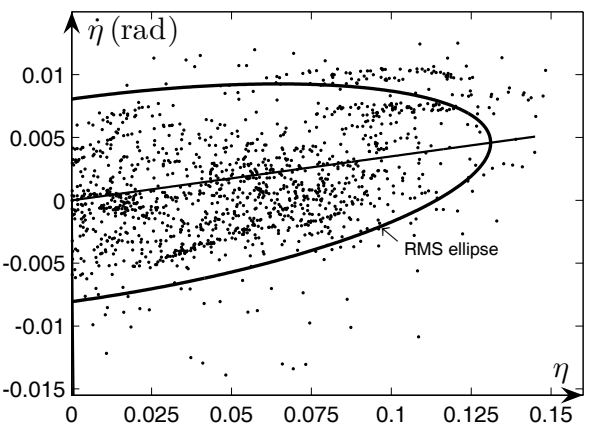

Fig. 10. The trace space.

the ultra-low energy heavy ions can be a substitution for the RF focusing. The field choice technique providing the high acceleration rate and current transmission was proposed. The method of the geometric parameter choice providing the required field distributions for the structures involved was developed. This analytical method was verified by means of POISSON SUPERFISH code. Numerical simulations of the high-intensity lead ion beam dynamics in Wideröe type structure with the RF focusing by the first nonsynchronous harmonic as well as with the spatial periodic electrostatic focusing was carried out. It was shown that ESU is the unique adequate problem solving of the ultra-low energy high-intensity heavy-ion beams focusing.

References

1. S. V. Petrenko *et al*., *Rev. Sci. Instrum.* **77**, 03C112 (2006).
2. Ya. B. Fainberg, *Zh. Tekh. Fiz.* **29** (5), 568 (1959).
3. M. L. Good, *Bull. Amer. Phys. Soc.* **27** (6), 16, K11 (1952).
4. V. V. Kushin, *At. Energ.* **29** (2), 123 (1970).
5. I. M. Kapchinskij and V. A. Teplyakov, *Prib. Tekh. Eksp.* **2**, 19 (1970).
6. V. S. Tkalich, *Zh. Eksp. Teor. Fiz.* **32** (3), 625 (1957).
7. E. S. Masunov and N. E. Vinogradov, *Zh. Tekh. Fiz.* **71** (9), 79 (2001).
8. E. S. Masunov and S. M. Polozov, *Phys. Rev. ST Accel. Beams* **11**, 074201 (2008).
9. P. L. Kapitsa, *Zh. Eksp. Teor. Fiz.* **21** (5), 588 (1951).
10. L. D. Landau and E. M. Lifshitz, *Mechanincs*, 3nd edn. (Butterworth-Heinenann, Oxford, 2004).
11. M. Hénon and C. Heiles, *Astron. J.* **69** (1), 73 (1964).
12. I. M. Kapchinskiy, *Theory of resonance linear accelerators*, Accel. and Storage Rings Series, Vol. 5 (Harwood Academic Pablishers, New York, 1985).
13. R. Lednický, Project of the Nuclotron-based Ion Collider fAcility (NICA) at JINR, Dubna: Perspectives of heavy ion and spin physics, to appear in *Proc. 18th Int. Spin Phys. Symp.* (Charlottesville, USA, 2008).
14. K. Halbach and R. F. Holsinger, *Part. Accel.* **7** (4), 213 (1976).

International Journal of Modern Physics A
Vol. 24, No. 5 (2009) 857–868

World Scientific
www.worldscientific.com

BEAM-BASED FEEDBACK SYSTEM FOR THE INTERNATIONAL LINEAR COLLIDER

VALENTIN IVANOV

Muons, Inc., 522 N.Batavia Ave., Batavia, Illinois 60510, USA
vivanov@fnal.gov

The algorithms and computer codes for linac Feedback system were developed at SLAC during 1991–2004. The efficiency of that system have been demonstrated for the SLC, CLIC, TESLA and NLC projects. International Linear Collider (ILC) has its own features. Ground motion (GM) oscillations play a dominant role here. It forced to implement a new version of the Linac Feedback Simulation Code based on the previous developments. A set of benchmark tests and realistic simulations for the whole ILC structure have been performed. The effects of different GM models, BPM resolution, time intervals, initial misalignments, a dispersion-free steering (DFS), and a quad jitter have been studied.

Keywords: Feedback system; Kalman's filter; particle accelerator.

PACS numbers: 29.27.Bd; 43.38.Ew

1. Introduction

Feedback systems are necessary elements of modern linear colliders, providing an effective method for relaxing tight tolerances of the design. For the ILC, extensive feedback systems control the beam parameters, such as beam position, energy, final focusing luminosity, etc., under ground motion and other sources of perturbation. This system should include a number of sensors (beam position monitors) and actuators (dipole magnets). It allows precision beam tuning and provides pulse-to-pulse diagnostics.

2. Beam Dynamics Under Ground Motion (GM) and Technical Noise

Typical requirements for the ILC design parameters are:

- Electron and positron linacs of 10.5 km length each;
- Accelerating gradient = 31.5 MV/m in 1.3 GHz cavities;
- Injection energy = 15 GeV;
- Extraction energy = 250 GeV;

- Initial energy spread = 150 MeV;
- Bunch charge = 2×10^{10};
- Bunch length = 300 μm;
- Normalized vertical emittance = 20 nm;
- Normalized horizontal emittance = 800 nm;
- Main linac (ML) budget for vertical emittance = 8 nm;
- Optics: FODO lattice with β phase advance of 75°/60° in x/y plane.

Each quad has a cavity-style beam position monitor (BPM) and a vertical corrector—dipole magnet. A set of nominal initial misalignments in main linac (ML) includes:

- Quad offset = 300 μm;
- Quad rotation = 300 μrad;
- BPM offset = 300 μm;
- BPM resolution = 1 μm;
- Cavity offset = 300 μm;
- Cavity pitch = 300 μrad;
- Cryostat offset = 200 μm;
- Cryostat pitch = 20 μrad.

The simulations show the growth of vertical emittance in such a linac is more than 10,000 nm rad, so a dynamic beam-based alignment should be provided continuously after a static alignment.

The main sources of an emittance dilution are:

- Dispersion from Misaligned Quads or Pitched cavities;
- Transverse SR Wake fields: Misaligned cavities and cryomodules (CM);
- XY-coupling from rotated Quads;
- Transverse Jitter.

The GM was modeled with a 2-D power spectrum,[1] which include a diffusive corrected ATL term and a set of isotropic plane waves (Figure 1):

$$P(\omega, k) = \frac{A}{\omega^2 k^2}\left[1 - \cos\left(\frac{kB}{A\omega^2}\right)\right] + \sum_i D_i U_i. \tag{1}$$

$$U_i = \begin{cases} \frac{2}{\sqrt{(\omega/v_i)^2}}, & |k| \geq \frac{\omega}{v_i}, \\ 0, & |k| > \frac{\omega}{v_i}, \end{cases} \quad D_i = \frac{a_i}{1 + [d_i(\omega - \omega_i)/\omega_i]^4}. \tag{2}$$

Here the coefficients A, B, ω_i, a_i, d_i are individual sets for different sites: a quiet model A, an intermediate model B and an aggressive model C.

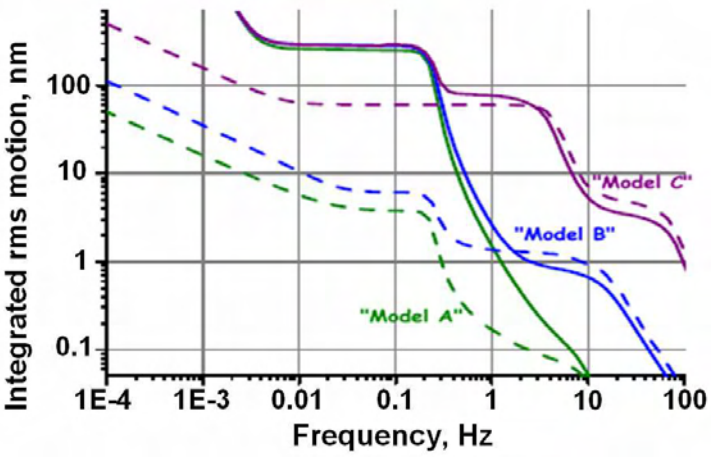

Fig. 1. The integrated absolute GM spectra (solid lines) and the integrated relative motion of 2 objects separated by 50 m distance (dashed lines).

3. Static and Dynamic Beam-Based Alignment

There are three main schemes for a static alignment:

- **One-to-One Steering**: Find BPM readings for which the beam should pass through the exact center of every quad, and use the correctors to steer the beam. The alignment generates a dispersion which contributes to the emittance dilution, and it is sensitive to the BPM-to-Quad offsets. Typically it reduces the emittance from ≈10,000 nm to ≈100 nm.
- **Dispersion Free Steering (DFS)**: Measure a dispersion via mismatching the beam energy to the lattice. Calculate the correction needed to zeroing the dispersion, and apply the correction. Make few iterations. This type of alignment can reduce the emittance growth to 5–7 nm.
- **Emittance (Dispersion & Wake) Bumps**: The goal is to minimize a beam size at the end of linac by varying the strength of the correctors. It can reduce the emittance growth to 2–3 nm.

The **Adaptive Alignment (AA) scheme** for a dynamic tuning[2] is a "local" method. It uses the BPM readings A_i of three (or more) neighboring quads to determine the correction for the central of them (Figure 2)

$$\Delta y_i = C\left\{A_{i+1} + A_{i-1} - A_i\left[2 + k_i L_i\left(1 - \frac{\Delta E}{2E}\right)\right]\right\}, \tag{3}$$

where C is a convergence factor, k_i is the inverse of i-th quad focusing length, L_i is the distance between successive quads, ΔE is the energy gain between successive quads, E is the beam energy at central quad.

The new position for the quad and BPM is $y_i^{new} = y_i^{old} - \Delta y_i$, and the procedure is repeated until the convergence is reached.

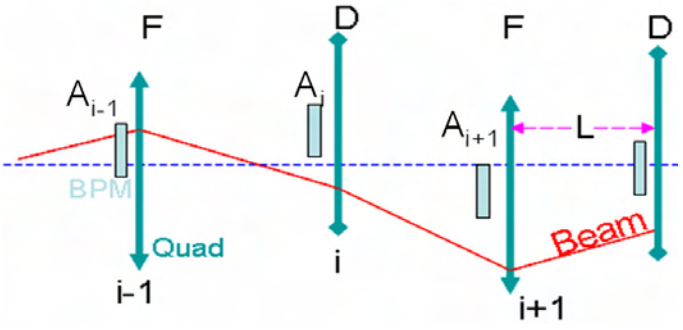

Fig. 2. Adaptive alignment scheme.

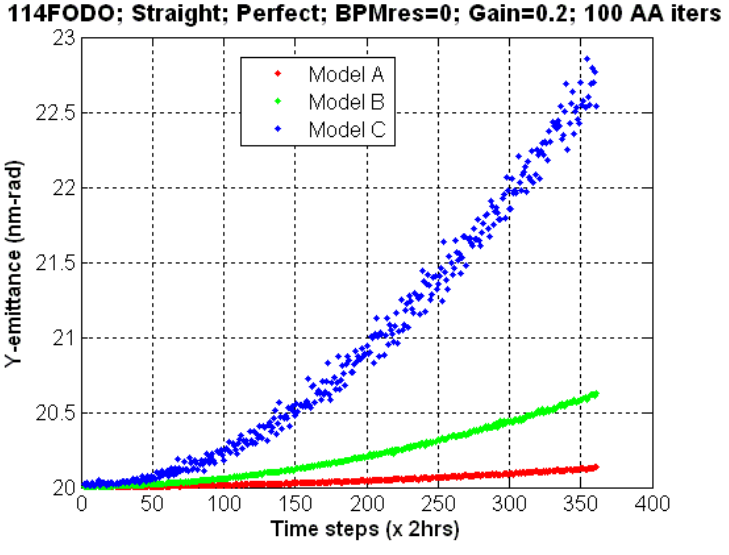

Fig. 3. Vertical emittance growth for the models A, B and C.

Figure 3 shows the emittance growth averaged over 20 GM random seeds after 100 AA iterations for initially perfectly aligned linac. The AA corrections have been applied each two-hour period after the GM. The total period of GM simulation is one month.

4. The Kalman Filter Model and the Optimal Control

The optimal control system is illustrated in Figure 4. Here the actuator vector $\vec{u}$ includes as a corrector signal as a measurement noise due to a limited BPM resolution. It affects on the control system via the state vector $\vec{X}$. Then the measurement system produces the BPM-read vector $\vec{Z}$, which is used to update the new state vector.

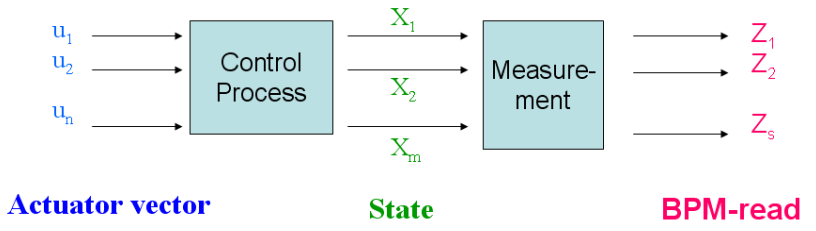

Fig. 4. Generalized scheme for the accelerator feedback system.

In that way, the control procedure consists of two steps.[3] Step 1 **Prediction** evaluates the state ahead

$$X_k = \hat{A}X_{k-1} + \hat{B}u_k + w_k, \tag{4}$$

and projects the error covariance ahead

$$P_k = \hat{A}P_{k-1}\hat{A}^T + Q_{k-1}. \tag{5}$$

Here w_k is the process noise which is assumed to be drawn from a zero mean multivariate normal distribution with covariance Q_k.

Step 2 **Correction** computes the optimal Kalman gain

$$K_k = P_k\hat{H}^T(\hat{H}P_k\hat{H}^T + R)^{-}1, \tag{6}$$

updates the estimation with a measurement Z_k

$$X_k = X_K + K_k(Z_k - \hat{H}X_k), \tag{7}$$

and updates the error covariance

$$P_k = (\hat{I} - K_k\hat{H})P_k. \tag{8}$$

5. General Feedback (FB) Model in the Linac Feedback System Code (LFSC)

The computer program LFSC (Linac Feedback Simulation Code) is a numerical tool for simulation of beam based feedback in high performance linacs. The code LFSC is based on the earlier version developed by a group of authors at SLAC[4–9] during 1990–2005. Later work[10] studied the beam jitter in ILC also. That code was successively used in simulation of SLC, TESLA, CLIC and NLC projects. It can simulate pulse-to-pulse feedback on timescale corresponding to 5–100 Hz, as well as slower feedbacks operating in the 0.1–1 Hz range in the Main Linac and Beam Delivery System.

The FB model is described by the following system of equations

$$\begin{aligned} X_{k+1} &= \Phi X_k + \Gamma u_k + L(y - HX_k), \\ \tilde{u}_k &= -KX_{k+1} + Nr_k, \\ u_{k+1} &= +g(\tilde{u}_k - u_k). \end{aligned} \tag{9}$$

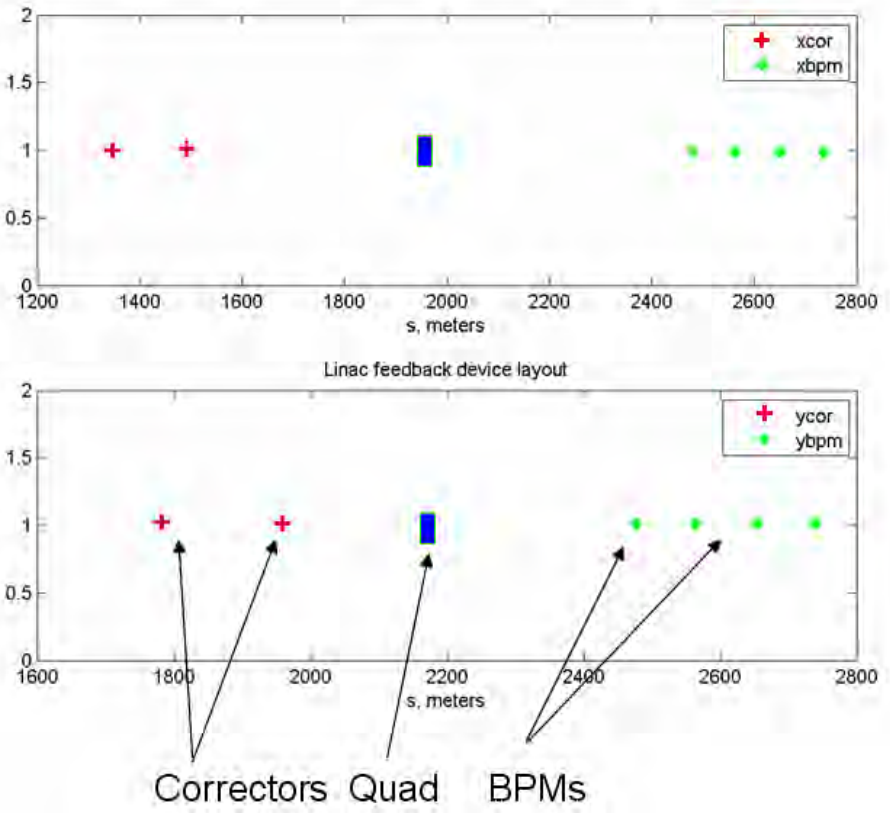

Fig. 5. Lattice layout: one FB loop of 2 correctors, 4 BPMs in each direction.

Here Φ is a system matrix for the dynamics of accelerator model; Γ is a control input matrix; L is a Kalman filter; H is an output matrix; K is a gain matrix; N is a controller-reference-input matrix; r is a vector of system set points; g is a gain factor.

6. Simple Benchmarks (Static and Dynamic Response)

The test problem we studied with LFSC was a perfectly aligned main linac of 114 FODO cells with 5 Hz repetition rate. The vertical offset for a Quad #50 varies as $dy_{50} = y_0 \cos(2\pi F t)$, where amplitude $y_0 = 80$ μm, and the frequency F varies in the range 0–0.5 Hz. The lattice with the only control loop is shown in Figure 5.

The efficiency of the control for static perturbation $F = 0$ is shown in Figure 6. The picture demonstrates the rate of decreasing of initial misalignment with time.

Dynamic response of the Kalman filter model is presented in Figure 7. One can see that initial misalignment can be effectively compensated for the perturbation frequencies ≤ 0.05 Hz.

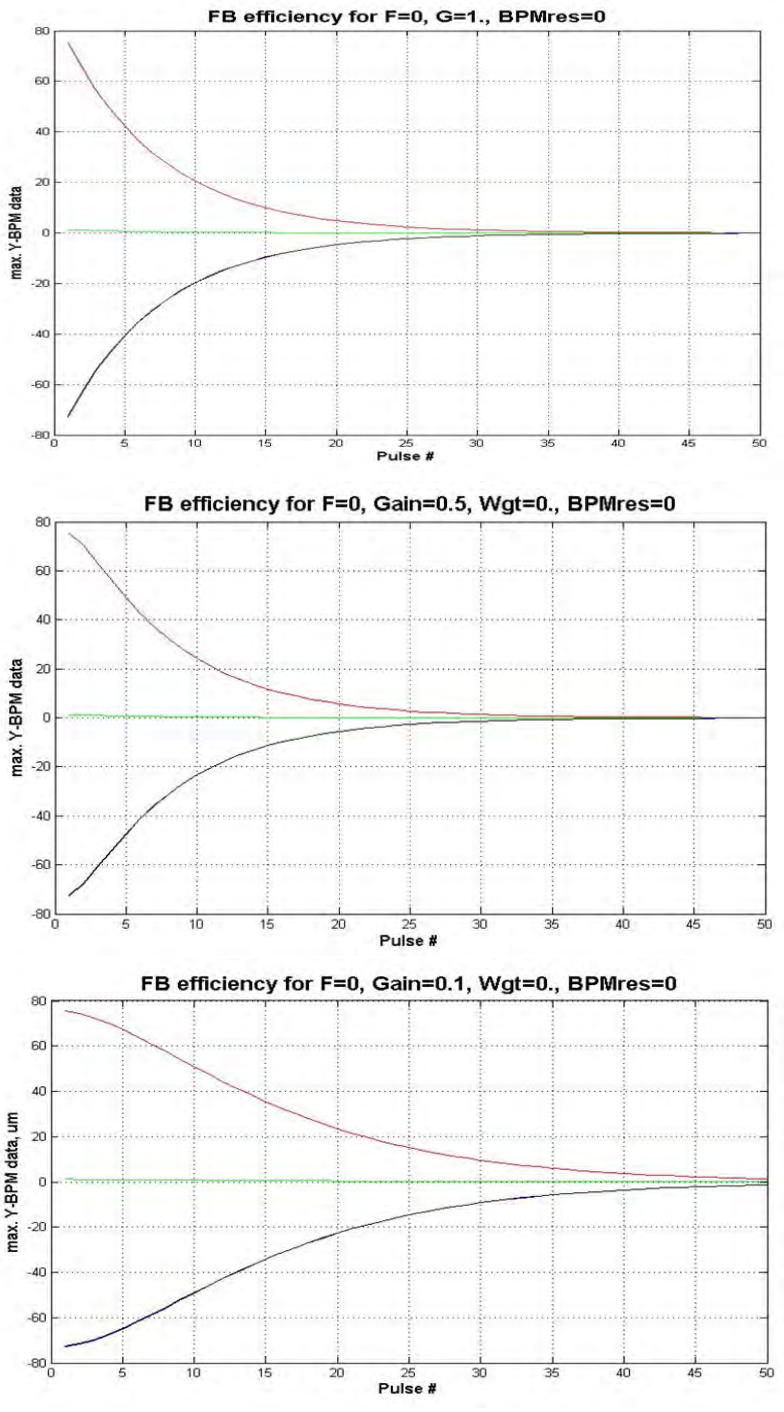

Fig. 6. Static response vs. gain g=1 (top), g=0.5 (middle) and g=0.1 (bottom). Different lines correspond to different BPMs.

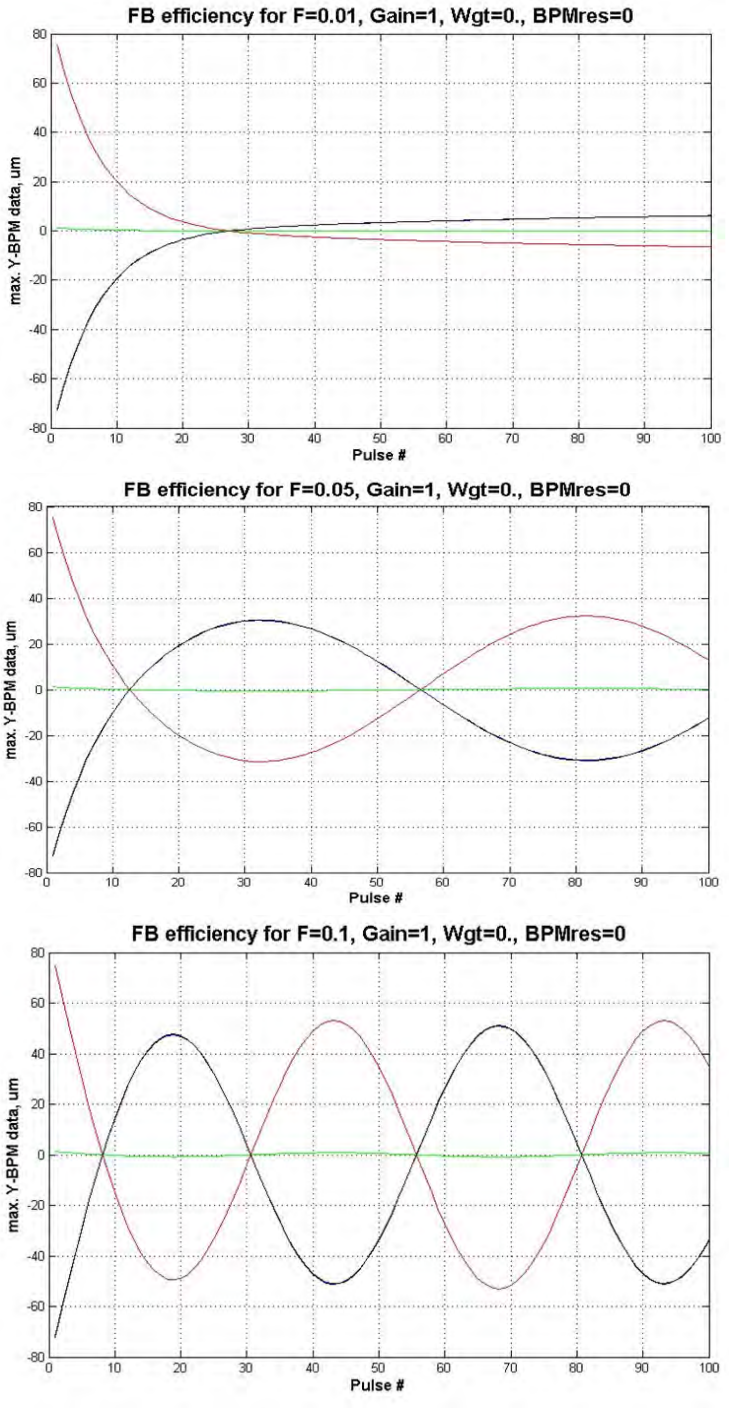

Fig. 7. Dynamic response for a varying frequency of perturbation; F=0.01 Hz (top), F=0.05 Hz (middle) and F=0.1 Hz (bottom).

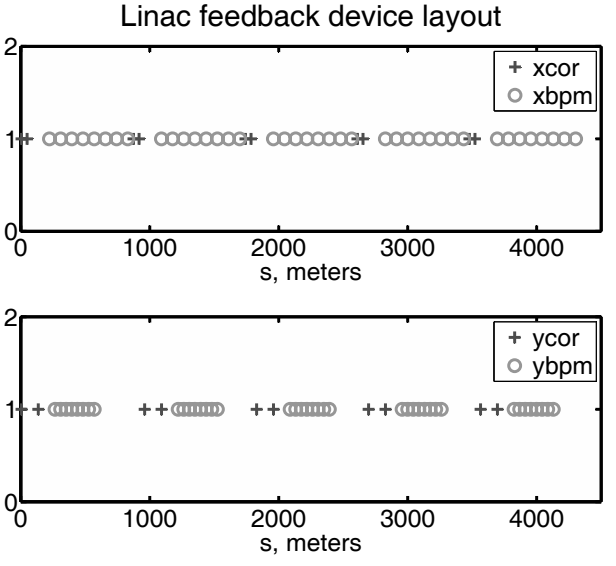

Fig. 8. Lattice layout: 5 FB loops of 2 correctors, 8 BPMs in each direction.

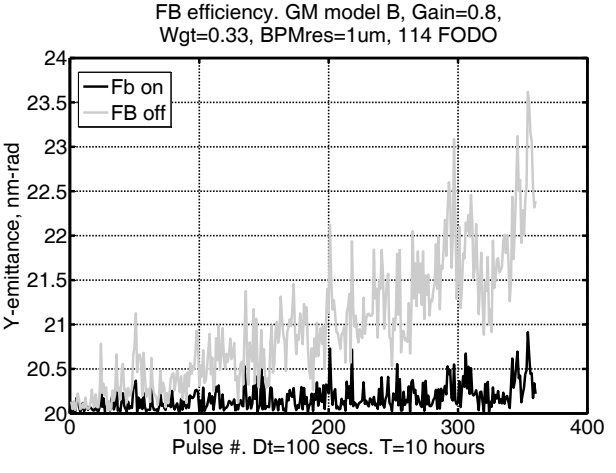

Fig. 9. The effect of FB control for entire linac; GM model B. BPM resolution = 1 μm.

7. FB System for ILC — Main Linac of 114 FODO Cells

The lattice layout for entire main linac is presented in Figure 8. It includes 5 control loops. Two correctors of each loop have phase shift of 90° to make the efficiency of correction independent from their positions in the lattice. Eight BPMs in each loop are used for averaging of BPM-read to reduce the effect of limited BPM resolution.

Figure 9 demonstrates the efficiency of FB control for total period of simulation T=10 hours. Control signals applied to the correctors with an interval of 100 s.

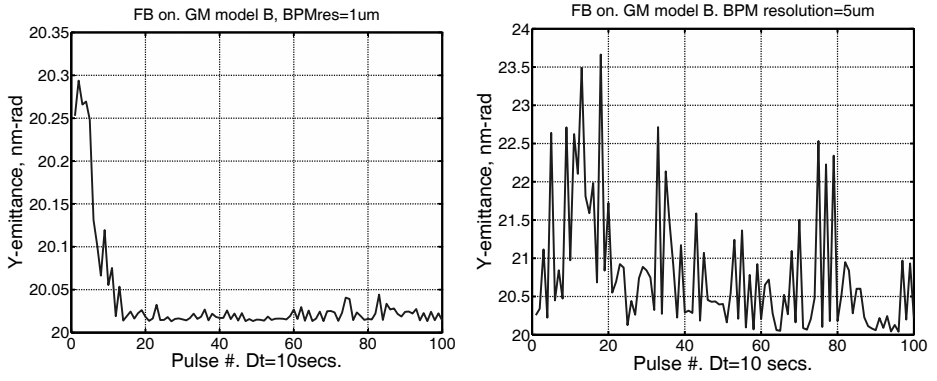

Fig. 10. Dynamics of vertical emittance for BPM resolution 1 μm (left) and 5 μm (right).

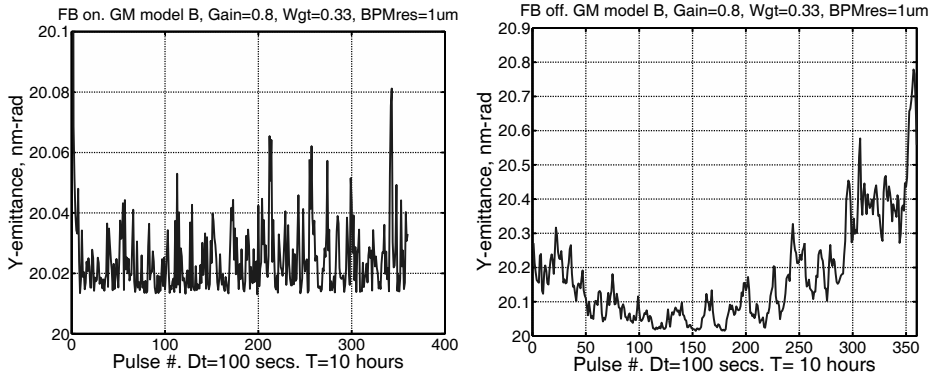

Fig. 11. Dynamics of vertical emittance for time interval of 1 hour (left) and and 10 hours (right) of GM between corrections.

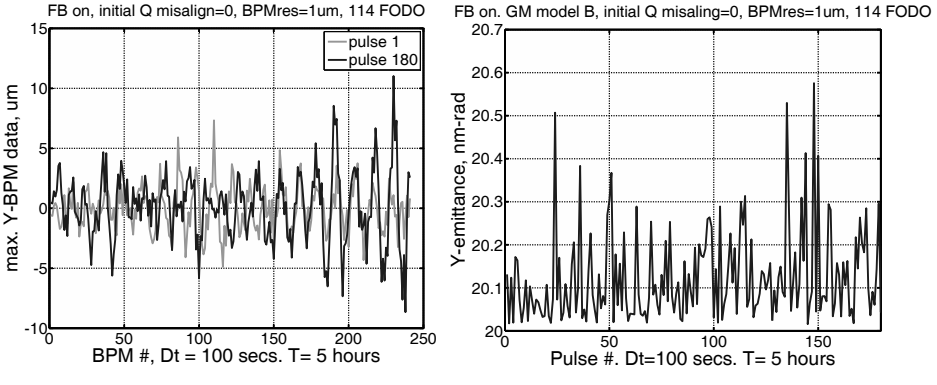

Fig. 12. Dynamics of a beam position (left) and vertical emittance (right) for perfect aligned linac.

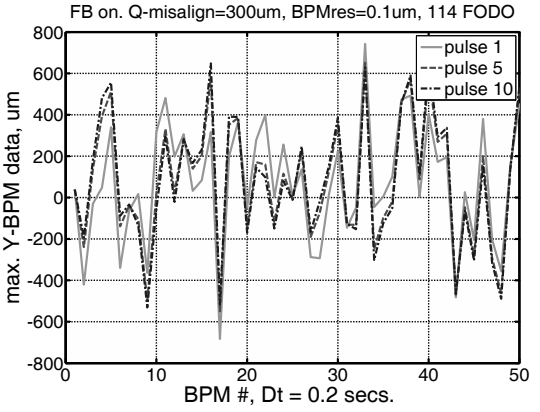

Fig. 13. Dynamics of a beam position for a random initial misalignment of 300 μm. Pulse 1—solid line, pulse 5—dashed line, pulse 10—dash-dotted line.

8. Effects of BPM Resolution, Time Interval and Initial Misalignment

There are many factors which determine the efficiency of a FB control system. The results presented in Figure 10 show that the BPM-read errors are negligible when the resolution is less the 1 μm.

Figure 11 shows the effect of time interval can preserve the vertical emittance for less than 10 hours of GM between corrections.

Beam position in the perfect aligned linac is shown in Figure 12 (left) for initial time moment and after 5 hours of FB control. Right picture shows the dynamics of vertical emittance for that case.

Figure 13 shows the beam position for random initial misalignments at different time moments.

References

1. A.Seryi et al., Recent developments of LIAR simulation code, EPAC'02, Paris, France.
2. V. Alexandrov, V. Balakin, A. Lunin, Experimental test of the adaptive alignment of the magnetic elements of linear collider, Proc. of XVIII International Linac Conference, 26-30 August 1996, Geneva, Switzerland.
3. http://en.wikipedia.org/wiki/Kalman_filter#The_Kalman_filter
4. T.Himel, L.Hendrickson et al., Use of Digital Control Theory State Space Formalism for Feedback at SLC, in Proc. of IEEE Part. Accel. Conf., SLAC-PUB-5470 (1991).
5. T.Himel et al., Adaptive Cascaded Beam-Based Feedback at the SLC, in Proc. of IEEE Part. Accel. Conf., SLAC-PUB-6125 (1993).
6. L.Hendrickson, S.Alison, T.Gromme et.al. Tutorial on beam-based Feedback systems for linacs, SLAC-PUB-6621, August 1994.
7. L.Hendrickson et.al. Feedback systems for linear colliders, SLAC-PUB-8055, April 1999.

8. P.N.Burrows et al., Nanosecond-timescale intra-bunch-train feedback for the linear collider, SLAC-PUB-11185, 2004.
9. L.Hendrickson et al., Beam-based Feedback for the NLC Linac, SLAC-PUB-10493, 2004.
10. A. Seryi, L. Hendrickson, G. White, Issues of stability and ground motion in ILC, SLAC-PUB-11661, January 2006.

International Journal of Modern Physics A
Vol. 24, No. 5 (2009) 869–878

World Scientific
www.worldscientific.com

GREEN'S FUNCTION TECHNIQUE IN FORMING INTENSIVE BEAMS

VALENTIN IVANOV
Muons, Inc., 522 N. Batavia Ave., Batavia, Illinois 60510, USA
vivanov@fnal.gov

The numerical extensions of the Green's function technique have been used to represent a space charge of intensive beams in three-dimensional (3D) case. The introduced trilinear approximation helps to avoid the numerical noise of space charge density on the beam boundary, peculiar to the commonly used piecewise-constant approximation. Both artificial and real singularities for the potential and field gradients have been analyzed. The efficiency of the suggested numerical algorithms has been demonstrated by benchmark tests. The design of the electron gun for an X-band sheet-beam klystron has been done using these algorithms.

Keywords: Green's function; beam optics; klystron gun.

PACS numbers: 29.27.Bd

1. Introduction

One of the most powerful tools to solve mathematical physics problems is the Green's function method. The importance of this method is that it occupies an intermediate place between purely numerical and analytical methods. Thus, an arbitrary-order derivative can be evaluated analytically, when the solution of the initial-boundary problem is represented as an integral convolution of the field source density with the Green's function. In this case, evaluation of derivatives is performing with no accuracy loss in contrast to using the correspondent numerical scheme. The algorithms and numerical results presented in this paper stem from the earlier works of the author.[1,2,3] Some other computationally fast approaches based on the Green's function formalism (so-called "templates") have been developed,[4,5] such as the analytical representation of the field of an ellipsoidal bunch.[6] They drastically decrease the calculation time in the case of ultra relativistic bunches in accelerating structures.

2. Analytical Technique for Evaluation of a Space Charge Potential in 3D

The potential of the electrostatic field of electrodes and space charge of the beam can be represented by a sum of a single-layer potential of surface sources σ and

volume potential of sources ρ

$$\phi(x_0,y_0,z_0)=\int\limits_S \sigma(x,y,z)G(x_0,y_0,z_0;x,y,z)dS+$$
$$\int\limits_V \rho(x',y',z')G(x_0,y_0,z_0;x,y,z)dV,\ (x,y,z)\in S,\ (x',y',z')\in V. \quad (1)$$

Applying the boundary conditions to the integral representation (1), one can get an integral equation for the field source σ. The continuity equation

$$\mathrm{div}\vec{j}=0,\ \vec{j}=\rho\vec{v} \quad (2)$$

with the initial values for the emission current

$$\vec{j}|_{S_0}=\vec{j_0} \quad (3)$$

on the emitter surface S_0, gives an equation for the space charge ρ, but the motion equation

$$\dot{\vec{p}}=Z(\vec{E}+[\vec{v}\times\vec{B}],\ \vec{E}=-\nabla\phi,\ \vec{p}=\frac{m\vec{v}}{\sqrt{1-(v/c)^2}} \quad (4)$$

yields the velocity v of a particle with a charge Z and rest mass m. Here c is the speed of light in vacuum.

The magnetic field B includes as an external magnetic field B_0 of solenoids or permanent magnets as the self-consistent field of a relativistic beam

$$\vec{B}(\vec{r})=\frac{4\pi}{\mu_0}\int\limits_V \frac{[\vec{j}(\vec{r}')\times\vec{v}(r')]}{|\vec{r}-\vec{r}'|^3}dV,\ \vec{r}'\in V, \quad (5)$$

where μ_0 is a permeability of vacuum.

Eqs. (1)–(5) form a complete set of nonlinear equations for the functions σ,ρ,v and B.

In the 3D case the analytical integration over a brick-type element can be done analytically also. Let us introduce a rectangular mesh $\{x_i\}\times\{y_j\}\times\{z_k\}$, and a space charge distribution approximated by a tri-linear form

$$\begin{aligned}\rho(x,y,z)\ =\frac{1}{h_xh_yh_z}\{&[(\rho_{i+1,j,k}(x-x_i)+\rho_{i,j,k}(x_{i+1}-x))\,(y_{j+1}-y)+\\ &(\rho_{i+1,j+1,k}(x-x_i)+\rho_{i,j+1,k}(x_{i+1}-x))\,(y_{j+1}-y)]\,(z_{k+1}-z)+\\ &[(\rho_{i+1,j,k+1}(x-x_i)+\rho_{i,j,k+1}(x_{i+1}-x))\,(y_{j+1}-y)+\\ &(\rho_{i+1,j+1,k+1}(x-x_i)+\rho_{i,j+1,k+1}(x_{i+1}-x))\,(y_{j+1}-y)]\,(z-z_k)\}.\end{aligned} \quad (6)$$

Then the potential of this charge distribution can be represented by an integral

$$\phi(x_0,y_0,z_0)=\sum_{i,j,k}\int\limits_{x_i}^{x_{i+1}}\int\limits_{y_j}^{y_{j+1}}\int\limits_{z_k}^{z_{k+1}}\rho(x,y,z)G(x_0,y_0,z_0;x,y,z)dxdydz, \quad (7)$$

where the Green's function of a point source is described by a formula

$$G(x_0, y_0, z_0; x, y, z) = \frac{1}{4\pi\varepsilon_0\sqrt{(x-x_0)^2+(y-y_0)^2+(z-z_0)^2}} \equiv \frac{1}{4\pi\varepsilon_0 R}. \quad (8)$$

Here R is a distance between an observation point (x_0, y_0, z_0) and a source point (x, y, z) , and ε_0 is the vacuum permittivity.

Accordingly the potential evaluation can be reduced to evaluation of 4 integrals

$$I_1 = \iiint \frac{xdxdydz}{R},\ I_2 = \iiint \frac{xydxdydz}{R},$$
$$I_3 = \iiint \frac{xyzdxdydz}{R},\ I_4 = \iiint \frac{dxdydz}{R}, \quad (9)$$

and the other integrals can be expressed through these by cyclic replacement of variables x, y and z. Using linear replacement of variables $\hat{x} = x - x_0,\ \hat{y} = y - y_0,\ \hat{z} = z - z_0$ and a contraction $r = \sqrt{x^2+y^2+z^2}$ these integrals can be evaluated analytically

$$J_1 = \iiint \frac{xdxdydz}{r} = \frac{y}{4}\left[rz + (x^2+y^2)\ln|z+r|\right] + \frac{z^3}{6}\ln|y+r| +$$
$$\frac{x^2}{2}\left[z\ln|y+r| + y\ln|z+r| - z + xtg^{-1}\left(\frac{z}{x}\right) - xtg^{-1}\left(\frac{zy}{xr}\right)\right] + \quad (10)$$
$$\frac{1}{36}\left[6x^2z - 2z^3 + 3zyr + 6x^3\left(tg^{-1}\left(\frac{zy}{xr}\right) - tg^{-1}\left(\frac{z}{x}\right)\right) - 3y(y^2+3x^2)\ln|z+r|\right],$$

$$J_2 = \iiint \frac{xydxdydz}{r} = \frac{zr^3}{12} + \frac{3}{24}(x^2+y^2)[zr + (x^2+y^2)\ln|z+r|, \quad (11)$$

$$J_3 = \iiint \frac{xyzdxdydz}{r} = \frac{r^5}{15}, \quad (12)$$

$$J_4 = \iiint \frac{dxdydz}{r} = xy\ln|z+r| + yz\ln|x+r| + xz\ln|y+r| +$$
$$-\frac{1}{2}\left[x^2tg^{-1}\frac{yz}{xr} + y^2tg^{-1}\frac{xz}{yr} + z^2tg^{-1}\frac{xy}{zr}\right]. \quad (13)$$

The last integral was evaluated analytically[7], but the result was presented in complex form, not appropriate for direct utilization. That result also has errors.

Electric field components $\vec{E} = -\nabla\phi$ can be evaluated as the derivatives of the potential, for example,

$$E_z(x,y,z) \equiv -\frac{\partial}{\partial z}\phi(x,y,z)$$
$$= \sum_{i,j,k} \int_{x_i}^{x_{i+1}} \int_{y_j}^{y_{j+1}} \int_{z_k}^{z_{k+1}} \rho(x,y,z)\frac{\partial}{\partial z}G(x_0,y_0,z_0;x,y,z)dxdydz. \quad (14)$$

The following set of integrals needed for this case

$$J_{1z} = \iint \frac{dxdy}{r} = -ztg^{-1}\left(\frac{xy}{zr}\right) + y\ln|x+r| + x\ln|y+r|, \tag{15}$$

$$J_{2z} = \iint \frac{xdxdy}{r} = \frac{1}{2}\left[yr + (x^2+z^2)\ln|y+r|\right], \tag{16}$$

$$J_{3z} = \iint \frac{zdxdy}{r} = zJ_{1z}, \tag{17}$$

$$J_{4z} = \iint \frac{xydxdy}{r} = \frac{1}{3}r^{3/2}, \tag{18}$$

$$J_{5z} = \iint \frac{xzdxdy}{r} = \frac{z}{2}\left[yr + (x^2+z^2)\ln|y+r|\right], \tag{19}$$

$$J_{6z} = \iint \frac{xyzdxdy}{r} = \frac{z}{3}r^{3/2}. \tag{20}$$

3. Singularity Problems

Actually, the potential of an electric field is a regular limited function in all space, so the logarithmic terms in formulas (10)–(13), (15)–(19) produce artificial singularities, which must be excluded in program implementation. Furthermore the field gradients have real singularities on the vertices and edges of cubic cells at the beam boundary (point "a").[8] Those singularities result in numerical noise, leading to artificial halo formation around the beam etc. All these singularity problems have been successfully overcome by using a high-order approximation for the space charge density.[1] The space charge distribution and its approximations are presented in Fig. 1.

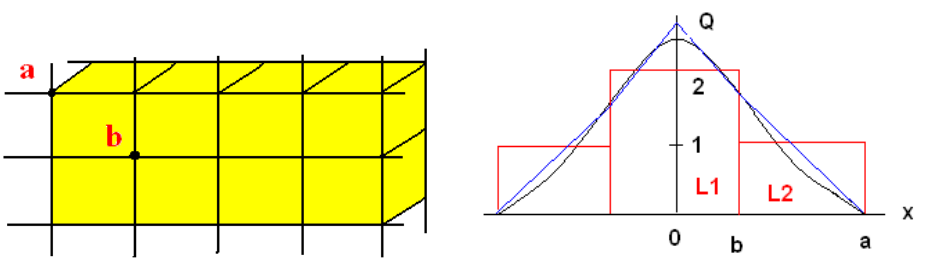

Fig. 1. On the field singularity of charged cubic cells.

Both integrals over elements $L1$ and $L2$ have singularities at the point "b". These integrals should be weighted with coefficients $Q1$ and $Q2$ associated with the elements in the electric field evaluation. As a result singular terms are compensated at internal points of the beam for any smooth approximation, where $Q1 = Q2$, but they keep the singularity for a piecewise constant approximation where $Q1 \neq Q2$. The electric field at the boundary point $x = b$ has no singularity for smooth approximations because the singular integrals over element $L2$ are multiplied by

$Qb = 0$. The singularity occurs for a piecewise constant approximation because the space charge coefficient $Q2 \neq 0$ this case.

4. Benchmark Results

One of simplest test is the potential of a sphere of radius R with uniformly distributed total charge Q. In that case the charge density $\rho = \frac{3Q}{4\pi R^3}$, and the exact solution for potential is given by the formula

$$\phi(r) = \begin{cases} q\left[\frac{(R^2-r^2)}{2} + \frac{1}{r}\right] & r < R, \\ \frac{Q}{R} & r > R. \end{cases} \tag{21}$$

Actually a discrete set of charged cubes can represent this sphere. We put $R = 1$ and $Q = 1$ in our tests, and we use a uniform mesh for space charge in each direction. We will compare this exact solution with the analytical integration for piecewise-constant and linear approximations of space charge. In addition the numerical integration over the brick element is used

$$\phi_\diamond = \sum_i^n \sum_j^n \sum_k^n a_i a_j a_k \frac{\rho(x_i, y_j, z_k)}{\sqrt{(x_x - x_0)^2 + (y_j - y_0)^2 + (z_k - z_0)^2}}, \tag{22}$$

where a_i, a_j, a_k—weights, and x_i, y_j, z_k—nodes of a Gaussian quadrature in 3D of order n. We will use $n = 2$ in our simulations, so this is an 8-node formula, which is quite enough for our goal.

Figure 2 shows the potential distribution for exact solution and for different integration schemes.

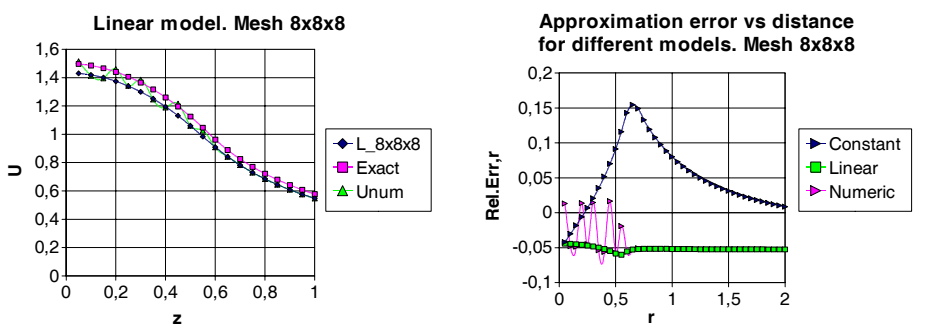

Fig. 2. Left: Exact solution for a potential distribution (magenta), analytic integration (blue) and numerical integration (green). Right: Relative error for different integration schemes.

One can see the oscillations in the numerical integration for the 'near' zone. That is because our quadrature formula does not take into account the singularity of the integrand function. It has a good accuracy in the "far" zone. The right graph in

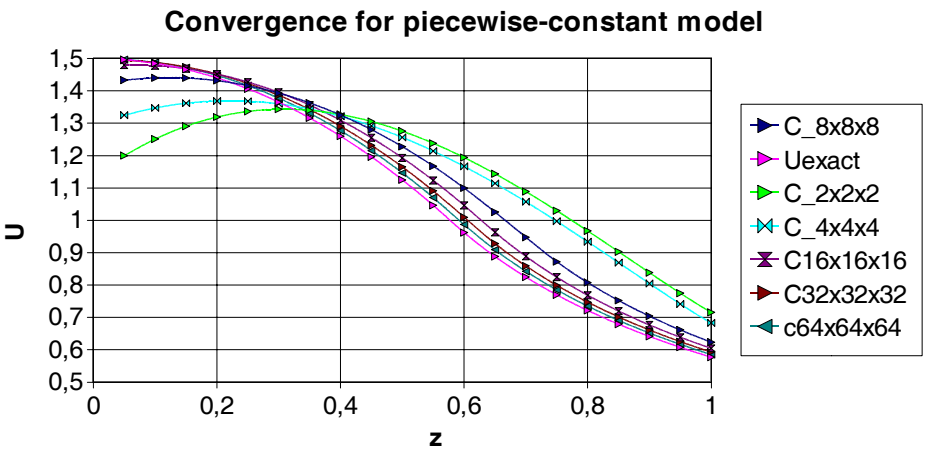

Fig. 3. Exact solution for the potential of sphere (magenta), and analytic integration for the piecewise-constant model in a mesh refinement.

Figure 2 demonstrates a substantial difference in accuracy of computations between piecewise-constant and linear approximations.

Figures 3 and 4 demonstrate the convergence rate for both approximations in varying of number of mesh cells in each direction from 2 to 64.

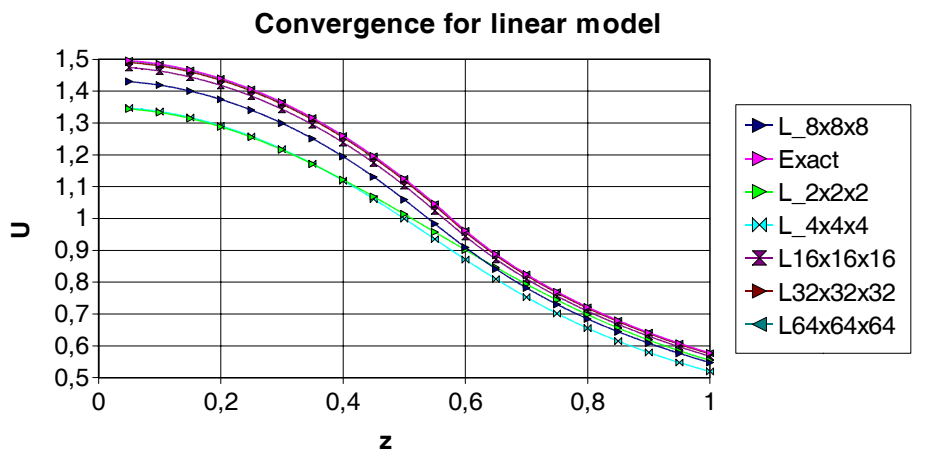

Fig. 4. Convergence of analytical integration for a linear approximation of the space charge distribution.

Figures 5 and 6 shows the convergence rate for both models and the run time dependence in a mesh refinement.

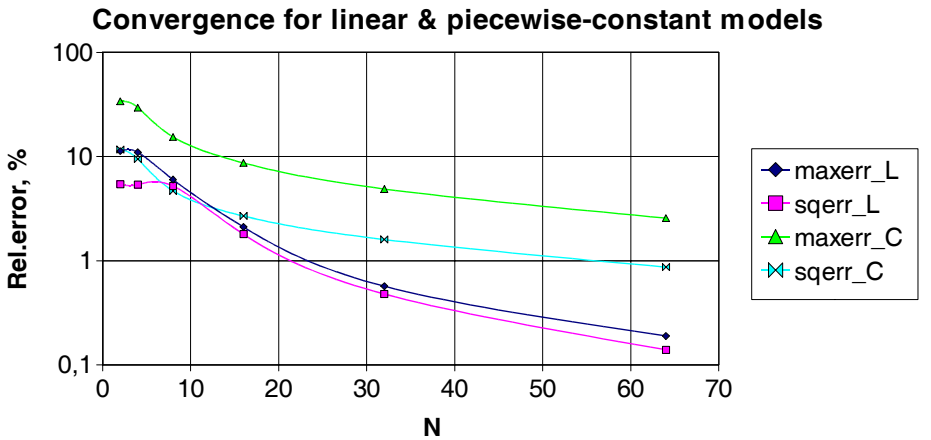

Fig. 5. Maximal and mean square errors for piecewise-constant and linear models vs. the number of nodes in each direction

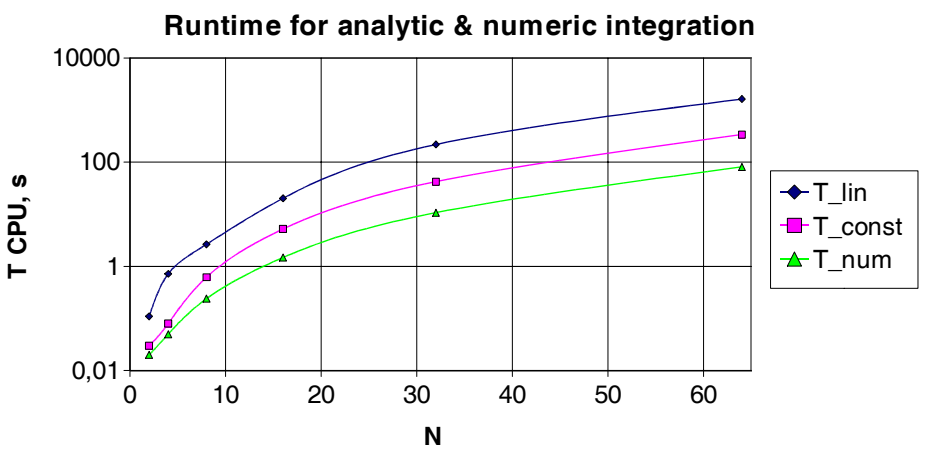

Fig. 6. CPU-time for piecewise-constant and linear models vs. the number of mesh nodes in each direction

5. The Adaptive Algorithm of Integration

One can see that numerical integration is the fastest computational algorithm, compared with both analytical schemes, but it has low accuracy near to the field-source region. The idea of an adaptive integration scheme is to combine the numerical and analytical approaches, and switch from the analytical scheme in near region to the numerical one in the far zone. The criterion for this switch is a relative distance from the field source compared to the dimension of the source.

Figure 7 demonstrates how it works for the example of a very coarse mesh of 2 x 2 x 2 cells representing a sphere. The left part of this picture corresponds to the criterion $r = 2.2$. It is close to a sphere of radius $R = 1$, and it produces a reasonably large jump in the inter face region. The right picture shows very smooth passage from one algorithm to the other.

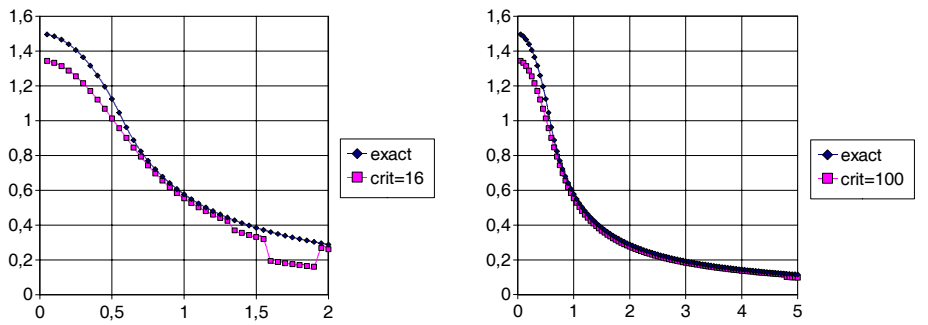

Fig. 7. Worse mesh 2x2x2 cells shows clearly the influence of the adaptation criterion

Figure 8 demonstrates that such a smooth inter face can be reached for a small value of the switch criterion, when the mesh is fine enough.

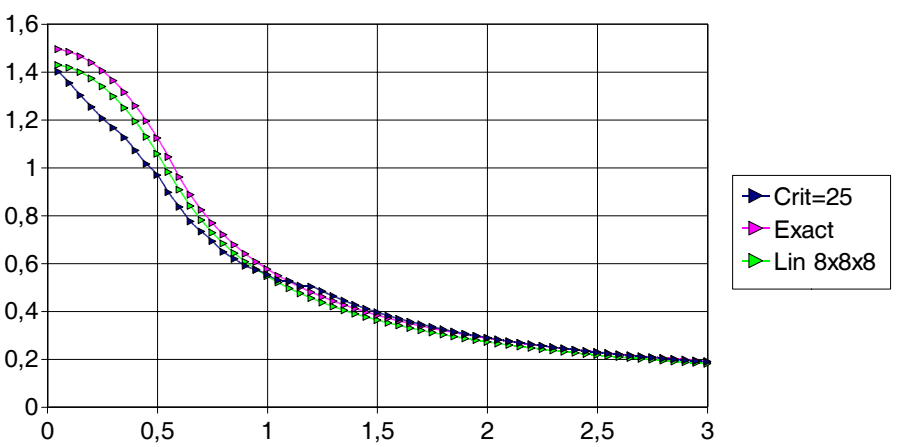

Fig. 8. The adaptive integration algorithm can reduce the run time dramatically (factor of 5–10) with accuracy loss of about 0.5–1%

6. Sheet-Beam Gun Design

Our simulations of beam optics for a sheet beam gun for an X-band klystron is an example of a realistic design. This type of gun is able to overcome the power limitations peculiar to the classical axially-symmetric klystron guns. Here the electron beam emitted from a cylindrically-shape cathode is compressed in one transverse direction, and is almost parallel in the other. As a result we get a sheet beam in the anode slot. The effect of space charge repulsion is much less in this gun compared with a cylindrical beam.

Figure 9 shows the geometry shape of anode and cathode assemblies, and the geometry model with triangular surface elements.

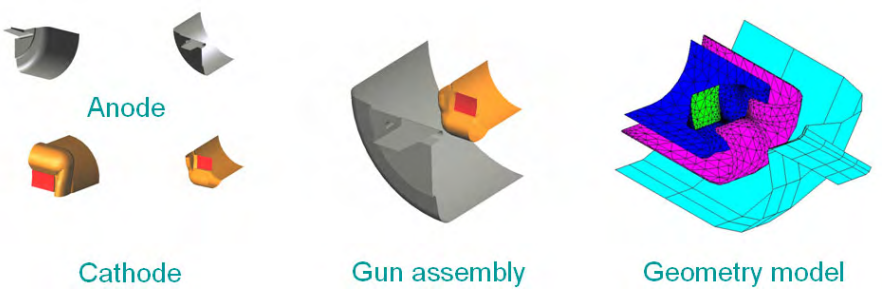

Fig. 9. Parts, assembly and geometry model of a sheet-beam gun.

Figure 10 demonstrates the results of a computer simulation for beam optics. It takes 10 iterations on space charge to reach a convergence of about 1% for a total beam current on a mesh of 10,000 brick elements. The total simulation time was 65 minutes with a desktop PC 1.4 GHz.

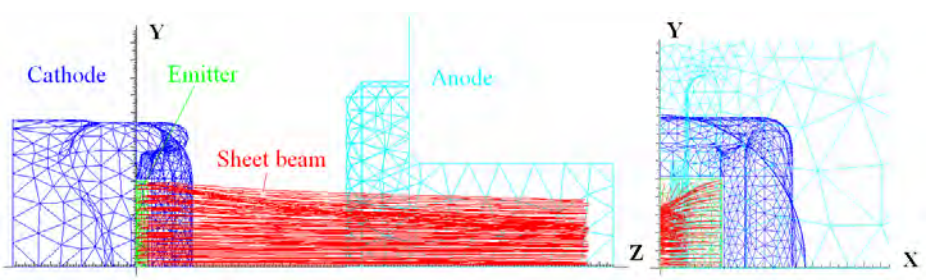

Fig. 10. Beam optics for a sheet-beam gun of X-band klystron.

Acknowledgments

Special thanks to Dr. L. Vorobiev and Dr. P. Lucas for the fruitful discussion and criticism.

References

1. V. Ivanov. Numerical methods for analysis of 3D non stationary flows of charged particles, 15. Trudy Instituta Matematiki, Izd-vo "Nauka", Sibirskoe Otdelenie, 1989.— p.172–187.
2. V. Ivanov, A. Krasnykh, Analytical computations in solution of 3D problems of physical electronics by BEM//ACES-2002, March 18-22, 2002, Monterey, CA.
3. V. Ivanov, A. Krasnykh, G. Scheitrum, D. Sprehn, L. Ives, G. Miram, 3D Modeling Activity for Novel High Power Electron Guns at SLAC, PAC-2003, May 12–16, 2003, Portland, USA.
4. L. G. Vorobiev, R. C. York, High Current Beam Simulation using Templates, `http://cern.ch/AccelConf/e02/PAPERS/WEPLE092.pdf`, EPAC 2002, Paris.
5. L. G. Vorobiev, R. C. York, Calculation of longitudinal fields of high-current beams in the vicinity of conducting chambers, PAC'99, March 29th–April 2nd, pp. 2781–2783, New York, 1999.
6. M. Krasilnikov, Space charge algorithm for the multi ensemble model, Nucl. Instr. & Meth. in Phys. Research, A **558** (2006) 69–73.
7. Ji Quang, S. Lidia, R. Ryne, C. Limborg-Deprey, Three-dimensional quasi static model for high brightness beam dynamic simulation, Phys.Rev. Special Topics—Accel.& Beams, 9, 044204 (2006).
8. G. Fikera, Uspekhi mat. nauk. 1975. T. 30. Vyp. 3. S. 105-124.

International Journal of Modern Physics A
Vol. 24, No. 5 (2009) 879–892

World Scientific
www.worldscientific.com

BEAM DYNAMICS OPTIMIZATION FOR THE XFEL PHOTO INJECTOR

MIKHAIL KRASILNIKOV

PITZ, Deutsches Elektronen-Synchrotron,
Platanenallee 6, Zeuthen, 15738, Germany
mikhail.krasilnikov@desy.de

The main challenge for the European XFEL photo injector is the production of 1 nC electron beams with a normalized transverse emittance of 0.9 mm mrad. The photo injector setup consists of a 1.5-cell L-band rf gun cavity supplied with solenoids for beam focusing and emittance compensation and the first accelerating section with 8 TESLA superconducting cavities. The first 4 cavities are used as a booster to provide by proper choice of its position, gradient and phase matching conditions for the emittance conservation.

For optimization of the beam dynamics in the photo injector, a staged algorithm, based on ASTRA simulations, has been developed. The first stage considers the emission of electrons from a photo cathode. The cathode laser energy and its transverse parameters are adjusted to produce a bunch charge of 1 nC in presence of space charge forces (including image charge at the cathode) and Schottky-like effects. The second stage contains rf gun cavity and solenoid optimization. The booster position, gradient and initial phase are optimized at the third stage yielding the minimum emittance at the photo injector exit. Results of the XFEL photo injector optimization will be presented.

Besides simulations experimental studies towards XFEL photo injector are carried out. The photo injector test facility at DESY in Zeuthen (PITZ) develops photo injectors for FELs, including FLASH and the European XFEL. A thorough comparison of measured data with results of beam dynamics simulations is one of the main PITZ goals. Detailed experimental studies on photo emission processes, thermal emittance, transverse and longitudinal phase space of the electron beam are being performed together with beam dynamics simulations. This aims to result in better understanding of beam dynamics in high brightness photo injectors. Experimentally obtained photo injector characteristics (like thermal emittance) have to be used in an additional optimization of the photo injector resulting in more realistic beam dynamics simulations. Results of these studies will be reported as well.

Keywords: Photo injector; FEL; emittance.

PACS numbers: 29.27.Bd, 29.25.Bx

1. Introduction

Modern linac based Free-Electron Lasers (FELs) require high brightness electron beams. rf photo injectors are capable of producing high charge electron beams with extremely small transverse emittance. A transverse normalized beam emittance of

0.9 mm mrad for 1 nC bunch charge at the injector exit is the main challenge for the European XFEL photo injector.[1]

2. XFEL Photo Injector Concept

High densities of the transverse phase space (or small emittance) imply space charge dominated beams in a photo injector. Since the high charge is extracted from the photo cathode at almost zero energy the Coulomb repulsion forces play a significant role in the dynamics of the electrons within the bunch. Strong nonlinearities of the space charge field in the cathode vicinity result in beam emittance growth. In order to provide a small emittance in the photo injector, several techniques have to be applied. Solenoid compensation[2] implies reversing the correlations along the bunch by applying a solenoid lens. By proper choice of the solenoid parameters the space charge force acts at some distance reducing transverse phase space nonlinear correlations along the bunch and resulting in a projected emittance minimum. Electron beams accelerated in the rf gun still remain space charge dominated, which leads to an emittance increase. In order to keep the emittance small further beam acceleration by a booster must be applied. For efficient emittance conservation, matching conditions based on the invariant envelope technique provide a quasi laminar beam regime.[3] This requires proper choice of the booster position, gradient and phase.

The XFEL photo injector consists of an rf gun, a standard accelerating module (ACC1), and a diagnostic section. The electron bunch is emitted from a Cs_2Te cathode illuminated by a UV laser pulse in a high accelerating field (60 MV/m peak field on the cathode) and accelerated up to 6.3 MeV in the normal conducting 1.3 GHz 1,5-cell rf gun cavity. A solenoid, centered 0.276 m downstream of the cathode, focuses the beam into the first accelerator module which is located after a drift length of about 3.5 m. A bucking solenoid is to be used to compensate the magnetic field at the cathode. The accelerator module increases the energy to about 160–170 MeV.

Cathode laser pulse shaping is a key issue for the photo injector performance. In order to reduce the space charge effect, especially during emission from the cathode a flat top temporal profile with 20 ps FWHM and 2 ps rise and fall time is foreseen for the European XFEL photo injector. A radially homogeneous transverse profile is required with a diameter chosen as a compromise between thermal and space charge induced emittance.

3. Simulation of Beam Dynamics in Photo Injector

In order to optimize photo injector parameters, a number of beam dynamics simulations have been performed. The ASTRA code[4] was used to simulate electron beam properties from the photo cathode till the photo injector exit (z=15 m). An electron beam has been tracked in the external electromagnetic fields of the rf gun with solenoids and the accelerating module (ACC1) with eight TESLA cavities. The first four cavities have been used as a booster, so the gradient and the phase

of these cavities were tuned to minimize the beam emittance. RF gradient of the second four cavities was assumed close to the maximum available (peak field of 50 MV/m), its phase has been tuned to minimize an rms energy spread of the electron beam.

4. XFEL Photo Injector Optimization Strategy

A multi-staged approach has been used for the optimization of the photo injector:

(1) emission from the photo cathode
(2) optimization of the rf gun parameters
(3) booster optimization
(4) minimization of the beam energy spread

The beam normalized rms projected emittance $\varepsilon = \sqrt{\varepsilon_{nx}\varepsilon_{ny}}$ has been used as a goal function for the minimization of the nominal XFEL photo injector setup:

$$\Phi_{goal} = \left[\varepsilon\Big|_{z=15m} + L \cdot \frac{d\varepsilon}{dz}\Big|_{z=15m}\right] \cdot \Pi_1 \cdot \Pi_1 ... \cdot \Pi_K, \tag{1}$$

where not only the emittance but also its slope $\dfrac{d\varepsilon}{dz}$ is used to calculate the emittance trend at some distance L (typically $L \sim 5$ m) from the injector exit ($z = 15$ m). A penalty factor $\Pi_n = \Pi(p_n)$ has been used in order to eliminate solutions which can not be realized experimentally. This factor implies an exponential growth of the goal function if the photo injector parameter p_n is outside the specified range $[p_{from}; p_{to}]$:

$$\Pi(p) = \begin{cases} \exp\left(\frac{p_{from}-p}{p_{to}-p_{from}}\right), & \text{if } p < p_{from} \\ \exp\left(\frac{p-p_{to}}{p_{to}-p_{from}}\right), & \text{if } p > p_{to} \\ 1, & \text{otherwise.} \end{cases} \tag{2}$$

Various machine parameters and electron beam properties are considered for the penalty factor at different optimization stages. Mainly a longitudinal positions of the gun solenoid and the booster were affecting the penalty factor in the optimization of the XFEL photo injector.

The aperture of the FLASH/PITZ beam line (which is assumed to be similar to the XFEL one) has been also used; possible charge losses are considered as an additional contribution to the penalty factor.

4.1. *Emission from the photo cathode*

This step serves as a pre-run of the rf gun optimization (subsection 4.2). For the given cathode laser and rf gun parameters the laser power is tuned to produce a bunch charge of 1 nC. The tracking stops at z=7 cm (right after the first iris of the gun cavity), what corresponds to the total extracted charge which will be

transported downstream. Several ASTRA computations run in parallel to reduce computation time.

The main physical effects governing the emission process are space charge, including image charge from the cathode, and electromagnetic forces of the rf gun cavity. Another important emission feature is a Schottky-like effect[5] in rf guns, i.e. the enhancement of the photo emission resulting from an electric field at the cathode surface. In other words, a bunch charge of 1 nC could be reached in different ways. The simplest model is a "pure" photo effect, which implies no influence of the electric field at the cathode on the QE of the photo cathode. This does not exclude an integral impact of the space charge, especially in the case of extremely high space charge density at the cathode (e.g. small transverse size of the laser spot). Another model allows the emission due to the presence of an electric field at the moment of emission of the corresponding part of an electron beam. Both models are implemented in ASTRA. In the case of emission with Schottky-like effect the charge of macro particles Q_{mp} is calculated according to:[4]

$$Q_{mp} = \frac{Q_{b0} + s_1 \cdot E(t) + s_2\sqrt{E(t)}}{N_p}, \tag{3}$$

where Q_{b0} corresponds to the charge produced by photo effect ($Q_{b0} \sim$ laser power), the term $s_1 \cdot E(t) + s_2\sqrt{E(t)}$ is related to the additional charge due to the Schottky-like effect in the presence of field $E(t)$ at a moment of the macro particle emission, N_p is the number of macro particles used for simulations. This model is valid for both above mentioned emission models, $s_{1,2} = 0$ corresponds to the "pure" photo effect.

Simulated rf gun phase scans for a given bunch charge are shown in Fig. 1. Two sets of simulations have been performed. The first did not apply Schottky-like effect, $Q_{b0} = 1.02$ nC in order to produce a 1 nC beam at the rf gun launch phase of maximum energy gain (zero phase). The second simulation involves the macro particle charge dependence on the electric field at the cathode at the moment of emission according to Eq. (3) with $Q_{b0} = 0.5$ nC, $s_1 = 0.16$ nC·m/MV, $s_2 = 0.089$ nC·(m/MV)$^{1/2}$.

Despite the charge and the beam energy for both simulations are the same, the transverse phase space differs significantly (Fig. 2) resulting in different transverse rms emittances at $z = 4.3$[a]: $\varepsilon_{n,x}^{noSchottky} = 4.9$ mm·mrad and $\varepsilon_{n,x}^{Schottky} = 2.5$ mm·mrad. These simulations were performed to illustrate the importance of the emission process in an rf gun and the necessity to take into account experimental data for correct simulations - namely, the gun phase scan for the given bunch charge, when Schottky-like effects are observed for rf guns with Cs_2Te photo cathodes.[6] Usually experimental phase scans for a bunch charge are used to obtain constants s_1 and s_2 used in ASTRA simulations by fit of the simulated charge to the measured one.

[a]PITZ beamline layout has been used for these simulations.

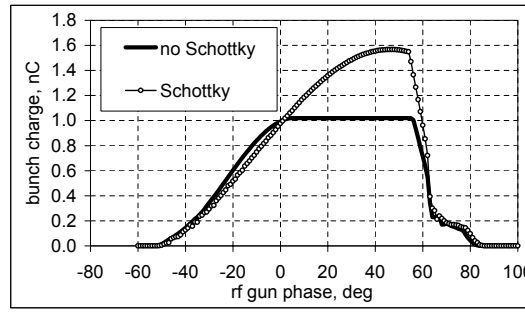

Fig. 1. Gun phase scan—bunch charge vs. gun launch phase. Zero phase is referred to as an rf gun launch phase yielding the maximum beam energy gain. Both ASTRA simulations were aimed to produce a 1 nC electron beam at zero phase.

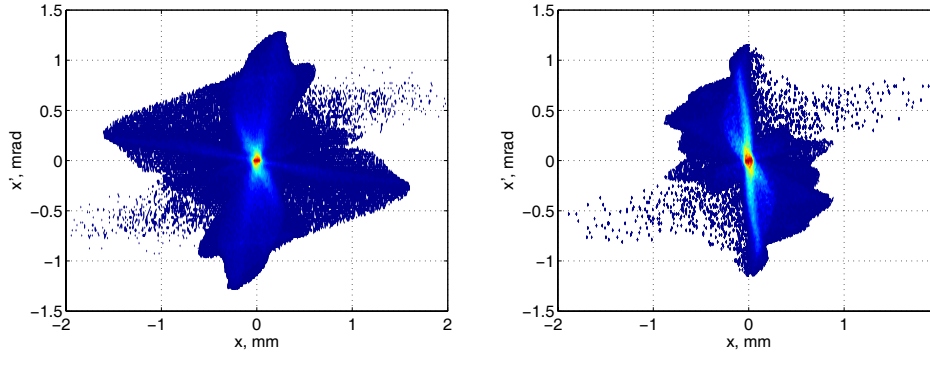

Fig. 2. Simulated transverse phase for the case without (left) and with Schottky-like effect (right).

4.2. *Optimization of the rf gun parameters*

Main parameters optimized at this stage are:

- cathode laser transverse rms size[b]
- main solenoid peak field
- longitudinal position of the main solenoid
- launch phase of the rf gun

The gun rf gradient has been fixed at 60 MV/m peak field at the cathode, which is the XFEL photo injector project parameter. An emittance reduction with an increase of the gun gradient[7] has been taken into account. Further increase of the gun gradient is restricted by the limits of the rf system.[8]

[b]Transverse profile of the cathode laser is assumed to be radial homogeneous.

The temporal laser profile was fixed to be a flat-top with 20 ps FWHM and 2 ps rise and fall time. The influence of the rise and fall time on the beam projected emittance has been studied additionally (see section 5.3). The pulse length is a compromise between space charge reduction during emission and nonlinearities in the longitudinal phase space due to the rf field of the gun and ACC1 cavities. These nonlinearities are planned to be compensated by the 3rd harmonics cavity[1] operated strongly off-crest. The 3rd harmonics section is located in the linac downstream the injector and out of the scope of this paper.

The main contribution to the penalty factor at this stage is the longitudinal position of the main solenoid. Its further shift downstream the beam line is restricted by the mechanical construction of the coaxial coupler of the gun. This results in the solenoid centering at z=0.276 m, what is close to its actual position at PITZ and FLASH.

Definitely, an optimized transverse size of the cathode laser is also determined by the initial thermal emittance of the electron beam. According to the model of Cs_2Te cathodes,[9] the initial kinetic energy of the photo electrons is $E_k = 0.55$ eV. This model does not include bending of energy levels in CS_2Te in presence of electric field (rf and space charge) applied during electron emission from the cathode. Recent thermal emittance measurements at PITZ[10] yielded $E_k = 1.4$ eV. Simulations for different values of the thermal kinetic energies have been performed (for results see section 5.3). The increase of the initial kinetic energy of electrons E_k can be also (at least partially) explained by cathode surface imperfections (roughness, contamination level, etc).

The optimization of the rf gun parameters starts with tuning of the photo emission (see subsection 4.1). Afterward a 1 nC electron beam is tracked until the beam waist (typically first 5 m of the beam line were sufficient to contain a beam waist). A beam monitor (containing all particle coordinates) near the waist location is saved and used as an input beam for the booster optimization (subsection 4.3)

In order to establish an initial simplex of rf gun parameters a Monte-Carlo[11] method has been used. The best solutions have been used as initial simplexes for the subsequent optimization using the Nelder-Mead algorithm.[12] Every optimization parameter has been centered to the initial guess and normalized to the range where significant emittance growth takes place. This range can be obtained by numerical study of the corresponding parameter influence on the emittance growth (see section 5.3). Typically 10% emittance growth has been used in order to find search parameter ranges, needed for dimensionless variables used in the optimization algorithm.

4.3. *Booster optimization*

For each set of rf gun parameters the booster has to be optimized for a minimum emittance at the injector exit. ASTRA tracks the electron beam obtained from the previous stage (4.2). Main parameters to be optimized at this stage:

- longitudinal position of the booster
- booster gradient (peak field)
- rf phase of the booster.

As it has been mentioned before the first four TESLA cavities of ACC1 are used as a booster for the XFEL photo injector. For the nominal photo injector settings gradient and phases in all the cavities of the booster were assumed to be equal.

The technique of the invariant envelope is used to obtain an initial guess for the booster optimization. The booster entrance is positioned near the electron beam waist, the booster normalized accelerating gradient γ' is chosen to provide a quasi laminar beam regime:[3]

$$\gamma' = \frac{2}{\sigma_i}\sqrt{\frac{I}{3I_0\gamma_i}}, \tag{4}$$

where σ_i and γ_i are transverse rms size and normalized beam energy at the entrance of the booster, I is a beam current, $I_0 = 17$ kA is the Alfven current. Such a proper choice of the initial parameters accelerates the 3-dimensional search procedure.

As contributions to the penalty factor the two following assumption have been used at this stage of optimization: 1) longitudinal start position of the booster has to be greater than z=2.5 m due to mechanical restrictions of the beam line; 2) upper limit for the booster peak field was chosen to be 50 MV/m (close to the limit of the TESLA cavities capability).

4.4. *Minimization of the beam energy spread*

The second half of ACC1 consists of four TESLA cavities operated at 50 MV/m peak field. Their phases were synchronously tuned to minimize the rms energy spread of the beam at z=15 m.

Because of the weak dependence of the beam emittance on the phase of the second half of ACC1 (ϕ_3) (Fig. 3), the phase with minimum rms momentum spread is chosen in order to conduct the beam into the matching section (minimizing chromatic effects). The phase of the absolute emittance minimum (emittance decrease 0.25 %) corresponds to rather large energy spread and this can cause a significant emittance growth in quadrupoles of the matching section.

5. Optimized XFEL Photo Injector

Beam dynamics optimization of the XFEL photo injector resulted in a setup summarized in Table 1[c].

Corresponding external electromagnetic fields along the beam line are shown in Fig. 4.

[c]Values of optimized parameters are shown in bold.

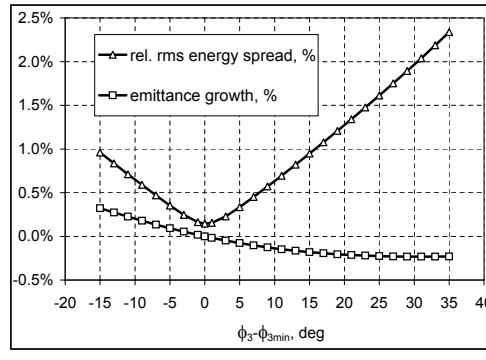

Fig. 3. Typical dependence of electron beam parameters on the phase ϕ_3 of the second half of ACC1. Relative rms energy spread ($\sigma_E/\langle E\rangle$) is plotted together with emittance growth $\varepsilon(\phi_3)/\varepsilon(0)-1$. Zero phase $\varepsilon_3 = 0°$ corresponds here to the phase of the minimum energy spread.

Table 1. Optimized parameters of the XFEL photo injector.

subsystem	parameter	value	unit
rf gun cavity	E_{cath}	60	MV/m
	launch phase ϕ_{1opt}	**-0.7**	deg
cathode laser	FWHM	20	ps
	rise/fall time	2	ps
	$\sigma_{x,y}$	**0.45**	mm
solenoid	peak field B_z^{opt}	**-0.2294**	T
	center	**0.276**	m
ACC1, cav.1-4	cav.1 center	**4.04**	m
	peak field E_z	**24.5**	MV/m
	phase ϕ_{2opt}	**-15**	deg
ACC1, cav.5-8	peak field E_z	50	MV/m
	phase	**5**	deg
electron beam	charge, Q	1	nC
	thermal kinetic energy E_k	0.55	eV
	mean energy	167	MeV
	rms energy spread	0.25	MeV
	rms projected normalized emittance $\varepsilon_{x,y}(z = 15\ m)$	0.7	mm mrad

5.1. *Electron beam properties along the beam line*

Beam rms transverse size $\sqrt{\sigma_x \cdot \sigma_y}$ and rms projected transverse emittance $\sqrt{\varepsilon_x \cdot \varepsilon_y}$ are shown in Fig. 5. The transverse rms beam size of 240 μm at the injector exit corresponds to the beta-function value of $\beta_{x,y}(z = 15\ \text{m}) = 28$ m.

Mean kinetic energy and rms energy spread are shown in Fig. 6, a relative energy spread of 0.15% has been simulated.

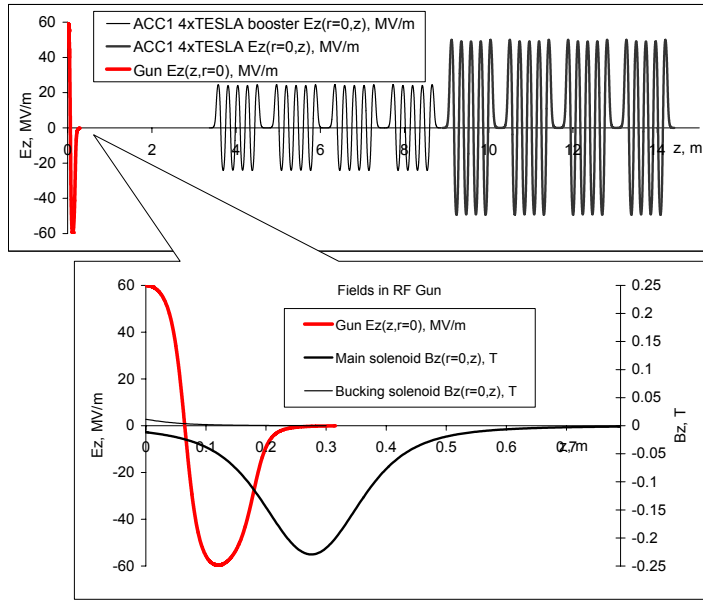

Fig. 4. Electromagnetic fields in the XFEL photo injector

RMS bunch length and longitudinal emittance are shown in Fig. 7 as a function of the distance from the cathode. An electron bunch length of 2 mm rms or 7 ps FWHM has been obtained at the injector exit.

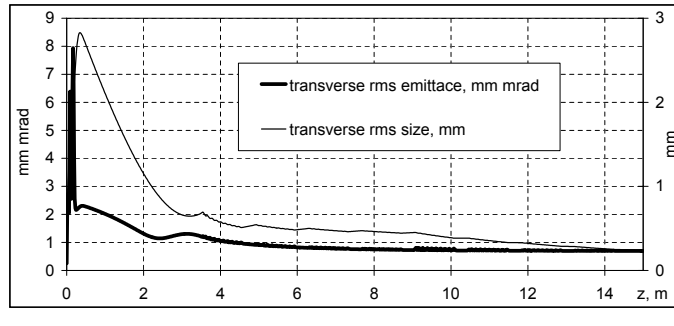

Fig. 5. Beam rms transverse size and projected normalized emittance along the beam line.

5.2. *Transverse and longitudinal phase space*

The characteristic s-shape of the transverse phase space is shown on the left plot in Fig. 8. On the right plot of Fig. 8 the longitudinal phase space of the electron beam at the injector exit (z=15 m) is presented. It should be noted that the longitudinal

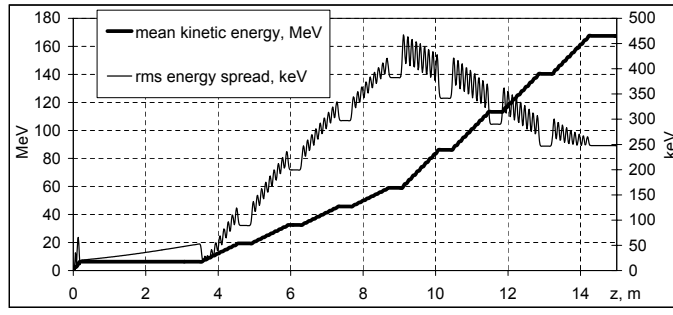

Fig. 6. Beam mean kinetic energy and rms energy spread along the beam line.

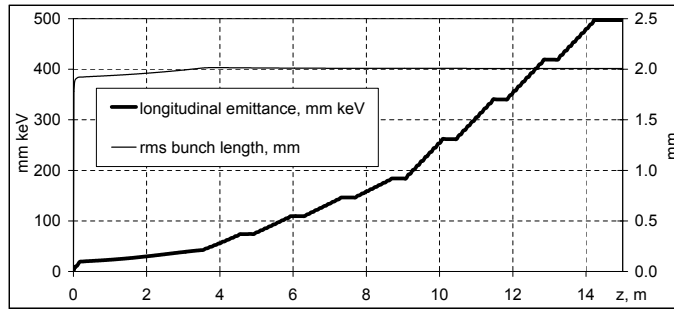

Fig. 7. RMS bunch length and longitudinal emittance along the beam line.

phase space nonlinearity has to be corrected by the third harmonics section downstream the injector.[1] The third harmonics cavities operated at 3.9 GHz (wavelength 77 mm) strongly off-crest in deceleration mode introduce nonlinear correlations in the longitudinal phase space compensating the nonlinearities originating from the injector.

The transverse phase space contains a rather large fraction of peripheric particles, which indeed do not contribute the FEL lasing process. These particles belong mainly to the head and tail, and the local (slice) emittance of these parts of the bunch is rather high (Fig. 9, left plot). The transverse emittance is shown in the right plot of Fig. 9 as a function of the number of core particles taken into consideration for the emittance calculations. Only 1% charge cut in the phase space results in more than 14% projected emittance reduction.

5.3. *Influence of key photo injector parameters*

Besides simulations of the optimized setup it is of great importance to study dependences of electron beam properties on machine parameters, which could deviate from the optimized values due to systematic (e.g. precision of set parameter value

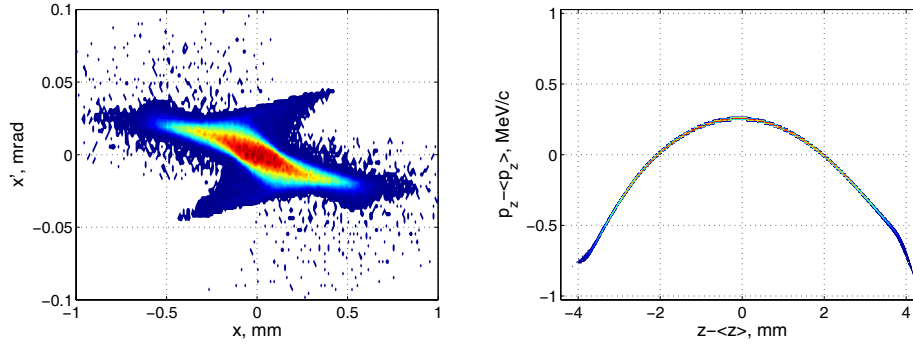

Fig. 8. Transverse (left) and longitudinal (right) phase space of the electron beam at the injector exit (z=15 m).

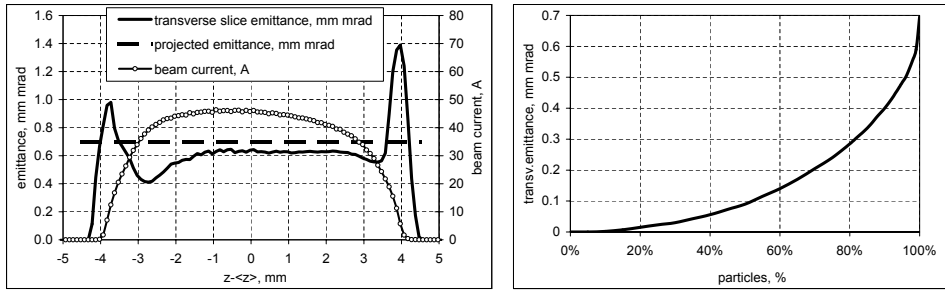

Fig. 9. Left: transverse slice emittance of the electron beam at the injector exit is shown together with projected emittance level and beam current distribution. Right: core emittance—emittance of the beam core vs. number of particles.

to hardware) or stochastic (e.g. jitter) reasons. Another reason to know such dependencies is a normalization procedure of photo injector parameters. A parameters range corresponding to a definite emittance growth (e.g 10%) is used to obtain a dimensionless variable. This makes search parameter space more homogeneous. Corresponding studies have been performed.

The most sensitive parameter for the emittance of an electron beam is the solenoid peak field. An emittance growth $\dfrac{\varepsilon - \varepsilon_{min}}{\varepsilon_{min}}$ due to the deviation of the main solenoid peak field B_z from the optimized value B_z^{opt} (Tab. 1) is shown in Fig. 10 (left). A 0.3% deviation from the optimum peak field[d] results in a 10% emittance growth. The sensitivity of the electron beam emittance on variation of the cathode laser spot size is illustrated in Fig. 10 (right).

[d]In terms of the main solenoid current this corresponds to 1.2 A around the optimum value of 393 A.

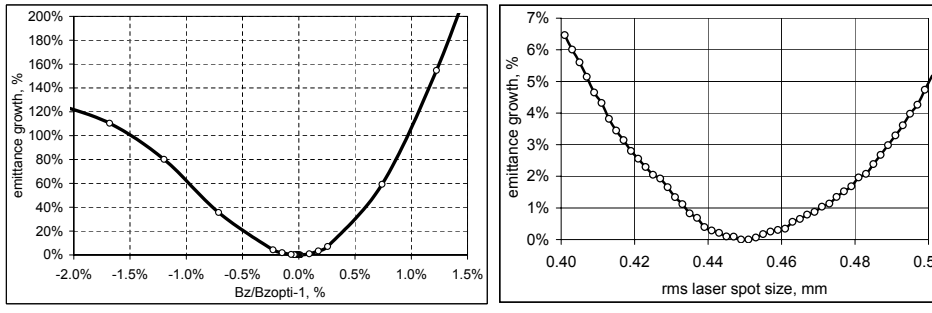

Fig. 10. Emittance growth vs. deviations of injector parameters from the optimized values: main solenoid peak field (left) and rms beam size of the cathode laser (right).

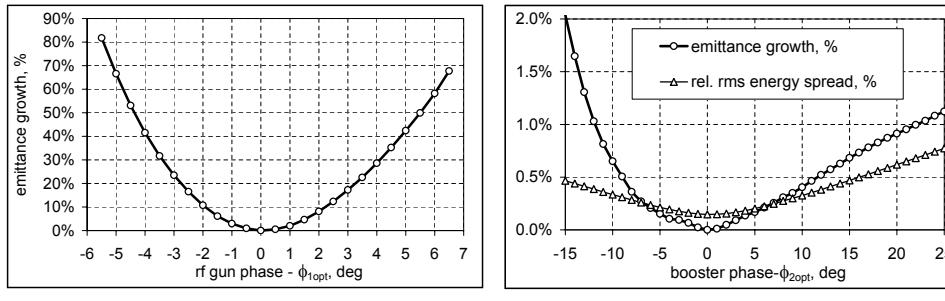

Fig. 11. Left: emittance growth as a function of rf gun launch phase. Right: emittance growth $\varepsilon/\varepsilon(\phi_{2opt}) - 1$ and relative rms energy spread $\sigma_E/\langle E\rangle$ as a function of the booster phase.

Another important parameter, whose variation could dilute the quality of the electron beam at the injector exit is the rf gun launch phase. The dependence of the emittance growth due to the variation of the rf gun launch phase is shown in Fig. 11 (left), where the phase is centered to the optimum value ($\phi_{1opt} = -0.7^\circ$ in Tab.1). According to these simulations, a 10% emittance growth can be caused by an rf gun phase variation of $\pm$ 2°. This is much more relaxing than requirements for the phase variation tolerances based on beam energy and bunch charge stability considerations.[1] An additional charge jitter should be also expected from a charge dependence on rf gun phase (Fig. 1), where the Schottky-like effect results in a non-zero slope $dQ/d\phi_1$.

A booster phase scan—the dependence of the emittance growth as a function of the rf phase of the first four cavities in ACC1—is shown in Fig. 11 on the right plot together with the relative energy spread. It should be noted that tolerances for the energy spread are more stringent, because bunch compression schemes imply rather hard demands on energy correlations within the bunch.

The sensitivity of the beam emittance to the booster gradient is shown in Fig. 12 (left), where emittance growth is shown as a function of the peak electric field in the booster.

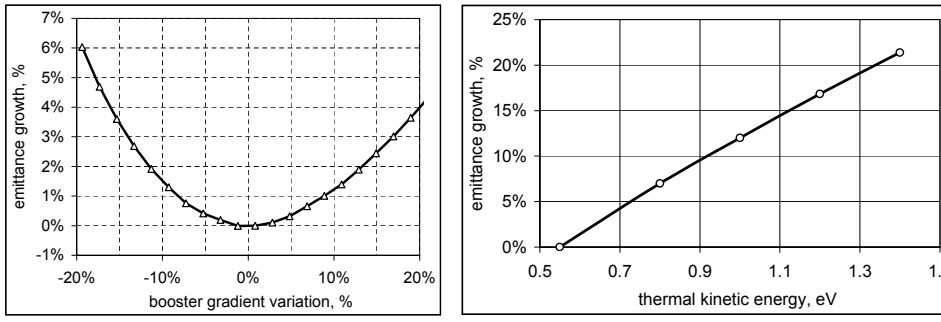

Fig. 12. Left: emittance growth as a function of the booster gradient variation from the optimum value (24.5 MV/m peak field). Right: emittance growth vs. initial kinetic energy of photo electrons. As a reference, the model value E_k=0.55 eV has been used.

The optimized setup for the XFEL photo injector (Tab. 1) assumed the thermal kinetic energy of photo electrons to be 0.55 eV. This corresponds to the theoretical model for Cs_2Te photo cathodes.[9] The projected transverse emittance for this case (0.7 mm mrad) contains more than 50% thermal emittance (0.38 mm mrad), which is uncorrelated and cannot be compensated. Recent measurements performed at PITZ[10] yielded initial kinetic energies of ∼1.4 eV. In order to study the influence of the thermal emittance on the final projected emittance of the electron beam at the injector exit, corresponding simulations have been performed. Emittance growth as a function of the initial kinetic energy of photo electrons is shown in Fig. 12 (right). From this plot the increase of the initial thermal kinetic energy close to the measured one (1.4 eV) results in more than 20% increase of the final emittance.

The cathode laser temporal profile plays a significant role in a formation of the electron beam projected emittance. A flat-top profile with 20 ps FWHM has been used. The rise and fall time is responsible for the contribution to the projected emittance from head and tail of the bunch (Fig. 9). The dependence of the emittance growth due to the variation of the rise and fall time is shown in Fig. 13(left). As a reference, a projected emittance for the cathode laser with 2 ps has been used. Typical temporal laser profiles used for the simulations are shown in the right plot of Fig. 13.

6. Conclusions

The beam dynamics optimization procedure for the European XFEL photo injector has been developed using a staged strategy, including photo emission, rf gun and booster parameter tuning. Application of this approach based on ASTRA simulations resulted in an optimized photo injector setup delivering a projected normalized transverse emittance of 0.7 mm mrad for 1 nC beam. The influence of photo injector key parameters has been studied; the most sensitive parameters are main solenoid

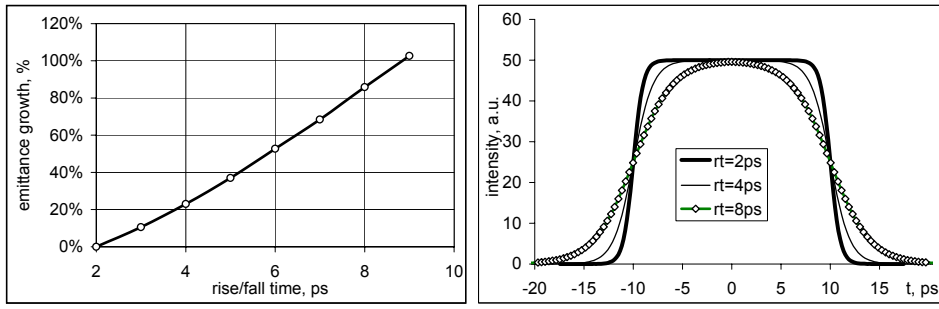

Fig. 13. Emittance growth vs. rise/fall time of the cathode laser. Examples of temporal laser profiles used for the simulations (right plot), rise and fall time were varied whereas the length (FWHM) was fixed to 20 ps.

strength, rise and fall time of the cathode laser temporal profile and initial kinetic energy of the photo electrons.

Acknowledgments

The author thanks F. Stephan, K. Floettmann, C. Boulware and the PITZ group members for useful discussions.

References

1. M. Altarelli *et al*, The European X-Ray Free Electron Laser, DESY 2006-097 (2007).
2. B.E. Carlsten, Space Charge Induced Emittance Compensation in High Brightness Photoinjectors, Part. Accel 49 (1995) p27-65.
3. L. Serafini and J. B. Rosenzweig, *Phys. Rev. E* **55**, 7565 (1997).
4. K.Floettmann, A Space charge Tracking Algorithm (ASTRA), user manual, http://www.desy.de/~mpyflo/Astra_dokumentation/.
5. G. Suberlucq, Development and production of photo cathodes for the CLIC test facility, in *Proc. of 18th International FEL conference*, Rome, Italy, 1996, p. II-131.
6. M.Krasilnikov et al, *NIMA*, **558**, 249-252 (2006).
7. M. Krasilnikov et al., Recent developments at PITZ, in *Proc. PAC'05* USA, Knoxwille, May 2005, p. 1012.
8. S.Rimjaem et al., Tuning and Conditioning of a New High Gradient Gun Cavity at PITZ, in *Proc. EPAC'08*, Italy, Genoa
9. K.Floettmann Note on the thermal emittance of electrons emitted by Cesium Telluride photo cathodes, TESLA FEL Reports 1997-01, 1997.
10. S.Lederer et al., Investigations on the Thermal Emittance of Cs2Te Photocathodes at PITZ, in *Proc. FEL 2007*, Russia, Novosibirsk, p.350.
11. N.Metropolis and S.Ulam, The Monte Carlo Method, *J. Amer. Stat. Assoc.*, **44**, 335-341 (1949).
12. J.A. Nelder and R. Mead, *Computer Journal*, **7**, 308-313 (1965).

International Journal of Modern Physics A
Vol. 24, No. 5 (2009) 893–907

World Scientific
www.worldscientific.com

ROBUST STABILITY ANALYSIS OF LINEAR PERIODIC SYSTEMS WITH TIME DELAY

OLGA N. LETYAGINA* and ALEXEY P. ZHABKO†

Faculty of Applied Mathematics and Control Processes, Saint-Petersburg State University, 35 Universitetskii pr., Saint Petersburg, 198504, Russia

** olga.spbu@gmail.com*

† zhabko@apmath.spbu.ru

In this paper, a procedure for construction of quadratic Lyapunov-Krasovskii functionals for linear time delay systems with periodic coefficients is proposed. Functionals are used to derive robust stability conditions. The problem of computation of Lyapunov matrices for functionals is reduced to computation of solutions of an auxiliary two-point boundary problem for a special delay free system of matrix equation.

Keywords: Time delay systems; systems with periodic coefficients; Lyapunov-Krasovskii approach; Lyapunov matrices; robust stability.

PACS numbers: 11.25.Hf, 123.1K

1. Introduction

Mathematical modeling of beam dynamics in a charged-particle accelerator or plasma behavior in modern tokamaks with some simplification assumptions leads to a system of nonlinear differential equations.[1] Linearization of these equations in a neighborhood of a specified acceleration program or plasma burn scenario allows to focus on the study of linear non-stationary systems. A cycle form of control processes leads to periodic coefficients of the linearized system. Taking into account Coulomb interaction of particles, and signal delay in a feedback channel force to introduce time delay in the model.[2] Electromagnetic field fluctuation and engineering inaccuracies postulate a problem of robustness with respect to coefficients inaccuracy.

Problems of constructing a Lyapunov quadratic functional and analyzing its properties for linear periodic systems with time delay are treated in this paper. It is shown that these functionals can be used to investigate solutions of the examined systems for asymptotical stability and robustness.

One of the basic methods for the stability analysis of systems with time delay is the method of Lyapunov functionals, which was suggested in the work by Krasovskii.[3] For the linear systems, a problem of finding quadratic functionals with

preassigned derivative was studied in [4]. One of the basic difficulties in application of functionals is a lack of computational algorithms for the corresponding Lyapunov matrices. It has been shown in [5] that for the case of systems with time delay, the matrices satisfy an auxiliary delay free system of matrix equations with a certain set of two-point boundary conditions. The first attempt to construct lower bounds for quadratic functionals was presented in [6]. In this work it is shown that Lyapunov quadratic functionals have only cubic estimations. For this purpose a Lyapunov quadratic functional was modified to the complete type functional in [7]. The complete type Lyapunov quadratic functionals are shown to be useful in solving such problems as estimation of robustness bounds[8] and calculation of exponential estimates for time delay systems.[9]

In this paper we propose a procedure for construction of quadratic functionals whose time derivative includes terms which depend on the past states of the system and show how one can use such functionals for robust stability analysis of time delay systems. It is also shown in the paper that these functionals admit a quadratic lower bound. At the end we present an example of computation of the corresponding Lyapunov matrix.

2. Preliminaries

In this paper we consider the following time delay system

$$\dot{x}(t) = \sum_{i=0}^{m} A_i(t)x(t-h_i), \tag{1}$$

where $A_j(t)$ are $n \times n$ matrices with periodic, continuous coefficients, i.e. $A_j(t+T) = A_j(t)$, $j = \overline{0,m}$, $0 = h_0 < h_1 < h_2 < \ldots < h_m$ are positive delays.

We will denote by $x(t, t_0, \varphi)$ the solution the of system (1) with the initial conditions $\{t_0, \varphi(\theta)\}, \theta \in [t_0 - h_m, t_0]$, and by $x_t(t_0, \varphi)$ the following segment $\{x(t+\theta, t_0, \varphi) | \theta \in [-h_m, 0]\}$ of the solution. If the initial function is not important or clear of the context we will drop the argument φ in these notations.

The space of continuous initial functions $\mathbb{C}([-h_m; 0], \mathbb{R}^n)$ is provided with the supremum norm $||\varphi||_{h_m} = \max\limits_{\theta \in [t_0 - h_m, t_0]} ||\varphi(\theta)||$.

2.1. *Cauchy formula*

Let $n \times n$ matrix function $K(t, s)$ which is defined for $t \geq s$ satisfy the matrix equation

$$-\frac{\partial K(t,s)}{\partial s} = \sum_{i=0}^{m} K(t, s+h_i)A_i(s+h_i), s < t \tag{2}$$

with the following initial condition: $K(t, s) = 0, s < t, K(t, t) = I$. K(t,s) is known as the fundamental matrix of the system (1). With the help of this matrix one may

present the solution $x(t, t_0, \varphi)$ in the explicit form, see [10],

$$x(t, t_0, \varphi) = K(t, t_0)\varphi(t_0) + \sum_{i=1}^{m} \int_{-h_i}^{0} K(t, t_0 + h_i + \tau) A_i(t_0 + h_i + \tau)\varphi(t_0 + \tau)\, d\tau. \quad (3)$$

Lemma 2.1. *K(t,s) as a function of t with a specified (fixed) value of s satisfies the matrix equation*

$$\frac{\partial K(t,s)}{\partial t} = \sum_{i=0}^{m} A_i(t) K(t - h_i, s), t > s$$

with the initial condition: $K(t,s) = 0, t < s, K(s,s) = I$.

2.2. *Method of Lyapunov functionals*

With respect to system (1) the method of functionals is based on the following classic Krasovskii theorem.[9]

Theorem 2.1. *Let the functional* $\upsilon(\cdot)$ *be known and satisfy the following conditions:*

1) there are such $\alpha_1 > 0$ *and* $\alpha_2 > 0$ *that for every solution of the system (1) the inequalities hold:*

$$\alpha_1 ||x(t)||^2 \le \upsilon(x_t) \le \alpha_2 ||x_t||^2_{h_m}, t \ge 0;$$

2) there is $\beta > 0$ *such that along every solution of the system (1) holds:*

$$\frac{d\upsilon(x_t)}{dt} \le -\beta ||x(t)||^2, t \ge 0.$$

Then the system (1) is asymptotically stable.

Remark 2.1. The concepts of the asymptotically and exponentially stable are equivalent for the systems of the form (1).

In order to be able to use Theorem 2.1, it is necessary to have a constructive method for computation of the functionals that satisfy its conditions. A method of the functional construction is presented in Section 3.

3. Complete Type Lyapunov Functionals

Let W_0 be a positive definite symmetric $n \times n$ matrix. Let $\varphi(\theta)$ be a continuous initial function on $[t_0 - h, t_0]$. Consider the functional

$$\omega_0(x(t)) = x^T(t) W_0 x(t).$$

We are looking for the functional such that

$$\frac{d\upsilon(t, x_t(t_0, \varphi))}{dt} = -\omega_0(x(t, t_0, \varphi)), \quad t \ge t_0.$$

If the system (1) is exponentially stable then the functional exists and can be written as

$$v(t_0,\varphi)=\int\limits_{t_0}^{\infty}\omega_0(x(t,t_0,\varphi))\,dt.$$

Using Eq. (3) one can write it as

$$\begin{aligned}v(t_0,\varphi)=&\int\limits_{t_0}^{\infty}\Big[K(t,t_0)\varphi(t_0)+\sum_{i=1}^{m}\int\limits_{-h_i}^{0}K(t,t_0+h_i+\tau_1)A_i(t_0+h_i+\tau_1)\\&\varphi(t_0+\tau_1)\,d\tau_1\Big]^T W_0\Big[K(t,t_0)\varphi(t_0)+\sum_{i=1}^{m}\int\limits_{-h_i}^{0}K(t,t_0+h_i+\tau_2)\\&A_i(t_0+h_i+\tau_2)\varphi(t_0+\tau_2)\,d\tau_2\Big]\,dt\\=&\,\varphi^T(t_0)U(t_0,t_0)\varphi(t_0)+2\varphi^T(t_0)\sum_{i=1}^{m}\int\limits_{-h}^{0}U(t_0,t_0+\tau_2+h_i)\\&A_i(t_0+h_i+\tau_2)\cdot\varphi(t_0+\tau_2)d\tau_2+\sum_{i,k=1}^{m}\int\limits_{-h_i}^{0}\int\limits_{-h_k}^{0}\varphi^T(t_0+\tau_1)A_i^T(t_0+h_i+\tau_1)\\&U(t_0+\tau_1+h_i,t_0+\tau_2+h_k)\cdot A_k(t_0+h_k+\tau_2)\varphi(t_0+\tau_2)\,d\tau_1\,d\tau_2.\end{aligned}$$

Here matrix $U(\tau_1,\tau_2)$ is defined as

$$U(\tau_1,\tau_2)=\int\limits_{\max\{\tau_1,\tau_2\}}^{\infty}K^T(t,\tau_1)W_0K(t,\tau_2)\,dt. \tag{4}$$

The value of the functional on the trajectory segment is

$$\begin{aligned}v(t,x_t)=&\,x^T(t)U(t,t)x(t)+2x^T(t)\sum_{i=1}^{m}\int\limits_{-h_i}^{0}\Big[U(t,\tau+h_i+t)A_i(t+h_i+\tau)\\&\cdot x(t+\tau)\Big]\,d\tau+\sum_{i,k=1}^{m}\int\limits_{-h_i}^{0}\int\limits_{-h_k}^{0}\Big(x^T(t+\tau_1)A_i^T(t+h_i+\tau_1)\\&\cdot U(\tau_1+h_i+t,\tau_2+h_k+t)A_k(t+h_k+\tau_2)x(t+\tau_2)\,d\tau_1\,d\tau_2\Big).\end{aligned} \tag{5}$$

Consider a functional of the form

$$\omega(x_t)=\sum_{i=0}^{m}x^T(t-h_i)W_ix(t-h_i)+\sum_{i=1}^{m}\int\limits_{-h_i}^{0}x^T(t+\tau)R_ix(t+\tau)\,d\tau, \tag{6}$$

here W_j, $j=\overline{0,m}$ and R_j, $j=\overline{1,m}$ are positive definite $n\times n$ matrices.

For this case we have the same formulas for the functional $v(t, x_t)$

$$\frac{dv(t, x_t(t_0, \varphi))}{dt} = -\omega(x_t), \quad t \geq 0\,,$$

$$v(t_0, \varphi) = \int_{t_0}^{\infty} \omega(x_t)\, dt.$$

Functional $v(t_0, \varphi)$ may be split into two components. Each of them corresponds to one of the two terms on the right-hand side of (6).

The component of $v(t_0, \varphi)$ which corresponds to the delay term

$$\omega_j(x(t - h_j, t_0, \varphi)) = x^T(t - h_j, t_0, \varphi) W_j x(t - h_j, t_0, \varphi)$$

is

$$v_j(t_0, \varphi) = \int_{t_0}^{\infty} x^T(t - h_j, t_0, \varphi) W_j x(t - h_j, t_0, \varphi)\, dt.$$

This equality can be rewritten

$$\begin{aligned} v_j(t, x_t) = {} & x^T(t) U_j(t, t) x(t) + 2x^T(t) \sum_{i=1}^{m} \int_{-h_i}^{0} U_j(t, \tau + h_i + t) A_i(t + h_j + \tau) \\ & \cdot x(t + \tau)\, d\tau + \sum_{i,k=1}^{m} \int_{-h_i}^{0} \int_{-h_k}^{0} \Big(x^T(t + \tau_1) A_i^T(t + h_i + \tau_1) \\ & \cdot U_j(\tau_1 + h_i + t, \tau_2 + h_k + t) A_k(t + h_k + \tau_2) x(t + \tau_2)\, d\tau_1\, d\tau_2 \Big) \\ & + \int_{-h_j}^{0} x^T(t + \tau) W_j x(t + \tau)\, d\tau, \end{aligned}$$

where $U_j = \int_{\max\{\tau_1, \tau_2\}}^{\infty} K^T(t, \tau_1) W_j K(t, \tau_2)\, dt$, $j = \overline{0, m}$.

We now address the component of $v(t_0, \varphi)$ which corresponds to the integral term

$$\omega_{m+j}(x_t(t_0, \varphi)) = \int_{-h_j}^{0} x^T(t + \tau, t_0, \varphi) R_j x(t + \tau, t_0, \varphi)\, d\tau.$$

This component can be expressed as

$$v_{m+j}(t_0, \varphi) = \int_{t_0}^{\infty} \left(\int_{-h_j}^{0} x^T(t + \tau, t_0, \varphi) R_j x(t + \tau, t_0, \varphi)\, d\tau \right) dt.$$

Changing the integration order in the double integral, one obtains the following expression

$$\begin{aligned}\upsilon_{m+j}(t,x_t) = h\Big[&x^T(t)U_{m+j}(t,t)x(t) + 2x^T(t)\sum_{i=1}^{m}\int_{-h_i}^{0} U_{m+j}(t,\tau+h_i+t)\\ &\cdot A_i(t+h_i+\tau)x(t+\tau)\,d\tau + \sum_{i,k=1}^{m}\int_{-h_i}^{0}\int_{-h_k}^{0}\Big(x^T(t+\tau_1)A_i^T(t+h_i+\tau_1)\\ &\cdot U_{m+j}(\tau_1+h_i+t,\tau_2+h_k+t)A_k(t+h_k+\tau_2)x(t+\tau_2)\,d\tau_1\,d\tau_2\Big)\Big]\\ &+\int_{-h_j}^{0}(h_j+\tau)x^T(t+\tau)R_jx(t+\tau)\,d\tau.\end{aligned}$$

Gathering all the components together we obtain

$$\begin{aligned}\upsilon(t,x_t) = {}& x^T(t)U(t,t)x(t) + 2x^T(t)\sum_{i=1}^{m}\int_{-h_i}^{0} U(t,\tau+h_i+t)A_i(t+h_i+\tau)\\ &\cdot x(t+\tau)\,d\tau + \sum_{i,k=1}^{m}\int_{-h_i}^{0}\int_{-h_k}^{0}\Big(x^T(t+\tau_1)A_i^T(t+h_i+\tau_1)\\ &\cdot U(\tau_1+h_i+t,\tau_2+h_k+t)A_k(t+h_k+\tau_2)x(t+\tau_2)\,d\tau_1\,d\tau_2\Big)\\ &+\sum_{i=1}^{m}\int_{-h_i}^{0} x^T(t+\tau)[W_i+(h_i+\tau)R_i]x(t+\tau)\,d\tau,\end{aligned}\tag{7}$$

where $U = \int\limits_{\max\{\tau_1,\tau_2\}}^{\infty} K^T(t,\tau_1)WK(t,\tau_2)\,dt$, $W = \Big[W_0 + \sum\limits_{i=1}^{m}(W_i + h_iR_i)\Big]$. It is the Lyapunov-Krasovskii functional associated with (6).

The Lyapunov-Krasovskii functional $\upsilon(t,x_t)$ constructed from a given $\omega(t,x_t)$ (6) is of the complete type, i.e. there exists $\mu > 0$ such that $\omega(t_0,\varphi) < 2\mu\upsilon(t_0,\varphi)$ holds for all initial conditions $\{t_0,\varphi\}$. In addition, the existence of Lyapunov-Krasovskii functionals of the complete type is necessary and sufficient for the exponential stability of the differential delay equation (1). As $U(\tau_1,\tau_2)$ in (7) takes over the role of a classical quadratic Lyapunov matrix for systems without delays, we call it the delay Lyapunov matrix associated with (7). In the following we will study its properties.

Using properties of the matrices $K(t,s), W$ we obtain the following properties of $U(\tau_1,\tau_2)$:

- the dynamic property

Assume that $\tau_2 > \tau_1$, then $\max\{\tau_1, \tau_2\} = \tau_2$.
Partial derivative of (4) with respecto to τ_1 and τ_2 is equal to:

$$\frac{\partial U}{\partial \tau_1}(\tau_1, \tau_2) = -A_0^T(\tau_1)U(\tau_1, \tau_2) - \sum_{i=1}^{m} A_i^T(\tau_1 + h_i)U(\tau_1 + h_i, \tau_2)\,, \tag{8}$$

$$\frac{\partial U}{\partial \tau_2}(\tau_1, \tau_2) = -U(\tau_1, \tau_2)A_0(\tau_2) - \sum_{i=1}^{m} U(\tau_1, \tau_2 + h_i)A_i(\tau_2 + h_i) - K(\tau_2, \tau_1)W\,. \tag{9}$$

- the symmetry property

$$U^T(\tau_1, \tau_2) = U(\tau_2, \tau_1)\,. \tag{10}$$

- the algebraic property
  If $\tau_1 = \tau_2 = \tau$, then from the dynamic property we have

$$\begin{aligned}\frac{dU}{d\tau}(\tau, \tau) = \frac{d}{d\tau}\left(\int_{\tau}^{\infty} K^T(t, \tau)W K(t, \tau)\,dt\right) &= -A_0^T(\tau)U(\tau, \tau) \\ &- \sum_{i=1}^{m} A_i^T(\tau + h_i)U(\tau + h_i, \tau) - U(\tau, \tau)A_0(\tau) \\ &- \sum_{i=1}^{m} U(\tau, \tau + h_i)A_i(\tau + h_i) - W\,. \end{aligned} \tag{11}$$

  This property associates Lyapunov matrix $U(\tau_1, \tau_2)$ with W.
- the periodicity property
  This property is following from periodic property of $K(t, s)$: $K(t + T, \tau + T) = K(t, \tau)$, hence,

$$U(\tau_1 + T, \tau_2 + T) = U(\tau_1, \tau_2). \tag{12}$$

Remark 3.1. The periodic property of $A_j(t), j = \overline{0, m}$ is not necessary for construction of the functionals, Lyapunov matrix and derivation of the matrix properties (8)–(11).

The Lyapunov-Krasovskii functional v constructed from a given ω is of the complete type.

Now we will get lower and upper bounds for the functionals of the complete type. Let $P_j, j = \overline{0, m}$ be positive definite $n \times n$ matrices. We consider a functional

$$u(x_t) = x^T(t)P_0x(t) + \sum_{i=1}^{m} \int_{-h_i}^{0} x^T(t + \theta)P_i x(t + \theta)\,d\theta. \tag{13}$$

Lemma 3.1. *Let $W_j > 0$, $j = \overline{0,m}$, $R_j > 0$, $j = \overline{1,m}$. If the system (1) is exponentially stable then for the functional of complete type (7) the following condition is satisfied on the solutions of system (1)*

$$\beta_1 u(x_t) \le \upsilon(x_t), t \ge t_0, \tag{14}$$

here β_1 is a positive constant.

Proof. Consider the following functional

$$\widehat{\upsilon} = \upsilon(x_t) - \beta u(x_t).$$

Along the trajectories of the system (1) the derivative of the functional is

$$\frac{d\widehat{\upsilon}(x_t)}{dt} = -\widehat{\omega}(x_t) = -\omega(x_t) - \beta\frac{du(x_t)}{dt}, t \ge t_0.$$

Note that

$$\frac{du(x_t)}{dt} = 2x^T(t)P_0\Big[\sum_{i=0}^{m} A_i(t)x(t-h_i)\Big]\sum_{i=1}^{m}\Big[x^T(t)P_ix(t) - x^T(t-h_i)P_ix(t-h_i)\Big].$$

Therefore,

$$\widehat{\omega}(x_t) = [x^T(t), x^T(t-h_1), ..., x^T(t-h_m)]M(\beta)\begin{bmatrix} x(t) \\ x(t-h_1) \\ ... \\ x(t-h_m) \end{bmatrix}$$
$$+ \sum_{i=1}^{m}\int_{-h_i}^{0} x^T(t+\theta)R_ix(t+\theta)\,d\theta,$$

where

$$M(\beta) = diag(W_0, W_1, ..., W_m) + \beta\begin{pmatrix} D & P_0A_1(t) & \dots & P_0A_m(t) \\ A_1^T(t)P_0 & -P_1 & \dots & 0 \\ . & . & \dots & 0 \\ . & . & \dots & 0 \\ . & . & \dots & 0 \\ A_m^T(t)P_0 & 0 & \dots & -P_m \end{pmatrix},$$

$D = P_0A_0(t) + A_0^T(t)P_0 + \sum_{i=1}^{m} P_i.$

The matrix $M(0) > 0$. Let β^* be a minimal positive solution of the equation $det(M(\beta)) = 0$. For each $\beta_1 \in [0, \beta^*]$ the matrix $M(\beta_1) \ge 0$, and therefore $\widehat{\omega}(x_t) \ge 0$.

From the last inequality we conclude that

$$\widehat{\upsilon}(\varphi) = \int_{t_0}^{\infty} \widehat{\omega}(x_t(\varphi))\,dt \ge 0,$$

and therefore

$$\upsilon(x_t) \geq \beta^* u(x_t). \qquad \square$$

Lemma 3.2. *The following condition are satisfied for the functional (7)*

$$\upsilon(x_t) \leq \beta_2 u(x_t), t \geq t_0,$$

where β_2 is a positive constant.

Proof. The proof is similar to the the proof of Lemma 3, see [9]. $\square$

Theorem 3.1. *If the system (1) is exponentially stable, $W_j > 0$, $j = \overline{0,m}$, $R_j > 0$, $j = \overline{1,m}$, then the following condition is satisfied for all solutions of the system (1)*

$$\alpha_1 ||x(t)||^2 \leq \upsilon(x_t) \leq \alpha_2 ||x_t||^2_{h_m}, t \geq t_0.$$

Here α_1, α_2 are positive constants.

Proof. Follows from Lemma 3.1 and Lemma 3.2. $\square$

4. Existence Issue

Lemma 4.1. *Let $\widehat{U}(\tau_1, \tau_2)$ be a solution of the equation (8) with initial conditions (10)–(12). Then functional $\upsilon(t, x_t)$ where U replace with $\widehat{U}$ satisfies*

$$\left.\frac{d\upsilon(t,x_t)}{dt}\right|_{(1)} = -\sum_{i=0}^{m} x^T(t-h_i)W_i x(t-h_i) - \sum_{i=1}^{m} \int_{-h_i}^{0} x^T(t+\tau)R_i x(t+\tau)\, d\tau.$$

Proof. The statement can be proved by direct calculation. $\square$

Theorem 4.1. *Let system (1) be exponentially stable, then matrix (4) is the unique solution of matrix equations (8), (10)–(12).*

Proof. The fact that matrix (4) satisfies these equations is trivial. Assume by contradiction that matrix equations (8), (10)–(12) admit at least two solutions $U^{(1)}(\tau_1, \tau_2)$ and $U^{(2)}(\tau_1, \tau_2)$. Each of the two solutions defines the corresponding functional $\upsilon^{(j)}(t, x_t), j = 1, 2$, of the form (5). Exponential stability of system (1) implies that

$$\Delta\upsilon(t_0, \varphi) = \upsilon^{(2)}(t_0, \varphi) - \upsilon^{(1)}(t_0, \varphi) = 0,$$

for any initial function φ. If we define the difference

$$\Delta U(\tau_1, \tau_2) = U^{(2)}(\tau_1, \tau_2) - U^{(1)}(\tau_1, \tau_2),$$

then

$$0 = \Delta v(t_0,\varphi) = \varphi^T(t_0)U(t_0,t_0)\varphi(t_0) + 2\varphi^T(t_0)\sum_{i=1}^{m}\int\limits_{-h_i}^{0}\Big(U(t_0,\tau+h_i+t_0)$$

$$\cdot A_i(t_0+h_i+\tau)\varphi(t_0+\tau)\Big)d\tau + \sum_{i,k=1}^{m}\int\limits_{-h_i}^{0}\int\limits_{-h_k}^{0}\Big(\varphi^T(t_0+\tau_1)A_i^T(t_0+h_i+\tau_1) \quad (15)$$

$$\cdot U(\tau_1+h_i+t_0,\tau_2+h_k+t_0)A_k(t_0+h_k+\tau_2)\varphi(t_0+\tau_2)\,d\tau_1\,d\tau_2\Big).$$

Given a vector γ, define the piecewise continuous initial function

$$\varphi(t_0+\theta) = \begin{cases} \gamma, & \text{for } \theta = 0, \\ 0, & \text{for } \theta \in [-h_m, 0). \end{cases}$$

For this function equality (15) takes the form

$$\gamma^T \Delta U(t_0,t_0)\gamma = 0.$$

As the last equality holds for any vector γ and the matrix $\Delta U(t_0,t_0)$ is symmetric, one may easily conclude that

$$\Delta U(t_0,t_0) = 0. \quad (16)$$

Now, given two vectors γ and μ, let us select $\tau \in (h_{j-1}, h_j]$ and sufficiently small $\varepsilon > 0$ such that $\tau+\varepsilon < h_{j-1}$. Then we can define the following piece-wise continuous initial function

$$\varphi(t_0+\theta) = \begin{cases} \gamma, & \text{for } \theta = 0, \\ \mu, & \text{for } \theta \in [-\tau, -\tau+\varepsilon], \\ 0, & \text{for all other points of segment } [-h_m, 0]. \end{cases}$$

If $\varepsilon > 0$ is small then the first integral in (5) is proportional to ε while the double integral is proportional ε^2 so that (5) for this initial function can be written as

$$0 = 2\varepsilon\gamma^T \sum_{i=j}^{m}\Big[\Delta U(h_j,\tau+h_i)A_i(\tau+h_i)\Big]\mu + o(\varepsilon),$$

where

$$\lim_{\varepsilon\to+0}\frac{o(\varepsilon)}{\varepsilon} = 0.$$

The fact that γ and μ are arbitrary vectors and that ε can be made arbitrarily small implies that

$$\sum_{i=j}^{m}\Delta U(h_j,\tau+h_i)A_i(\tau+h_i) = 0.$$

The last equality holds for all $\tau \in (h_{j-1}, h_j]$, and using the continuity of the arguments we arrive at the following condition

$$\sum_{i=j}^{m} A_i^T(\tau + h_i)\Delta U(\tau + h_i, h_j) = 0, \tau \in (h_{j-1}, h_j]. \tag{17}$$

Now (17) holds for all $j = \overline{1,m}$. For $j = 1$ we therefore obtain the differential equation

$$\frac{\partial \Delta U(\tau_1, \tau_2)}{\partial \tau_1} = -\sum_{i=0}^{m} A_i^T(\tau_1 + h_i)\Delta U(\tau_1 + h_i, \tau_2),$$

if $\tau_2 > \tau_1$, or if $\tau_2 = h_1$ concludes that

$$\frac{d\Delta U(\tau_1, h_1)}{d\tau_1} = -A_0^T(\tau_1)\Delta U(\tau_1, h_1), \tau_1 \in [0, h_1].$$

We are looking for a solution of this equation which satisfies the condition (16). The solution of this equation is trivial, that is $\Delta U(\tau_1, \tau_2) = 0, \tau_1 \in [0, h_1]$ or $U^{(2)}(\tau_1, \tau_2) = U^{(1)}(\tau_1, \tau_2), \tau_1 \in [0, h_1]$.

Considering Eqs. (8) and (19) on the interval $(h_1, h_2]$ and for $j = 2$ we obtain the following delay equation $\frac{d\Delta U(\tau_1, h_2)}{d\tau_1} = -A_0^T(\tau_1)\Delta U(\tau_1, h_2) - A_1^T(\tau_1)\Delta U(\tau_1 + h_1, h_2), \tau_1 \in [h_1, h_2]$. But on the interval $[0, h_1]$, $\Delta U(\tau_1, \tau_2)$ is constantly 0, therefore $\Delta U(\tau_1, \tau_2) = 0$ for $\tau_1 \in (h_1, h_2]$. Continuing this process, we conclude that $\Delta U(\tau_1, \tau_2) = 0$, $\tau_1, \in [0, h_m]$, i.e. $U_1(\tau_1, \tau_2) = U_2(\tau_1, \tau_2)$ for all $\tau_1 \in [-h_m, h_m]$. The same way we can prove the theorem for a variable τ_2. Hence, whenever (1) is exponentially stable, the unique solution of (8), (10)–(12) is given by the integral equation (4). □

Theorem 4.2. *Let $x^{(1)}(t) = e^{st}\varphi(t)$ and $x^{(2)}(t) = e^{-st}\psi(t)$ be the solutions of the system (1), where $\varphi(t), \psi(t)$ are periodic vectors and $\varphi(t_0) \neq 0$, $\psi(t_0) \neq 0$. Then there exists such W that system (8), with (10)–(12) have no solution.*

Proof. Similar proof as for Thm. 3, see [9, p. 204]. □

5. Exponential Estimation and Robust Stability

5.1. *Exponential estimation*

Definition 5.1. The system (1) is said to be exponentially stable if there exist $\sigma > 0$ and $\gamma \geq 1$ such that for every solution $x(t, \varphi)$ and for each initial function φ the following exponential estimate holds

$$||x(t, \varphi)|| \leq \gamma e^{-\sigma(t-t_0)}||\varphi||_{h_m}, t \geq t_0. \tag{18}$$

We can find constants σ and γ by the instrumentality of the functional υ (7) if the system (1) is exponentially stable. Indeed, let $P_0 = W_0$ and $P_j = R_j, j = \overline{1,m}$ in

(13). From Lemma 3.2 we see that the functional (7) satisfies the estimate $\upsilon(x_t) \leq \beta_2 u(x_t)$. One can then easily verify that from (13) we have the following inequality

$$\frac{d\upsilon(x_t)}{dt} + u(x_t) \leq 0, t \geq t_0,$$

therefore

$$\frac{d\upsilon(x_t)}{dt} + \frac{1}{\beta_2}\upsilon(x_t) \leq 0, t \geq t_0.$$

This means that

$$\upsilon(x_t(\varphi)) \leq \upsilon(\varphi)e^{-\frac{1}{\beta_2}(t-t_0)}.$$

From Theorem 3.1 we get

$$\alpha_1||x(t)||^2 \leq \upsilon(x_t), \quad \upsilon(\varphi) \leq \alpha_2||\varphi||^2_{h_m}.$$

Finally, we find necessary constants for exponential estimate

$$\gamma = \sqrt{\frac{\alpha_2}{\alpha_1}}, \quad \sigma = \frac{1}{2\beta_2}.$$

5.2. *Robust stability*

Let the nominal system (1) be exponentially stable. In this section we consider the perturbed equation

$$\dot{y}(t) = \sum_{j=0}^{m}(A_j(t) + \Delta_j(t))y(t - h_j). \tag{19}$$

Matrices $\Delta_j(t), j = \overline{0, m}$ are piecewise continuous matrix functions and assumed to satisfy the following inequalities

$$\sup_t ||\Delta_j(t)|| \leq \rho_j, \quad j = \overline{0, m}, \tag{20}$$

where ρ_j are positive numbers.

The principal goal of the section is to find lower bounds for $\rho_j, j = \overline{0, m}$ such that the perturbed equation remains stable for all $\Delta_j(t), j = \overline{0, m}$ within restrictions (20).

To derive such lower bounds we will use the functional (7) constructed for nominal system (1). The first time derivative of the functional (7) along solutions of Eq. (19) is

$$\frac{d\upsilon(y_t)}{dt} = -\omega(y_t) + 2\Big[\sum_{i=0}^{m}\Delta_i(t)y(t - h_i)\Big]^T l(t, y_t), t \geq t_0.$$

Here

$$l(t, y_t) = U(t, t)y(t) + \sum_{i=1}^{m}\int_{-h_i}^{0} U(t, t + h_i + \theta)A_j(t + h_i + \theta)y(t + \theta)\, d\theta.$$

Define three variables

$$\nu = \max_{\tau_1,\tau_2\in[0,h_m]} ||U(\tau_1,\tau_2)||; \quad a_j = \sup_t ||A_j(t)||, j = \overline{0,m};$$

$$\lambda_{\min} = \min\{\min_{0\le j\le m}[\lambda_{\min}(W_j)], \min_{1\le j\le m}[\lambda_{\min}(R_j)]\}.$$

The following estimates hold

$$\left|\left|\sum_{i=0}^{m}\Delta_i y(t-h_i)\right|\right| \le \left(\sum_{i=0}^{m}\rho_i^2\right)^{1/2}\left[\sum_{k=0}^{m}||y(t-h_k)||^2\right]^{1/2}\left(\sum_{i=0}^{m}\rho_i^2\right)^{1/2}\sqrt{\frac{\omega(y_t)}{\lambda_{\min}}},$$

and

$$\begin{aligned}||l(t,y_t)|| &\le \nu\left(1+\sum_{i=1}^{m}a_i^2h_i^2\right)^{1/2}\left[||y(t)||^2+\sum_{i=1}^{m}\int_{-h_i}^{0}||y(t+\theta)||^2\,d\theta\right]^{1/2}\\ &\le \nu\left(1+\sum_{i=1}^{m}a_i^2h_i^2\right)^{1/2}\sqrt{\frac{\omega(y_t)}{\lambda_{\min}}}.\end{aligned}$$

As a result we get

$$\frac{dv(y_t)}{dt} \le -\omega(y_t)\left[1-\frac{2\nu}{\lambda_{\min}}\left(\sum_{i=1}^{m}\rho_i^2\right)^{1/2}\left(1+\sum_{i=1}^{m}a_i^2h_i^2\right)^{1/2}\right].$$

Then the system (19) remains stable for all perturbations satisfying (20) if the values of $\rho_j, j=\overline{0,m}$ are such that

$$\sum_{i=0}^{m}\rho_i^2 \le \frac{\lambda_{\min}^2}{4\nu^2}\left(1+\sum_{i=1}^{m}a_i^2h_i^2\right).$$

6. Computation Issue

Here we will assume that $T=h$ and the system (1) has only one delay term

$$\dot{x}(t) = A_0(t)x(t) + A_1(t)x(t-h), t\ge 0. \tag{21}$$

To that end, we at first define several matrices $D(\tau) = U(\tau,\tau)$, $U_1(\tau_1,\tau_2) = U(\tau_1,\tau_2)$, $U_2(\tau_1,\tau_2) = A_1^T(\tau_1+h)U^T(\tau_2,\tau_1+h)$. Hence, $D^T(\tau) = D(\tau)$ is symmetrical.

From Eq. (8) we obtain $\dfrac{\partial U_1}{\partial\tau_1}(\tau_1,\tau_2) = -A_0^T(\tau_1)U(\tau_1,\tau_2) - A_1^T(\tau_1+h)U(\tau_1+h,\tau_2)$ and $\dfrac{\partial U_2}{\partial\tau_2}(\tau_1,\tau_2) = A_1^T(\tau_1+h)\dfrac{\partial U}{\partial\tau_2}(\tau_2,\tau_1+h) = A_1^T(\tau_1+h)\Big[-A_0^T(\tau_2)U(\tau_2,\tau_1+h) - A_1^T(\tau_2+h)U(\tau_1+h,\tau_2+h)\Big]^T$. After a change of variables we have

$$\begin{cases}\dfrac{\partial U_1}{\partial\tau_1}(\tau_1,\tau_2) = -A_0^T(\tau_1)U_1(\tau_1,\tau_2) - U_2(\tau_1,\tau_2),\\[2ex] \dfrac{\partial U_2}{\partial\tau_2}(\tau_1,\tau_2) = -U_2(\tau_1,\tau_2)A_0(\tau_2) - A_1^T(\tau_1)U_1(\tau_1,\tau_2)A_1(\tau_2).\end{cases} \tag{22}$$

$$\begin{cases} U_1(\tau,\tau) = D(\tau), \\ U_2(\tau,\tau) = \dfrac{1}{2}(W + D'(\tau)) - P(\tau) - A_0^T(\tau)D(\tau), \\ U_2(0,\tau) = A_1^T(h)U_1^T(\tau,h). \end{cases} \tag{23}$$

Here $P(\tau) = \dfrac{dU(\tau,\tau)}{d\tau}$ and $P^T(\tau) = -P(\tau)$.

We apply the modified second-order Runge-Kutta method to solve Eq. (22). We consider the matrices $D(\tau)$, $P(\tau)$ to be the method's initial conditions.

Let us consider a more general type of the system (22)

$$\begin{cases} \dfrac{\partial U_1}{\partial \tau_1} = f_1(\tau_1,\tau_2,U_1,U_2), \\ \dfrac{\partial U_2}{\partial \tau_2} = f_2(\tau_1,\tau_2,U_1,U_2). \end{cases} \tag{24}$$

Let vector functions $f_j, j = 1,2$ be k times continuously differentiable with respect to τ_j and $(k+1)$ times continuously differentiable with respect to other variables.

Consider more general initial conditions for (24)

$$U_1(\tau,\tau) = \Phi_1(\tau), U_2(\tau,\tau) = \Phi_2(\tau). \tag{25}$$

Theorem 6.1. *If $\Phi_j \in \mathbb{C}^{k+1}(\mathbb{R}^1), j = 1,2$ then there exists a unique solution of the system (24) with initial conditions (25) which is $(k+1)$ times continuously differentiable.*

Proof. Rely on the convergence method of Picard which applies to the system of integral equations

$$\begin{cases} U_1(\tau_1,\tau_2) = \Phi_1(\tau_2) + \displaystyle\int_{\tau_2}^{\tau_1} f_1(\theta,\tau_2,U_1(\theta,\tau_2),U_2(\theta,\tau_2))\,d\theta, \\ U_2(\tau_1,\tau_2) = \Phi_2(\tau_1) + \displaystyle\int_{\tau_1}^{\tau_2} f_2(\tau_1,\theta,U_1(\tau_1,\theta),U_2(\tau_1,\theta))\,d\theta. \end{cases}$$

□

Corollary 6.1. *If the following conditions are satisfied*

$$\begin{cases} f_j(\tau_1+h,\tau_2+h,U_1,U_2) = f_j(\tau_1,\tau_2,U_1,U_2), \\ \Phi_j(t+h) = \Phi_j(t), \\ j = 1,2. \end{cases}$$

then the solution of (24), (25) is periodic

$$U_j(\tau_1+h,\tau_2+h) = U_j(\tau_1,\tau_2), j = 1,2.$$

Let $k = 2$, then $U_j \in \mathbb{C}^3(\mathbb{R}^2)$.

The algorithm of the method is

$$U_1(\tau_1, \tau_2 + \Delta) = U_1(\tau_1 + \Delta, \tau_2 + \Delta) - \frac{1}{2}(k_1 + \widetilde{k}_1) + o(\Delta^2),$$

where

$$\begin{cases} k_1 = \Delta f_1(\tau_1 + \Delta, \tau_2 + \Delta, U_1^{11}, U_2^{11}), \\ \widetilde{k}_1 = \Delta f_1(\tau_1, \tau_2 + \Delta, U_1^{11} - k_1, U_2^{00} + k_2). \end{cases}$$

By analogy we can define other parameters of the method for finding a function U_2. Then formula for U_2 is

$$U_2(\tau_1, \tau_2 + \Delta) = U_2(\tau_1, \tau_2) + \frac{1}{2}(k_2 + \widetilde{k}_2) + o(\Delta^2),$$

where

$$\begin{cases} k_2 = \Delta f_2(\tau_1, \tau_2, U_1^{00}, U_2^{00}), \\ \widetilde{k}_2 = \Delta f_2(\tau_1, \tau_2 + \Delta, U_1^{11} - k_1, U_2^{00} + k_2). \end{cases}$$

Remark 6.1. For the case of systems with more than one delay, this method can be modified. But the dimension of the systems (22), (23) will increase.

7. Conclusions

In this paper, some explicit expressions for the complete type Lyapunov-Krasovskii functionals are obtained along with some robust stability results based on the use of functionals.

References

1. V. Belyakov and et al., *Fusion Engineering and Design* **45**, 55 (1999).
2. D.A. Ovsyannikov and et al., *Nucl. Fusion* **46**, (2006).
3. N. N. Krasovskii, *On the application of the second method of Lyapunov for equations with time delays.* (Prikl. Mat. Mekh 20, 1956).
4. Infante and Castelan, *J. Diff. Equs.* **29**, 439-451 (1978).
5. V. L. Kharitonov, *Systems & Control Letters* **55**, 610 (2006).
6. W. Juang, *J. of Math. Analysis and Applictions* **142**, 83 (1989).
7. V. L. Kharitonov and A. P. Zhabko, *Automatica* **39**, 15 (2003).
8. V. L. Kharitonov and S. I. Niculescu, *IEEE Trans. on Automatic Control* **48**, 127 (2003).
9. V. L. Kharitonov, *Herald of the SPbGU* **10**, 110 (2005).
10. R. Bellman and K.L. Cooke, Differential-Difference Equations, in *Mathematics in Science and Engineering*, Vol. 6 (Academic Press, New York, 1963), p. 480.

International Journal of Modern Physics A
Vol. 24, No. 5 (2009) 908–922

World Scientific
www.worldscientific.com

HIGH-ORDER DESCRIPTION OF THE DYNAMICS IN FFAGs AND RELATED ACCELERATORS

KYOKO MAKINO,* MARTIN BERZ,† PAVEL SNOPOK‡ and CAROL JOHNSTONE§

Department of Physics and Astronomy, Michigan State University,
Fermi National Accelerator Laboratory, USA
Department of Physics and Astronomy, University of California Riverside, USA
**makino@msu.edu*
†*berz@msu.edu*
‡*snopok@gmail.com*
§*cjj@fnal.gov*

In this paper, we describe newly developed tools for the study and analysis of the dynamics in FFAG accelerators based on transfer map methods unique to the code COSY INFINITY. With these new tools, closed orbits, transverse amplitude dependencies and dynamic aperture are determined inclusive of full nonlinear fields and kinematics to arbitrary order. The dynamics are studied at discrete energies, via a high-order energy-dependent transfer map.

The order-dependent convergence in the calculated maps allows precise determination of dynamic aperture and detailed particle dynamics. Using normal form methods, and minimal impact symplectic tracking, amplitude- and energy-dependent tune shifts and resonance strengths are extracted. Optimization by constrained global optimization methods further refine and promote robust machine attributes.

Various methods of describing the fields will be presented, including representation of fields in radius-dependent Fourier modes, which include complex magnet edge contours and superimposed fringe fields, as well as the capability to interject calculated or measured field data from a magnet design code or actual components, respectively.

Keywords: FFAG; differential algebra; COSY INFINITY; dynamic aperture; symplectic tracking.

PACS numbers: 29.20.D-, 29.20.dg, 29.27.Bd, 87.56.bd, 41.85.Lc, 41.75.Lx, 41.75.-i

1. Introduction

The broad class of FFAG-type accelerators is experiencing an international revival in the quest for high beam power, duty cycle, reliability and, in the case of the spiral-sector FFAG, the potential for compactness at reasonable cost.[1,2,3,4,5] The FFAGs proposed have the high average current and duty cycle characteristic of the cyclotron combined with the smaller aperture, losses, and energy variability of the synchrotron. Although new accelerator prototypes are often simulated with conventional tracking codes, these codes do not provide much flexibility in the field

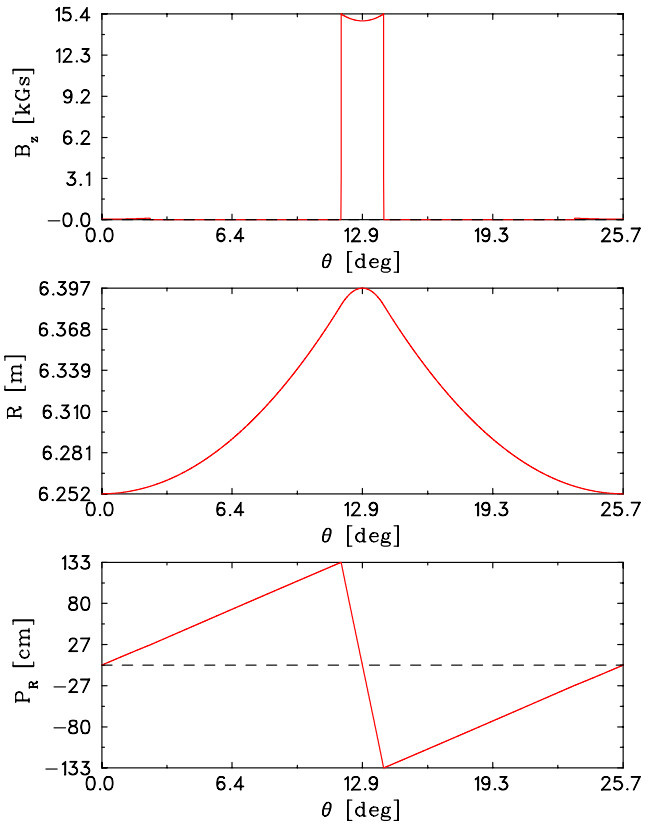

Fig. 1. B_z (vertical) field at injection for nonscaling FFAG lattice showing sharp cutoff of field at end of CF magnet, along with the radius of the injected orbit along the periodic cell and the angle as measured with respect to a normal projection relative to a radial line.

description and are limited to low order in the dynamics. This limitation can be inadequate to fully demonstrate performance including dynamic aperture where strong nonlinearities due to edge fields and other high-order effects appear. This is particularly true for the FFAGs. In the muon FFAGs, for example, the large beam emittances require the inclusion of kinematical (or angle) effects in the Hamiltonian, which implies that codes which fully describe the kinematics are necessary.[6,7]

The current number of supported design and optimization codes that can adequately describe the complex field and magnet contours for both the scaling and nonscaling FFAG variants is limited. Outside of COSY, present public codes include only the cyclotron code CYCLOPS,[8] and the field-map code ZGOUBI.[9,10] The former, which utilizes fields and their geometry expanded in polar coordinates, has limited accuracy in this application primarily due to lack of out-of-plane expansion order, and in handling of edge-field effects; this is particularly true for the case of rapid azimuthal field fall off at magnet edges (as in the FFAG field profile of Fig. 1), an effect not present in cyclotrons. The results and derived performance

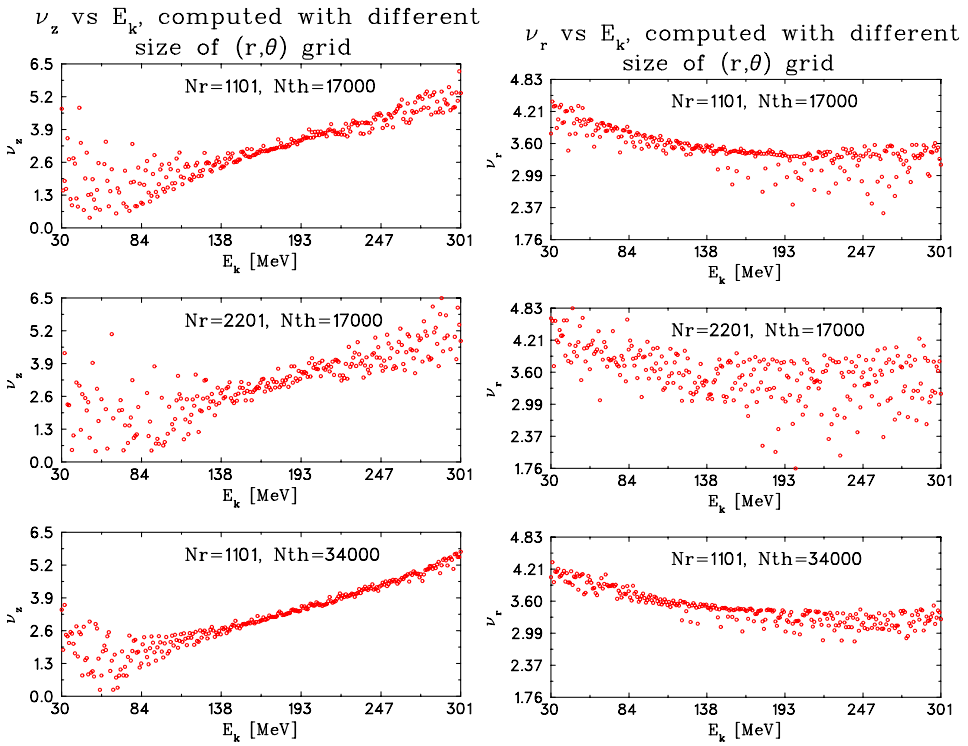

Fig. 2. Radial and azimuthal tunes for a 14-cell, 30–400 MeV nonscaling proton FFAG showing dependence on number of radial (N_r) and azimuthal (N_θ) mesh points used in field calculation.

can be strongly dependent on the integration step size across such an edge with Fig. 2 showing results for different mesh sizes. Since Cyclops remains a cyclotron code, it does not directly incorporate field data, either calculated or measured, primarily derives only closed orbits and tunes for an FFAG, and has no standard models to handle fringe fields. (Particle tracking and dynamics require another associated code.) The latter code, ZGOUBI, is presently being used successfully in FFAG development, but requires dedicated effort and expertise to implement an FFAG design, particularly when expressed in terms of the conventional magnetic component definitions. At present, some modern analysis tools for symplectic tracking, global optimization, tuneshifts and chromaticities, and resonance analysis are not as yet available.

In the following an analysis of a 14-cell, linear-field nonscaling 400-MeV FFAG for protons is compared between MAD, ZGOUBI, and CYCLOPS. (In MAD, the simulations were performed at discrete energies based on a derived closed orbit.) The results from MAD reflect a simple hard-edge. Field modeling in Cyclops reflected the hard edge representation, but experienced difficulty in calculating tunes with strong sensitivity to the fineness of mesh size discretization near the edge (Fig. 2). A considerable degree of effort[11] was expended in ZGOUBI to effect both the edge

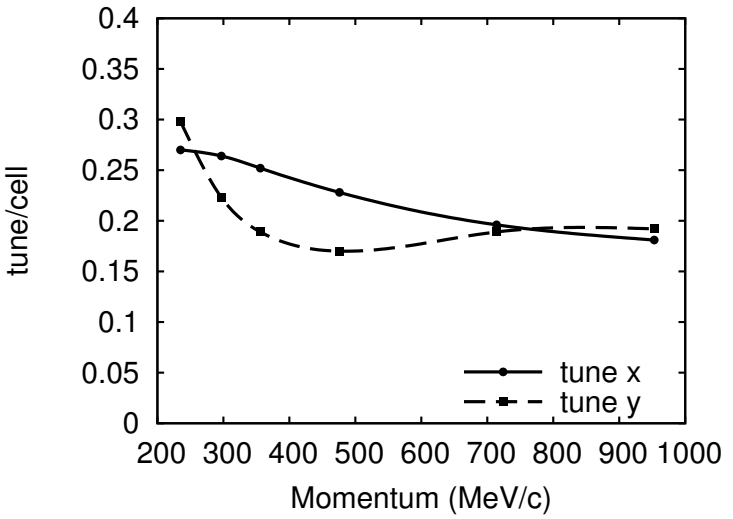

Fig. 3. Dependence of cell tune on momentum in an example of a nonscaling, linear-field FFAG which is tune-stabilized about 90°. Solution obtained from the approximated equations.

contour and a hard edge in order to reproduce the MAD model and results. (The parameters of the Enge function, the convention in ZGOUBI for the fringe-field model, were adjusted by hand to emulate a hard-edge fall-off.) The final tune dependence in the figure reflects repetitive tuning of the edge angle, again by hand, to most closely reproduce the desired results of the simpler MAD simulation. Figs. 3–5 show the MAD and final ZGOUBI results for this specific lattice. Tune dependence of the 14-cell ring modeled in Cyclops using the field and edge profile of Fig. 1 at injection coupled to the design linear-field gradient and linear edge specified in the design model is shown in Fig. 2. Note the sensitivity and large distribution in the tune calculation, especially at low-field points.

Modern extensions of the transfer map-based philosophy[12,13] as implemented in the arbitrary order code COSY INFINITY[14,15] address both limitations: high-order and accurate dynamics. Yet, the standard field configurations which, in turn, are based on the standard complement of accelerator components are not able to realize a general description for the FFAG concept—such as combined function magnets with complex edge and/or nonlinear field profiles.

Further, in promoting advanced accelerator design, the ability to perform extended parameter optimization has become increasingly important, if not critical. Although effective optimization requires initial conditions that rely on educated, experienced choices by the designer, subsequent manual adjustment and local optimization are rarely fully optimal and often fail for advanced accelerators such as the FFAGs. Large-scale global optimization, which not only probes local neighborhoods, additionally searches over extended domains of parameter space for suitable solutions. Recent significant advances in global optimization,[16,17,18,19,20] illustrated

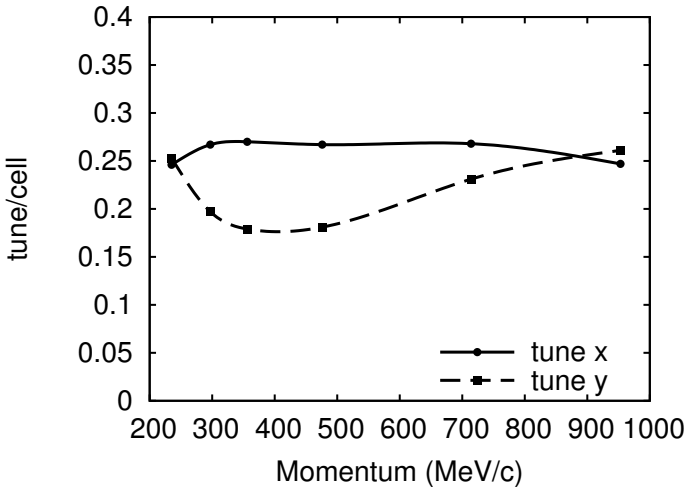

Fig. 4. Dependence of cell tune on momentum in an example of a nonscaling, linear-field FFAG which is tune-stabilized about 90°. Tune as modeled in MAD.

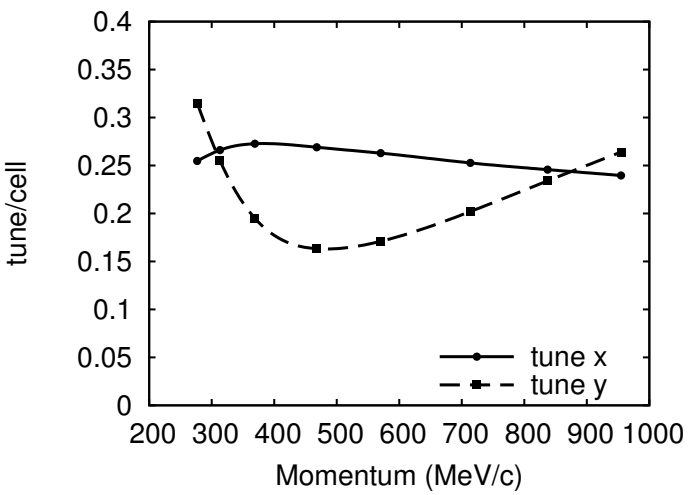

Fig. 5. Tune dependence of the nonscaling, linear-field FFAG in the code ZGOUBI as initially modeled in MAD (previous figure) for a single cell. Significant adjustment of edges and Enge-function parameters was required to achieve approximate agreement with the intended design described by the MAD simulations and analytical approximations.

by the various different directions of cutting edge research including genetic optimization, divide and conquer approaches, and verified methods, have led to a state of the art in optimization such that they significantly simplify and promote the design process. Further, they can prove critical in achieving a robust, state-of-the art design both in dynamical performance and technical criteria for critical accelerator technologies such as the FFAGs.

In the following, methods are described that allow the description and analysis of FFAGs and related types of accelerators. The approaches developed have the capability to model the wide array of FFAG design parameters and complicated fields in the presence of very large emittance beams. Description of arbitrary field profiles will be presented, including a representation in radius-dependent Fourier modes, which include terms describing the effects of magnet edges along with superimposed fringe fields from the different modes. Alternatively, data from magnet design codes and field measurements can be used in place of these representations.

2. Field Models

In the following various methods are discussed to describe the transverse focusing properties of FFAGs and how these methods are applied over the full acceleration range. The methods differ in level of sophistication and accuracy, as demanded by the level of complexity of the design fields and physical configuration of the individual components.

2.1. *General Combined-Function Magnets in COSY*

In a number of specific cases it is possible to describe an FFAG lattice in terms of standard COSY beamline elements. For these machines an extended set of combined function magnets have been implemented both with tilted and curved entrance edges and a choice of conventional fringe field models. Alternatively, actual data, either measured or from a magnet design code, can be entered for a calculation using exact fringe fields. The description of these elements allow a rather sophisticated level of design as long as the fields of individual elements do not strongly overlap (implying interaction between components and unnatural fringe fields) and as long as the field profiles are not unusual or extreme functions of radius or azimuthal angle. For details we refer to [14].

The disadvantage of this approach is that it is based on a description relative to a reference orbit and therefore relies on the deflection properties about this orbit. Studying multiple reference energies, as must be done for an FFAG, makes for a rapidly expanding problem dimensionally and one that quickly becomes difficult to analyze. To counter this expansion, in the next sections, we provide field descriptions in terms of a laboratory-based coordinate system that applies to all possible reference orbits and reduces the descriptive magnitude of the problem.

2.2. *Generalized FFAG Magnets*

An enhancement of the above approach that provides greater flexibility and control, entails the superimposition of combined-function (CF) magnets. A "universal" FFAG magnet can be effectively described in terms of superimposed CF magnets with arbitrary, high-order (individual multipole) fields. Each overlay retains the required complex edge curves and associated high-order dynamics. This approach is

new in that the effective centers of the constituent multipoles do not have to coincide physically in the CF magnet. This approach produces a truly arbitrary field profile which is difficult or impossible to reproduce in other codes.

Further, since FFAGs have completely periodic lattices, it is sufficient to define a "half cell" for a repetitive simulation; that is, the structure is defined from one reflective symmetry point to another. Geometric closure of an orbit requires that all orbits, even off-reference ones, must be parallel at such points, or "reflection" does not hold; i.e. all derivatives must be zero for stable orbits. Hence it is sufficient to construct only a half cell map from which the full cell map is automatically generated. In the full cell, the model extends from one symmetry point at the center of a CF magnet, past the next to the same symmetry point in the identical CF magnet in the sequence. For the half cell, the model extends only to the next symmetry point—from the center of the horizontally focusing CF magnet to the center of the horizontally-defocusing CF magnet, for example. The remaining half of the full cell is generated by reflection to find closed orbit and optical properties at any energy and for tracking of particle distributions.

In this manner, the full FFAG can be constructed from $2n$ sector-shaped half cells, each of which has a sector angle of π/n. The $2n$ half cells are arranged in n identical pairs consisting of one half cell and its mirror image to form the full periodic unit, or full cell. As a consequence of this symmetry, all closed orbits therefore cross the half cell boundaries perpendicularly and parallel to one another. The lines normal to the orbits at these symmetry points actually form a radial line to the geometric center of the FFAG.

Within each full cell, there are either two or three magnets, depending on the FFAG base unit cell, a FODO, doublet, or triplet structure, and each magnet has a radial field profile $B_{y,i}$ given by

$$B_{y,i} = B_{0,i} \cdot P_{B,i}(r)$$

where $B_{0,i}$ is a reference field value and $P_{B,i}$ is a dimensionless polynomial in the polar radius r.

The magnets are bounded by curves describing their effective field boundaries. Specifically, the first magnet is bounded by the exit curve P_{12}; note that the repeated mirror symmetric arrangement entails that its entrance curve is also specified by P_{12}. The second magnet is bounded by the entrance curve P_{21}. In the two-bend case, P_{21} also defines the exit curve due to the imposed mirror symmetry. In the three-bend case, the exit curve of the second bend is specified by P_{22}, and the entrance curve of the third bend is specified by P_{31}. The details of the arrangements are shown in Fig. 6.

All curves in the (x, z) midplane are represented in terms of a parameter t in the form

$$(x, z)_{ij}(t) = \vec{P}_{ij}(t) \text{ where } t \in [0, 1]$$

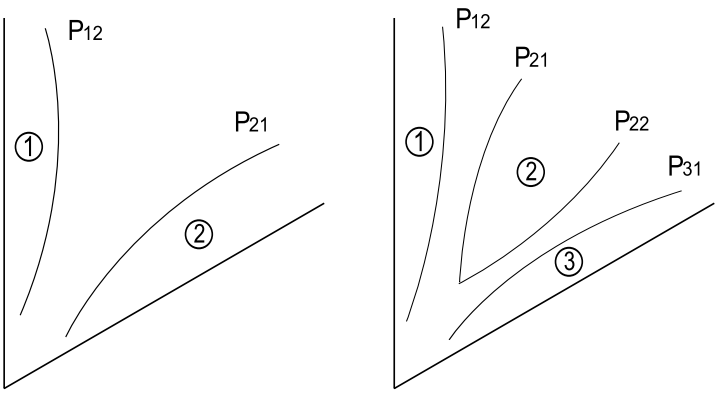

Fig. 6. The curves describing the effective field boundaries of the FFAG magnets in a cell of angle π/n in the two-bend (left) and three-bend (right) case.

where the origin of the coordinate system is at the center of the accelerator. In the vicinity of an edge curve, the fringe field belonging to the magnet bounded by that curve is given by an Enge Function

$$B_y(x,z) = \bar{B} \cdot \frac{1}{1+\exp(P_i(d/D_i(r)))}$$

where $\bar{B}$ is the main field acting at the point closest to (x,z) on the effective field boundary and P_i is a polynomial. Note that $\bar{B}$ is the sum of the contributions from the individual multipoles. The quantity d is the distance of the point (x,z) to the effective field boundary, and D_i is the aperture of magnet i, which is allowed to vary with radius in polynomial form.

Enge functions provide significant flexibility for the description of most types of realistic field fall-offs by appropriately choosing the coefficients of the polynomial in the exponential function. Thus, fringe field profiles based on other explicit functions are usually not necessary, at least in early stages of design.

Fringe fields of neighboring curves are allowed to overlap. Overall, the fringe field description is very similar to the approach that has been followed very successfully in the study of high-resolution particle spectrographs.

The advantage of this particular field model is that it allows a relatively simple adjustment of the main parameters commonly studied in the design of FFAG magnets while providing a fully Maxwellian and realistic field description. Specifically, the radial field variation appearing in $P_{B,i}(r)$ affects both the horizontal and vertical focusing for quadrupole and higher fields and only horizontal focusing for dipole, and the edge curves $\vec{P}_{ij}(t)$ affect both horizontal and vertical focusing. The Enge fall off is well known to represent realistic field profiles which can be adjusted to accurately describe most magnets and can even approximate a rapid, hard edge fall-off which is useful for comparison with codes without fringing fields.

2.3. *Radius-Dependent Fourier Decomposition*

From the early days of the study of FFAGs (see for example [21, 22]), midplane fields are often described in terms of azimuthal Fourier modes. This description allows the capture of most of the effects relevant to the focusing while abstracting from the specific shapes of the magnets that provide the desired fields. We provide this option by allowing a field description of the form

$$B_y(r,\phi) = a_0(r) + \sum_{j=1}^{n} a_j(r)\cos\left(j(\phi-\phi_0(r))\right) + \sum_{j=1}^{n} b_j(r)\sin\left(j(\phi-\phi_0(r))\right).$$

The Fourier coefficients $a_j(r)$ and $b_j(r)$ as well as the phase angle $\phi_0(r)$ are described in terms of polynomials in r. Higher values of n obviously allow for more faithful modeling, while all of the common focusing effects can be observed already for lower values of n.

In some instances it is desirable to capture more radial detail than can be revealed by the polynomials $a_j(r)$ and $b_j(r)$. Specifically, let us assume we are given a table of a_{ij} on a grid of equidistant radii $r_i = i \cdot \Delta r$, let P_j be the polynomial of best fit to all data points, and let $\bar{a}_{ij} = a_{ij}/P_j(i\Delta r)$. We then perform a Gaussian wavelet interpolation[23] of the form

$$a_j(r) = P_j(r) \cdot \sum_i \bar{a}_{ij} G_\sigma(r - i\Delta r)$$

where $G_\sigma(x) = \exp\left(-x^2/\sigma^2\right)/\sigma\sqrt{\pi}$ with $\sigma \approx 1.5\Delta r$.

2.4. *Gaussian Wavelet Representation of Polar Midplane Data*

Beyond the tools useful to quickly provide field models for the initial design phase, in addition it is possible to describe the fields in terms of three-dimensional field models of various levels of sophistication as soon as such field data are known. As a first step, let us assume we are given a field representation in terms of midplane data $B_y^{(i,j)}$ in polar coordinates r and ϕ on a regular polar grid with spacing Δr and $\Delta\phi$. The midplane field is then described in terms of these as a wavelet representation of the form

$$B_y(r,\phi) = \sum_{i,j} G_{\sigma r}(r - r_i) \cdot G_{\sigma\phi}(\phi - \phi_j) \cdot B_y^{(i,j)}$$

where the Gaussian wavelet G_σ has the form $G_\sigma(x) = \exp\left(-x^2/\sigma^2\right)/\sigma\sqrt{\pi}$, and σ is chosen as approximately $1.5\Delta r$ and $1.5\Delta\phi$, respectively. From the midplane representation, the field is then reconstructed by conventional out-of-plane expansion.

Note that this representation has some inherent limitations since the out-of-plane is sensitive to errors in the field data in the midplane. It should hence be used with caution only after the effect of such errors on the quality of the resulting expansion in the domain of interest is established. One way to remedy this situation is to utilize the midplane data to first obtain a Fourier representation as described in section 2.3. Another method is described in the next section.

2.5. *Field Representations from Three-Dimensional Data*

From a mathematical point of view, the knowledge of magnetic fields in the midplane is sufficient to determine the fields at any point in space based on a power series expansion. Specifically, Maxwell's equations impose well-known conditions on the Taylor coefficients that under the assumption of midplane symmetry allow the determination of out-of-plane coefficients from those in-plane. Using DA-based methods as described in for example [12], the process can even be fully automated to any order. However, any attempt of representing three-dimensional field data in terms of fields given only in the midplane is sensitive to measurement errors, since these can greatly affect any attempt of recovering high-order midplane derivatives.

It is thus desirable to utilize field descriptions that do not rely on the midplane data. Indeed, a much more favorable approach is the utilization of surface field data. As discussed in [24, 25, 26, 27], this approach has a tendency to smooth out any measurement errors and leads to more faithful three-dimensional representations.

Other field arrangements are potentially desirable in certain cases. For example, one may want to describe fields of air coil-dominated magnets directly based on a data file describing the geometry of pieces of the respective coils and their currents.[27,28,29] Furthermore, if it is deemed desirable, one can perform injection-to-extraction simulations by providing acceleration elements of varying degrees of sophistication, beginning from pillbox-type elements to more sophisticated analysis based on field harmonics.

3. Analysis Tools

Based on the field descriptions provided in the last section, there are various tools of the COSY environment that can be utilized for subsequent analysis.

- **Closed Orbits.** First, a set of closed orbits is being determined for a suitable collection of reference particle energies by optimization.
- **Arbitrary Order Maps.** For each of the closed orbits, a high-order energy-dependent transfer map around it is calculated. This includes all dynamics of the system to arbitrary order, including out-of-plane expansions of fields and any nonlinear terms in the Hamiltonian.[12,30]
- **Linear Properties of Maps.** For this local map, common linear beam functions including invariant ellipses and tunes near the closed orbit are determined.
- **Tracking.** The high-order transfer maps can be used to perform tracking to estimate the dynamic aperture, presence of resonances, etc. There are various methods to perform tracking in COSY that preserve the symplectic symmetry inherent in Hamiltonian systems, including methods that do so with minimal modifications based on the EXPO approach.[31,32,33]
- **Acceleration.** It is possible to describe the fields in terms of cavities of various sophistication, ranging from kicks over pillbox-type cavities to Fourier modes in space and time. Independent of the type of acceleration device used, in order

to study acceleration effects through such systems, the entire dynamic range in energy is sampled in steps of energy. For each such step, the map will be represented through a high-order map including energy dependence, and acceleration tracking is possible by suitably switching between maps.

- **Amplitude Dependent Tunes and Resonances.** In addition to the mere empirical study, there are various tools for analysis of nonlinear effects, including the normal form-based computation of high-order amplitude dependent tune shifts and resonances.[12]
- **Global Parameter Optimization.** COSY allows the automatic adjustment and optimization of arbitrary system parameters; and different from other tools, the search uses methods of global optimization with constraints over a prespecified search region, and not merely local optimization from a starting parameter setting.

4. Performance Examples

To provide an illustrative example of the behavior to be expected, we study a sample FFAG having sixfold symmetry, with focusing stemming from an azimuthal field variation expressed as a single Fourier mode as well as edge focusing. The system is studied to various orders of out-of-plane expansion, and conclusions about dynamic aperture are drawn. We show the results for orders three and five, which are typical for the situation of conventional out-of-plane expansion in codes like Cyclops. Because the DA method used in COSY[12] is not based on divided differences, the necessary in-plane derivatives can actually be calculated to any order desired with an accuracy that is always close to machine precision.[12]

The results of tracking without symplectification and with EXPO symplectification are shown in Figs. 7–12. Apparently symplectification greatly affects the dynamic aperture to be inferred in the system. Tracking is performed using the EXPO symplectification scheme which is known to minimize the alterations to the non-symplectic tracking results compared to other symplectification methods.

Figs. 7–12 show phase portraits in the $(x - a)$ plane (left) and the $(y - b)$ plane (right), where $a = p_x/p_0$, $b = p_y/p_0$ are normalized horizontal and vertical momenta correspondingly.

However, Figs. 11 and 12, which are both based on order eleven out-of-plane expansion, show significant additional effects and different dynamic aperture compared to the lower order cases as seen in Figs. 7 to 10, suggesting that the low order methods for out-of-plane expansion and dynamics are not sufficient to capture the details of the dynamics. It would in fact lead to an incorrect prediction of dynamic aperture, underestimating it in the horizontal direction and overestimating it in the vertical. Further increases in order beyond eleven do not significantly affect the details of the symplectic motion shown, but continue to influence the non-symplectic motion. A rough estimate reveals that in this particular case, the dynamics as seen in non-symplectic tracking seems to begin to stabilize around order 11, which is still rather easily obtained within the power of a modern workstation.

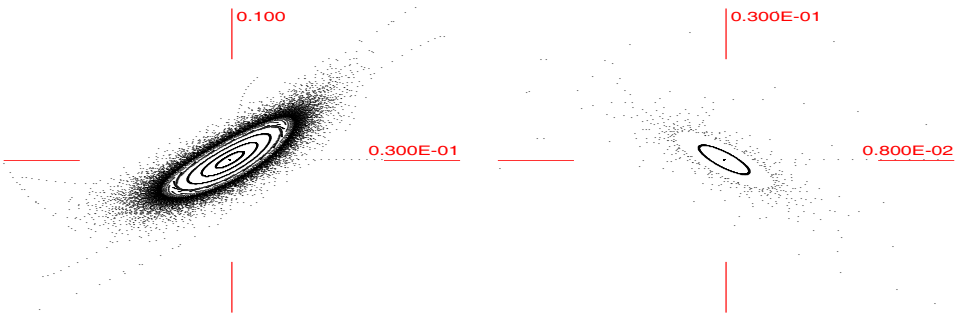

Fig. 7. Horizontal and vertical tracking in a model FFAG with third-order out of plane expansion, without symplectification. Left: $(x - a)$ plane, right: $(y - b)$ plane, where $a = p_x/p_0$, $b = p_y/p_0$ are normalized horizontal and vertical momenta correspondingly.

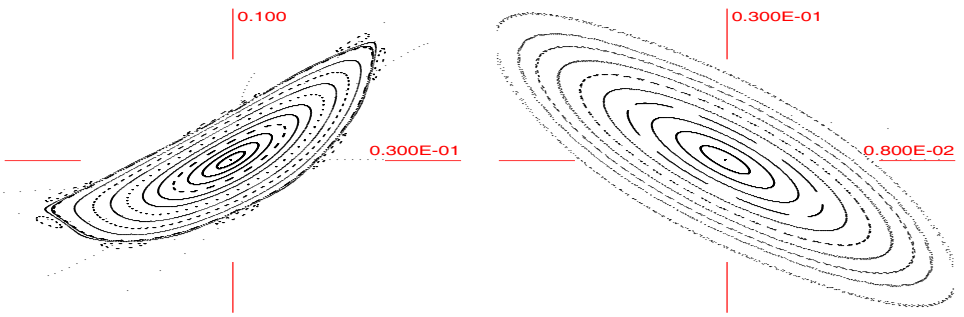

Fig. 8. Horizontal and vertical tracking in a model FFAG with third-order out of plane expansion, with EXPO symplectification. Left: $(x-a)$ plane, right: $(y-b)$ plane, where $a = p_x/p_0$, $b = p_y/p_0$ are normalized horizontal and vertical momenta correspondingly.

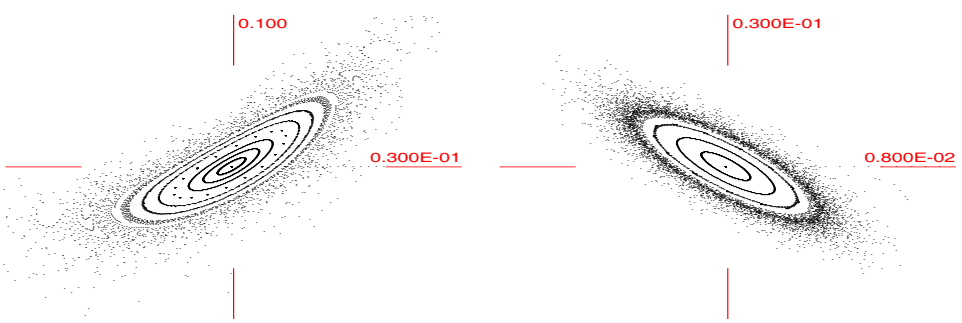

Fig. 9. Horizontal and vertical tracking in a model FFAG with fifth-order out of plane expansion, without EXPO symplectification. Left: $(x - a)$ plane, right: $(y - b)$ plane, where $a = p_x/p_0$, $b = p_y/p_0$ are normalized horizontal and vertical momenta correspondingly.

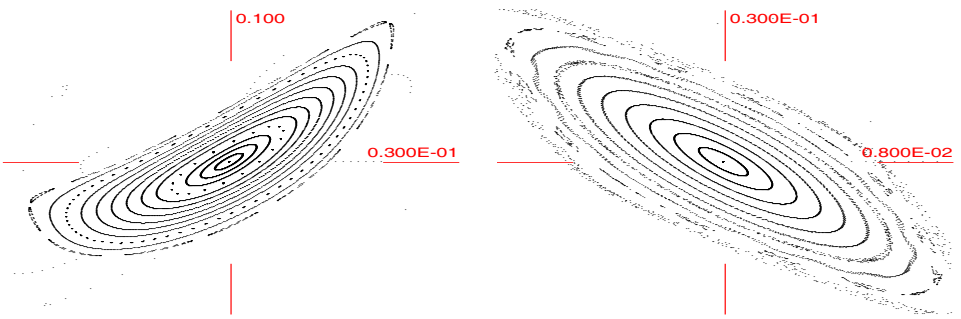

Fig. 10. Horizontal and vertical tracking in a model FFAG with fifth-order out of plane expansion, with EXPO symplectification. Left: $(x-a)$ plane, right: $(y-b)$ plane, where $a = p_x/p_0$, $b = p_y/p_0$ are normalized horizontal and vertical momenta correspondingly.

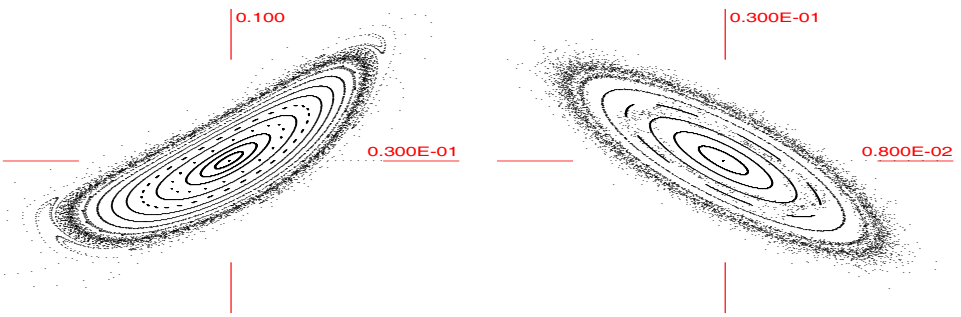

Fig. 11. Horizontal and vertical tracking in a model FFAG with eleventh-order out of plane expansion, without EXPO symplectification. Shows significant additional effects and different dynamic aperture compared to the lower order cases as seen in Figs. 2 to 5, suggesting that the low order methods for out-of-plane expansion and dynamics are not sufficient to capture the details of the dynamics. Left: $(x-a)$ plane, right: $(y-b)$ plane, where $a = p_x/p_0$, $b = p_y/p_0$ are normalized horizontal and vertical momenta correspondingly.

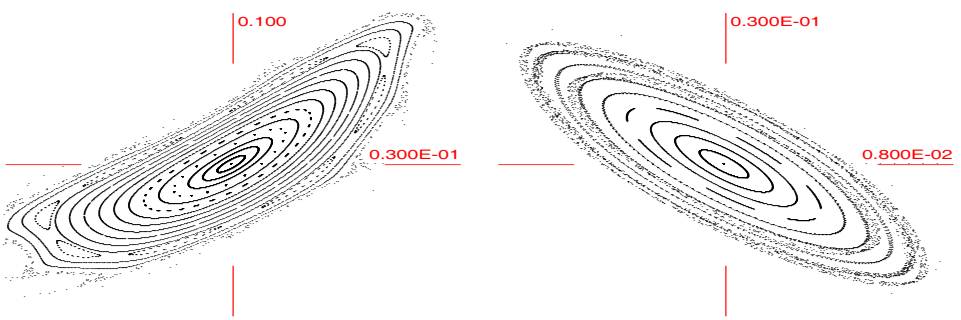

Fig. 12. Horizontal and vertical tracking in a model FFAG with eleventh-order out of plane expansion, with EXPO symplectification. Shows significant additional effects and different dynamic aperture compared to the lower order cases as seen in Figs. 2 to 5, suggesting that the low order methods for out-of-plane expansion and dynamics are not sufficient to capture the details of the dynamics. Left: $(x-a)$ plane, right: $(y-b)$ plane, where $a = p_x/p_0$, $b = p_y/p_0$ are normalized horizontal and vertical momenta correspondingly.

References

1. Chris Prior (Ed.). ICFA beam dynamics newsletter. Technical report, 2007.
2. M. K. Craddock. New concepts in FFAG design for secondary beam facilities and other applications. In *Proceedings, PAC05*, page 261, 2005.
3. Y. Mori. *Proceedings, FFAG05 Workshop*. FNAL, 2005.
4. K.R. Symon, D.W. Kerst, L.W. Jones, L.J. Laslett, and K.M. Terwilliger. Fixed-field alternating-gradient particle accelerators. *Physical Review*, 103:1837–1859, 1956.
5. Carol Johnstone and S. Koscielniak. *DPB Newsletter*, chapter The New Generation of FFAG Accelerators, pages 12–14. American Physical Society, 2008.
6. K. Makino and M. Berz. Effects of kinematic correction on the dynamics in muon rings. *AIP CP*, 530:217–227, 2000.
7. M. Berz, B. Erdélyi, and K. Makino. Fringe field effects in small rings of large acceptance. *Physical Review ST-AB*, 3:124001, 2000.
8. R Baartman et al. CYCLOPS. Technical report.
9. F. Meot. The ray-tracing code ZGOUBI. *Nuclear Instruments and Methods A*, 427:353–356, 1999.
10. F. Lemuet and F. Meot. Developments in the ray-tracing code ZGOUBI for 6-d multiturn tracking in FFAG rings, 2005.
11. T. Yokoi. Private communication.
12. M. Berz. *Modern Map Methods in Particle Beam Physics*. Academic Press, San Diego, 1999. Also available at http://bt.pa.msu.edu/pub.
13. M. Berz. Differential algebraic description of beam dynamics to very high orders. *Particle Accelerators*, 24:109, 1989.
14. M. Berz and K. Makino. COSY INFINITY Version 9.0 beam physics manual. Technical Report MSUHEP-060804, Department of Physics and Astronomy, Michigan State University, East Lansing, MI 48824, 2006. See also http://cosyinfinity.org.
15. M. Berz and K. Makino. COSY INFINITY Version 9.0 programmer's manual. Technical Report MSUHEP-060803, Department of Physics and Astronomy, Michigan State University, East Lansing, MI 48824, 2006. See also http://cosyinfinity.org.
16. M. Tawarmalani and N. Sahinidis. *Convexification and Global Optimization and Continuous and Mixed-Integer Programming*. Kluwer, 2002.
17. C. Floudas. *Nonlinear and Mixed-Integer Optimization*. Oxford University Press, 1995.
18. K. Lange. *Optimization*. Springer, 2004.
19. M. Berz, K. Makino, and Y.-K. Kim. Long-term stability of the Tevatron by validated global optimization. *Nuclear Instruments and Methods*, 558:1–10, 2005.
20. A. Poklonskiy. *Evolutionary Optimization Methods for Beam Physics*. PhD thesis, Michigan State University, East Lansing, Michigan, USA, 2008.
21. D. W. Kerst, E. A. Day, H. J. Hausman, R. O. Haxby, L. J. Laslett, F. E. Mills, T. Ohkawa, F. L. Peterson, E. M. Rowe, A. M. Sessler, J. N. Snyder, and W. A. Wallenmeyer. Electron model of a spiral sector accelerator. *Review of Scientific Instruments*, 31,10:1076–1106, 1960.
22. E. A. Crosbie. Use of the MURA transformation to generate the fields and calculate the motion of protons in the designed Argonne mini-aspun FFAG spiral sector accelerator. *IEEE Transactions on Nuclear Science*, NS-32, 5:2675–2677, 1985.
23. K. Makino. *Rigorous Analysis of Nonlinear Motion in Particle Accelerators*. PhD thesis, Michigan State University, East Lansing, Michigan, USA, 1998. Also MSUCL-1093.
24. S. L. Manikonda and M. Berz. Multipole expansion solution of the Laplace equation using surface data. *Nuclear Instruments and Methods*, 558,1:175–183, 2006.

25. S. L. Manikonda and M. Berz. An accurate high-order method to solve the Helmholtz boundary value problem for the 3D Laplace equation. *International Journal of Pure and Applied Mathematics*, 23,3:365–378, 2005.
26. S. L. Manikonda, M. Berz, and K. Makino. High-order verified solution of the 3D Laplace equation. *Transactions on Computers*, 4-11:1604–1610, 2005.
27. S. Manikonda. *High Order Finite Element Methods to Compute Taylor Transfer Maps*. PhD thesis, Michigan State University, East Lansing, Michigan, USA, 2006.
28. M. Lindemann. Rigorous field analysis of superconducting magnets and the influence on nonlinear dynamics in particle accelerators. Master's thesis, Michigan State University, East Lansing, Michigan, USA, 1998.
29. S. Manikonda, J. Nolen, M. Berz, K. Makino, and G.Weizman. Design of a superconducting quadrupole with elliptical acceptance and tunable higher order multipoles. Technical Report MSUHEP-060412, Department of Physics and Astronomy, Michigan State University, East Lansing, MI 48824, 2006.
30. M. Berz, B. Erdélyi, W. Wan, and K. Ng. Differential algebraic determination of high-order off-energy closed orbits, chromaticities, and momentum compactions. *Nuclear Instruments and Methods*, A427:310–314, 1999.
31. B. Erdélyi and M. Berz. Local theory and applications of extended generating functions. *International Journal of Pure and Applied Mathematics*, 11,3:241–282, 2004.
32. B. Erdélyi and M. Berz. Optimal symplectic approximation of Hamiltonian flows. *Physical Review Letters*, 87,11:114302, 2001.
33. B. Erdélyi. *Symplectic Approximation of Hamiltonian Flows and Accurate Simulation of Fringe Field Effects*. PhD thesis, Michigan State University, East Lansing, Michigan, USA, 2001.

International Journal of Modern Physics A
Vol. 24, No. 5 (2009) 923–940

World Scientific
www.worldscientific.com

CONCEPTUAL DESIGN OF A SUPERCONDUCTING QUADRUPOLE WITH ELLIPTICAL ACCEPTANCE AND TUNABLE HIGHER ORDER MULTIPOLES

SHASHIKANT MANIKONDA* and JERRY NOLEN†

Physics Division, Argonne National Laboratory,
9700 South Cass Avenue, Argonne, IL 60439, USA
**manikonda@anl.gov*
†*nolen@anl.gov*

MARTIN BERZ‡ and KYOKO MAKINO§

Department of Physics and Astronomy, Michigan State University,
East Lansing, MI 48824, USA
‡*berz@msu.edu*
§*makino@msu.edu*

For charged particle beams that are wider in the dispersive plane compared to the transverse plane it is cost efficient to utilize magnets that accept beams with elliptic cross section. In this paper we presents the conceptual design of a quadrupole magnet with elliptic cross section and with tunable higher order multipoles. The design consists of 18 superconducting race-track coils placed on two hollow concentric rhombic prism support structures.

To compute the magnetic field for the proposed design a new method of calculating 2D and 3D fields for the air core magnets based on differential algebra (DA) techniques is developed. We will present the new method and discuss its implementation of new numerical tools based on this method in the code COSY Infinity.

Keywords: Differential algebra; magnet design; beam physics.

PACS numbers: 29.30.Aj, 29.30.Ep, 41.85-p

1. Introduction

Next-generation radioactive beam facilities like the proposed AEBL[1,2] facility in US and the newly constructed BIGRips[3] facility in Japan, require the use of large aperture superconducting multipole magnets. Since the charged particle beams used in such facilities are wider in the dispersive plane than the transverse plane it is cost efficient to utilize magnets with elliptic cross sections. Such elliptic cross section design usually leads to generation of high order multipoles. In this paper we present a new design for a quadrupole magnet with an elliptic cross-section and with tunable higher order multipoles. The analysis of this design requires the

development of new numerical tools to compute the multipole expansion of the magnetic field starting from the Biot-Savart law and Ampere's law. The Differential Algebra (DA) techniques have been utilized to extract such multipole expansions for the air-core magnets.

In sections 2 and 3 we will present the background and discuss the theory and implementation of the new computational tools using the differential algebra (DA) techniques. In section 4 we present the details of the design of the new quadrupole magnet with tunable high order multipoles. We will discuss both the 2D and 3D design and also discuss the practicle range of multipole field strengths that can be achieved with this design.

2. Differential Algebra Techniques and Field Computations

In beam physics the DA techniques have traditionally been used for the computation of the high-order Taylor expansion of the transfer maps and design and analysis of accelerator lattices.[4,5,6,7] In recent years the DA techniques have been applied to solve DAEs, ODEs and PDEs.[8,9,10,11,12] For these applications the DA is used to develop techniques and algorithms to use a truncated Taylor expansion of a function on a computer. The numerical techniques based on DA have the unique advantage of getting high accuracy at a very small cost of the execution time and the computational resources compared to traditional techniques.

In the context of magnet design the DA techniques have so far been utilized to obtain magnetic fields from the analytic model of the magnet, consisting of line wire currents, obtained from codes like ROXIE.[13] The details of the method and it implementation are described in [14, 15]. The present work starts directly from the geometric model of the magnet and computes the multipole expansion of the fields. The method described in this paper is useful for both designing the magnets as well as multipole extraction of the fields, which can then be combined with the existing DA based transfer map computation tools. Hence, all the aspects from design of the magnet, extraction of transfer maps and finally its use in beam optic design and optimization can be performed in the same code.

3. Magnetic Field Due to Arbitrary Current Distribution

The Biot-Savart law and Ampere's law can be utilized to compute the magnetic field for an arbitrary current distribution. Usually, numerical integration is required to find the total magnetic field at any point. Below we describe a new scheme to perform such numerical integration using DA techniques.

For an arbitrary current distribution the proposed method discretizes the current domain and expresses the integral over the current domain as the sum of integrals over smaller intervals. For the line, surface or volume distribution we express the intervals in terms of one, two or three parameters and scale them such that the new interval is a box $[-1, 1]^n$, where $n \in 1, 2, 3$. We then Taylor expand the kernel appearing in the Biot-Savart law and the Ampere law in terms of the

observation point, $\vec{r}$, and previously defined parameters. Finally, we integrate in parameters over the interval $[-1,1]^n$ and then sum over all the intervals to get the multipole expansion of the magnetic field about the observation point $\vec{r}$.

We now discuss the above scheme for computing the magnetic field by using the example of the current in a straight wire with a finite rectangular cross section. This particular case is of practical importance and we will use this to develop tools to design new accelerator magnets. These tools will later be used to analyse the proposed design of the quadrupole magnet in the section 4.

3.1. *Magnetic field computation for a wire with a rectangular cross section using DA*

For the case of a rectangular box of length l, width w and breath b, let the cross section be described by the unit vectors $\hat{n}_w$ along the width, and $\hat{n}_b$ along the breath. The unit vector $\hat{n}_l = \hat{n}_w \times \hat{n}_b$ then defines the cross section plane and is along the direction of the length of the rectangular box. The central axis can be described by $\vec{V}_c = \vec{V}_{c_0} + \lambda_3 \hat{n}_l$, where the vector $\vec{V}_{c_0}$ is the center of a face on the rectangular box that is perpendicular to the unit vector $\hat{n}_l$, and $\lambda_3 \in [0, l]$. Any point inside the box is given by

$$\vec{V}_p^{box}(\lambda_1, \lambda_2, \lambda_3) = \vec{V}_{c_0} + \frac{1}{2}(\lambda_1 b \hat{n}_w + \lambda_2 w \hat{n}_b) + \lambda_3 \hat{n}_l, \tag{1}$$

where the parameters $\lambda_1, \lambda_2 \in [-1, 1]$. The parameters $(\lambda_1, \lambda_2, \lambda_3)$ then completely describe a rectangular box. The equation (1) will be used in the next two sections to express the Biot-Savart law and Ampere's law in the DA framework.

3.1.1. *Magnetic field of a wire with a rectangular cross section using the Biot-Savart law and DA*

We can choose the direction of the current flow in the wire to coincide with the unit vector $\hat{n}_l$ and the magnitude to be I_0. Using the Biot-Savart law, we can write the magnetic field at an observation point $\vec{r}$ as

$$\vec{B}(\vec{r}) = \frac{\mu_0}{4\pi} \frac{I_0}{bw} \int_{-1}^{1} \int_{-1}^{1} \left[\int_0^l \frac{\left(\hat{n}_l \times \left(\vec{r} - \vec{V}_p^{box} \right) \right)}{\left| \vec{r} - \vec{V}_p^{box} \right|^2} d\lambda_3 \right] d\lambda_2 d\lambda_1, \tag{2}$$

where μ_0 is the permeability of vacuum. In SI units, the value is exactly expressed by $\mu_0 = 4\pi \times 10^{-7} N A^{-2}$. To perform integration with respect to λ_3 in the equation (2), we first split the domain of integration into smaller intervals. Let the length l be divided into N parts of the size $h = l/N$. Then the parameter λ_3 can be written as

$$\lambda_3(i) = \left(i + \frac{1}{2} v \right) h,$$

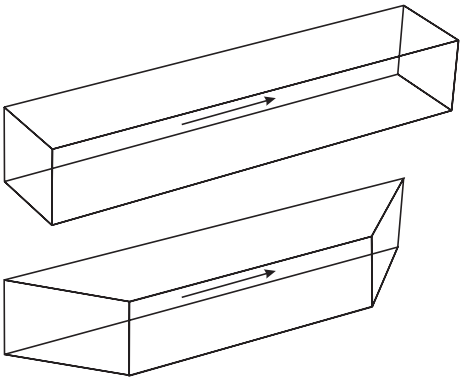

Fig. 1. The schematic digram of a finite length current wire with rectangular cross section and (a) straight ending (b) inclined ending.

where $i = 0.5, \ldots, (N - 0.5)$, and $v \in [-1, 1]$. The position of a point inside the box in terms of the new parameters $(\lambda_1, \lambda_2, v)$ is given by

$$\vec{V}_p^{box}(i, \lambda_1, \lambda_2, v) = \vec{V}_{c_0} + ih\hat{n}_l + \frac{1}{2}(\lambda_1 b\hat{n}_1 + \lambda_2 w\hat{n}_2 + vh\hat{n}_l). \tag{3}$$

The equation (2) can now be written as

$$\vec{B}(\vec{r}) = \frac{\mu_0}{4\pi}\frac{I_0}{bw}\sum_{i=0.5}^{i=N-0.5}\int_{-1}^{1}\int_{-1}^{1}\int_{-1}^{1}\frac{\left(\hat{n}_l \times \left(\vec{r} - \vec{V}_p^{box}(i)\right)\right)}{\left|\vec{r} - \vec{V}_p^{box}(i)\right|^2}\frac{l}{N}dvd\lambda_2 d\lambda_1. \tag{4}$$

The parameters $(\lambda_1, \lambda_2, v)$ and the position $\vec{r}(x, y, x)$ become the DA variables with respect to which the kernel of the integral in the equation (4) is expanded to a high order. In the DA framework it is straightforward to perform the volume integral over the resulting polynomial representation.

In the DA frame work it is also straightforward to treat the wires with rectangular cross sections that have curved endings rather than the straight endings that are perpendicular to the direction of the current flow. Let the two surfaces at the start and the end of the wire carrying the current be expressed as $\lambda_3 = g(\lambda_1, \lambda_2)$ and $\lambda_3 = f(\lambda_1, \lambda_2)$. We can use the equation (4) to find the magnetic field due to this new configuration by noting

$$h(\lambda_1, \lambda_2) = \frac{f(\lambda_1, \lambda_2) - g(\lambda_1, \lambda_2)}{N},$$

where the step h is now a function of the parameters (λ_1, λ_2). The equation (3) can be modified to express a point inside the rectangular box with curved endings as

$$\vec{V}_p^{box}(i, \lambda_1, \lambda_2, v) = \vec{V}_{c_0} + (g(\lambda_1, \lambda_2) + i \cdot h(\lambda_1, \lambda_2)) \cdot \hat{n}_l \tag{5}$$

$$+0.5 \cdot (\lambda_1 b \cdot \hat{n}_1 + \lambda_2 w \cdot \hat{n}_2 + v \cdot h(\lambda_1, \lambda_2) \cdot \hat{n}_l). \tag{6}$$

When the surfaces are just inclined planes, the functions f and g are just linear combinations of the parameters λ_1 and λ_2. The Figure 1 shows the schematic diagram of a wire with straight ending and inclined ending. The inclined ending case is useful in the implementation of the numerical tool to compute the magnetic field due to a current carrying coil with a rectangular cross section.

3.1.2. *Magnetic field of an infinitely long wire with a rectangular cross section using Ampere's law and DA*

Once again, we can choose the direction of the current in the infinitely long wire with a rectangular cross section to coincide with the unit vector $\hat{n}_l$ along the length of the wire. Let the vector $\vec{V}_p$ defined by

$$\vec{V}_p = \vec{V}_c + \frac{1}{2}\left(\lambda_1 b\hat{n}_b + \lambda_2 w\hat{n}_w\right), \tag{7}$$

describes a point inside a rectangle cross section with breath b and width w and centered at a point $\vec{V}_c$. The closest distance $r_\perp$ between the observation point $\vec{r}$ and the line passing through the point $\vec{V}_p$ and in the direction $\hat{n}_l$ is given by

$$r_\perp = \left|\left(\vec{r} - \vec{V}_p\right) - \left(\hat{n}_l \cdot \left(\vec{r} - \vec{V}_p\right)\right)\hat{n}_l\right|,$$

where $\vec{V}_p$ is given by the equation (7). Ampere's law can then be written as

$$\vec{B}\left(\vec{r}\right) = \int_{-1}^{1}\int_{-1}^{1} \frac{\mu_0}{2\pi}\frac{I_0}{b\cdot w}\frac{\left(\hat{n}_l \times \frac{\left(\vec{r}-\vec{V}_p\right)}{\left|\left(\vec{r}-\vec{V}_p\right)\right|}\right)}{r_\perp} d\lambda_1 \cdot d\lambda_2. \tag{8}$$

The equation (8) can be used to compute the magnetic field of an infinitely long wire with a rectangular cross section. The parameters (λ_1, λ_2) become the DA variables with respect to which the kernel of the integral in the equation (8) is expanded to high order, and DA integration is performed over the resulting polynomial representation.

3.1.3. *COSY INFINITY tools for magnetic field computations*

Due to their frequent use in the magnet design, a dedicated set of tools has been written for the rectangular cross section wire and coil in the code COSY INFINITY.[16,17] These tools use the differential algebraic framework available in COSY to Taylor expand, integrate and evaluate the kernels appearing in the equations(8) and (4).

For 2D design, a tool to compute the field for an infinitely long wire with a rectangular cross section has been implemented. For 3D design, a tool to compute the magnetic field of a finite length wire of a rectangular cross section has been implemented. A finite length wire can have the current entrance and exit planes inclined to the central axis or the direction of the current flow. By combining four such current wires, as shown in Figure 2, a separate tool to compute the magnetic

field of a current coil of a rectangular cross section has also been implemented. The wires have current entrance and exit planes tilted by 45° in opposite directions.

Using orders around 10, accuracy of about 14 digits can be achieved using these tools. In addition to providing highly accurate results in the form of the local Taylor expansion of the magnetic field, the DA based implementation has a unique advantage of easily obtaining the curl and divergence of the magnetic field at any given point. This offers one way to quickly verify if the magnetic field satisfies Maxwell's equations.

4. The Conceptual Design of an Asymmetric-Aperture Quadrupole Magnet with Adjustable Multipole Components

For charged particle beams that are wider in the dispersive plane than the transverse plane it is cost efficient to utilize magnets that accept beams with elliptic cross sections . In this section we present the conceptual design of a quadrupole magnet with an elliptic cross section and with tunable high order multipoles. The design consists of 18 superconducting racetrack coils placed on two hollow concentric rhombic prism support structures. It would require 28 racetrack coils to create the same number adjustable multipoles with circular aperture magnets (quadrupole through decapole).

A combination of superconducting racetrack coils is used to produce the desired magnetic field inside an elliptic cross section. By the proper choice of dimensions, current density, and placement of these coils, various combinations of the quadrupole field and the higher order multipole fields can be achieved. In this example, the support structure that holds these coils in place consists of two concentric hollow rhombic prisms, with the ratio of the diagonals of the rhombus is 2. The cross section view showing the arrangement of the current coils on the support structure is shown in Figure 3. The signs "+" and "−" indicate the direction of the current to produce a positive multipole term. The superconducting racetrack coils on the inner rhombic prism produce quadrupole and octupole fields. The racetrack

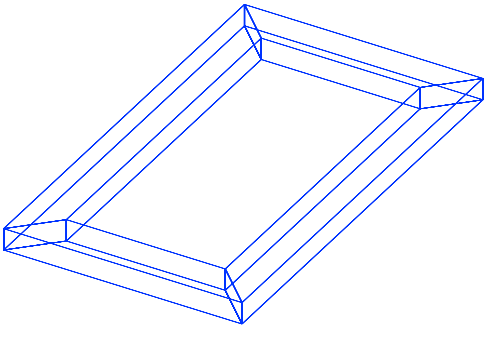

Fig. 2. The schematic digram of a current coil.

Table 1. The center position of the current carrying coils in the first quadrant.

Coil Description	**Position of Coils**		**Current**
	x	y	
Inner Coils			
Quadrupole	0.4473	0.8222E-01	-QI1
Octupole	0.3473	0.1322	-QI2
Octupole	0.1973	0.2072	+QI2
Quadrupole	0.9736E-01	0.2572	+QI1
Outer Coils			
Hexapole	0.5591	0.1604	+HI1
Decapole	0.4591	0.2104	+HI2
Decapole	0.3091	0.2854	-HI2
Hexapole	0.2091	0.3354	-HI1
Dipole Corrector	0.8385E-01	0.4172	-HI3

coils on the outer rhombic prism produce hexapole and decapole fields, and also allow for a limited dipole field for correction purposes. The numerical example discussed here the coil cross section are arbitrarily chosen to be square with a peak current density of 100 A/mm^2. This analysis applies applies strictly to air core magnets. In practice an external iron shield would most likely be used and field analysis would be done numerically with a 3D numerical code such as ROXIE.

Due to symmetry in the design about the central axis, it is sufficient to describe only one quarter of the magnet. Figure 4 shows one quarter of the cross section. The positions and the direction of the coils in this quarter are specified in Table 1. All the coils have square cross section with thickness of 0.1 m.

In Table 1 the quantities $QI1, QI2, HI1, HI2, HI3$ are the magnitude of the currents. For any given configuration of the inner current coils, the currents $(QI1, QI2)$ can be used as parameters to obtain different quadrupole and octupole strength. Similarly, for any given configuration of the outer coils, the currents $(HI1, HI2)$ can be used as parameters to get the desired hexapole and decapole field strength.

From the construction point of view it is cost efficient if the same type of coils can be used. We use current coils of the same shape and size to generate the quadrupole and hexapole fields. Also, we use the same type of current coils for octupole and decapole fields. For an optimized final design these arbitrary constraints can be relaxed.

4.1. *2D design of the quadrupole magnet*

For a 2D design the magnet is considered to be infinitely long, thus avoiding any fringe field effects. This leads to purely transverse magnetic fields (2D fields). In this case a coil can be viewed as two current wires of infinite length and finite cross section which are separated by certain distance. The currents in these wires are equal in magnitude but are opposite in direction. We can use Ampere's law, given by equation (8), to compute the magnetic field of individual wires. The total magnetic field is then the superposition of the fields produced by these wires. Below we show the results for two special cases that produce pure quadrupole and hexapole fields.

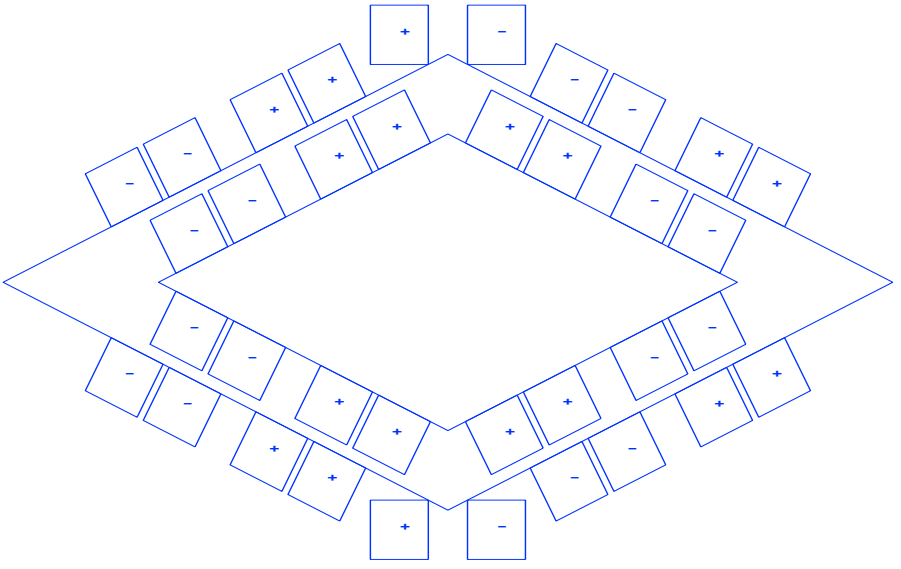

Fig. 3. The cross section view of the asymmetric-aperture multipole.

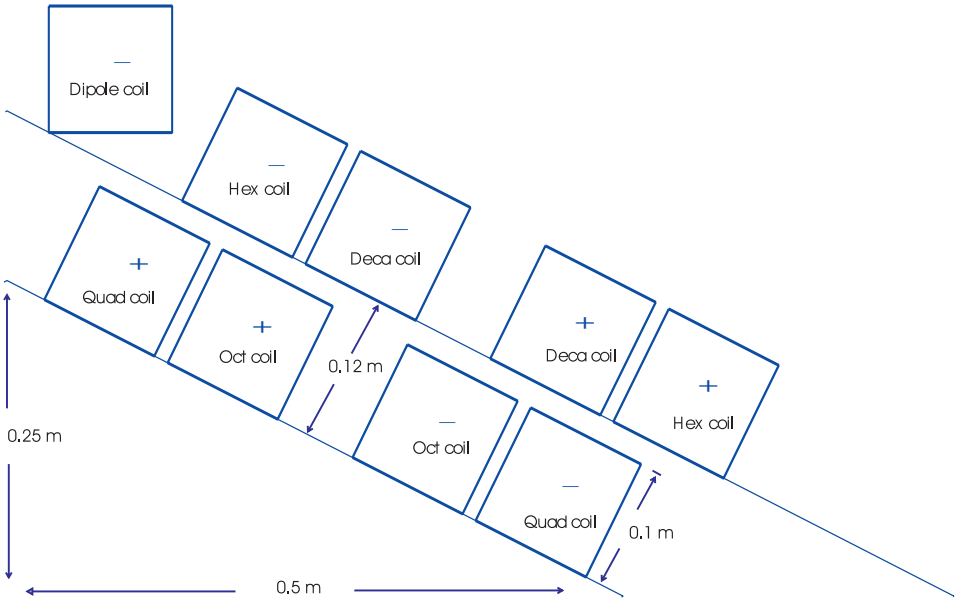

Fig. 4. The layout of the racetrack coils in the first quadrant.

Table 2. The amplitude of currents required for pure quadrupole and hexapole configurations.

Coil Description	Pure quadrupole configuration (million Amps)	Pure hexapole configuration (million Amps)
Inner Coils		
QI1	3.965	0
QI2	0.080	0
Outer Coils		
HI1	0	0.499
HI2	0	0.938
HI3	0	0.448

Current configuration required to generate a pure quadrupole component and hexapole component are given in Table 2. The fifth order Taylor expansion of the magnetic field about the point $(0.0, 0.0, 0.0)$, for each of these configurations is given in Table 3 and Table 4. The entries in the first and second column provide the Taylor expansion of x and y components of the magnetic field. Each row provides coefficient in the expansion whose exponent is described in column three. In the notation for the exponent the give expansion order with respect to x and y.

Table 3. The fifth order Taylor expansion of the magnetic field about the point (0.0,0.0,0.0) for the current configuration producing a pure quadrupole field.

Bx	By	xy
0.4440892098501E-15	0.000000000000	00
0.000000000000	46.09565826333	10
46.09565826333	0.000000000000	01
-0.7105427357601E-14	0.000000000000	20
0.1421085471520E-13	-0.1421085471520E-13	11
0.000000000000	0.1136868377216E-12	21
0.000000000000	-0.2842170943040E-13	12
0.7815970093361E-12	0.000000000000	03
-0.1421085471520E-13	0.000000000000	40
0.000000000000	0.5684341886081E-13	31
-0.2273736754432E-12	-0.1705302565824E-12	13
-0.4263256414561E-13	0.5684341886081E-13	04
0.000000000000	-3956.535097021	50
-19782.67548511	0.000000000000	41
0.000000000000	39565.35097021	32
39565.35097021	0.000000000000	23
0.000000000000	-19782.67548511	14
-3956.535097021	0.000000000000	05

Table 4. The fifth order Taylor expansion of the magnetic field about the point (0.0,0.0,0.0) for the current configuration producing a pure hexapole field.

Bx	By	xy
0.000000000000	-0.8604228440845E-15	00
-0.4718447854657E-15	0.000000000000	10
0.000000000000	-0.3885780586188E-15	01
0.000000000000	-18.24792017395	20
-36.49584034790	0.000000000000	11
0.000000000000	18.24792017395	02
-0.1776356839400E-14	0.000000000000	21
-0.1776356839400E-14	0.2664535259100E-14	12
0.2220446049250E-14	-0.4440892098501E-15	03
-0.1776356839400E-14	-0.3463895836830E-13	40
-0.2593480985524E-12	0.000000000000	31
0.000000000000	0.4547473508865E-12	22
0.1705302565824E-12	0.1953992523340E-13	13
0.4440892098501E-14	-0.4174438572591E-13	04
0.1776356839400E-14	0.8881784197001E-15	50
0.1421085471520E-13	0.1421085471520E-13	41
0.2842170943040E-13	0.3552713678801E-13	32
0.2131628207280E-13	0.000000000000	23
-0.5684341886081E-13	-0.7105427357601E-14	14
-0.4440892098501E-14	-0.3552713678801E-14	05

4.1.1. *Operational plots*

We now discuss the practical range of multipole field strength that can be achieved with this numerical example. We have mentioned that the currents $(QI1, QI2, HI1, HI2)$ can be used as parameters to get the desired quadrupole and higher order multipole strengths. However, there is a maximum limit on the current density that the superconducting coils can support. This puts a limit on the maximum quadrupole and other multipole field strength that can be achieved. Because of the fact that each multipole is achieved by superimposing the fields of several coils, this leads to operating diagrams showing achievable multipole settings.

To study this situation in detail, we now look at how the multipole strength depends on the currents. The matrix given in the equation (9) relates the multipole field strength at the horizontal half aperture to the currents in the coils for the specific case of a horizontal half aperture of 0.5 m and a vertical half aperture of 0.25 m. In the notation $B^y_{(1111)}$, the superscript denotes the "y" component of the magnetic field and the subscript (1111) gives the exponent in transport notation. Thus, $B^y_{(1111)}$ is the coefficient of x^4 in the Taylor expansion of the "y" component

of the magnetic field, or the decapole term in the expansion. The equations (10) provide relationships between the coefficients of other multipole terms in the Taylor expansion of the field to the principle multipole coefficients $B^y_{(11)}$, $B^y_{(111)}$ and $B^y_{(1111)}$.

$$\begin{bmatrix} B^y_0 \\ B^y_{(1)} \\ B^y_{(11)} \\ B^y_{(111)} \\ B^y_{(1111)} \\ B^y_{(11111)} \end{bmatrix} = \begin{bmatrix} 0 & 0 & -0.25137 & -0.04316 & +0.37029 \\ +5.76974 & +2.40063 & 0 & 0 & 0 \\ 0 & 0 & -3.89914 & -2.08907 & -1.45431 \\ -0.40613 & +15.44685 & 0 & 0 & 0 \\ 0 & 0 & +1.66569 & -2.32478 & +2.99743 \\ -31.32418 & -12.0759 & 0 & 0 & 0 \end{bmatrix} \cdot \begin{bmatrix} QI1 \\ QI2 \\ HI1 \\ HI2 \\ HI3 \end{bmatrix} \tag{9}$$

$$\begin{aligned} B^y_{(22)} &= -B^y_{(11)} \\ B^y_{(122)} &= -3B^y_{(111)} \\ -\frac{B^y_{(1122)}}{6} &= B^y_{(2222)} = B^y_{(1111)} \\ B^x_{(2)} &= B^y_{(1)} \\ B^x_{(12)} &= 2B^y_{(11)} \\ \frac{B^x_{(112)}}{3} &= -B^x_{(222)} = B^y_{(111)} \\ B^x_{(1112)} &= -B^x_{(1222)} = 4B^y_{(1111)} \end{aligned} \tag{10}$$

It can be seen from the coefficient of the two quadrupole coils (QI1 and QI2), given in the equation 9, that the inner pair (QI2) produces mainly an octupole term, whereas the outer pair (QI1) produces dominantly a quadrupole term. Then coefficients can be tuned in an optimized design by variation of the zero order coil geometry parameters.

4.1.2. *Operational plot for the quadrupole and the octupole fields*

From the equation (9) it can be seen that the quadrupole field strength and the octupole field strength are coupled via the currents $(QI1, QI2)$. We vary both of these current densities in the range $\left[-10^8, 10^8\right]$ A/m^2 and plot the resulting octupole field strength and the quadrupole field strength; the results are shown in Figure 5. This plot gives the possible values of the quadrupole and octupole strength that can be achieved with the configuration of the coils described in the section 4.

4.1.3. *Operational plot for the hexapole and decapole fields*

From the equation (9) it can also be seen that the dipole, hexapole and decapole field strength are coupled via the currents $(HI1, HI2, HI3)$. However, under normal

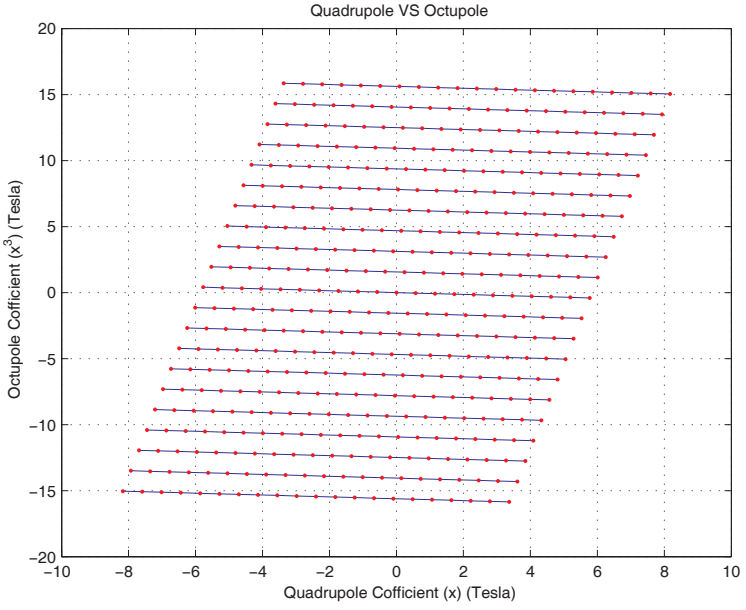

Fig. 5. The operational plot for the quadrupole and the octupole. The coefficients are computed at the horizontal half aperture.

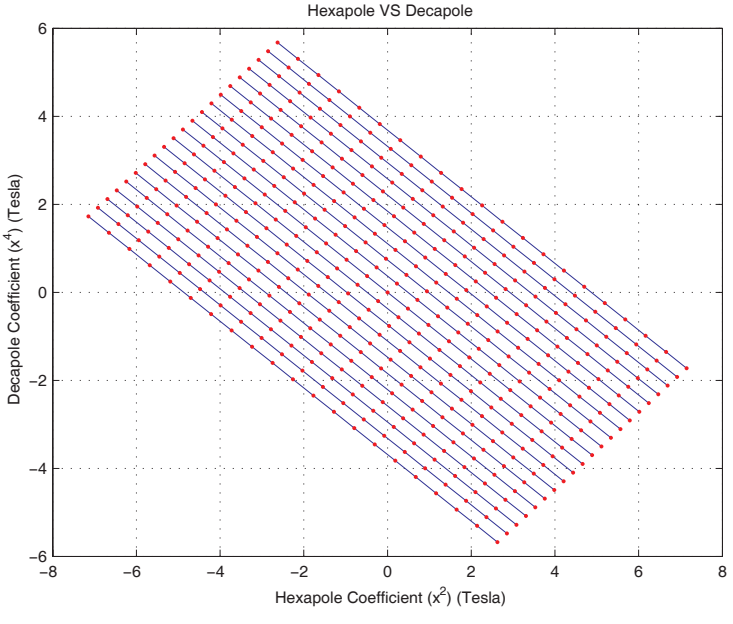

Fig. 6. The operational plot for the hexapole and the decapole. The coefficients are computed at the horizontal half aperture.

operation, we have a strict requirement of zero dipole field for this magnet. The dipole field is set zero by the proper choice of the current $HI3$. Once again we vary the current densities of all currents in the range $\left[-10^8, 10^8\right]$ A/m^2 and plot the decapole field strength versus the hexapole field strength; the results are shown in Figure 6. This plot gives the possible values of the hexapole and decapole strength that can be achieved with the configuration of the coils described in the section 4.

4.1.4. *Optimization of the operational region*

As mentioned above the details of terms in the matrix given in the equation (9) are influenced by the geometrical design parameters of the system. In order to optimize the operational region of the currents and the fields, we need to find the optimal geometric configuration of the coils described in the section 4, where the optimal design is defined as the one that would decouple the influence of the octupole coil current on the quadrupole component of the field and vice versa. And, at the same time maximize the coupling strength of the current in quadrupole coils on the quadrupole component of the field, and maximize the coupling strength of the current in octupole coils on the octupole component of the field. The same type of optimization is also required for the hexapole and decapole components of the field. Alternatively, for a specific optical system the zero order parameters can be chosen to emphasize operation in a necessary region of the 2D operating diagram. For example, this example is more effective in the upper right quadrant of Figure 5 than in the upper left quadrant.

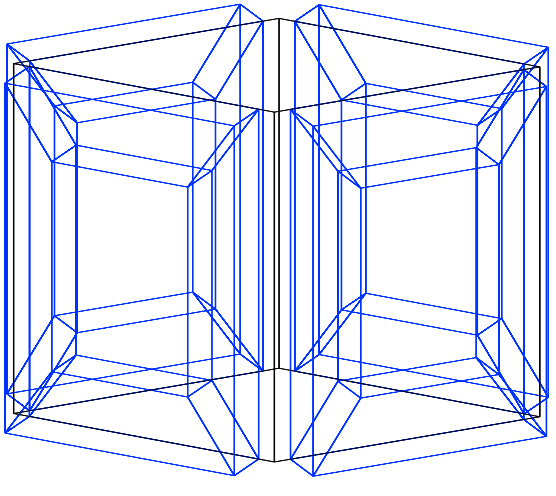

Fig. 7. The three dimensional layout of quadrupole coils.

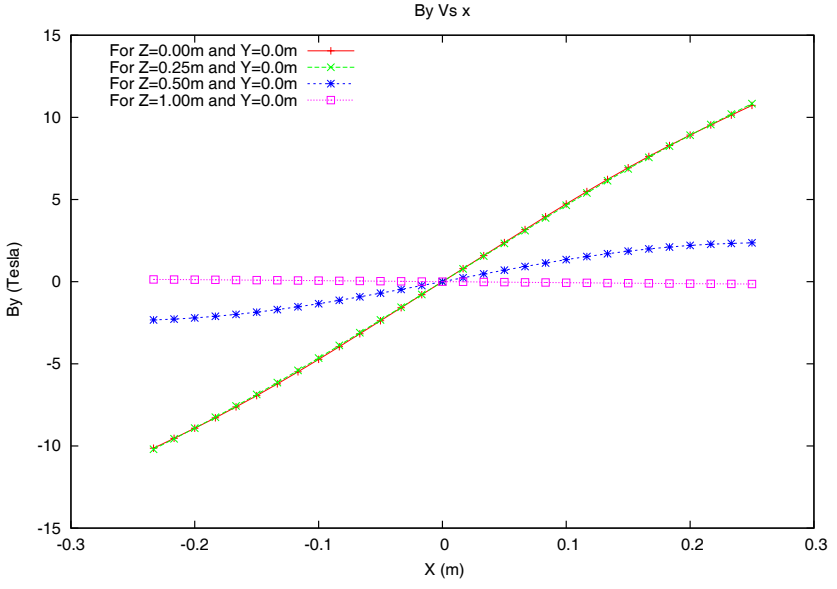

Fig. 8. The plot for B_y vs x on four planes.

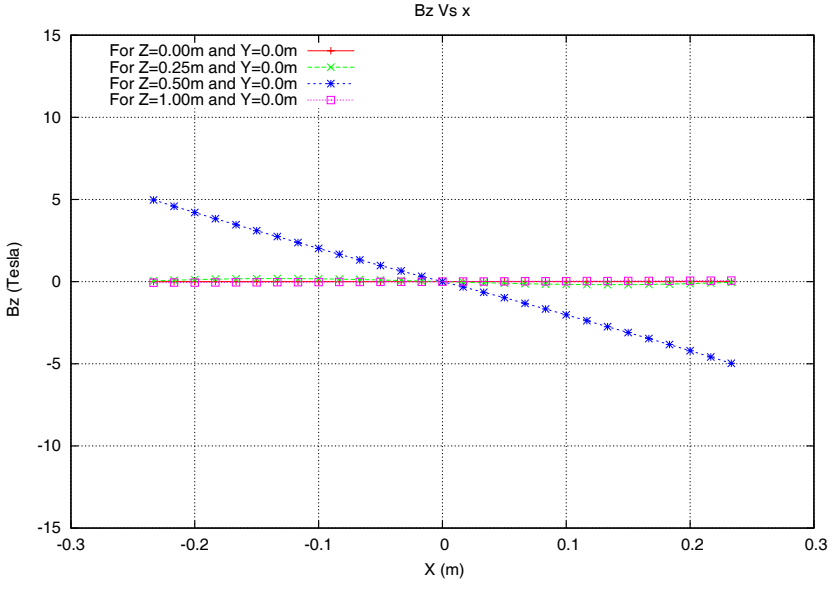

Fig. 9. The plot for B_z vs x on four planes.

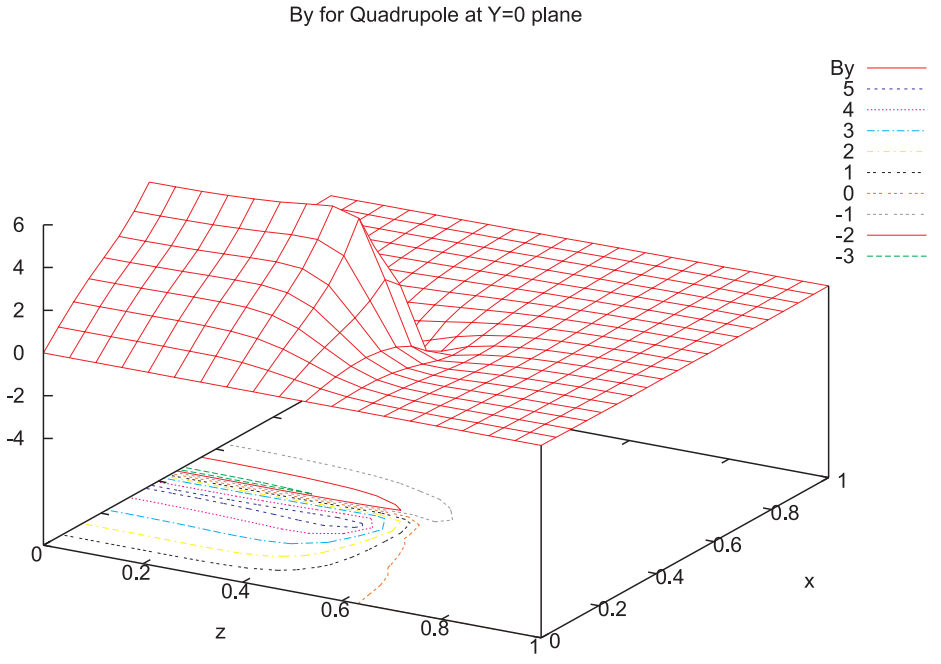

Fig. 10. The plot of Y component of magnetic field on the midplane, $y = 0\ m$. Only the magnetic field in the first quadrant is shown.

4.2. *3D design of the quadrupole and the fringe field analysis*

We consider a magnet of length 1 m, extending from $-0.5\ m \leq z \leq 0.5\ m$, and cross-section described by the design presented in the section 4.1. The 3D layout of the quadrupole with four current coils is shown in Figure 7. We compute the magnetic field generated by this coil configuration on four different planes, perpendicular to the central axis, located at the center $z = 0\ m$, quarter length $z = 0.25\ m$, the entrance of the magnet $z = 0.5\ m$ and out side the magnet $z = 1.0\ m$. The DA based tool to compute field for rectangular cross-section coils, described in section 3.1.3, is used to compute multipole expansion of the field. Figures 9 shows the x, y, z components of the magnetic field on these planes. Note that since the length of the magnet is large compared to the aperture of the magnet, the magnetic field in x, y at the center of the magnet is nearly identical to the magnetic field obtained by the 2D design in the section 4.1. In the z direction the magnitude of the magnetic field is of the order $\sim 10^{-16}$, which is zero for all practical purposes. As we start going away from the center, we observe deviation from the ideal behavior ($z = 0$). We see that at $z = 0.25\ m$ there is no significant deviation from ideal behavior in the x and y components of the magnetic field. In the z direction we notice that the magnetic field is nonzero. However, the magnitude is still small compared to the components B_x and B_y. At the entrance of the magnet we see that the magnetic

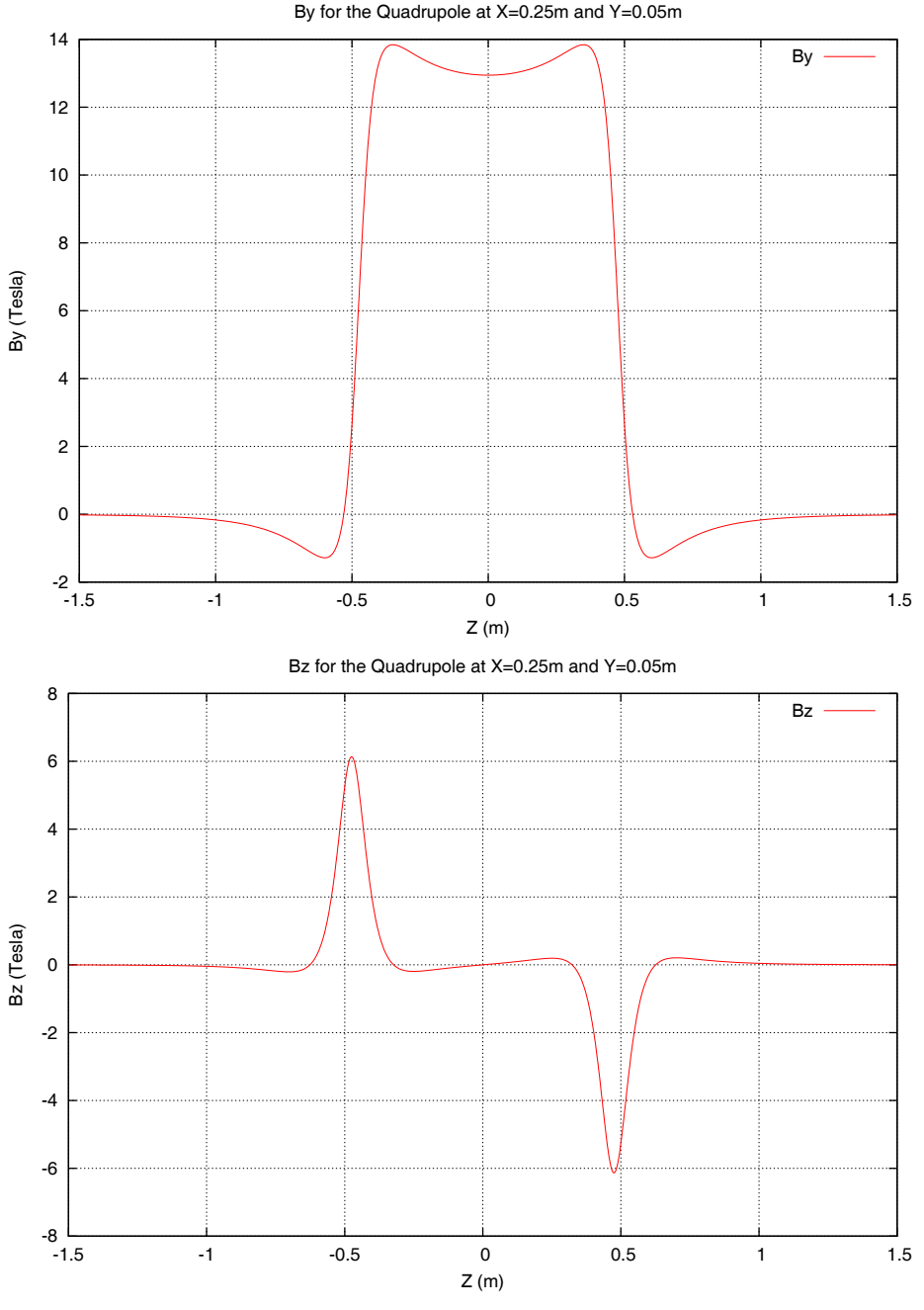

Fig. 11. Upper plot shows the y component and the lower plot shows the z component of magnetic field along the length of the magnet.

field in x, y falls by a factor of five. But the z component is almost three times as large as the field in x or y. On a plane 0.5 m away from the entrance of the magnet the overall field falls off significantly and its magnitude is $\sim 10^{-1}$ $tesla$.

The figure 10 shows the y-component of the magnetic field on the first quadrant of the magnet on the $y = 0$ m plane. The region stretches from the center of the magnet to $0.5m$ (half length of the magnet) outside the magnet in both x and z directions. Here the fringe field fall off in the region can be clearly seen. Finally, in figure 11 we show the plot of y and z component of the magnetic field along the length of the magnet.

5. Summary

A new concept for a superconducting quadrupole with elliptic acceptance and tunable high order multipoles is presented. The DA techniques have been utilized to design and optimize the magnet in a simple and efficient way. The DA based techniques have the advantage of providing the complete multipole decomposition of the field. From the detailed 3D analysis it is possible to construct the high order transfer map for the magnet. And thus provide means to perform the integrated simulations of both the design and optimization of accelerator magnets and also the beam optics using such magnets in the same code.

Acknowledgments

This work was supported by the U.S. Department of Energy, Office of Nuclear Physics, under Contract No. DE-AC02-06CH11357.

References

1. J.A. Nolen. Plans for an Advanced Exotic Beam facility in the U.S. In *Proceedings of the Ninth International Conference on Nucleus-Nucleus Collisions -(NN2006)*, volume 787, pages 84–93, 2007.
2. J.A. Nolen. Overview of the u.s. rare isotope accelerator proposal. *Nuclear Physics A*, 734:661–668, 2004.
3. Toshiyuki Kubo. In-flight ri beam separator bigrips at riken and elsewhere in japan. In *14th International Conference on Electromagnetic Isotope Separators and Techniques Related to their Applications*, volume 204, pages 97–113, 2003.
4. M. Berz. Differential algebraic description of beam dynamics to very high orders. *Particle Accelerators*, 24:109, 1989.
5. M. Berz. Differential algebra - a new tool. Technical Report LBL-27033, Lawrence Berkeley Laboratory, Berkeley, CA, 1989.
6. M. Berz. High-order description of accelerators using differential algebra and first applications to the SSC. In *Proceedings, Snowmass Summer Meeting*, Snowmass, Co, 1988.
7. M. Berz. Differential algebra - a new tool. In *Proceedings of the 1989 IEEE Particle Accelerator Conference*, page 1419. IEEE, 1989.
8. S. L. Manikonda and M. Berz. Multipole expansion solution of the Laplace equation using surface data. *Nuclear Instruments and Methods*, 258:175–183, 2006.

9. K. Makino. *Rigorous Analysis of Nonlinear Motion in Particle Accelerators*. PhD thesis, Michigan State University, East Lansing, Michigan, USA, 1998. Also MSUCL-1093.
10. J. Hoefkens. *Verified Methods for Differential Algebraic Equations*. PhD thesis, Michigan State University, East Lansing, Michigan, USA, 2001.
11. J. Hoefkens, M. Berz, and K. Makino. Efficient high-order methods for ODEs and DAEs. In G. Corliss, C. Faure, A. Griewank, L. Hascoët, and U. Naumann, editors, *Automatic Differentiation of Algorithms from Simulation to Optimization*, pages 343–348. Springer, 2002.
12. Y. F. Chang and G. F. Corliss. ATOMFT: Solving ODEs and DAEs using Taylor series. *Computers and Mathematics with Applications*, 28:209–233, 1994. see also http://www.mscs.mu.edu/ georgec/Pubs/journ.html#1994a.
13. S. Russenschuck. A computer program for the design of superconducting accelerator magnets. Technical Report CERN AT/95-39, CERN, 1995.
14. B. Erdélyi. *Symplectic Approximation of Hamiltonian Flows and Accurate Simulation of Fringe Field Effects*. PhD thesis, Michigan State University, East Lansing, Michigan, USA, 2001.
15. G. Sabbi. Magnetic field analysis of HGQ coil ends. Technical Report TD-97-040, Fermilab, 1997.
16. M. Berz and K. Makino. COSY INFINITY beam physics manual. Technical Report MSUHEP-60804, Department of Physics and Astronomy, Michigan State University, East Lansing, MI 48824, 2006. see also http://cosy.pa.msu.edu.
17. M. Berz and K. Makino. COSY INFINITY programmer's manual. Technical Report MSUHEP-60803, Department of Physics and Astronomy, Michigan State University, East Lansing, MI 48824, 2006. see also http://cosy.pa.msu.edu.
18. Manikonda Shashikant. *High order finite element methods to compute Taylor transfer maps*. PhD thesis, Michigan State University, East Lansing, Michigan, USA, 2006.

International Journal of Modern Physics A
Vol. 24, No. 5 (2009) 941–951

World Scientific
www.worldscientific.com

ON THE BEAM DYNAMICS OPTIMIZATION PROBLEM

ALEXANDER D. OVSYANNIKOV,* DMITRI A. OVSYANNIKOV and
MIKHAIL YU. BALABANOV

Applied Mathematics and Control Processes Department, Saint Petersburg State University, Universitetskii prospekt 35, Petergof, Saint Petersburg, 198504, Russia
**ovs74@mail.ru*

SHENG-LUEN CHUNG

Electrical Engineering Department, National Taiwan University of Science and Technology, Taipei, Taiwan
schlung@mail.ntust.edu.tw

The problem of dynamics optimization for charged particle beams in RFQ accelerators is discussed in this article. The problems of the optimization of particle capture into the acceleration mode are analyzed. Accelerators with low injection energies are considered.

Keywords: Beam dynamics; optimization; RFQ accelerator.

PACS numbers: 29.27.Bd, 02.60.Pn, 02.30.Yy

1. Introduction

Nowadays an evident progress is achieved in development of the modern theory of charged particle accelerators and in building of new accelerators for medical purposes, technology, etc. Nevertheless, the problems of optimization of particle dynamics are still actual. This is caused mainly by the desire to increase the outgoing beam quality, achieve lossless particle acceleration and develop new accelerators, e.g. compact accelerators with high acceleration rates.

The optimal control theory based models for beam dynamics optimization in linear accelerators were developed in [1, 2, 3, 4, 5]. Various mathematical models for longitudinal and transversal motion of charged particles were proposed in these works.

Here we analyze a mathematical optimization model for longitudinal motion of charged particles in RFQ accelerators, proposed in [6], and considered also in [7, 8, 5]. The charged particles motion in an equivalent traveling wave is studied. We consider and optimize the synchronous particle motion and the whole beam simultaneously.

The main advantage of the previously developed approach is an opportunity to analyze the longitudinal and transversal motions separately. It is possible to obtain

a guaranteed good transversal dynamics at the longitudinal dynamics optimization step by minimization of the defocusing factor, which is essential at the subsequent transversal motion optimization step. However, the capture of particles into the acceleration mode is optimized implicitly in this approach using some quality functionals.

In this paper we propose a new approach, where one can control the particles grouping process by choosing a special functional, which allows to estimate explicitly the particle capture into acceleration mode and to optimize it. The problem of maximization for particles acceleration rate is also considered. The proposed optimization method with new functionals is tested on certain problems of beam optimization.

2. Optimization Problem Statement

Let us consider the longitudinal motion equation for charged particles in a radio frequency quadrupole (RFQ) structure:[9]

$$\frac{d\beta}{d\tau} = \frac{4eUT}{W_0 L}\cos(Kz)\cos(\tilde{\omega}\tau + \varphi). \tag{1}$$

Here β and z are the reduced velocity and longitudinal coordinate of a particle in the beam, respectively, $\tau = ct$, where t is time, $\tilde{\omega} = 2\pi\omega/c$, ω is the operating frequency of the accelerating high-frequency field, c is the velocity of light, U is the intervane voltage, T is the acceleration efficiency, W_0 and e are the rest energy of the particle and its charge, $K = 2\pi/L$, where L is the period length, φ is the synchronous particle phase. Let us assume $L = \beta_s\lambda$, where λ is the wavelength for the accelerating field, and β_s is the reduced velocity of the synchronous particle.

The longitudinal particle motion in an equivalent traveling wave is described as follows:

$$\frac{d\beta}{d\tau} = \frac{2eUT}{W_0 L}\cos(\tilde{\omega}\tau - Kz + \varphi). \tag{2}$$

The equations of motion for the synchronous particle and deviation equation for an arbitrary particle with respect to the synchronous particle are

$$\frac{d\beta_s}{d\tau} = \frac{2eUT}{W_0 L}\cos(\varphi), \tag{3}$$

$$\frac{d^2(z_s - z)}{d\tau^2} = \frac{2eUT}{W_0 L}(\cos(\varphi) - \cos(K(z_s - z) + \varphi)). \tag{4}$$

Here z_s is the longitudinal coordinate of the synchronous particle. Introducing a new variable $\psi = K(z_s - z)$ we can rewrite (3) and (4) as follows:

$$\frac{d(L^2)}{d\tau^2} = \frac{4eUT\lambda}{W_0}\cos(\varphi), \tag{5}$$

$$\frac{d^2}{d\tau^2}\left(\frac{\psi L}{2\pi}\right) = \frac{2eUT}{W_0 L}(\cos(\varphi) - \cos(\psi + \varphi)). \tag{6}$$

Let us denote $\Lambda = \beta_s/\beta_0$, $\eta = UT/(UT)_{\max}$, $\Omega^2 = \dfrac{4\pi e(UT)_{\max}}{W_0 L_0^2}$. Here β_0 is the initial reduced velocity of the synchronous particle, $L_0 = \beta_0\lambda$, $(UT)_{\max}$ is the maximal admissible value of the U times T product. We also introduce $s = \Omega\tau$ as another new variable. In terms of this new variable the equations (5) and (6) are

$$(\Lambda^2)' = 2k\eta\cos(\varphi), \tag{7}$$

$$\psi'' + 2\frac{\Lambda'}{\Lambda}\psi' + \frac{\Lambda''}{\Lambda}\psi - \frac{\eta}{\Lambda^2}(\cos\varphi - \cos(\varphi+\psi)) = 0. \tag{8}$$

where the prime symbol denotes a derivative with respect to the new independent variable s, and $k = \Omega/\tilde{\omega}$.

Eq. (7) describes the synchronous particle dynamics. Eq. (8) under different initial conditions describes the particle beam behavior in terms of the deviation from the synchronous particle motion. Eqs. (7), (8) are considered simultaneously over a certain interval $s \in [0, T_s]$. Here the laws of variation along the accelerator for $\eta(s)$ and $\varphi(s)$ have to be chosen taking into account the required beam properties and accelerator parameters.

We consider guaranteeing maximal capture of particles into the acceleration mode and maximization of the acceleration rate to be the main aims of an RFQ structure optimization. The following values are used for quality estimations and structure and beam dynamics analysis.

Introduce the parameter p_c allowing us to validate that the particle is inside the region bounded by the beam separatrix in the (ψ, ψ') plane, which can be considered as the condition of particle capture into the acceleration mode:

$$p_c(\psi, \psi') = \frac{(\psi')^2}{2} + V(\psi). \tag{9}$$

Here the function $V(\psi)$ is defined as

$$V(\psi) = -\frac{\eta}{\Lambda^2}(\psi\cos(\varphi) - \sin(\psi+\varphi)). \tag{10}$$

Hence, the separatrix equation is:

$$p_c(\psi, \psi') = V_c, \tag{11}$$

where

$$V_c = V(-2\varphi) = \frac{\eta}{\Lambda^2}(2\varphi\cos(\varphi) - \sin(\varphi)). \tag{12}$$

The condition of particle capture into the acceleration mode may be stated as:

$$p_c(\psi, \psi') < V_c. \tag{13}$$

Let the parameter p_l denote the length estimate for the structure being optimized:

$$p_l = \beta_0\lambda\frac{1}{2\pi k}\int_0^{T_s}\Lambda(s)ds. \tag{14}$$

Let us also introduce $p_E = (\beta_s^2 - \beta_0^2)/\beta_0^2 \cong (W_k^s - W_k^0)/W_k^0$ as a characteristic of kinetic energy increment for the synchronous particle relative to its value at the entrance of the accelerator in the non-relativistic case:

$$p_E = \Lambda^2 - 1. \tag{15}$$

The parameters $p_\beta = (\beta - \beta_s)/\beta_s$ and $p_w = (W_k - W_k^s)/W_k^s$ are the velocity and energy deviations respectively for a particle in the beam with respect to the synchronous particle:

$$p_\beta = -k\left(\psi' + \psi\frac{\Lambda'}{\Lambda}\right), \quad p_w = (p_\beta + 1)^2 - 1. \tag{16}$$

We can now formulate the longitudinal motion optimization problem in the following way. Find the laws of variation for the functions $\eta(s)$ and $\varphi(s)$ such that the maximal (preassigned) particles capture into the acceleration mode and attaining the assigned energy values are guaranteed with a maximal acceleration rate. The restrictions by the defocusing factor must be fulfilled:

$$p_{def} = \frac{2k^2\eta|\sin(\varphi)|}{\Lambda^2}. \tag{17}$$

Taking into account the defocusing factor restrictions at the longitudinal motion optimization step provides us with reasonable parameters of transversal motion and successful choice of structure parameters at the transversal motion optimization step.[5,8]

3. Solution Method

Consider in a formal way the problem stated above. Let us examine the following equations:

$$x' = f(s, x, u), \qquad x(0) = x_0, \tag{18}$$

$$y' = F(s, x, y, u), \quad y(0) = y_0 \in M_0. \tag{19}$$

Here $x = (x_1, x_2, x_3)^*$, $y = (y_1, y_2)^*$, $u = (u_1, u_2)^*$, the set $M_0 = \{y| -\pi_1 \le y_1 \le \pi_2, \theta_1 \le y_2 \le \theta_2\}$ is a set of assigned initial values for the beam trajectories, $-\pi \le -\pi_1 < \pi_2 \le \pi$, $s \in [0, T_s]$, T_s has a fixed value.

We say that the subsystem (18) describes the program motion dynamics, while the subsystem (19) describes the dynamics of the beam of trajectories or the dynamics of motions perturbed at initial values.

The equations (18), (19) actually are the former equations (7), (8) written in the normal form using new notation:

$$x_1 = \Lambda^2,\ x_2 = \eta,\ x_3 = \varphi, \quad y_1 = \psi,\ y_2 = \psi', \quad u_1 = \eta'(s),\ u_2 = \varphi'(s). \tag{20}$$

$$x_1' = 2\xi, \quad x_2' = u_1, \quad x_3' = u_2, \tag{21}$$

$$y_1' = y_2, \quad y_2' = \frac{x_2(\cos(x_3) - \cos(y_1 + x_3)) - 2\xi y_2 - (\xi' - \xi^2/x_1)y_1}{x_1}. \tag{22}$$

Here $\xi = kx_2\cos(x_3)$, $\xi' = k(u_1\cos(x_3) - u_2x_2\sin(x_3))$. As a control function we consider a vector function $u(s)$, belonging to the class D of piecewise continuous functions over $[0, T_s]$.

Simultaneously with the equations (18), (19) let us consider the equation for variation of the particles distribution density $\rho(s, y)$ along the trajectories of (19):

$$\begin{aligned} \rho' &= -\rho\,\mathrm{d}iv_y F(s, x, y, u), \\ \rho(0, y(0)) &= \rho_0(y_0), \end{aligned} \tag{23}$$

where $\rho_0(y_0)$ is the particle distribution density on the set M_0. For the case under consideration, $\mathrm{d}iv_y F$ in Eq. (23) is equal to

$$\mathrm{d}iv_y F = -2\xi/x_1. \tag{24}$$

Let us define the penalty function $h(p, a)$ to be used for the construction of the quality functionals:

$$h(p, a) = \begin{cases} (p - a)^2, & p > a \\ 0, & p \le a. \end{cases} \tag{25}$$

Let us consider the following functionals for the evaluation of the dynamical process. The functional $J_1(u)$ is an integral estimate of the deviation of particles in the beam from the area captured into acceleration mode (taking into account the particle distribution density along the trajectories):

$$J_1(u) = \int_0^{T_s} \int_{M_{s,u}} h(p_c, V_c)\rho(s, y_s)dy_s\,ds. \tag{26}$$

Here the set $M_{s,u}$ is a cross-section of the beam of trajectories of the subsystem (19) at the moment s. The trajectories start from the set M_0 under a control $u(s)$ and a corresponding program motion $x(s)$:

$$M_{s,u} = \{y_s | y_s = y(s, y_0, x(s), u(s)), y_0 \in M_0, x(0) = x_0\}. \tag{27}$$

Using the new notation of (20), we have $p_c = p_c(x(s), y_s)$, $V_c = V_c(x(s))$.

The functional $J_2(u)$ estimates the length of the accelerating structure:

$$J_2(u) = p_l = \beta_0\lambda\frac{1}{2\pi k}\int_0^{T_s} \sqrt{x_1(s)}\,ds. \tag{28}$$

The terminal functional J_3 estimates the deviation of the kinetic energy increase for the synchronous particle from the desired value a_E at the end of the accelerator channel:

$$J_3(u) = (p_E(x_1(T_s)) - a_E)^2. \tag{29}$$

The functional $J_4(u)$ provides an integral estimate over the beam for particle energy deviations from the energy of the synchronous particle at the exit of the accelerator, when they overcome a certain acceptable value a_w:

$$J_4(u) = \int\limits_{M_{T_s,u}} h(p_w^2, a_w)\rho(T_s, y_{T_s})dy_{T_s}. \tag{30}$$

Here we consider $p_w = p_w(x(T_s), y_{T_s})$ using the proposed notation.

The integral functional $J_5(u)$ estimates the defocusing factor p_{def} deviation from a given value a_d in order to minimize its influence on the transversal motion:

$$J_5(u) = \int\limits_0^{T_s} h(p_{def}, a_d)ds, \tag{31}$$

$p_{def} = p_{def}(x(s))$.

We consider a weighted sum of the above functionals as the main functional to be optimized:

$$J(u) = \sum_{i=1}^{5} c_i J_i(u). \tag{32}$$

To minimize the functional (32) one can use various numerical optimization methods. Hereafter we will examine an analytical representation of the variation of such type of functionals. The functional (32) may be represented in a generalized form as follows:

$$J(u) = \int\limits_0^{T_s} \left(\varphi_1(s, x(s), u(s)) + \int\limits_{M_{s,u}} \varphi_2(s, x(s), y_s, u(s))\rho(s, y_s)dy_s\right)ds$$
$$+ g_1(x(T_s)) + \int\limits_{M_{T_s,u}} g_2(y_{T_s})\rho(T_s, y_{T_s})dy_{T_s}, \tag{33}$$

Let us consider the auxiliary functions $\chi(s)$, $\mu(s, y_s)$, which satisfy the following equations along the trajectories of (18), (19), (23):

$$\frac{d\chi}{ds} = -\left(\frac{\partial f}{\partial x}\right)^* \chi + \left(\frac{\partial \varphi_1}{\partial x}\right)^* + \int\limits_{M_{s,u}} \left(\left(\frac{\partial \varphi_2}{\partial x}\right)^* - \left(\frac{\partial F}{\partial x}\right)^* \mu\right) \rho\, dy_s, \tag{34}$$

$$\frac{d\mu}{ds} = -\left(\frac{\partial F}{\partial y}\right)^* \mu + \left(\frac{\partial \varphi_2}{\partial y}\right)^*, \tag{35}$$

with the conditions on the right end:

$$\chi(T_s) = -\left(\frac{\partial g_1(x(T_s))}{\partial x}\right)^*, \tag{36}$$

$$\mu(T_s) = -\left(\frac{\partial g_2(y_{T_s})}{\partial y}\right)^*. \tag{37}$$

Let us introduce the function H_1 with the arguments s, x, u and χ such that

$$H_1(s, x, \chi, u) = \chi^* \cdot f(s, x, u) - \varphi_1(s, x, u), \tag{38}$$

and the function H_2 with the arguments s, x, y, u, μ:

$$H_2(s, x, y, \mu, u) = \mu^* \cdot F(s, x, y, u) - \varphi_2(s, x, y, u). \tag{39}$$

Thus the gradient of the functional (33) may be expressed in the following form:

$$grad\, J(u) = -\partial H_1/\partial u - \int\limits_{M_{s,u}} (\partial H_2/\partial u)\rho\, dy_s, \tag{40}$$

where x, y, ρ are the solutions of the system (18), (19), (23) which correspond the control $u = u(s)$; the auxiliary functions χ, μ, satisfy the equations (34), (35) with the conditions (36), (37) on the right end, respectively.

4. Numerical Optimization

Using the analytical representation (40) for the gradient of the functional (33) we developed a technique for the optimization of the proposed functional (32). This technique was approved by longitudinal beam motion optimization in a proton RFQ accelerator. The developed optimization process consists of several steps. The optimization procedure based on the idea of the plan construction for the search of controls using gradient descent methods. The optimization technique includes study and optimization of the accelerator by parts: particle pre-grouping, grouping and acceleration parts are considered with corresponding priority functionals for different optimization steps. At the first step we form initial approximations for controls by means of consecutive choice, combination and variation of controls using the genetic algorithm[10,11] (with different modifications of data coding). The most effective for RFQ structures is the derivative coding method, which is a result of the supposed monotonicity of controls. At the second and third steps the main task is the beam grouping, when almost 100% of particles are captured into acceleration mode. For these steps changes of the defocusing factor along the accelerating structure are essential. At the fourth step we solve the problem of final beam production with a prescribed energy value and a maximal acceleration rate. Then we consider the optimization problem for the whole accelerating structure to obtain a minimal length accelerator for a given output energy value and minimal losses. The constraints for the defocusing factor should be considered at all times. The effectiveness of the optimization is provided by using different weight ratios, i.e. the change of functionals priority at different optimization steps. It is noteworthy that the weight ratio correction is carried out using the previously obtained results analysis to determine which weights influence the system more, and where are their effective areas.

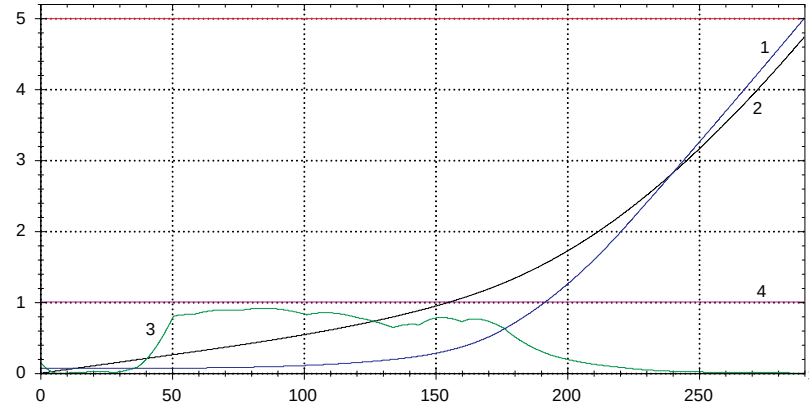

Figure 1. Parameters of program motion (1—variation of energy (MeV); 2—variation of length of structure (m); 3—variation of defocusing factor (×100); 4—upper bound of defocusing factor (×100)).

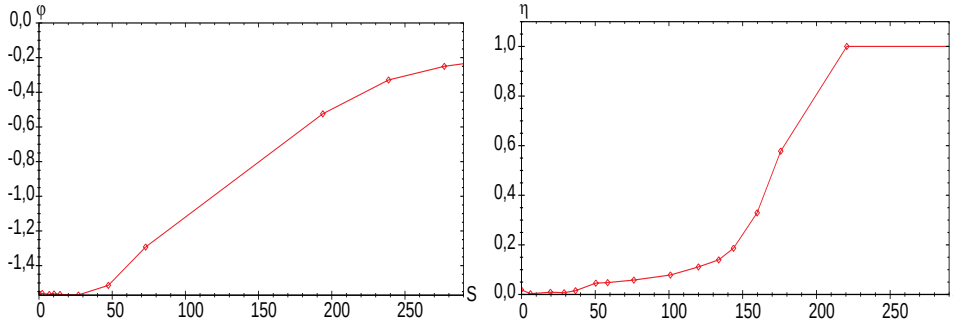

(a) variation of synchronous phase

(b) variation of acceleration intensity

Figure 2. Control functions.

Optimization was carried out for the proton accelerator at 352 MHz frequency. The following limitations were taken into account: $(UT)_{\max} \leq 45\,kV$, $p_{def} \leq 0.01$. One of the aims of this study was the construction of the accelerator with smaller injection energy. From our research, it is possible to obtain a structure with injection energy values between 50 and 80 keV, and almost 100% particles captured into the acceleration mode. For the output energy of 3 to 5 MeV this gives the acceleration rate of more than 1 MeV/m. Fig. 1–3 correspond to the accelerator with the injection energy value of 70 keV, the output energy of 5 MeV, and the length of 4.7 m; for Fig. 4–6 the injection energy is 60 keV, the output energy is 5 MeV, and the length is 4.5 m. The properties of program motions, controls, and phase space portraits of beams in separatrices are illustrated.

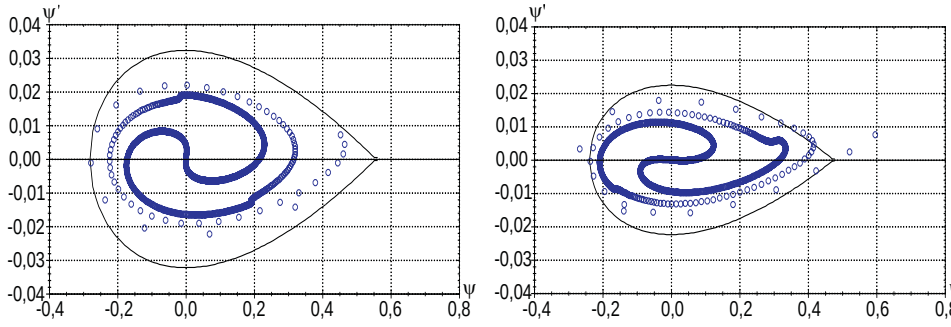

(a) energy is 4 MeV at length of structure 3,8 m

(b) energy is 5 MeV at length of structure 4,7 m

Figure 3. Phase portrait of beam in (ψ, ψ') plane and separatrix.

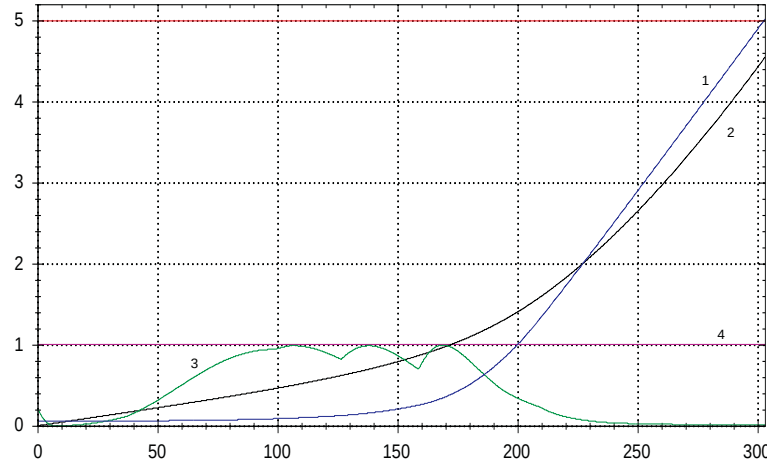

Figure 4. Parameters of program motion (1—variation of energy (MeV); 2—variation of length of structure (m); 3—variation of defocusing factor (×100); 4—upper bound of defocusing factor (×100)).

5. Conclusion

The proposed technique and new functionals allow us to analyze the problem of capturing the particles with decreased injection energies into the acceleration mode and to estimate the possibility of compact RFQ accelerators. The effectiveness of the approach of separate studies for longitudinal and transversal motions was shown in [5, 6, 7, 8]. The calculations that were carried out confirmed the advantages of this approach. The proposed technique may be generalized to the case of Coulomb's repulsion between the particles. It may be useful to additionally investigate a functional of particle phase grouping monotony at the step of longitudinal motion analysis, as it was proposed in [5].

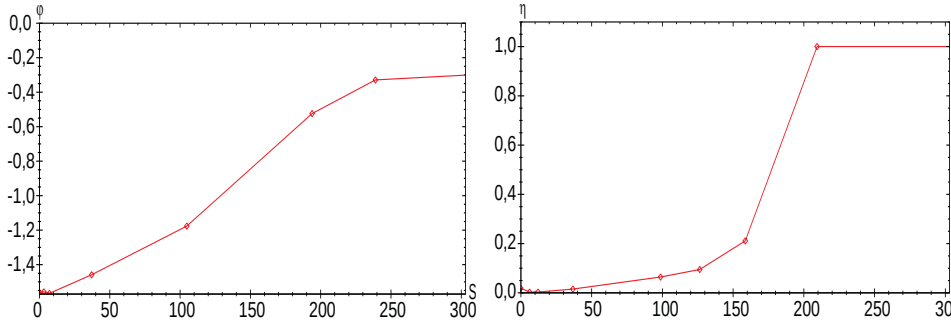

(a) variation of synchronous phase

(b) variation of acceleration intensity

Figure 5. Control functions.

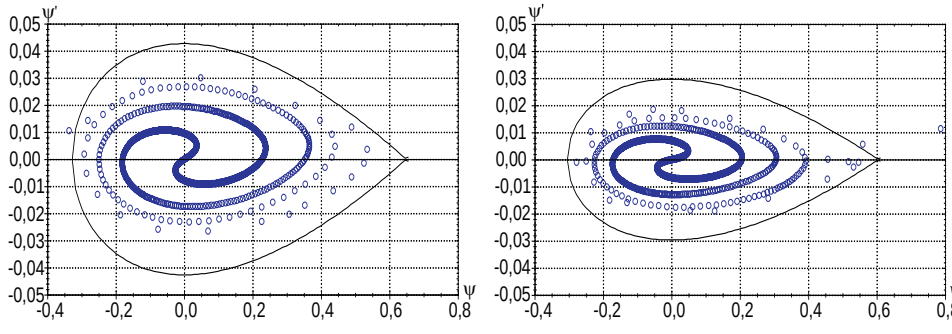

(a) energy is 3 MeV at length of structure 2,9 m

(b) energy is 5 MeV at length of structure 4,5 m

Figure 6. Phase portrait of beam in (ψ, ψ') plane and separatrix.

Acknowledgments

The work is done under support of the National Taiwan University of Science and Technology and Saint-Petersburg State University Joint Research Project No. RP07-05.

References

1. O. I. Drivotin, A. E. Loukianova, D. A. Ovsyannikov, Yu. N. Garvish, Yu. A. Svistunov, and Vorogushin M. F. The choice of acceleration structure for pet-system. In *Proceedings of European Particle Accelerator Conf., Vol. 1*, pages 783–785, Barselona, Spain, 1996.
2. D. A. Ovsyannikov. *Modeling and Optimization of Charged Particle Beam Dynamics*. Leningrad State University, Leningrad, 1990.

3. D. A. Ovsyannikov. Mathematical methods of optimization of charged partical beams dynamics. In *Proceedings of European Particle Accelerator Conf., Vol. 2*, pages 1382–1384, Barselona, Spain, 1996.
4. D. A. Ovsyannikov. Modeling and optimization problems of charged particle beams dynamics. In *Proceedings of the 4th European Control Conference*, pages 390–394, Brussels, Belgium, 1997.
5. D. A. Ovsyannikov, A. D. Ovsyannikov, Yu. A. Svistunov, A. P. Durkin, and M. F. Vorogushin. Modeling and optimization problems of charged particle beams dynamics. In *Nuclear Instruments and Methods in Physics Research, section A 558*, pages 11–19, 2006.
6. B. I. Bondarev, A. P. Durkin, and A. D. Ovsyannikov. New mathematical optimization models for rfq structures. In *Proceedings of the 1999 Particle Accelerator Conference*, pages 2808–2810, New York, 1999.
7. B. I. Bondarev, A. P. Durkin, S. Vinogradov, D. A. Ovsyannikov, and A. D. Ovsyannikov. Rfq optimization: Method and codes. In *Proc. of the 6th International Computational Accelerator Physics Conference, September 11–14*, Darmstadt, Germany, 2000.
8. A. D. Ovsyannikov. New approach to beam dynamics optimization problem. In *Proc. of the 6th International Computational Accelerator Physics Conference, September 11–14*, Darmstadt, Germany, 2000.
9. I. M. Kapchinsky and V. A. Teplyakov. Linear ion accelerator with spartially homogeneous strong focusing. In *Prib. Tekh., Eksp. N2*, 1970.
10. Nicholas Freitag McPhee Riccardo Poli, William B. Langdon. *A Field Guide to Genetic Programming*. ISBN 978-1-4092-0073-4. 2008.
11. Simon Haykin. *Neural Networks: A Comprehensive Foundation*. ISBN 0132733501. Pearson Education, 2nd edition, 1998.

International Journal of Modern Physics A
Vol. 24, No. 5 (2009) 952–958

World Scientific
www.worldscientific.com

OPTIMIZATION OF A RADIAL MATCHING SECTION

ALEXANDER D. OVSYANNIKOV and DMITRI A. OVSYANNIKOV*

Faculty of Applied Mathematics and Control Processes,
Saint Petersburg State University, Saint Petersburg, Russia
**dovs45@mail.ru*

SHENG-LUEN CHUNG

Electrical Engineering Department, National Taiwan University of Science and Technology,
Taipei, Taiwan
schlung@mail.ntust.edu.tw

Optimization approach to define geometry (parameters) of the radial matching section in an RFQ accelerator is suggested. This approach gives wider opportunities for the design of the radial matching section because it does not have certain prescribed laws of variation of focusing strength along the section.

Keywords: Optimization; matching section; RFQ.

PACS numbers: 29.27.Bd, 02.60.Pn, 02.30.Yy

1. Introduction

Acceptance at the entrance of the RFQ accelerator, as it is known, depends on the time of arrival and rotates with the frequency of the RF field. On the other hand, the input beam has constant emittance, not changing in time. Thus, there is a problem of the beam matching to the accelerating RFQ channel. It was suggested in [1] to provide the transverse matching of the beam with the accelerating channel using radial matching sections, and particular laws of change of the focusing strength in these sections have been considered. Later, this problem was addressed by different authors.[2,3,4] In this paper the new approach for the solution of the problem is suggested. Parameters of the radial matching section are defined by solving the optimization problem described in the article.

2. Problem Statement

For the radial matching section of the accelerator, charged particle dynamics in the x, y plane which is perpendicular to the longitudinal axis in the case of microcanon-

ical charge distribution can be described by the following equations:[5]

$$\frac{d^2x}{d\tau^2} = \frac{eU}{W_0a^2}\cos(\theta\tau+\varphi_0)x - \frac{eI}{2W_0\pi\varepsilon_0\nu r_x r_y}\left(1-\frac{r_x-r_y}{r_x+r_y}\right)x = Q_x(\tau,\varphi_0,r_x,r_y)x, \quad (1)$$

$$\frac{d^2y}{d\tau^2} = -\frac{eU}{W_0a^2}\cos(\theta\tau+\varphi_0)y - \frac{eI}{2W_0\pi\varepsilon_0\nu r_x r_y}\left(1+\frac{r_x-r_y}{r_x+r_y}\right)y = Q_y(\tau,\varphi_0,r_x,r_y)y, \quad (2)$$

where $\tau = ct$, $\theta = 2\pi\omega/c$, U is the intervane voltage, W_0 is the charged particle rest energy, ω is the accelerating field frequency, φ_0 is the initial phase, c is the velocity of light, a is the radius of the channel, $\nu = \dot{z}$ is the longitudinal velocity of a particle which is constant along the matching section, r_x and r_y are the normalized beam envelopes, I is the beam current.

Eqs. (1) and (2) can be transformed into the system of equations

$$\frac{d\xi}{d\tau} = A_x\xi, \quad \frac{d\eta}{d\tau} = A_y\eta, \quad (3)$$

where $\xi = (\xi_1,\xi_2)$, $\xi_1 = x$, $\xi_2 = \dfrac{dx}{d\tau}$, $\eta = (\eta_1,\eta_2)$, $\eta_1 = y$, $\eta_2 = \dfrac{dy}{d\tau}$, and the matrices A_x and A_y have the form

$$A_x = \begin{pmatrix} 0 & 1 \\ Q_x & 0 \end{pmatrix}, \quad A_y = \begin{pmatrix} 0 & 1 \\ Q_y & 0 \end{pmatrix}. \quad (4)$$

Let the set of conditions for system (3) at some instant τ fill the ellipses

$$\xi^* G_x \xi \le 1, \quad \eta^* G_y \eta \le 1, \quad (5)$$

in the planes $\left(x, \dfrac{dx}{d\tau}\right)$ and $\left(y, \dfrac{dy}{d\tau}\right)$ correspondingly, and $\det G_x = \det G_y = 1$. Then, the matrices G_x and G_y satisfy the following system of matrix equations

$$\frac{d}{d\tau}G_x = -A_x^* G_x - G_x A_x, \quad \frac{d}{d\tau}G_y = -A_y^* G_y - G_y A_y. \quad (6)$$

The system of equations (6) should be solved on the interval from the entrance into the regular part of the accelerator to the entrance into the radial matching section, i.e. from $\tau = T$ to $\tau = 0$. Initial conditions for the system (6) are the matrices of ellipses defining acceptances of the regular part of the accelerator, depending on an initial phase φ_0:

$$G_x(T,\varphi_0) = G_{x,T}(\varphi_0), \quad G_y(T,\varphi_0) = G_{y,T}(\varphi_0). \quad (7)$$

The optimization problem for the radial matching section is to find a function $a(\tau)$, i.e. law of the radius change along the matching sections, providing under the conditions (7) the maximum possible overlapping of families of ellipses at the entrance of the radial matching section.

Let us consider the functions

$$\Phi_x(\varphi_0) = \mathrm{Sp}(G_x(0,\varphi_0) - B_x)^2 \quad \text{and} \quad \Phi_y(\varphi_0) = \mathrm{Sp}(G_y(0,\varphi_0) - B_y)^2, \tag{8}$$

where B_x, B_y are given matrices, Sp is the trace of the corresponding matrix. Functions $\Phi_x(\varphi_0)$ and $\Phi_y(\varphi_0)$ characterize deviations of ellipses G_x and G_y at $\tau = 0$ from the given ellipses B_x and B_y, accordingly.

Introduce the functional

$$J(a) = c_1 \int_{\varphi_1}^{\varphi_2} \Phi_x(\varphi_0) d\varphi_0 + c_2 \int_{\varphi_1}^{\varphi_2} \Phi_y(\varphi_0) d\varphi_0, \tag{9}$$

estimating the degree of mutual overlapping of ellipses corresponding to various initial phases at the entrance of the matching section. Here φ_1 and φ_2 are limits of variation of initial phase φ_0; c_1, c_2 are some positive constants.

3. Solution Method

Let us represent elements of the matrices $G_x(\tau,\varphi_0)$ and $G_y(\tau,\varphi_0)$ as follows

$$G_x = \begin{pmatrix} \frac{1+\alpha_x^2}{\nu_x} & \alpha_x \\ \alpha_x & \nu_x \end{pmatrix}; \quad G_y = \begin{pmatrix} \frac{1+\alpha_y^2}{\nu_y} & \alpha_y \\ \alpha_y & \nu_y \end{pmatrix}, \tag{10}$$

where $\nu_x = r_x^2$, $\nu_y = r_y^2$. Notice that values α_x, ν_x, and α_y, ν_y are the so-called Courant-Snyder or Twiss parameters.[6] Now the equations (6) can be written in the following form

$$\begin{array}{ll} \frac{d\nu_x}{d\tau} = -2\alpha_x, & \frac{d\alpha_x}{d\tau} = -Q_x(\tau,\varphi_0,r_x,r_y)\nu_x - \frac{1+\alpha_x^2}{\nu_x} \\ \frac{d\nu_y}{d\tau} = -2\alpha_y, & \frac{d\alpha_y}{d\tau} = -Q_y(\tau,\varphi_0,r_x,r_y)\nu_y - \frac{1+\alpha_y^2}{\nu_y} \end{array} \tag{11}$$

Rewrite the system (11) as a system of the equations of the form

$$\frac{d\sigma}{d\tau} = f(t,\sigma,\varphi,u), \tag{12}$$

with the corresponding conditions on the right end

$$\sigma(T) = \sigma(T,\varphi), \quad \varphi \in [\varphi_1,\varphi_2]. \tag{13}$$

Here $\sigma = (\sigma_1,\sigma_2,\sigma_3,\sigma_4)$, $\sigma_1 = \alpha_x$, $\sigma_2 = \nu_x$, $\sigma_3 = \alpha_y$, $\sigma_4 = \nu_y$; $u = a(\tau)$ is a control function; initial phase value $\varphi = \varphi_0$ belongs to some interval. The functional (9) can be written in the form

$$J(u) = \int_{\varphi_1}^{\varphi_2} g(\sigma(0,\varphi)) d\varphi. \tag{14}$$

Note that the optimization of the functional (14) over the control functions $u = a(\tau)$ can be viewed as a nonstandard problem of the optimal control theory.

We introduce a vector-function $\psi(\tau, \varphi)$ satisfying on the trajectories of the system (12) the following differential equations

$$\frac{d\psi(\tau,\varphi)}{d\tau} = -\left(\frac{\partial f(\tau, \sigma(\tau,\varphi), \varphi, u)}{\partial \tau}\right)^* \psi, \tag{15}$$

with the initial conditions

$$\psi(0,\varphi) = \left(\frac{\partial g(\sigma(0,\varphi))}{\partial \sigma}\right)^*, \quad \varphi \in [\varphi_1, \varphi_2]. \tag{16}$$

Using the increment method (see [7, 8]) and the vector-function $\psi(\tau, \varphi)$the variation of the functional (14) can be represented as

$$\delta J(u, \Delta u) = -\int_0^T (p(\tau))^* \Delta u(\tau) d\tau. \tag{17}$$

Here the vector-function $p(\tau)$ is expressed as follows

$$p(\tau) = \int_{\varphi_1}^{\varphi_2} \left(\frac{\partial f(\tau, \sigma(\tau,\varphi), \varphi, u)}{\partial u}\right)^* \psi(\tau,\varphi) d\varphi, \tag{18}$$

where the vector-function $\psi(\tau, \varphi)$ is the solution of the auxiliary system of differential equations (15) with special initial conditions (16).

The vector-function $p(\tau)$ can be used as a "direction" (anti-gradient) for minimization of the functional (12) in the space of admissible controls $u(\tau)$ (for example, continuous functions with values in some bounded compact set). We set

$$u_\varepsilon(\tau) = u(\tau) + p(\tau)\varepsilon, \tag{19}$$

where $\varepsilon > 0$ and $u_\varepsilon(\tau)$ is the variation of the control $u(\tau)$.

In the case of smooth control functions it is possible to consider the following variation of the control[8]

$$u_\varepsilon(\tau) = u(\tau + \varepsilon\delta(\tau)), \quad \tau \in [0, T]. \tag{20}$$

Here $\varepsilon \in [0, 1]$ is a parameter; $\delta(\tau)$ is a smooth function such that $0 \le \tau + \varepsilon\delta(\tau) \le T$. Then obviously $u_\varepsilon(\tau)$ is always an admissible control, we have $\Delta u(\tau) = du(\tau)/d\tau\, \varepsilon\delta(\tau) + o(\varepsilon)$ and the variation of the functional (14) can be written in the following form

$$\delta J = -\varepsilon \int_0^T (p(\tau))^* \frac{du(\tau)}{d\tau} \delta(\tau) d\tau. \tag{21}$$

This representation of the functional variation can also be used for minimization of the functional (12) and gives an obvious hint at function $\delta(\tau)$ selection.

The obtained analytic representations (15), (21) of the variation of the functional (9) were used to find geometric parameters of radial matching section of the RFQ accelerator of protons (initial energy 45 keV, output energy 5 MeV, intervane

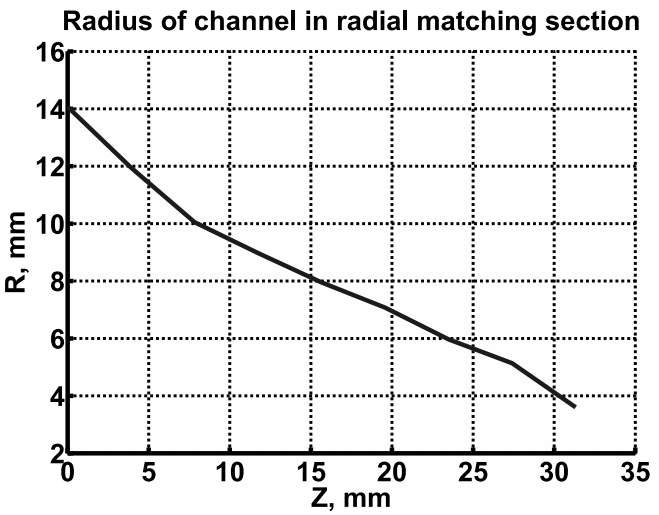

Fig. 1.

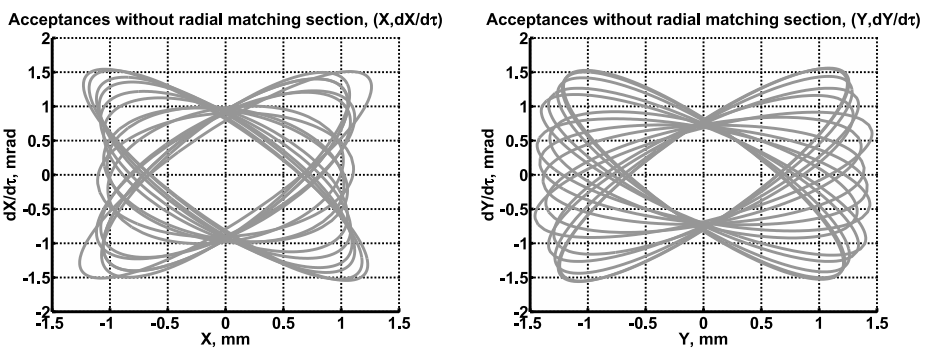

Fig. 2.

voltage 100 kV, RF field frequency 352 MHz, initial cell length 3.91 mm). One of the possible choices of the law of variation of the channel radius along the radial matching section is presented in Figure 1. In Figure 2 the RFQ acceptances without radial matching section are shown. The illustration of the radial matching section effect is shown in Figure 3.

4. Conclusion

New mathematical models and methods of the RFQ structure optimization were suggested in [9, 10]. In this paper the optimization approach to find geometric parameters of the radial matching section is discussed. The mathematical model

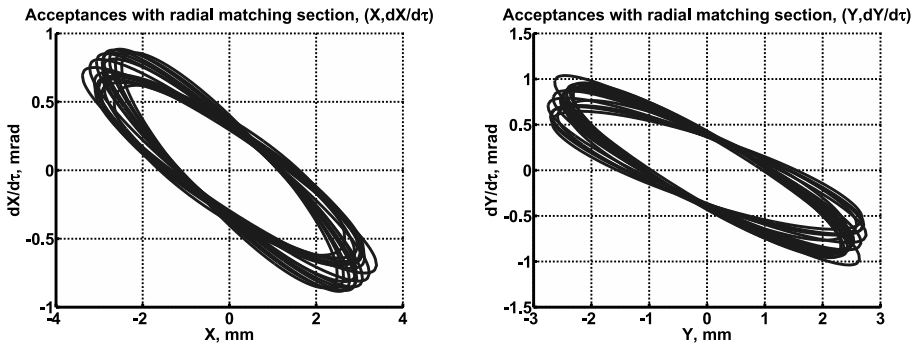

Fig. 3.

of the optimization using the Courant-Snyder parameters is developed and the analytical representation of gradients of the functional to be minimized is found. That allows developing different methods of the directional optimization. It should be noted, that the proposed approach can be utilized to optimize the transverse dynamics in accelerators if the dynamics is adequately described by linear equations. In particular, this method can be used to minimize the growth of the effective emittance in the RFQ channel. The nonlinear effects can be taken into account while considering the nonlinear optimization models.[7,8,10] The proposed approach can also be used to calculate the tolerances of geometric parameters of the channel.

Acknoweldgments

The work is done under support of the National Taiwan University of Science and Technology and Saint-Petersburg State University Joint Research Project No. RP07-05.

References

1. K. R. Crandall, R. H. Stokes, T. P. Wangler. RF Quadrupole Beam Dynamics Design Studies. In: Proceedings of Linear Accelerator Conference, Montauk, 1979, p. 205.
2. N. Tokuda, S. Yamada. New Formulation of the RFQ Radial Matching Section. In: Proceedings of Linear Accelerator Conference, Santa Fe, 1981, p. 313.
3. A. I. Balabin, V. S. Kabanov, I. M. Kapchinsky, V. V. Kushin, I. M. Lipkin. On beam matching with RFQ channel. Journal of Technical Physics, 1985, Vol. 55(3), p. 586–590.
4. K. R. Crandall. RFQ Radial Matching Section and Fringe Fields Proc. Linac Conference, GSI Darmstadt Report GSI-84-11, p. 88(1984).
5. I. M. Kapchinsky. Theory of linear resonance accelerator. Moscow, Energoizdat, 1982, 310 p.
6. M. Reiser. Theory and Design of Charged Particle Beams. New York, 1994, 607 p.
7. D. A. Ovsyannikov. Modeling and Optimization of Charged Particles Beam Dynamics. Lenigrad, 1990, 312 p.

8. A. D. Ovsyannikov. Control of program and disturbed motions. St.Petersburg, Vestnik SPbGU, Vol. 10 (4), 2006, p. 111–124.
9. A. D. Ovsyannikov, B. I. Bondarev, A. P. Durkin. New Mathematical Optimization Models for RFQ Structures, Proceedings of the 18th Particle Accelerator Conference, New York, USA, 1999, p. 2808–2810.
10. D. A. Ovsyannikov, A. D. Ovsyannikov, Yu. A. Svistunov, A. P. Durkin, M. F. Vorogushin. Beam dynamics optimization: models, methods and applications // Nuclear Instruments and Methods in Physics Research, section A 558 (2006), p. 11–19.

International Journal of Modern Physics A
Vol. 24, No. 5 (2009) 959–973

World Scientific
www.worldscientific.com

EVOLUTIONARY ALGORITHM FOR THE NEUTRINO FACTORY FRONT END DESIGN

ALEXEY A. POKLONSKIY

Department of Physics & Astronomy, Michigan State University, Biomedical Physical Sciences Bldg., East Lansing, Michigan, 48824, USA
poklonsk@msu.edu

DAVID NEUFFER

MS 221, Fermi National Accelerator Laboratory, Batavia, Illinois, 60510, USA
neuffer@fnal.gov

The Neutrino Factory is an important tool in the long-term neutrino physics program. Substantial effort is put internationally into designing this facility in order to achieve desired performance within the allotted budget. This accelerator is a secondary beam machine: neutrinos are produced by means of the decay of muons. Muons, in turn, are produced by the decay of pions, produced by hitting the target by a beam of accelerated protons suitable for acceleration. Due to the physics of this process, extra conditioning of the pion beam coming from the target is needed in order to effectively perform subsequent acceleration. The subsystem of the Neutrino Factory that performs this conditioning is called Front End, its main performance characteristic is the number of the produced muons.

Evolutionary Algorithms demonstrated themselves as a reliable and efficient tool for exploration, optimization and ultimately decision-making during the design process. In this work we describe the scenario for the Neutrino Factory Front End production optimization via the GATool Evolutionary Algorithm implemented in COSY Infinity and discuss the results of this optimization.

Keywords: Genetic algorithm; neutrino factory; accelerator design.

PACS numbers: 41.85.Ct, 41.75.Lx

1. Neutrino Factory

1.1. *Purpose and History*

The Neutrino Factory is a very important facility for the long-term neutrino physics program. Modern technologies of particle accelerators open the possibility to build an accelerator complex to produce and capture more than 10^{20} muons per year. The idea of the accelerator where the pions are injected into a storage ring, decay to produce muons captured within the same ring and then further decay into a neutrino beam was proposed several times by different researchers starting from

Koshkarev in 1974. All proposed designs suffered from the same basic problem: the resulting neutrino beam intensity was low [1].

Current design of the Neutrino Factory was proposed by Geer in 1997 [2]. He suggested to create muons from an intense pion source at low energies, then compress their phase space to produce a bright beam which is then accelerated to the energies of several tens of GeV and injected into a storage ring with long straight sections, where they decay into highly intense neutrino beams

$$\mu^- \to e^- \nu_\mu \bar{\nu}_e \,, \quad \mu^+ \to e^+ \bar{\nu}_\mu \nu_e \tag{1}$$

that can be used for the extensive study of neutrino oscillations [3] and neutrino interactions with the required high precision. Studies performed so far have shown that the Neutrino Factory gives the best performance among all considered neutrino sources over virtually all of the parameter space (except, for the case when θ_{13} turns out to be large). However, its time scale and cost are still being actively investigated [4].

1.2. *Design Overview*

The Neutrino Factory is a secondary beam machine; that is, a production beam is used to create secondary beams that eventually provide the desired flux of neutrinos. For the Neutrino Factory the production starts from a high intensity proton beam that is accelerated to a moderate energy (beams of 2–50 GeV have been considered by various groups) and impinges on a target, typically made from a high-Z material (baseline choice is a liquid Hg jet). Collisions between the proton beam and the target nuclei produce secondary beams of pions that quickly decay (26.0 ns) into longer-living (2.2 μs) muon beams. The remaining part of the Neutrino Factory is used to condition the muon beam, rapidly accelerate it to the desired final energy of a few tens of GeV, and then store it in a decay ring with long straight sections where the intense beam of neutrinos is produced from the decaying muons (see (1)). The resulting beam can be used to hit a detector located hundreds or thousands of kilometers from the source or some other scenario.

The Feasibility Study II [5] that was carried out jointly by the Brookheaven National Laboratory (BNL) and the U.S. Neutrino Factory and Muon Collider Collaboration, established most of the current Neutrino Factory design ideas. Although a number of other ideas and their variations of existing ones was proposed since FS II, later studies mainly concentrated on the exploration of the already proposed concepts and their combinations. The main goals were set to a cost/performance analysis and development of the consensus on a baseline design for the facility [6]. It is noteworthy that the FS II design is highly influenced by a specific scenario of sending a neutrino beam from BNL to a detector in Carlsbad, New Mexico. More generally, however, this design exemplified the Neutrino Factory for which the Feasibility Studies had demonstrated technical feasibility, established a cost baseline, and the expected range of physics performance. Another important feature of this

scheme is that such a Neutrino Factory could be comfortably constructed on site of an existing U.S. laboratory, such as BNL or Fermi National Accelerator Laboratory (FNAL).

Here we list the main components of a Neutrino Factory (see example of the RLA-acceleration based variant of the FS IIa design in Figure 1) and their primary functions:

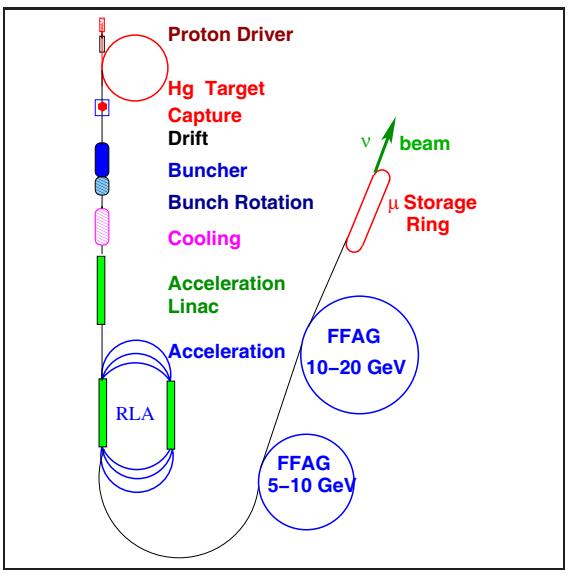

Fig. 1. Neutrino Factory schematics from the Feasibility Study IIa (RLA acceleration variant).

- **Proton Driver** provides 4 MW beam of a moderate energy (several GeV) protons on target.
- **Target** A high-Z target is put inside a 20 T solenoidal field (superconducting solenoid) to capture pions produced in the interactions of the inciding proton beam with the nuclei of the target material (liquid Hg jet) (see the longitudinal distribution of the particles 12 m from the target obtained from the MARS simulation code [7] in Figure 2).
- **Front End** consists of the parts of the Neutrino Factory between the target and the acceleration section. As can be seen in Figure 2, pions that are produced by nuclear collisions on target occupy significantly large longitudinal phase space. The transverse phase space is mainly determined by the strength of the magnetic field inside the solenoidal capture channel. According to the properties of the dynamics of particles in the solenoid, the particles with the transverse momentum satisfying the following condition

$$p_{\perp} < 0.3\frac{BR}{2},$$

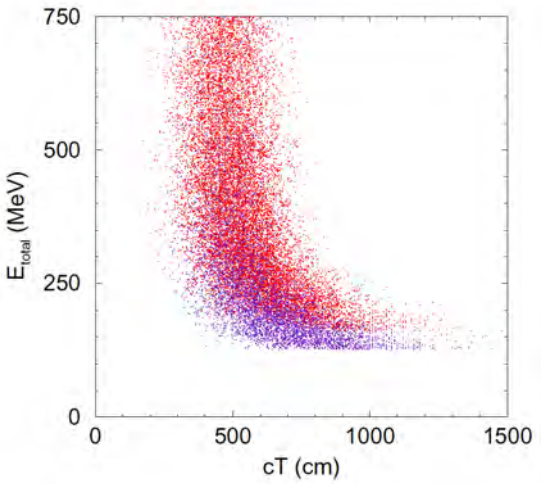

Fig. 2. Distribution of particles' energies 12m from the target calculated by MARS, $E_{\text{total}} = E_0 + T$, where E_0 is a rest energy (105.6 MeV for muons), T—kinetic energy.

where B is a solenoidal field strength, R is a radius of the solenoid, are captured after the target. In order to efficiently accelerate the beam, it has to be preconditioned to be fully contained within the capture transverse acceptance (30 π mm·rad) and the longitudinal acceptance (150 mm) of the subsequent accelerating section. Another constraint that the resulting beam has to satisfy is that only the particles that are contained within the longitudinal bucket of the accelerating system (bucket area depends on the RF frequency, phase and a field gradient) are considered captured to the accelerating regime. Transverse emittance has to be decreased by cooling in order to achieve optimal intensity. Hence the main figure of merit for the Front End is the ratio of the produced and captured muons to the number of incoming pions. See example of the longitudinal dynamics of a beam with a relatively small initial phase space in Figure 3.
Front End consists of the following subsystems:

- **Capture.** The magnetic field at the target is smoothly tapered down to a much lower value (2 T) which is then maintained through the bunching and phase rotation sections to keep the beam confined in the channel.
- **Decay.** This region is just an empty magnetic lattice where pions are allowed to decay to muons and where the particles of the resulting beam develop the correlation between a longitudinal coordinate and an energy.
- **Bunching and Phase Rotation.** First, the large beam of muons is bunched with RF cavities of modest gradient. Their frequencies decrease as we proceed down the beam line. After bunching, another set of RF cavities with changing frequencies is used to rotate the beam in longitudinal phase space in order to reduce its energy spread and match the frequency to the one of the downstream RF cavities, for efficient acceleration.

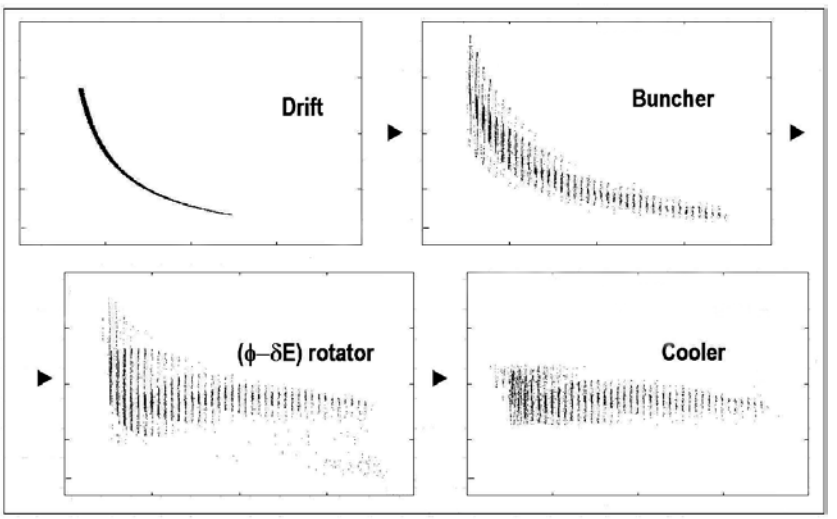

Fig. 3. Example of the longitudinal beam dynamics in the Front End (phase-energy plane).

  - **Ionization Cooling.** A solenoidal focusing channel filled with high-gradient RF cavities and LiH absorbers cools the transverse normalized RMS emittance of the beam. On this stage muons in the momentum range of 150–400 MeV/c pass through the absorbers (made from LiH in the baseline design) thus losing the total momentum (both longitudinal and transverse components). They are then reaccelerated in RF cavities to regain only the longitudinal momentum component. The total effect is a decrease in the transverse momentum spread and, therefore, reduction of the transverse emittance.

- **Acceleration.** Increases the beam kinetic energy from $\approx$ 138 MeV to a final energy in the range of 20–50 GeV. A superconducting pre-acceleration linac with solenoidal focusing is used to increase the muon beam energy to 1.5 GeV. It is then followed by a Recirculating Linear Accelerator (RLA), arranged in a dogbone geometry, that increases the beam energy to 5 GeV. Finally a pair of cascaded Fixed-Field Alternating Gradient (FFAG) rings with combined-function doublet magnets is used to bring beam energy up to 20 GeV. Additional FFAG stages could be added to reach a higher beam energy.
- **Storage and Decay Ring.** A compact racetrack-shaped superconducting storage ring in which $\approx$ 35% of the stored muons decay to neutrinos and are then sent towards the detector located approximately 3500 km from the ring. Muons survive in a ring for $\approx$ 500 turns.

The baseline Front End schematics from the latest International Scoping Study [8] is demonstrated in Figure 4. The baseline proton driver has an energy of 10 GeV, capture system is a 12 m long channel where the solenoidal field drops from initial 20 T to 2 T at the end while the channel radius increases from 75 mm to 250 mm.

It is followed by a 100 m long decay section where the pions decay to muons and develop a correlation between the temporal position and an energy. This correlation is then employed by the 50 m long bunching section in order to split the beam into a train of bunches via a set of RF cavities of a modest gradient and decreasing frequencies. Then another set of RF cavities with higher gradients in the 50 m long rotator section is employed to rotate the beam in the longitudinal phase space to reduce its energy spread. The achieved final RMS energy spread in this scheme is ≈ 10.5 %. Then 80 m long channel filled with high-gradient 201.25 MHz RF cavities and LiH absorbers in the solenoidal field is used to cool the transverse normalized RMS emittance from 17 π mm·rad to ≈ 7 mm·rad at a central muon momentum of ≈ 220 MeV/c.

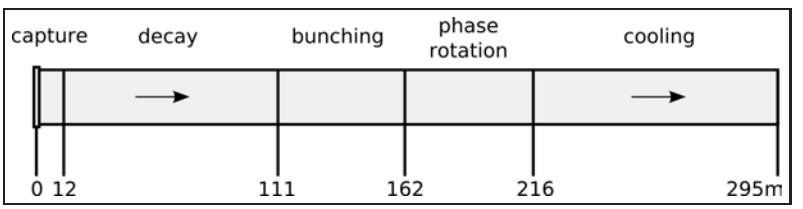

Fig. 4. The baseline Front End schematics from the latest International Scoping Study.

2. Evolutionary Algorithms

Evolutionary algorithms form a family of optimization methods that use a set of points to explore the objective function landscape. They are inspired by the process of evolution described by Darwin in his revolutionary work "Origin of Species" first published in 1859 [9]. According to it, the main driving forces of evolution are the variability in living organisms and the natural selection implicitly performed on them by the environment. Over time those forces shape different species to be very sophisticated inhabitants of the environment, i.e. make them fit to it.

If we view an objective function as an environment and points in a search space as organisms evolving to find the best places in this environment (which are for our purposes minima), we can easily sketch a general model of evolution suitable for optimization which is called *Evolutionary Algorithm* (EA) (see Figure 5). Having the evidence of the efficiency of this algorithm in the form of a variety of very well-fit organisms on Earth, there emerged a strong belief that its main principles can be applied to function optimization problems equally successfully.

Note that it actually is a meta-algorithm and that many conventional optimization algorithms described earlier can be formulated in this form. Because of this generality, the family of Evolutionary Algorithms typically includes only the ones that imitate the processes of evolution more straightforwardly and more accurately. A particularly important distinctive feature of EAs is that the members of the population actively exchange information about the search space. However the boundary

```
Generate initial population, evaluate fitness
While stop condition not satisfied do
    Produce next population by
        Selection
        Recombination
    Evaluate fitness
End while
```

Fig. 5. Evolutionary Algorithm.

is blurry and some EAs, for example the Differential Evolution [10], are closer to multi-point direct search methods than to "true" Evolutionary Algorithms.

It is worth noting that EA does not pose any restrictions on the search space and members of the population which, multiplied by a variety of different approaches to define fitness, selection, recombination and mutation, leads to a very broad field of applications. Examples include a wide variety of the optimization problems: numerical optimization, combinatorial optimization, circuit design, scheduling problems, video and sound quality optimization, control systems, image analysis, marketing and economics, traffic control, manufacturing and many others. While EAs do not explicitly guarantee to find even a local minimum, practical applications demonstrate that frequently they are able to find a global minimum or at least produce a practically acceptable solution.

Each of those applications is usually tied to a particular flavour of the Evolutionary Algorithms. Genetic Algorithms (GAs) [11] often encode parameters as strings of bits and modify them with logical operators thus are better suited for combinatorial optimization, for example for a class of problems equivalent to the famous Traveling Salesman Problem [12]. Genetic and Evolutionary Programming [13] evolve computer programs. Evolution Strategies (ES) [14] and Differential Evolution (DE) both use real numbers and arithmetic evolutionary operators for continuous function optimization. It is also worth noting a rapidly increasing interest in the development of the optimizers mimicking various optimization and search processes of nature: *Particle Swarm Optimization*, *Ant Colony Optimization*, *Tabu Search*, *Cultural algorithm*, etc. [15] and their successful application to many real-world problems.

Distinctive advantages of the EAs include:

- relative ease of implementation,
- ability to efficiently find global optima avoiding local ones even in very large search spaces,
- no requirements on the objective function other than the ability to calculate its value at every point of the search space,

- good tolerance to noise,
- ability to work even when the traditional search methods fail.

The interest to the field of EAs is steadily growing, active research on the development of the EAs and their applications produced a large number of publications: bibliography on Evolutionary Computation as of now contains more than 4000 entries on Evolutionary Computation and related areas [16].

3. Implementation

The algorithm we implemented uses the best features of the Evolutionary Strategies (ES), Genetic Algorithms (GA) and Differential Evolution (DE). From Evolutionary Strategies we adopted the representation of a potential solution as a vector of the real numbers, i.e. vector of a problem arguments:

$$\mathbf{x} = \left(x_1, x_2, \ldots, x_v\right)^{\mathrm{T}}. \tag{2}$$

Then the population members are:

$$\mathbf{x}_i = \left(x_{i1}, x_{i2}, \ldots, x_{iv}\right)^{\mathrm{T}},\ i = 1, \ldots, N$$

and

$$\mathbf{f} = \left(f(\mathbf{x}_1), f(\mathbf{x}_2), \ldots, f(\mathbf{x}_N)\right)^{\mathrm{T}} = \left(f_1, f_2, \ldots, f_N\right)^{\mathrm{T}} \tag{3}$$

is a vector containing function evaluations for the members of the population, $\underline{f}$ and $\overline{f}$ denote the minimum and maximum function values of the population members, correspondingly. Noting the success of the ES and DE both using such representation, we suggested that it is more adequate for the optimization of the problems with the real-valued parameters than the binary encoding frequently used in GAs.

It supports several methods for fitness scaling: Linear, Proportional and Rank; several methods for selection: Roulette Wheel, Stochastc Uniform and Tournament; two types of mutation: Uniform and Gaussian; Arithmetic (or Continuous) crossover with additinal randomization. The next generation is produced from the previos by means of mutation and crossover essential for exploration and exploitation of the search space as well as elite members transfer which is essential for the preservation of the already found solutions. The algorithm itself is presented in Fig. 6, its default parameters are listed in Fig. 7, for more detailed description of the algorithm and its parameters see [17].

4. Optimization

As can be seen from the Front End design description examples of the parameters that can be changed for different sections include:

(1) *Capture and Decay:* the length of the section L_{D} and the focusing fields.

```
Randomly generate initial population, set predefined
    members, if any
Calculate objective function values, scale to fitnesses
Update statistics
While any of the stop conditions is not satisfied do
    Perform Roulette Wheel/Stochastic Uniform/Tournament
        Selection
    Generate next population
        Produce mutants by Uniform/Gaussian Mutation
        Produce children by Continuous Crossover
        Copy elite members
    Replace old population with newly generated
    Calculate objective function values, scale to
        fitnesses
    Update statistics
End while
```

Fig. 6. GATool search algorithm.

```
Reproduction:    number of elite = 10, mutation rate = 0.2
Mutation:        UNIFORM, gene mutation probability = 0.1
Crossover:       HEURISTIC, ratio = 0.8, randomization is on
Fitness scaling: RANK
Selection:       STOCHASTIC UNIFORM
Creation:        UNIFORM
Areal:           initial box = [-10,10] x ... x [-10,10]
                 global box  = [-10,10] x ... x [-10,10]
                 killing is off
Stopping:        max generations = 1000,
                 stall generations = 25,
                 tolerance = 1E-5
```

Fig. 7. GATool's default parameters (see Appendix B, [17] for detailed description of parameters).

(2) *Bunching:* the length of the section L_{B}, RF voltages V_{B}^{i}, $i = \overline{1, n_{\mathrm{rfs}}}$ or initial and final voltage and the law of voltage increase (linear, quadratic, etc.). Final frequency is usually strictly specified by the cooling/accelerating subsections of the whole accelerator, but can also be varied if it can benefit the total Neutrino Factory performance.
(3) *Phase Rotation:* the length $L_{\varphi\mathrm{R}}$, RF voltage $V_{\varphi\mathrm{R}}$ of the phase-energy rotation section, number N of full RF field oscillation periods separating the main central particle (with $n = 0$) and the second central particle, and the vernier parameter δ (see [18] for detailed explanation). Also the kinetic energy T_{c} of the main central particle can be changed (usually T_{c} is taken as the peak of energy distribution of the particles of the beam).
(4) *Ionization Cooling:* parameters of the RF cavities ($\nu_{\mathrm{rf,cool}}$, $V_{\mathrm{rf,cool}}$, $\varphi_{\mathrm{rf,cool}}$); placement, width, material and the location of absorbers, focusing field strength and profile.

For our study we consider the exploration of the cooling section: we varied the RF cavities parameters and the desired momentum of the central particles in the beam within the ranges obtained from the physical considerations in order to find a configuration which would provide optimal production parameters.

Most of the numerical studies of the beam dynamics in the Front End is done with ICOOL—the de-facto standard Muon Collaboration particle tracking code originally developed for the ionization cooling simulations of the muon beams in 1999 [19] and actively developed over years to include new elements and models (available at `http://pubweb.bnl.gov/users/fernow/www/icool/readme.html`). It simulates beam dynamics in accelerator coordinates, performing particle-by-particle propagation through materials and electromagnetic fields. Field can given by built-in models that include most common accelerator elements and their approximations, be calculated from field maps or Fourier coefficients and read from files. ICOOL accurately models the decays of particles and their interactions with matter including energy loss, energy straggling and multiple Coulomb scattering. The beam can be generated from the uniform or Gaussian distributions or read from an input file.

ICOOL belongs to the family of so-called ray tracing codes, i.e. it calculated particle dynamics via the Runge-Kutta or the Boris numerical integration methods. For the description of dynamics it uses Frenet-Serret coordinate system. This is a right-handed system where s is tangent to the reference orbit, y is vertical and x is the third orthogonal coordinate. In a circular orbit x is in the radial direction. The reference orbit is defined to be that path where the transverse coordinates x and y and the transverse momenta p_x and p_y always remain zero. The shape of the reference orbit in a global Cartesian coordinate system is determined by the curvature parameter.

Various tools are developed to analyze the date produced by ICOOL simulation. The code that is used as a standard for the emittance calculation is called ECALC9

[20]. It allows user to compute number of particles in the fixed phase space volumes. The input is given as a file that contains the particle type, maximum and minimum value for p_z in GeV/c, two different cuts for transverse acceptance in m·rad (to obtain number of particles that correspond to two different acceptance cuts with all other cuts the same at once), a longitudinal acceptance cut in m·rad and a RF frequency to determine the RF bucket area for another longitudinal cut.

The toolchain that was developed for the optimization consists of the 4 programs:

- *COSY Infinity [21]:* provided the implementation of GATool optimization method.
- *ICOOL:* performed actual simulations of the beam dynamics in the Front End with the parameters values passed from COSY.
- *ECALC9:* performed analysis of the results of the ICOOL simulations, calculated the number of particles within desired acceptance that served as the objective function value.
- *glue.pl* is a Perl script that was used to control other programs in the toolchain. It was setting up the Front End lattice to ICOOL based on the control parameters provided by COSY, running ICOOL and then ECALC9 to obtain the objective function value which it was then passing back to COSY for the whole optimization run.

Initial distribution consists of 8000 particles after the target was generated by MARS simulation code for the 24 GeV proton beam on the Hg jet target [7]. The Front End lattice that was used for this study starts from the target and included capture, decay, bunching and phase rotation regions as well as cooling section and a matching between phase rotation and cooling subsystems:

- Capture: 15.25 m of the vacuum channel immersed in a solenoidal field that falls off starting from 20 T on the target to 2 T at the end of the channel. At the same time radius of the channel increases from 0.075 m to 0.3 m.
- Decay: vacuum channel of a constant aperture of 0.3 m immersed in a constant solenoidal field of 2 T.
- Bunching: vacuum channel of a constant aperture of 0.3 m and a total length of $L = 21$ m immersed in a constant solenoidal field of 2 T. An array of RF cavities separated by drifts so as to perform the adiabatic bunching (28 cells, each consists of the drift of 0.125 m, followed by RF cavity of 0.5 m and another drift of 0.125 m). Particles are bunched around the central momentum of 0.280 GeV/c. An integer number of wavelength that separate two reference particles is 7, initial RF gradient is set to 15 MV/m, the law that determines the RF gradient at the longitudinal coordinate z counted from the start of the buncher is

$$V_{\mathrm{rf}} = V_{0,\mathrm{rf}} \frac{z}{L} .$$

- Phase rotation: vacuum channel of a constant aperture of 0.3 m and a total length of $L = 24$ m immersed in a constant solenoidal field of 2 T. An array of RF cavities separated by drifts so as to perform the rotation of the beam in the longitudinal space by decelerating higher-energy bunches and accelerating lower-energy ones (32 cells, each consists of the drift of 0.125 m, followed by RF cavity of 0.5 m and another drift of 0.125 m). Vernier offset δ is 0.1, RF gradient is 15 MV/m for all cavities.
- Cooling: vacuum channel of a constant aperture of 0.3 m and a total length of $L = 93$ m immersed in an alternating solenoidal field of the maximum strength ≈ 2.5 T. An array of the 124 cells (0.75 m each), containing LiH absorbers to provide total momentum loss and RF field to provide longitudinal momentum regain to cool the transverse emittance of the beam. The first four cells are immersed in the solenoidal field designed so as to match the transverse particle dynamics in phase rotation section to the one of the cooling section. All RF cavities have the frequency of 201.25 MHz, field gradient is 18 MV/m and the RF phase is 30 degrees.

This particular design is shorter than the one of the baseline and is aimed to study the cost gains versus the performance losses resulted from shortening the Front End by removing some of its elements that were originally present. Another goal is to study the potential of this design for the Muon Collider project [22].

We used the described lattice as a reference design and explored its performance related to changes in the following control parameters:

- RF frequency in cooling section (also influences the following accelerator section): $\nu_{\mathrm{rf,cool}} \in [200, 204]$ MHz.
- RF field gradient in cooling section: $V_{\mathrm{rf,cool}} \in [12, 20]$ MV/m.
- RF field phase in cooling section: $\varphi_{\mathrm{rf,cool}} \in [0, 360]$ degrees.
- Central momentum in the first 4 matching sections of the cooling channel: $p_{\mathrm{c,match}} \in [0.22, 0.24]$ GeV/c.

The values of the cuts to set up ECALC9 analysis were obtained as an estimate of the acceptance of the subsequent acceleration subsystem:

- minimum and maximum p_z: 0.100 GeV/c and 0.300 GeV/c, correspondingly;
- transverse acceptance cut: 30E-3 m·rad;
- longitudinal acceptance cut: 0.25 m·rad;
- RF frequency for the bucket calculation set to a value used by RF cavities of the cooling section (on of the control parameters).

The number of particles withing the specified acceptance (n_2) was chosen as an objective value to be maximized. GATool parameters were set to default values (see Figure 7, p.967), population size for this 4-dimensional problem was set to 250 (dimension×62.5) which provides a good compromise between the total time of the

search given the expensiveness of the objective function calculation (see below) and a setting that is known to provide good GATool performance.

Even though 2000 particles were used instead of 8000 in order to reduce the computation time (ICOOL integrates each particle dynamics separately) one simulation run of the described Front End lattice still takes approximately 0.4 hour on a Pentium IV 2Mhz computer with 1Gb of memory. Therefore the calculations needed to perform one step of the GATool optimization took approximately 100 hours. Since a typical number of generations needed for GATool to explore the parameters space and converge can get above 100, subsequent studies (possibly on more realistic and thus more computationally expensive lattices), one can clearly benefit from even the embarrassingly simple parallelization of the objective function evaluation.

Several of the best obtained results (elite in GATool terminology) from three runs (each of them took several months to complete on a single machine) were evaluated using the described scheme and the full initial number of particles of 8000. The control parameters and objective function values for the found designs are listed along with the reference design provided in Table 1. Range of the values of the objective function with control parameters from the regions listed earlier on combinations occurred during the optimization is from 15 to 497. From the table it is seen that the optimization of the current scheme with control parameters in the specified ranges was unable to achieve the designs that have statistically (simulation includes stochastic processes) significantly better production efficiency. Although this can not serve as a rigorous proof of the nonexistence of such designs, noting generally good performance of the GATool on other problems, we can suggest that this gives reason to believe that the reference design is, indeed, optimal. Relatively small deviations of the optimal RF frequency (201.20–201.55) solution and RF gradient (17.67–18.88) among all the solutions except for the 1st opt. run, best suggest that the reference parameters are also robust and located near the global optimum. This observation is particularly important here since the parameters of the devices that are calculated by numerical simulations eventually have to be implemented by physical devices operating with finite precision and subject to construction errors.

The best solution obtained from the 1st optimization run provided one of the best performance and with one of the smallest small RF gradient (among other solutions) which is generally easier/cheaper to manufacture. However, its final frequency is different from the frequency of the current baseline accelerating section thus additional studies on the combined performance might reveal additional benefits or drawbacks of this solution. The best solution from the 3rd optimization run provided the same performance on the frequency that is much closer to the reference 201.25 and thus might be preferable. Some of the other sets of parameters that provide similar production performances can also be useful since they might be easier or cheaper to obtain, or provide additional opportunities for the designers

of the downstream sections of the Neutrino Factory. Another important result that is obtained is that we established a framework for the Neutrino Factory Front End lattice numerical optimization. It can be used for many optimization scenarios, including, for example, a simultaneous optimization of all control parameters of the most realistic Front End simulation on the large ranges of the parameter values.

Table 1. Results of the Front End design optimization (in ascending order sorted on the production rate for the 8000 particles initial beam). Column 5 and 6 contain the results of the simulations for 2000 and 8000 particles in the initial beam, correspondingly. The number of the particles in the exit beam per each particle in the initial beam is listed in parentheses

Parameters	$\nu_{\mathrm{rf,cool}}$ [MHz]	$V_{\mathrm{rf,cool}}$ [MV/m]	$\varphi_{\mathrm{rf,cool}}$ [degrees]	$p_{\mathrm{c,match}}$ [GeV/c]	n_2 (from 2000) [particles]	n_2 (from 8000) [particles]
reference parameters	201.25	18.00	30.000	0.220	498 (0.249)	1740 (0.218)
3rd opt. run, 6th best	201.46	17.77	11.320	0.229	480 (0.240)	1791 (0.224)
3rd opt. run, best	201.40	17.06	12.648	0.226	492 (0.246)	1782 (0.223)
1st opt. run, best	200.55	17.10	26.970	0.220	467 (0.234)	1780 (0.222)
3rd opt. run, 5th best	201.28	17.76	12.457	0.226	484 (0.242)	1773 (0.222)
3rd opt. run, 3rd best	201.47	17.67	13.470	0.228	485 (0.243)	1762 (0.220)
3rd opt. run, 2nd best	201.42	17.68	12.555	0.226	486 (0.243)	1750 (0.219)
3rd opt. run, 7th best	201.34	17.68	12.020	0.226	479 (0.240)	1746 (0.218)
2nd opt. run, 2nd best	201.24	18.91	20.520	0.228	471 (0.236)	1714 (0.214)
3rd opt. run, 4th best	201.48	17.75	11.860	0.227	485 (0.243)	1669 (0.209)
2nd opt. run, best	201.20	18.88	22.477	0.230	497 (0.249)	1643 (0.205)

5. Conclusions

In this work we described our Genetic Algorithm and demonstrated its applicability to a real-life problem of the accelerator physics. We developed a method for the Neutrino Factory Front End optimization and obtained some practically useful numerical results. We are planning to use this method for the subsequent studies in design and optimization of this facility. We also hope to see more problems of accelerator physics to be approached using this approach.

References

1. D. G. Koshkarev. Proposal for a decay ring to produce intense secondary particle beams at the sps.
2. S. Geer. Neutrino beams from muon storage rings: Characteristics and physics potential. *Phys. Rev.*, D57:6989–6997, 1998.
3. M. Apollonio et al. Oscillation physics with a neutrino factory. ((g)) ((u)). *CERN Yellow Report on the Neutrino Factory*, 2002.
4. Michael S. Zisman. International scoping study of a future accelerator neutrino complex. In *Proceedings of EPAC 2006*, pages 2427–2429, Edinbrugh, Scotland, 2007.
5. S. Ozaki, R. Palmer, M. Zisman, J. Gallardo, and (eds.). Feasibility study-II of a muon-based neutrino source. Technical Report BNL-52623, Muon Collider Collaboration, June 2001. see http://www.cap.bnl.gov/mumu/studyii/FS2-report.html.

6. J. S. Berg, S. A. Bogacz, S. Caspi, J. Cobb, R. C. Fernow, J. C. Gallardo, S. Kahn, H. Kirk, D. Neuffer, R. Palmer, K. Paul, H. Witte, and M. Zisman. Cost-effective design for a neutrino factory. *Phys. Rev. ST Accel. Beams*, 9(1):011001, Jan 2006.
7. N. V. Mokhov and A. van Ginneken. Pion production and targetry at $\mu^+\mu^-$ colliders. Technical Report Fermilab-Conf-98/041, Fermi National Accelerator Laboratory, January 1998. Published Proceedings of the 4th International Conference on Physics Potential and Development of Muon Colliders, San Francisco, California, December 10-12, 1997.
8. J.S. Berg et al. Iss scoping study: Accelerator design concept for future neutrino factories. Technical Report RAL-TR-2007-23, RAL, 2007.
9. Charles Darwin. *The Origin of Species by Means of Natural Selection, or the Preservation of Favoured Races in the Struggle for Life*. London: John Murray, 6 edition, 1872.
10. Rainer Storn and Kenneth Price. Differential evolution - a simple and efficient adaptive scheme for global optimization over continuous spaces. Technical Report TR-95-012, Berkeley, CA, 1995.
11. David E. Goldberg. *Genetic Algorithms in Search, Optimization, and Machine Learning*. Addison-Wesley Professional, 1st ed. edition, 1989.
12. P. Prinetto, M. Rebaudengo, and M. Sonza Reorda. Hybrid genetic algorithms for the traveling salesman problem. In *Proc. of the International Conference on Neural Networks and Genetic Algorithms*, pages 559–566, 1993.
13. John R. Koza. *Genetic Programming: On the Programming of Computers by Means of Natural Selection*. Complex Adaptive Systems. The MIT Press, December 1992.
14. Schwefel H.-P. *Evolution and optimium seeking*. Wiley, New York, 1991.
15. Johannes J. Schneider and Scott Kirkpatrick. *Stochastic Optimization*. Scientific Computing. Springer, 1st edition, November 2006.
16. Bibliography on Evolutionary Computation. on-line. `http://www.fmi.uni-stuttgart.de/fk/evolalg/eabib.html`.
17. Alexey Poklonskiy. *Evolutionary Optimization Methods for Accelerator Design*. PhD thesis, Michigan State University, USA, 2008.
18. A.A. Poklonskiy, D.A. Ovsyannikov, A.D. Ovsyannikov, D. Neuffer, and M. Berz. Exploring the bunching section of the neutrino factory. In *Physics and Control, 2005. Proceedings. 2005 International Conference*, pages 272–277, August 2005.
19. R.C. Fernow. Icool, a simulation code for ionization cooling of muon beams. In *Proc. 1999 Particle Accelerator Conference*, page 3020, New York, 1999. see http://pubweb.bnl.gov/people/fernow/.
20. R.C. Fernow. Physics analysis performed by ecalc9. Neutrino Factory and Muon Collider Notes MUC-NOTE-COOL_THEORY-280, Brookhaven National Laboratory, 2003. see http://www-mucool.fnal.gov/notes/notes.html.
21. M. Berz and K. Makino. COSY INFINITY Version 9.0 programmer's manual. Technical Report MSUHEP-060803, Department of Physics and Astronomy, Michigan State University, East Lansing, MI 48824, 2006. see also http://cosyinfinity.org.
22. Muon Collider Collaboration. $\mu^+\mu^-$ collider: A feasibility study. Technical Report BNL-52503, Fermilab-Conf-96/092, LBNL-38946, Muon Collider Collaboration, jul 1996. pres. at the Snowmass'96 workshop.

International Journal of Modern Physics A
Vol. 24, No. 5 (2009) 974–986

World Scientific
www.worldscientific.com

CALCULATION OF NONLINEAR TUNE SHIFT USING BEAM POSITION MEASUREMENT RESULTS

PAVEL SNOPOK,* MARTIN BERZ† and CAROL JOHNSTONE‡

University of California, Riverside, CA, USA
Michigan State University, East Lansing, MI, USA
Fermi National Accelerator Laboratory, Batavia, IL, USA
*snopok@gmail.com
†berz@msu.edu
‡cjj@fnal.gov*

The calculation of the nonlinear tune shift with amplitude based on the results of measurements and the linear lattice information is discussed. The tune shift is calculated based on a set of specific measurements and some extra information which is usually available, namely that about the size and particle distribution in the beam and the linear optics effect on the particles. The method to solve this problem uses the technique of normal form transformation.

The proposed model for the nonlinear tune shift calculation is compared to both the numerical results for the nonlinear model of the Tevatron accelerator and the independent approximate formula for the tune shift by Meller et al. The proposed model shows a discrepancy of about 2%.

1. Introduction

Finding the nonlinear tune shift depending on the position of the particle in the beam might be an elaborate task, because the nonlinear component of the dynamics is not known to the desired precision or because there are reasons to doubt the correspondence between the model and the machine optics.

At the same time, there is still a way to find the tune shift, if there is a set of specific measurements and some extra information which is usually available, namely that about the geometry of the beam (its size and particle distribution) and the linear effect of the optics on the particles (in the form of a one-turn linear transfer matrix).

The tune of a system is one of the most important characteristics of the dynamics of particles. For linear systems, the tune stays constant, while in the nonlinear case it might change, mainly depending on the position of the particle in the beam (the so-called tune shift with amplitude), but also depending on other parameters of the system.

Consider the problem of evaluation of the tune shift with amplitude in the nonlinear case using some extra information obtained by the specific kind of mea-

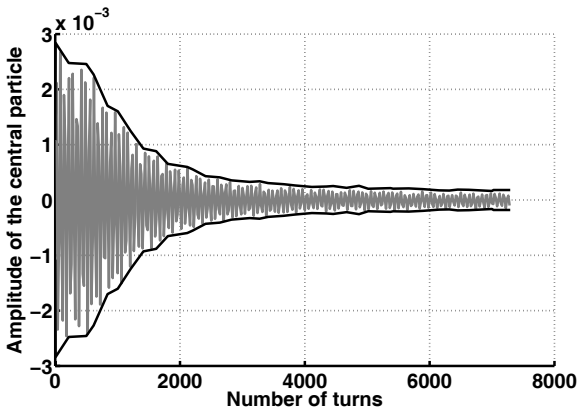

Fig. 1. Measurement results: horizontal position of the center of mass over a number of turns and its envelope.

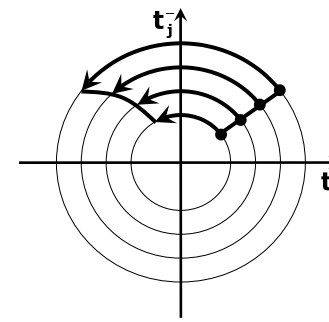

Fig. 2. Behavior of particles in normal form coordinates.

surements. All the proposed methods have been tested on the Tevatron accelerator model[1] and measurements,[2] but the algorithm for finding the tune shift with amplitude is applicable to other machines. In fact, the algorithm should stay valid for any other synchrotron, as long as one can proceed with a linear normal form transformation. The normal form transformation is the core of the method.[3] Throughout the article the new set of coordinates, after the normal form transformation is applied to the pair of transversal phase space coordinates $(x, p_x/p_0)$ or $(y, p_y/p_0)$, is denoted (t^+, t^-). Here x and y are horizontal and vertical positions, respectively, of the particle under consideration, p_x and p_y are the horizontal and vertical components of the momentum, respectively, p_0 is the reference momentum. The horizontal and vertical planes are assumed to be uncoupled.

2. Calculation Results versus Measurement Results

Suppose that one only has the information on the linear component of the dynamics of the particles in the accelerator. Assume that there is some extra information available: the size of the beam, the particle distribution type and also the results of the special type of measurements of the beam position. A corrector is introduced into the accelerator optics to kick the beam in the horizontal or vertical direction. Once the strength of the corrector is known, the displacement of the center of the beam can be found. After the corrector is turned on and off instantaneously, the amplitude of the beam center of mass decreases due to the filamentation of the beam, not the damping, as the motion is symplectic. The position of the center of mass of the beam is then registered after each turn of the particles. One sample of the measurement data for the horizontal position is shown in Fig. 1.

In the normal form coordinates the initially displaced beam behaves in a very similar fashion, which allows to restore the information about the nonlinear tune. The normal form transformation is a nonlinear change of coordinates, such that

after the transformation the dynamics of the particles is represented in a very systematic way. The details of the transformation algorithm can be found in [3]. The most important part for this study is that after the normal form transformation all the particles follow concentric circles with angular velocity depending on the amplitude. This is the key fact allowing to establish a connection between the nonlinear tune shift with amplitude and the behavior of the beam.

The function connecting the initial and final coordinates of the particles after one full revolution (called the transfer map) has the form:

$$\mathcal{M} = \begin{pmatrix} \cos 2\pi\mu(r) & -\sin 2\pi\mu(r) \\ \sin 2\pi\mu(r) & \cos 2\pi\mu(r) \end{pmatrix}, \tag{1}$$

where the tune $\mu(r)$ can be represented in the following form:

$$\mu = \mu_0 + c_1 r^2 + c_2 r^4 + \dots. \tag{2}$$

Here μ_0 is a constant linear tune, c_1, c_2 are the coefficients of the higher order terms in the expansion of the dependence of the tune μ on the particle's amplitude in the normal form coordinates, where the amplitude is defined to be $r = \sqrt{(t^+)^2 + (t^-)^2}$ for the particle with normal form coordinates (t^+, t^-).

Figure 2 schematically shows the positions of four particles with initial positions chosen along some fixed polar angle, after several turns. Particles cannot leave their corresponding circles, but the rotation frequencies are different for different radii. Assume that the outer particles move faster than the inner particles. In this particular case the outer particle will leave the inner particle behind in the phase. As a result of such a redistribution of particles, the center of mass of the beam initially displaced from the origin shifts toward the origin of the coordinate system and then oscillates around it. In other words, the amplitude of the center of mass of the beam in the normal form coordinates decreases until it reaches a stable value.

As it is assumed that an accurate linear lattice description is available, one may use the linear normal form transformation, for which the information on the linear dynamics is sufficient, to obtain the information on the distribution of the beam in the linear normal form coordinates after the kick. The linear normal form transformation is discussed in great detail in [3]. In new coordinates all the particles follow circles with the same angular frequency μ_0. Hence, the linear transformation does not provide any information on the coefficients in the expansion (2) describing the nonlinear tune shift. At the same time the linear transformation is sufficient to obtain an approximate initial distribution of the beam in the normal form coordinates.

Since the tune of the particle can also be viewed as the limit of the total phase advance divided by the number of turns when the number of turns goes to infinity, the average tune for a large number of turns is the same in both sets of coordinates, as the contribution of the normal form transformation and the inverse normal form transformation becomes negligible. Hence, if the nonlinear tune of the particle in

the normal form coordinates is found, then the nonlinear tune of that particle in the original coordinates is the same.

As a rule, $c_1 r^2$ is the dominating term in the expansion (2). Accelerator designers try to avoid high order nonlinearities, unless there is a specific need of them. Hence, finding the coefficient c_1 is the most important part. Later, if there are multiple measurements available, the coefficient c_2 could be attempted to be found as well.

If the transfer map $\mathcal{M}$ from Eq. (1) is known, one can track the behavior of particles for arbitrary many turns. That, in turn, allows us to find the number of turns corresponding to the moment when the amplitude of the center of mass is at the half of its value after the kick, $N_{1/2}$. This establishes the connection between c_1 and $N_{1/2}$. The number $N_{1/2}$ can be found from the measurements (Fig. 1).

The general scheme for establishing the connection between c_1 and $N_{1/2}$ is as follows:

(1) The outer particle of the beam having the amplitude R rotates with a frequency $\mu(R)$, and hence, after $1/|\mu(R) - \mu_0|$ turns this particle phase advance is 2π bigger (or smaller, depending on the sign of c_1) than that of the particle close to the origin; assume that the kick is weak enough and the beam is not displaced too far from the origin. In fact, in most cases the kick is such that the origin is still inside the part of the phase space covered by the beam.
(2) R depends on the strength of the kick and the initial particle distribution, the value of R can be found as the maximum of the deviations of particle positions from the origin after the linear normal form transformation, that is, all the components to find R are known.
(3) The value of c_1 is not known, but one can always fix a certain c_1 and using the form of the transfer map (1) obtain the value of $N_{1/2}$ as a function of c_1 and R.
(4) Once the algorithm for finding $N_{1/2}(c_1)$ is established, it can be used multiple times to obtain the correct value of the coefficient c_1 for a known value of $N_{1/2}$ inferred from the measurements as discussed above; it is a typical one-parameter optimization problem.

Hence, the problem under consideration has been reduced to establishing a dependence of $N_{1/2}$ on various values of c_1 and R. Depending on the initial distribution of particles this can be a complicated task, which is not possible or not feasible to solve analytically to obtain an explicit expression for $c_1 = c_1(N_{1/2})$. This problem is addressed below and solved numerically for various distributions.

3. Sector Approximation, Uniform Particle Distribution

Let our initial distribution be uniform in the sector bounded by the two radii R_1, R_2 and two angles φ_1, φ_2 (Fig. 3). This is a very simple and unrealistic case, but it is instructive to consider it first in order to obtain basic formulas.

After N turns each particle of this distribution will have the phase advance of

$$\theta_N(r) = 2\pi N \mu(r) = 2\pi N(\mu_0 + c_1 r^2 + c_2 r^4)$$

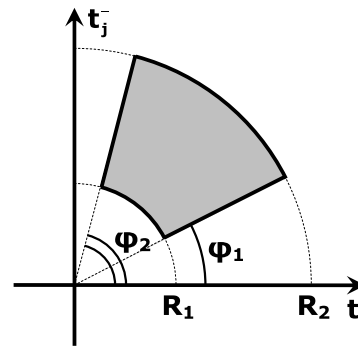

Fig. 3. Uniform particle distribution in the sector.

(orders up to 4 are taken into account). Hence, the particle with radius $R_1 < r < R_2$ located on the front (back) line of the distribution will have a phase difference of $\Delta\theta_N(r) = 2\pi N(\mu(r) - \mu(R_1))$ with respect to the inner particle.

To find the centroid of the resulting planar figure, bounded by two radii R_1, R_2 and two curves given by $\phi_1+\theta_N(r)$, $\phi_2+\theta_N(r)$, $R_1 < r < R_2$ three integral formulas are used:

$$S = \iint r dr d\theta; \quad x_c = \frac{1}{S}\iint r^2 \cos\theta dr d\theta; \quad y_c = \frac{1}{S}\iint r^2 \sin\theta dr d\theta.$$

For the case under consideration:

$$\begin{cases} x_c^{(N)} = & \frac{1}{S}\int_{R_1}^{R_2}\int_{\varphi_1+\theta_N(r)}^{\varphi_2+\theta_N(r)} r^2\cos\theta d\theta dr; \\ y_c^{(N)} = & \frac{1}{S}\int_{R_1}^{R_2}\int_{\varphi_1+\theta_N(r)}^{\varphi_2+\theta_N(r)} r^2\sin\theta d\theta dr. \end{cases} \tag{3}$$

Hereafter, $x_c^{(N)}$ and $y_c^{(N)}$ are the coordinates of the beam center of mass in the normal form coordinate system (t^+, t^-).[3]

Let us simplify the form of the last two integrals. Without loss of generality one can assume $-\varphi_1 = \varphi_2 = \varphi$ (the angle can be changed as only the radius is the quantity of interest). In addition to that the coordinate θ is changed to $\psi + \theta_N(r)$. Then one has $d\theta = d\psi$, and the integrals transform to:

$$x_c^{(N)} = \frac{1}{S}\int_{R_1}^{R_2}\int_{-\varphi+\theta_N(r)}^{\varphi+\theta_N(r)} r^2\cos\theta d\theta dr = \frac{1}{S}\int_{R_1}^{R_2}\int_{-\varphi}^{\varphi} r^2\cos(\psi+\theta_N(r)) d\psi dr; \tag{4}$$

$$y_c^{(N)} = \frac{1}{S}\int_{R_1}^{R_2}\int_{-\varphi+\theta_N(r)}^{\varphi+\theta_N(r)} r^2\sin\theta d\theta dr = \frac{1}{S}\int_{R_1}^{R_2}\int_{-\varphi}^{\varphi} r^2\sin(\psi+\theta_N(r)) d\psi dr. \tag{5}$$

After integrating with respect to ψ, under the remaining integral one can use the some trigonometric identities ultimately obtaining

$$\begin{aligned} x_c^{(N)} &= \frac{1}{S}\int_{R_1}^{R_2} r^2 \left\{\sin(\varphi+\theta_N(r)) - \sin(-\varphi+\theta_N(r))\right\} dr \\ &= \frac{2}{S}\sin\varphi \int_{R_1}^{R_2} r^2 \cos\theta_N(r) dr, \\ y_c^{(N)} &= \frac{1}{S}\int_{R_1}^{R_2} r^2 \left\{-\cos(\varphi+\theta_N(r)) + \cos(-\varphi+\theta_N(r))\right\} dr \\ &= \frac{2}{S}\sin\varphi \int_{R_1}^{R_2} r^2 \sin\theta_N(r) dr. \end{aligned} \tag{6}$$

These integrals cannot be found analytically due to the polynomial nature of the argument θ_N. Even if one assumes $\theta_N \propto r^2$, the result is a complicated expression given in terms of Fresnel functions

$$\begin{aligned} \int_{R_1}^{R_2} r^2 \cos\theta_N(r) dr &= \frac{1}{4\pi N c_1}\left(R_2 \sin(2\pi N c_1 R_2^2) - R_1 \sin(2\pi N c_1 R_1^2)\right) \\ &\quad - \frac{1}{8\pi (N c_1)^{3/2}}\left(\mathrm{S}(2(Nc_1)^{1/2} R_2) - \mathrm{S}(2(Nc_1)^{1/2} R_1)\right), \\ \int_{R_1}^{R_2} r^2 \sin\theta_N(r) dr &= -\frac{1}{4\pi N c_1}\left(R_2 \cos(2\pi N c_1 R_2^2) - R_1 \cos(2\pi N c_1 R_1^2)\right) \\ &\quad - \frac{1}{8\pi (N c_1)^{3/2}}\left(\mathrm{C}(2(Nc_1)^{1/2} R_2) - \mathrm{C}(2(Nc_1)^{1/2} R_1)\right), \end{aligned} \tag{7}$$

where $\mathrm{S}(x) = \int_0^x \sin(\frac{\pi}{2}t^2)dt$, and $\mathrm{C}(x) = \int_0^x \cos(\frac{\pi}{2}t^2)dt$.[4] The shape of the graphs of Fresnel functions explains the behavior of the beam center of mass shown in Fig. 1: both $\mathrm{C}(x)$ and $\mathrm{S}(x)$ oscillate around $\frac{1}{2}$ as $x \to \infty$ with slowly decreasing amplitude. Hence, the difference of the two C or S functions oscillates around zero, provided the arguments are proportional, which is the case in Eqs. (7). To illustrate this the graph of the function $\mathrm{S}(1.5x) - \mathrm{S}(x)$ is shown in Fig. 4.

To calculate the integrals (4)–(5) in the general case, numerical integration methods should be employed. For this study the adaptive Simpson quadrature method[5] is used. The main issue with the sector approximation is that it is not sharp enough, and only works for beams which are displaced by the transversal kick in such a way that the whole beam is away from the origin. To handle the situation with a beam that crosses the origin, and to be more precise with the conclusions about the centroid, attention should be paid to the exact shape and position of the beam after the kick.

4. Elliptical Beam, Uniform Distribution

Let us assume that the particles in the beam are distributed uniformly (we will consider the general case later), and the beam has an elliptical shape. Then after

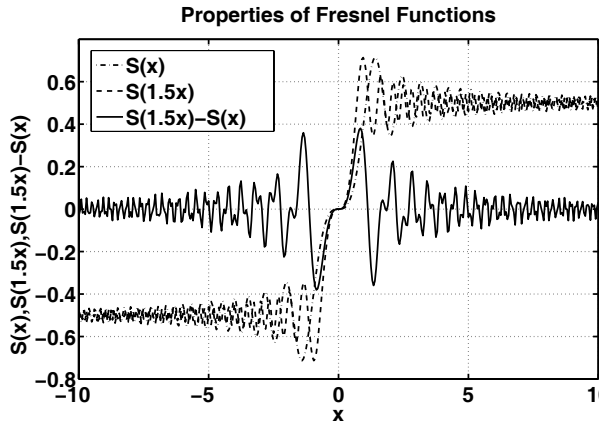

Fig. 4. $\mathrm{S}(1.5x) - \mathrm{S}(x)$ function graph.

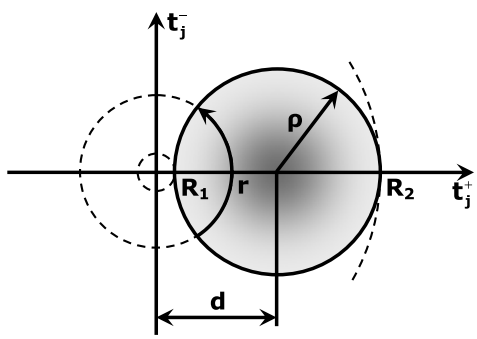

Fig. 5. $R_1 = d - \rho > 0$.

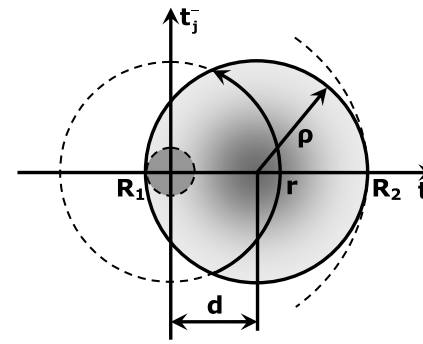

Fig. 6. $R_1 = d - \rho < 0$.

the transformation to the normal form coordinates, the beam has an elliptical shape again, and the axes of the transversal section of the beam are equal. Then the boundary curve for the beam in the normal form coordinate pair is a circle, and the parametric representation for it can be found in the form of the equations for two half-circles: $(r, \varphi_1(r))$, $(r, \varphi_2(r))$. Without loss of generality it can be assumed that the resulting circle has its center on the horizontal axis, with the coordinates $(d, 0)$, where $d > 0$ is known (similar to the previous section: the angular position of the distribution of particles does not matter, since we are ultimately interested in the distance to the origin from the center of the distribution which is invariant from the angle). Let ρ be the radius of the beam, then the beam lies between $R_1 = d - \rho$ and $R_2 = d + \rho$, where it is often the case that the radius R_1 is less than zero, which means that the origin (0,0) is inside the beam (Fig. 5–6). Both d and ρ parameters can be found by applying the linear normal form transformation to the displaced beam boundaries. Below it will be shown that the two cases $R_1 > 0$ and $R_1 < 0$ can be treated in a uniform way. For the moment let us assume that $R_1 > 0$.

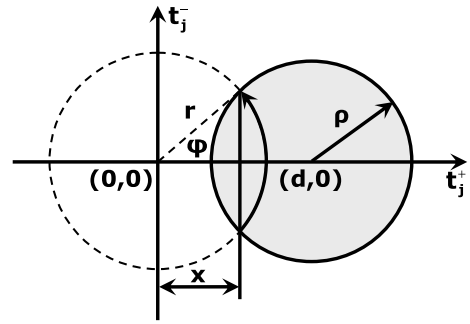

Fig. 7. The intersection of two circles.

Similar to the previous section, the centroid of the beam has the coordinates

$$\begin{cases} S = \displaystyle\int_{R_1}^{R_2}\int_{-\varphi(r)+\theta_N(r)}^{\varphi(r)+\theta_N(r)} r d\theta dr; \\ x_c^{(N)} = \dfrac{1}{S}\displaystyle\int_{R_1}^{R_2}\int_{-\varphi(r)+\theta_N(r)}^{\varphi(r)+\theta_N(r)} r^2\cos\theta d\theta dr; \\ y_c^{(N)} = \dfrac{1}{S}\displaystyle\int_{R_1}^{R_2}\int_{-\varphi(r)+\theta_N(r)}^{\varphi(r)+\theta_N(r)} r^2\sin\theta d\theta dr; \end{cases} \tag{8}$$

the only difference being that φ is now a function of r.

To simplify the integral expression, some additional information is needed on the intersection of two circles, as we are integrating along the arcs of a circle and the boundary curve is also a circle. Let us consider two circles: the first one centered at the origin $(0,0)$ and having a radius r, and the second one centered at $(d,0)$ and having a radius ρ (Fig. 7). This setup gives

$$\begin{cases} x^2 + y^2 = r \\ (x-d)^2 + y^2 = \rho \end{cases} \quad \text{or} \quad x = \frac{r^2 - \rho^2 + d^2}{2d}, \tag{9}$$

which yields

$$\cos\varphi(r) = \frac{x}{r} = \frac{r^2 - \rho^2 + d^2}{2dr}, \quad \varphi(r) = \arccos\left(\frac{r^2 - \rho^2 + d^2}{2dr}\right).$$

Using the resulting expression for φ and trigonometric identities, similar to what is done in the previous section, one obtains

$$\begin{aligned} &\int_{R_1}^{R_2}\int_{-\varphi(r)+\theta_N(r)}^{\varphi(r)+\theta_N(r)} r^2\cos\theta d\theta dr = 2\int_{R_1}^{R_2} r^2\sin\varphi(r)\cos\theta_N(r)dr \\ &= 2\int_{R_1}^{R_2} r^2 \sin\arccos\left(\frac{r^2-\rho^2+d^2}{2dr}\right)\cos\theta_N(r)dr \\ &= 2\int_{R_1}^{R_2} r^2\sqrt{1-\left(\frac{r^2-\rho^2+d^2}{2dr}\right)^2}\cos\theta_N(r)dr, \end{aligned} \tag{10}$$

and hence

$$\begin{cases} S = \int_{R_1}^{R_2} r\sqrt{1-\left(\frac{r^2-\rho^2+d^2}{2dr}\right)^2}\,dr; \\ x_c^{(N)} = \frac{1}{S}\int_{R_1}^{R_2} r^2\sqrt{1-\left(\frac{r^2-\rho^2+d^2}{2dr}\right)^2}\cos\theta_N(r)dr; \\ y_c^{(N)} = \frac{1}{S}\int_{R_1}^{R_2} r^2\sqrt{1-\left(\frac{r^2-\rho^2+d^2}{2dr}\right)^2}\sin\theta_N(r)dr. \end{cases} \tag{11}$$

The integrand is not simplified further here, as the non-uniform density beam case will be considered in the next section, which only makes the integrand more complicated, thus not allowing any simplification of the general form.

Let us consider a special case of $R_1 = d - \rho < 0$ with the layout corresponding to Fig. 6. For $0 < r < |R_1|$, the intersection of the two circles in (9) is purely imaginary, and hence the whole contour ($r, \varphi \in [-\pi, \pi)$) belongs to the beam, and one can assume for such r that φ goes from $-\pi$ to π. This is the approach used later for the non-uniform distribution.

5. Elliptical Beam, Normal or Arbitrary Distribution

Assume that the beam distribution is normal in both directions in every pair of coordinates, and each two directions are independent. As the beam is round in the normal form coordinates, the variances σ_x and $sigma_y$ in both eigen-directions are the same, i.e. $\sigma = \sigma_x = \sigma_y$, and hence the resulting density of the bivariate distribution is defined by the formula

$$f(x,y) = \frac{1}{2\pi\sigma^2}\exp\left(\frac{-((x-d)^2+y^2)}{2\sigma^2}\right),$$

as the mean values for the distribution are d and 0. Note that this formula is only valid for the initial distribution, when $\theta_N = 0$, and after N turns θ_N should be subtracted from the value of the angle.

A typical particle distribution after various number of turns is shown in Fig. 8.

In the case of the non-uniform distribution the expressions for S, x_c, and y_c are essentially the same as in Eqs. (11), except that now the integrand is complicated by the additional factor of $f(r\cos(\theta-\theta_N), r\sin(\theta-\theta_N))$. The term "$-\theta_N$" is introduced to always take the density of the initial normal distribution:

$$\begin{cases} S = \int_{R_1}^{R_2}\int_{-\varphi(r)+\theta_N(r)}^{\varphi(r)+\theta_N(r)} r f(r\cos(\theta-\theta_N), r\sin(\theta-\theta_N))d\theta dr; \\ x_c^{(N)} = \frac{1}{S}\int_{R_1}^{R_2}\int_{-\varphi(r)+\theta_N(r)}^{\varphi(r)+\theta_N(r)} r^2\cos\theta f(r\cos(\theta-\theta_N), r\sin(\theta-\theta_N))d\theta dr; \\ y_c^{(N)} = \frac{1}{S}\int_{R_1}^{R_2}\int_{-\varphi(r)+\theta_N(r)}^{\varphi(r)+\theta_N(r)} r^2\sin\theta f(r\cos(\theta-\theta_N), r\sin(\theta-\theta_N))d\theta dr. \end{cases} \tag{12}$$

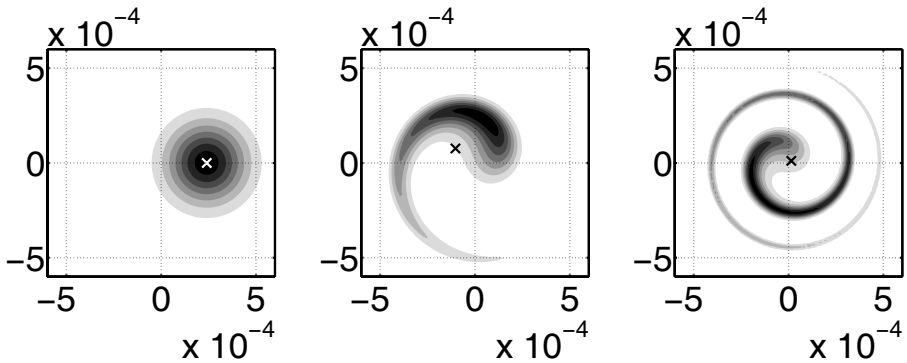

(a) initial distribution (b) after 1000 turns (c) after 3000 turns

Fig. 8. Particle distribution in the beam, the cross indicates the center of mass of the beam.

6. Numerical Experiment Results

All the numerical results of this section are based on the Tevatron model available on the Fermi National Accelerator Laboratory website.[1] All the calculations are performed using the arbitrary order code COSY INFINITY[6] written by Martin Berz, Kyoko Makino, et al. at Michigan State University. The source code for the lattice is in the format of the MAD programming environment,[7] for which a converter[8] to COSY INFINITY is readily available.

The calculation method described above allows one to find the dependence $r = r(N, c_1, c_2)$ for elliptical beams with an arbitrary particle distribution, the only requirement being that the initial distribution density function is known. Having this data available and employing various optimization methods, one can find the correct values of c_1 based on one particular measurement or both coefficients c_1 and c_2, provided that measurements for different kick strengths are available.

Let us compare the results of the proposed algorithm to the values obtained by tracking the nonlinear model of the Tevatron accelerator.

We use the beam position monitor (BPM) measurement results[2] similar to those shown in Fig. 1. The number of turns after which the amplitude of the center of mass falls down to half of its value varies depending on the BPM. Taking the average over the total of 115 reliable BPMs, one obtains that $N_{1/2} = 1021$.

A parameter fitting procedure results in the expected value of $c_1 = -2511$ for the initial beam amplitude after the kick of $r = 0.24 \cdot 10^{-3}$. Taking into account that $\mu_0 = 0.585$, one obtains

$$\mu \approx \mu_0 + c_1 r^2 = 0.585 - 1.4463 \cdot 10^{-4}. \tag{13}$$

To conceive how close the obtained value of c_1 is to the realistic value of the tune shift with amplitude, a comparison was performed in COSY using the nonlin-

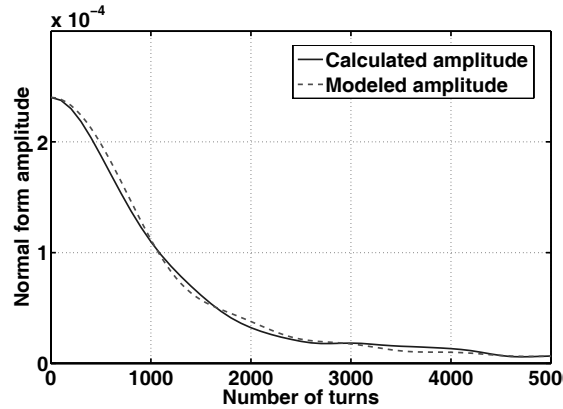

Fig. 9. Calculation results and the comparison with the nonlinear model.

ear model of the Tevatron available at the official lattice page at Fermilab.[1] The model reflects changes made to the accelerator as of November 2005, while the measurement results are dated January 2006. Hence, there are strong reasons to assume that the model distribution tracking should yield results comparable to the calculated value of the tune shift, and therefore, the measurements. The COSY calculation shows that the expected value of c_1 for the nonlinear model should be -2541, which means the calculated value found by applying the algorithm differs from the model value by 1.2%. At the same time, only the information about the distribution of the particles in the beam, the size of the beam, and the linear dynamics was used to find the nonlinear tune shift. Necessary additional information was extracted from the measurements.

Figure 9 shows the graphs of the calculated amplitude with $c_1 = -2511$ and the model amplitude with $c_1 = -2541$. The slight difference between the graphs can be explained not only by using different c_1's, but also by the fact that the fourth order term $c_2 r^4$ in the expansion of μ has not been taken into account. Also the nonlinear model represents an approximation to the real machine's optics. At the same time, the similarity of the graphs allows to conclude that the model represents the real machine quite accurately, at least for the low order nonlinearities affecting the tune shift (mainly the sextupole content of the ring).

Also, the validity of the approach studied is perfectly supported by the independent calculations done earlier. There is an estimate of the nonlinear tune shift[9] based on the approach by R.Meller et al.,[10] given by the following formula:

$$\mu \approx \mu_0 - \kappa A^2, \quad \kappa \approx \frac{1}{4\pi N_{1/2}}, \tag{14}$$

where A is the amplitude of the center of mass of the beam, measured in σ units of the beam under consideration. This formula is derived for the beams with a normal distribution of particles, and it represents a good approximation when the transversal kick is relatively weak (A is not too much greater then 1), and the

underlying dynamical system is weakly nonlinear with a quadratic term being the main contribution to the tune shift. It is noteworthy that Eq. (14) is connected to the initial distribution, the strength of the transversal kick and the transfer map of the system under consideration via A and $N_{1/2}$.

The comparison of the value κA^2 from Eq. (14) to the value of $c_1 r^2$, obtained by the calculation using the algorithm described above, leads to the following result: $\kappa = 7.96 \cdot 10^{-5}$, $A = 1.36$,

$$\mu \approx \mu_0 + \kappa A^2 = 0.585 - 1.4723 \cdot 10^{-4}, \tag{15}$$

that is, the difference between the values obtained using different approximations in Eqs. (13) and (15) is 1.75%.

7. Summary

The correspondence is found between the first and the most important term in the expansion of the nonlinear tune shift with amplitude and the BPM measurement results after the beam is kicked transversely. This correspondence can be found by fitting the parameter c_1. To be able to find the correct value of the parameter it is necessary to have the information on the behavior of the amplitude r of the center of mass. This amplitude can be found in the most general case using Eq. (12).

A method for the calculation of the nonlinear tune shift with amplitude was tested on the Tevatron BPM measurement results and compared to the nonlinear model calculations as well as the independent approximation formulas. In both cases the discrepancy was within 2%, which can be considered a very good result considering that only the information on the one-turn linear transfer map and the geometry of the beam has been used, while the lack of information on the nonlinear behavior was compensated by a single BPM measurement with one particular perturbation (kick) strength.

After the coefficient c_1 has been found, one might try finding the coefficient c_2 if multiple measurement results are available. On the other hand, in the case of the Tevatron, $c_2 r^4$ is 2 orders smaller than $c_1 r^2$, so in this particular study there was no attempt made to find c_2.

References

1. M. A. Martens. Tevatron lattice page. `http://www-ap.fnal.gov/~martens/tev_lattice/tev_lattice.html`.
2. Y. Alexahin. Private communication.
3. M. Berz. *Modern Map Methods in Particle Beam Physics*. Academic Press, San Diego, 1999. Also available at `http://bt.pa.msu.edu/pub`.
4. M. Abramowitz and I. A. Stegun (Eds.). *Handbook of Mathematical Functions with Formulas, Graphs, and Mathematical Tables*, pages 300–302. New York: Dover, 1972.
5. W. M. McKeeman. Algorithm 145: Adaptive numerical integration by Simpson's rule. *Communications of the ACM*, 5(12):604, 1962.
6. K. Makino and M. Berz. COSY INFINITY version 9. *Nuclear Instruments and Methods*, A558:346–350, 2005.

7. Methodical accelerator design. `http://mad.home.cern.ch/mad/`.
8. The MAD to COSY Converter. `http://cosy.pa.msu.edu/converters/mad2cosy`.
9. M. G. Minty and F. Zimmermann. *Measurement and Control of Charged Particle Beams*, pages 52–53. Particle acceleration and detection. Springer, 2003. ISBN 3-540-44187-5.
10. R. E. Meller, A. W. Chao, J. M. Peterson, S. G. Peggs, and M. Furman. Decoherence of kicked beams. Technical Report SSC-N-360, SSCL, 1987.

International Journal of Modern Physics A
Vol. 24, No. 5 (2009) 987–998

World Scientific
www.worldscientific.com

RECENT PROGRESS ON THE 6D COOLING SIMULATIONS IN THE GUGGENHEIM CHANNEL

PAVEL SNOPOK* and GAIL HANSON†

Deptartment of Physics and Astronomy, University of California, Riverside, CA 92521, USA
**pavel.snopok@ucr.edu*
†*gail.hanson@ucr.edu*

AMIT KLIER

Department of Particle Physics, Weizmann Inst. of Science, P.O. Box 26, Rehovot 76100, Israel
amit.klier@weizmann.ac.il

The RFOFO ring is considered to be one of the most promising six-dimensional cooling channels proposed for the future muon collider. It has a number of advantages over other cooling channels, but it also has certain drawbacks. The injection and extraction issue as well as the absorber overheating are its main problems. In this article the simulations of a possible solution to these problems, the RFOFO helix, commonly referred to as the Guggenheim channel, are studied in detail. The details of the tracking studies of both the idealized and realistic lattices are presented and compared to the performance of the underlying RFOFO cooling ring design.

Keywords: Muon collider; ionization cooling; six-dimensional dynamics simulations; Guggenheim cooling channel.

PACS numbers: 29.20.db, 29.27.-a, 29.27.Bd, 41.75.Lx

1. Introduction

In a muon collider design the muon beam 6D phase space volume must be reduced in order to be able to further accelerate it and inject into the storage ring. Ionization cooling is currently the only feasible option for cooling the beam within the muon lifetime ($\tau_0 = 2.19\ \mu s$). The RFOFO ring[1,2] is one of the feasible options currently under active investigation along with other designs.[3,4,5] The RFOFO ring provides an impressive reduction in the six-dimensional emittance in a small number of turns with a relatively low particle loss factor. However, the design of the injection and extraction channels and kickers is very challenging, and this ring could not be used as is, because the bunch train is too long to fit in the ring. Both problems would be

Table 1. RFOFO and Guggenheim parameters.

	RFOFO	**Guggenheim**
Circumference, [m]	33.00	32.86
Pitch, [m]	0	3.00
Pitch angle, [deg]	0	5.22
Radius, [mm]	5252.113	5230.365
Maximum axial field, [T]	2.77	2.80
Coil tilt (wrt orbit), [deg]	3.04	3.04
Average momentum, [MeV/c]	220	220
Reference momentum, [MeV/c]	201	201
RF frequency, [MHz]	201.25	201.25
RF gradient, [MV/m]	12.835	12.621
Absorber angle, [deg]	110	110
Absorber thickness on beam axis, [cm]	27.13	27.13

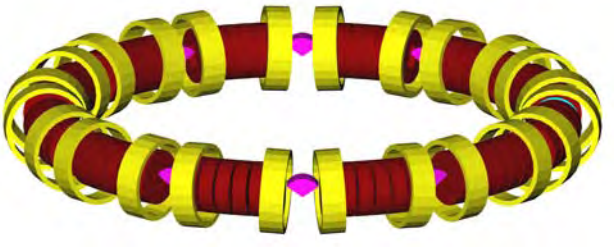

Fig. 1. RFOFO ring.

removed in the RFOFO helix, also known as the Guggenheim[a] channel.[6] In addition, utilizing the helix solves another important problem, namely, the overheating in the absorbers. Also, since the injection and extraction come naturally with the Guggenheim design, full use of all 12 cells for cooling is possible as opposed to the RFOFO ring in which RF cavities and absorbers in two of the 12 cells should be removed for the purposes of installing utility insertions.

2. Lattice Description, Modeling the Helix

The lattice of the Guggenheim channel is based on the RFOFO ring lattice[7,8] and inherits most of its parameters with little or no change. The RFOFO ring is shown in Fig.1, and its vital parameters are summarized and compared to the RFOFO helix parameters in Table 1. The only difference between the ring and the helix is the change in the elevation of the elements. The helix has a pitch of $\arcsin(H/R)$, where H is the distance between the corresponding elements of the two subsequent turns, and R is the radius of the helix. It should be noted that the radius of the helix is slightly smaller than the radius of the ring in order to keep the same path

[a]Refers to the Solomon R. Guggenheim Museum in New York with its helical gallery, details at `http://www.guggenheim.org/the_building.html`

length over one turn. Since the circumference of the original RFOFO ring is 33 m, its radius is 5252.113 mm, while the radius of the Guggenheim is 5230.365 mm.

The longitudinal magnetic field on axis has an approximately sinusoidal dependence on position with a peak magnitude of 2.8 T. The solenoids are tipped to produce an average vertical dipole field of 0.125 T on axis. The beam axis is displaced laterally with respect to the coil centers to minimize horizontal fields that cause unwanted deviations of the reference orbit. The desired horizontal magnetic field that changes the reference orbit from circular to helical is generated by tipping all the solenoids further by the fixed pitch angle of 5.22 degrees. The lattice transmits particles in the momentum band from 160 to 260 MeV/c.

The RF cavities are modeled using cylindrical pillboxes. The cavities are located in a dipole field in this design. The RF cavities are at a frequency of 201.25 MHz and have an accelerating gradient of 12 MV/m to compensate for the energy loss in absorbers.

The liquid-hydrogen wedge absorbers only extend part way across the gap, such that a particle on the reference orbit always loses the same amount of energy crossing the wedge. The absorber has a central thickness of 27.13 cm and a total wedge angle of 110 degrees. The absorber central plane is perpendicular to the direction of the beam.

3. Preliminary Analysis of the Lattice

All the simulations in this article are performed using the G4Beamline code by Tom Roberts,[9] based on the Geant4[10] simulation toolkit. G4Beamline performs a particle-by-particle tracking. Muon decay and stochastic processes can be either taken into account or turned off. The magnetic field of the solenoids is generated by the simulation software before the tracking and saved as a field map. The effect of all the solenoids in the lattice is taken into account at any point on the trajectory of each particle.

Since the Guggenheim is not symmetric as compared to the RFOFO ring, we consider only the middle half of the ring in the initial study sequence to avoid problems with significant field discrepancies at both ends of the structure. This layout is shown in Fig.2.

A Gaussian input beam[11] is typically used in the simulations with a normalized transverse emittance of 12 mm and a normalized longitudinal emittance of 18.4 mm. The reference particle momentum is 201 MeV/c. This value was chosen to make the circulation time on the helix equal to the 25th harmonic of 201.25 MHz. The initial beam has a correlation between the axial momentum and the transverse amplitude, to minimize the tendency for the particles in the bunch to spread out longitudinally in the solenoidal field.

Muons are injected at the boundary of the cell (the absorber central plane), where the transverse momentum vanishes for a reference orbit. The reference orbit is offset by -10.25 mm in x and by 17.62 mm in y at the beginning of the cell.

Fig. 2. Guggenheim helix.

By tracking the particles through the half-turn lattice repeatedly one can simulate the multiturn behavior in an idealized RFOFO helix.

The results of this simulation serve as the point of reference for all the subsequent simulations. Also, the results are compared to the RFOFO ring performance. By adjusting the parameters of the Guggenheim its performance can be made virtually the same as the RFOFO ring. However, one should not forget that in the realistic RFOFO ring, as opposed to the ideal case shown, only 10 cells out of 12 are filled with RF cavities and used for cooling, while the Guggenheim does not suffer such a decrease in performance.

4. 5-Turn Scheme

It is useful and instructive to study the multilayer Guggenheim layout, to see how significant the change in the field is when neighboring layers are added, and how it affects the performance. This allows one to draw conclusions about the efficiency of the unshielded structure and evaluate its feasibility.

The geometry of the helix is the same as in the one layer case. However, there are two major changes in the magnetic field: the longitudinal field at the beginning and at the end of the structure is severely affected due to the absence of the neighboring cells. This problem can be efficiently mitigated by introducing extra pair of coils before the first cell and after the last cell. These extra coils are marked in Fig.3. Using these extra coils is extremely important, especially in the beginning of the structure, because otherwise many particles will be lost right at the injection. The two coils at the end might not be dramatically important, especially since the particles from the Guggenheim are fed into a matching section of the downstream channel.

Another problem, namely, the asymmetry in the first and last turns of the helix, is a more serious issue. Fig.4 shows the vertical component of the magnetic field on the geometrical helix of radius $R = 5230.36$ mm and $H = 3000$ mm. It clearly demonstrates that the three middle turns are not affected and can still perform well,

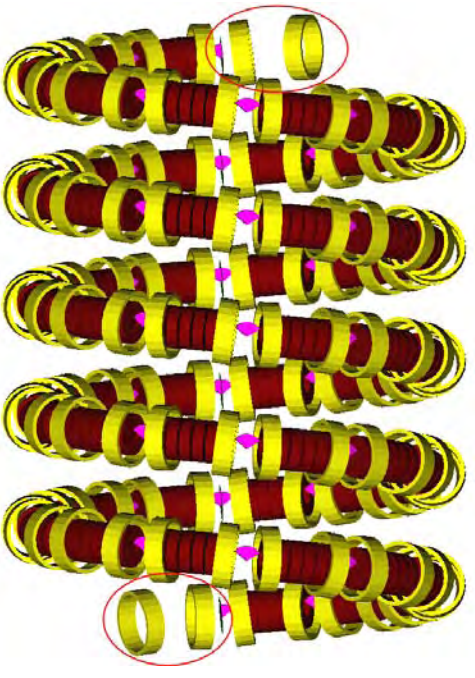

Fig. 3. Multilayer lattice.

while in the two extreme turns, especially in the innermost cells, the changes are drastic. Many particles are lost in cells 11 and 12 of the first and fourth turn, cells 1 and 2 of the second and last turn. These areas are marked in Fig.4. The changes in the longitudinal and radial components of the magnetic field on the geometric helix are not significant compared to the one layer scheme, Fig.5.

Various attempts were made to compensate for the change in the magnetic field; however, the most efficient way is probably to shield the layers from one another in the vertical direction. Another option might be to use only the inner turns, and replace the extreme turns by a simpler configuration of magnets generating a vertical field similar to the one of the full helix turn of tilted coils, but that requires a separate study.

5. Acceptance Analysis

To rule out one of the possible causes of particle loss for the 5-layer layout, namely, the loss due to the mismatch between the injected beam and the phase space that can be transmitted through the structure, acceptance studies are in order. The results of acceptance analysis at the central momentum are shown in Fig.6. They suggest that all particles in the beam at this particular momentum are within the transmitted volume. The full acceptance analysis has also been performed to locate loss regions, especially in the longitudinal direction.

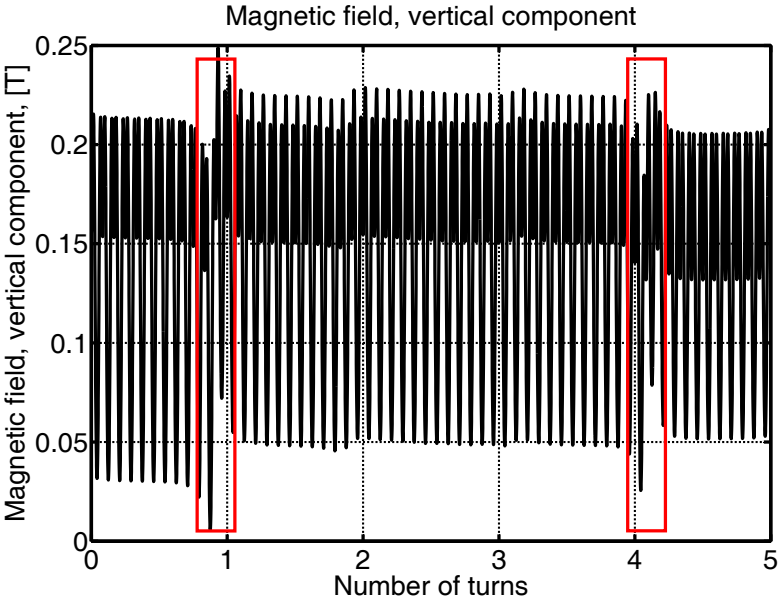

Fig. 4. Magnetic field discrepancies in the multiturn Guggenheim layout.

A 6-dimensional grid of 262144 particles was tracked through the 5-layer Guggenheim lattice in order to find the full 6-dimensional acceptance of the channel and check whether the beam commonly used for simulations is matched to the acceptance. The scatterplots of the acceptance are shown in Fig.7.

The analysis shows that the beam matches the acceptance of the structure, and no particle loss is attributed to the initial beam mismatch. However, the longitudinal size of the initial distribution is slightly larger than the accepted $160 \leq p_z \leq 260$ MeV/c as well as $-1 \leq t \leq 1$ ns. This fact is responsible for approximately 6% of the loss in transmission.

6. Realistic Scheme Analysis

The study of the 5-turn Guggenheim layout showed that vertical shielding is necessary between individual layers to eliminate the discrepancies in the vertical component of the magnetic field. Another study by A. Klier[12] showed that adding shielding material between layers does not affect the paraxial magnetic field significantly, as compared to the single layer case. Therefore, the idealized half turn lattice model described above in Section 3 can be used with no further modification to analyze the more realistic shielded case.

For a more realistic layout of the Guggenheim cooling channel it is necessary to consider the effects of the aluminum windows in the wedge absorbers as well as beryllium windows in the RF cavities. Including windows introduces new sources of scattering and degrades the cooling performance.

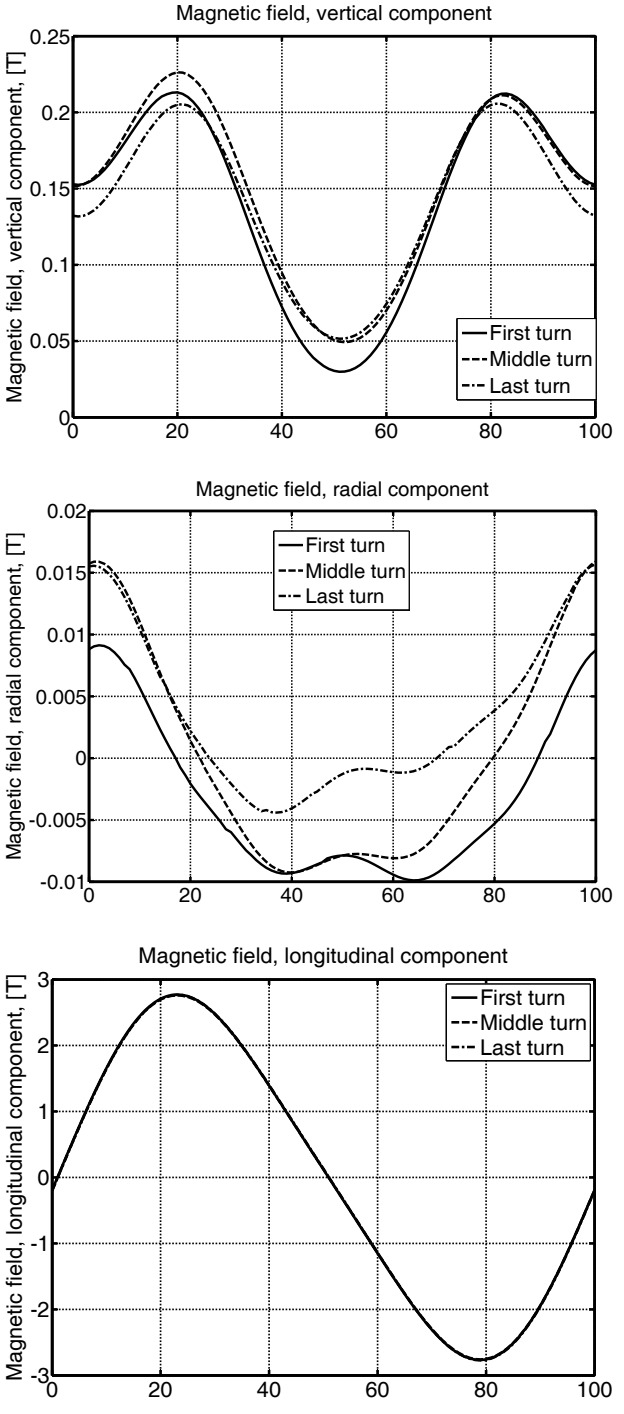

Fig. 5. Components of the magnetic field in various turns of the multiturn Guggenheim layout.

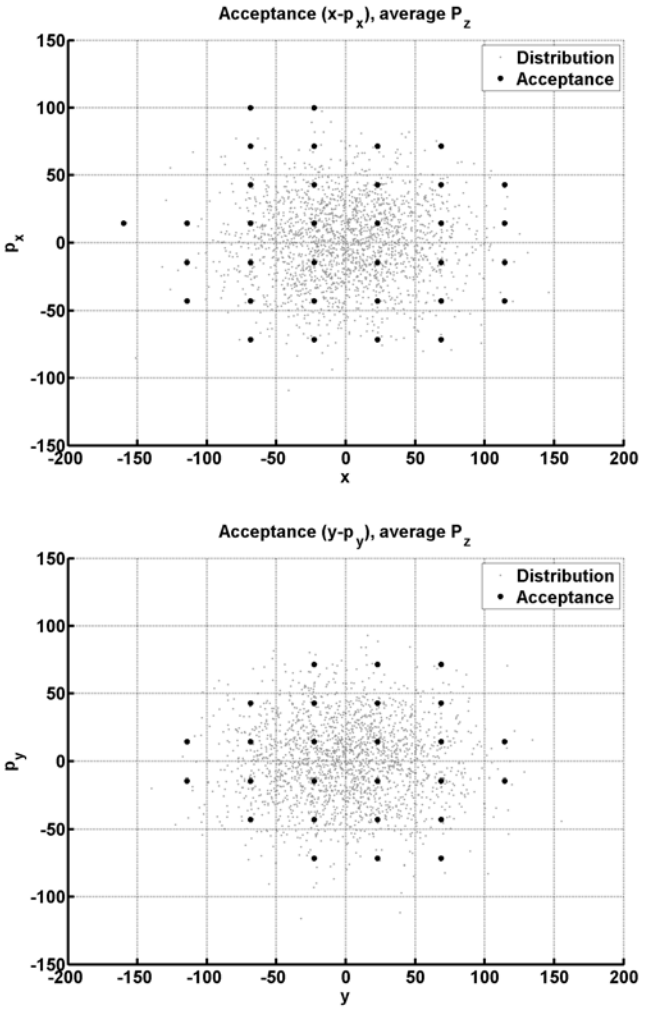

Fig. 6. Particle distribution vs. Guggenheim channel acceptance for the central momentum of $P_z = 220$ MeV/c.

The RF cavities are enclosed with tapered beryllium end windows. The RF windows are stepped in thickness radially, in order to provide minimum thickness near the beam axis and still control the temperature increase due to RF heating. The thickness of the windows is taken to be 175 and 350 μm for the internal windows and 50 and 100 μm for the external ones. These are the values suggested by the Neutrino Factory feasibility study II,[13] divided by 4.[1]

The absorbers are enclosed with aluminum windows 360 μm thick, located right next to and conforming to the wedge shape of the absorber. In addition to these windows, extra security windows of the same thickness are considered. The simulated security windows are planar and located axially on both sides of the wedge.

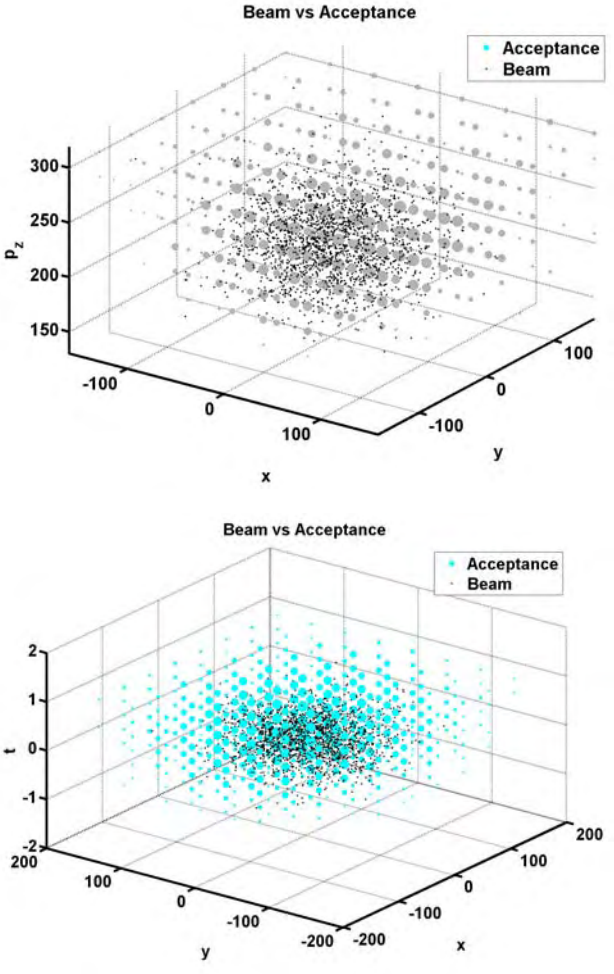

Fig. 7. Scatterplots of particle distribution vs. Guggenheim channel acceptance, $(x-y-p_z)$ and $(x-y-t)$ projections.

These additions result in considerable change of performance as compared to the ideal helix. The 6D emittance is reduced by a factor of 361 in the ideal case and the transmission is expected to be 51% after 15 turns (495 m), while in the realistic case the 6D emittance is reduced by a factor of 61 with the transmission of 48%. Other merit factors are compared in the next section. Still, the cooling performance of the realistic Guggenheim channel is very promising.

7. Summary, Simulation Results Comparison

The results of different simulations including the RFOFO ring, the ideal Guggenheim helix, the realistic Guggenheim helix and the 5-layer Guggenheim layout are summarized in Fig.8. Here the transverse emittance and longitudinal emittance are

Table 2. Decrease in variation for different models.

		Structure			
Parameter	Turn #	RFOFO ideal	Guggenheim ideal	Guggenheim realistic	Guggenheim 5 layers
σ_x [mm]	0	41.79	41.79	41.79	41.79
	5	25.48	27.05	28.81	30.72
	10	19.62	20.74	25.58	-
	15	18.71	19.47	26.60	-
σ_y [mm]	0	42.86	42.86	42.86	42.86
	5	24.14	27.72	30.10	38.08
	10	18.61	21.74	27.77	-
	15	18.24	20.81	26.73	-
σ_p [MeV/c]	0	27.85	27.85	27.85	27.85
	5	11.80	12.00	13.58	12.79
	10	7.98	8.40	11.55	-
	15	7.37	7.45	10.83	-
σ_t [ns]	0	0.298	0.298	0.298	0.298
	5	0.235	0.237	0.261	0.364
	10	0.171	0.166	0.201	-
	15	0.143	0.144	0.185	-

given in millimeters, the 6D emittance—in mm^3, the transmission—in percent of the initial number of particles in the beam. There are a number of factors introduced to evaluate the performance of cooling channels. Among them, the quantity M-factor, defined by $M = \frac{\varepsilon_6(\text{initial})}{\varepsilon_6(\text{final})} \times$ Transmission, is most useful for collider applications. All of the above criteria have been calculated using ECALC9 ver.2 by Gregg Penn, the de facto emittance calculation standard for the Muon Collaboration.[14,15]

In addition to the qualitative comparison represented by Fig.8 the quantitative results are summarized in Table 2. This table shows the change in the variation of the transverse coordinates x and y, total momentum p, and the time of flight t after a number of turns in the cooling channel for various models. The phase portraits in $(x - p_x)$, $(y - p_y)$ and $(t - p_z)$ before and after cooling are given in Fig.9.

It should be noted that the viability of the Guggenheim channel depends to a large extent on the issue of whether the RF cavities work in a magnetic field.[16] It should be proved by experiment that RF cavities at 12 MV/m do not break down in the magnetic field of up to 3 T (on the central axis). As an alternative, the open cell approach might be considered,[17] which allows the RF cavities to be moved outside the magnetic field.

Another issue is the behavior of the M-factor. As the graph in Fig.8 shows, the efficiency of the Guggenheim cooling channel at a fixed frequency decreases as the number of turns grow. After nine turns in the realistic Guggenheim, both the 6D emittance graph and the merit factor graph become essentially flat. To solve this problem, the concept of the tapered cooling channel is suggested,[18] where the radius of the helix decreases and the RF frequency increases with the number of turns. This concept is currently being investigated.

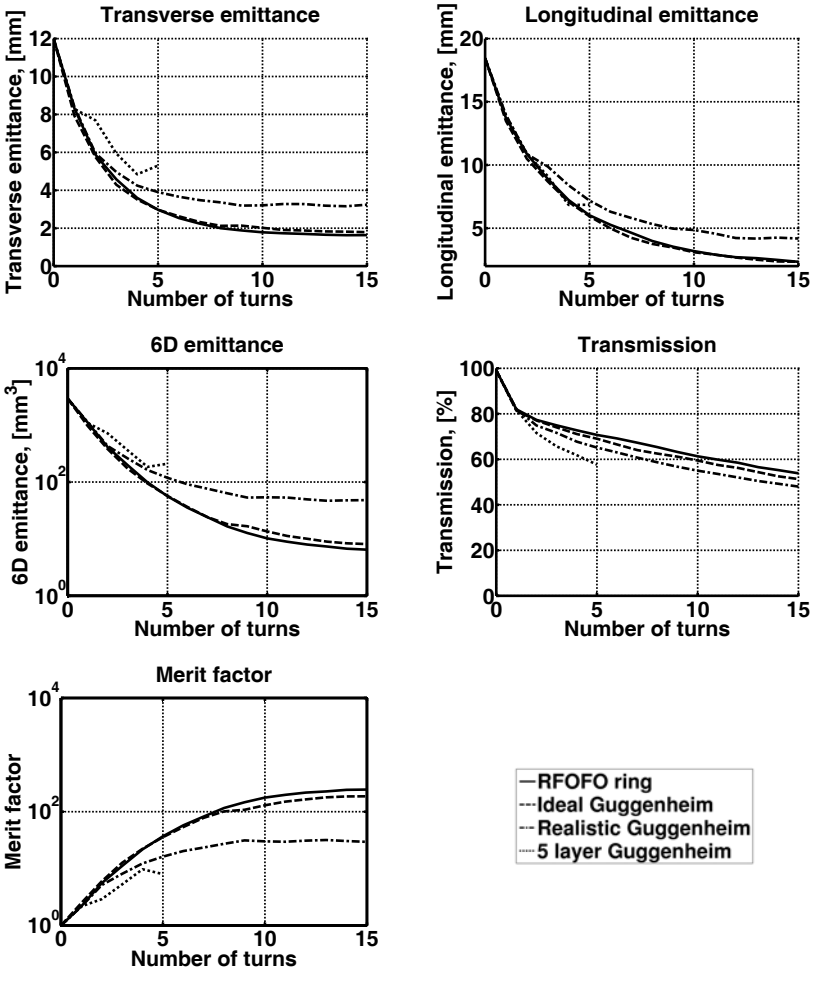

Fig. 8. Left to right, top to bottom: transverse emittance, longitudunal emittance, 6D emittance, transmission and merit factor for various models.

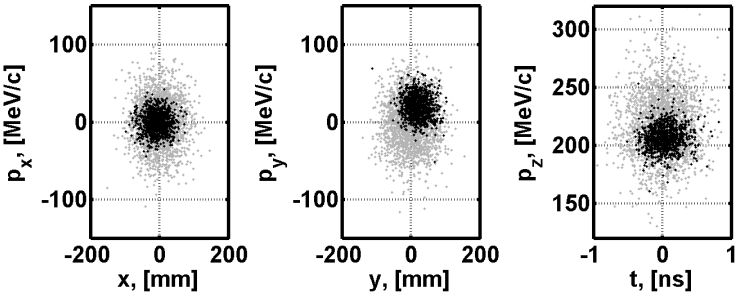

Fig. 9. Reduction in the 6D phase space due to cooling. Gray—initial distribution, black—after 15 turns in the realistic Guggenheim cooling channel (495 m).

References

1. R. Palmer et al. Ionization cooling ring for muons. *Phys. Rev. ST Accel. Beams*, 8(6):061003, Jun 2005.
2. J. S. Berg, R. C. Fernow, and R. B. Palmer. RFOFO ring cooler. *Journal of Physics G: Nuclear and Particle Physics*, 29:1657–1659, 2003. DOI: 10.1088/0954-3899/29/8/325.
3. D. Kaplan. MANX: A 6D ionization cooling experiment. arXiv: 0711.1523v1, 2007.
4. Y. Alexahin, K. Yonehara, and R. Palmer. 6D ionization cooling channel with resonant dispersion generation. In *Proceeding of Particle Accelerator Conference*, 2007.
5. C. Johnstone, M. Berz, and K. Makino. Linear quadrupole cooling channel for a neutrino factory. In *Proc. of Particle Accelerator Conference*, pages 3526–3529, 2005.
6. A. Klier. Last report on RFOFO and Guggenheim. NFMCC Friday Meetings, 2006.
7. Fernow R. C., Berg J. S., Gallardo J. C., and Palmer R. B. Muon cooling in the RFOFO ring cooler. In *Proceeding of Particle Accelerator Conference*, 2003.
8. A. Klier and Gail G. Hanson. Geant simulation of muon cooling rings. *Nucl. Phys. B—Proc. Suppl.*, 155, 1:277–278, 2006.
9. T. Roberts. G4Beamline, a "swiss army knife" for Geant4, optimized for simulating beamlines. http://www.muonsinc.com.
10. S. Agostinelli et al. Geant4—a simulation toolkit. *Nucl. Instr. and Meth. in Phys. Res. Sect. A*, 506(3):250–303.
11. V. Balbekov. Simulation of RFOFO ring cooler with tilted solenoids. MUC-NOTE-THEORY-264, 2002.
12. A. Klier. "Shielding" demonstration in a simplified RFOFO cell. KEK, International Neutrino Factory and Superbeam Scoping Study Meeting, 2006.
13. S. Ozaki, R. B. Palmer, M. S. Zisman, and J. C. Gallardo, editors. *Feasibility Study II of a Muon-Based Neutrino Source*, 2001.
14. R. Fernow. Phys. analysis performed by ECALC9. MUC-NOTE-THEORY-280, 2003.
15. G. Penn. ECALC9, fortran code.
16. R. Palmer. Studies of the 'rf in magnetic field' problem. NFMCC Friday Meeting, March 2008.
17. R. B. Palmer, J. S. Berg, and R. Fernow. Open cell lattices. NFMCC Friday Meeting, March 23, 2007.
18. R. B. Palmer and et al. A complete scheme of ionization cooling for a Muon Collider. In *Proceeding of Particle Accelerator Conference*, 2007.

International Journal of Modern Physics A
Vol. 24, No. 5 (2009) 999–1008

World Scientific
www.worldscientific.com

PLASMA STABILIZATION BASED ON MODEL PREDICTIVE CONTROL

MARGARITA SOTNIKOVA

Faculty of Applied Mathematics and Control Processes, Saint Petersburg State University, 35 Universitetskii pr., Saint Petersburg, 198504, Russia
s_margosha@mail.ru

The nonlinear model predictive control algorithms for plasma current and shape stabilization are proposed. Such algorithms are quite suitable for the situations when the plant to be controlled has essentially nonlinear dynamics. Besides that, predictive model based control algorithms allow to take into account a lot of requirements and constraints involved both on the controlled and manipulated variables. The significant drawback of the algorithms is that they require a lot of time to compute control input at each sampling instant. In this paper the model predictive control algorithms are demonstrated by the example of plasma vertical stabilization for ITER-FEAT tokamak. The tuning of parameters of algorithms is performed in order to decrease computational load.

Keywords: Model predictive control; plasma vertical stabilization.

PACS numbers: 11.25.Hf, 123.1K

1. Introduction

Tokamaks, as future nuclear power plants, currently present exceptionally significant research area. The basic problems are electromagnetic control of the plasma current, shape and position. High-performance plasma control in a modern tokamak is the complex problem. This is mainly connected with the design requirements imposed on magnetic control system and power supply physical constraints. Besides that, plasma is an extremely complicated dynamical object from the modeling point of view and usually control system design is based on simplified linear system, representing plasma dynamics in the vicinity of the operating point. This paper is focused on the control systems design on the base of Model Predictive Control (MPC).[1,2] Such systems provide high-performance control in the case when accurate mathematical model of the plant to be controlled is unknown. In addition, these systems allow to take into account constraints, imposed both on the controlled and manipulated variables.[3] Furthermore, MPC algorithms can base on both linear and nonlinear mathematical models of the plant. So MPC control scheme is quite suitable for plasma stabilization problems. However, predictive control algorithms are very time-consuming, since they require the repeated on-line solution of the

optimization problem at each sampling instant. Plasma vertical stabilization problem for the ITER-FEAT machine is considered to illustrate MPC algorithms. The problem of real-time implementation is investigated.

2. Control Problem Formulation

2.1. *Mathematical model of the plasma vertical stabilization process in ITER-FEAT tokamak*

The dynamics of plasma control process can be commonly described by the system of ordinary differential equations [4,5]

$$\frac{d\Psi}{dt} + RI = V, \tag{1}$$

where Ψ is the poloidal flux vector, R is a diagonal resistance matrix, I is a vector of active and passive currents, V is a vector of voltages applied to coils. The vector Ψ is given by nonlinear relation

$$\Psi = \Psi(I,\, I_p), \tag{2}$$

where I_p is the plasma current. The vector of output variables is given by

$$y = y(I, I_p). \tag{3}$$

Linearizing equations (1)–(3) in the vicinity of the operating point, we obtain a linear model of the process in the state space form. In particular, the linear model describing plasma vertical control in ITER-FEAT tokamak is presented below.

ITER-FEAT tokamak[6] has a separate fast feedback loop for plasma vertical stabilization. The Vertical Stabilization (VS) converter is applied in this loop. Its voltage is evaluated in the feedback controller, which uses the vertical velocity of plasma current centroid as an input. So the linear model can be written as follows

$$\begin{aligned} \dot{\mathbf{x}} &= \mathbf{A}\mathbf{x} + \mathbf{b}u, \\ y &= \mathbf{c}\mathbf{x} + du, \end{aligned} \tag{4}$$

where $\mathbf{x} \in \mathbf{E}^{58}$ is a state space vector, $u \in E^1$ is the voltage of the VS converter, $y \in E^1$ is the vertical velocity of the plasma current centroid.

Since the order of this linear model is very high, an order reduction is desirable to simplify the controller synthesis problem. The standard Matlab function ***schmr*** was used to perform model reduction **from 58th to 3rd** order. As a result, we obtain a transfer function of the reduced SISO model (from input u to output y)

$$P(s) = \frac{1.732 \cdot 10^{-6}(s - 121.1)(s + 158.2)(s + 9.641)}{(s + 29.21)(s + 8.348)(s - 12.21)}. \tag{5}$$

This transfer function has poles which dominate the dynamics of the initial plant. The unstable pole corresponds to vertical instability. It is natural to assume that two other poles are determined by the virtual circuit dynamic related to the most significant elements in the tokamak vessel construction. The quality of the model

reduction can be illustrated by the comparison of the Bode diagram for both initial and reduced models. Fig. 1 shows the Bode diagrams for initial and reduced 3^{rd} order models on the left and for initial and reduced 2^{nd} order model on the right. It is easy to see that the curves for initial model and reduced 3^{rd} order model are actually indistinguishable, contrary to the 2^{nd} order model.

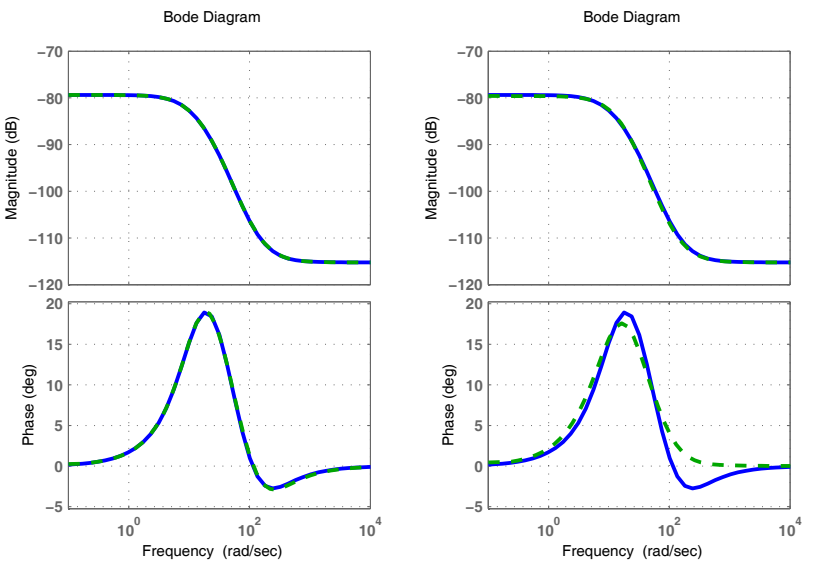

Fig. 1. Bode diagrams for initial (solid lines) and reduced (dotted lines) models.

In addition to plant model (5), we must take into account the following limits that are imposed on the power supply system

$$V_{\max}^{VS} = 0.6kV,\ I_{\max}^{VS} = 25kA, \tag{6}$$

where $V_{\max}^{VS}$ is the maximum voltage, $I_{\max}^{VS}$ is the maximum current in the VS converter. So, the linear model (5) together with constraints (6) is considered in the following as the basis for controller synthesis.

2.2. *Optimal control problem formulation*

The desired controller must stabilize vertical velocity of the plasma current centroid. One of the approaches to control synthesis is based on the optimal control theory. In this framework, plasma vertical stabilization problem can be stated as follows. One needs to find a feedback control algorithm $u = u(t, y)$ that provides a minimum of the quadratic cost functional

$$J = J(u) = \int_0^\infty (y^2(t) + \lambda u^2(t))dt, \tag{7}$$

subject to plant model (5) and constraints (6), and guarantees closed-loop stability. Here λ is a constant multiplier setting the trade-off between controllers performance and control energy costs.

Specifically, in order to find an optimal controller, LQG-synthesis can be performed. Such a controller has high stabilization performance in the unconstrained case. However, it is perhaps not the best choice in the presence of constraints.

Contrary to this, the MPC synthesis allows to take into account constraints. Its basic scheme implies on-line optimization of the cost functional (7) over a finite horizon subject to plant model (5) and imposed constraints (6).

3. Model Predictive Control Algorithms

3.1. *MPC Basic Principles*

Suppose we have a mathematical model, which approximately describes control process dynamics

$$\dot{\tilde{\mathbf{x}}}(\tau) = \mathbf{f}(\tau, \tilde{\mathbf{x}}(\tau), \tilde{\mathbf{u}}(\tau)), \quad \tilde{\mathbf{x}}|_{\tau=t} = \mathbf{x}(t). \tag{8}$$

Here $\tilde{\mathbf{x}}(\tau) \in \mathbf{E}^n$ is a state vector, $\tilde{\mathbf{u}}(\tau) \in \mathbf{E}^m$ is a control vector, $\tau \in [t, \infty]$, $\mathbf{x}(t)$ is the actual state of the plant at the instant t or its estimation based on measurement output.

This model is used to predict future outputs of the process given the programmed control $\tilde{\mathbf{u}}(\tau)$ over a finite time interval $\tau \in [t, t + T_p]$. Such a model is called **prediction model** and the parameter T_p is named **prediction horizon**. Integrating system (8) we obtain $\tilde{\mathbf{x}}(\tau) = \tilde{\mathbf{x}}(\tau, \mathbf{x}(t), \tilde{\mathbf{u}}(\tau))$—predicted process evolution over time interval $\tau \in [t, t + T_p]$.

The programmed control $\tilde{\mathbf{u}}(\tau)$ is chosen in order to minimize quadratic cost functional over the prediction horizon

$$J = J(\mathbf{x}(t), \tilde{\mathbf{u}}(\cdot), T_p) = \int_t^{t+T_p} ((\tilde{\mathbf{x}} - \mathbf{r}_x)' \mathbf{R}(\tilde{\mathbf{x}})(\tilde{\mathbf{x}} - \mathbf{r}_x) + (\tilde{\mathbf{u}} - \mathbf{r}_u)' \mathbf{Q}(\tilde{\mathbf{x}})(\tilde{\mathbf{u}} - \mathbf{r}_u)) d\tau, \tag{9}$$

where $\mathbf{R}(\tilde{\mathbf{x}})$, $\mathbf{Q}(\tilde{\mathbf{x}})$ are positive definite symmetric weight matrices, $\mathbf{r}_x$, $\mathbf{r}_u$ are state and control input reference signals. In addition, the programmed control $\tilde{\mathbf{u}}(\tau)$ should satisfy all of the constraints imposed on the state and control variables. Therefore, the programmed control $\tilde{\mathbf{u}}(\tau)$ over prediction horizon is chosen to provide minimum of the following optimization problem

$$J(\mathbf{x}(t), \tilde{\mathbf{u}}(\cdot), T_p) \to \min_{\tilde{\mathbf{u}}(\cdot) \in \Omega_u}, \tag{10}$$

where Ω_u is the admissible set given by

$$\Omega_u = \left\{ \tilde{\mathbf{u}}(\cdot) \in \mathbf{K}_n^0[t, t + T_p] : \tilde{\mathbf{u}}(\tau) \in \mathbf{U},\ \tilde{\mathbf{x}}(\tau, \mathbf{x}(t), \tilde{\mathbf{u}}(\tau)) \in \mathbf{X},\ \forall \tau \in [t, t + T_p] \right\}. \tag{11}$$

Here, $\mathbf{K}_n^0[t, t+T_p]$ is the set of piecewise continuous vector functions over the interval $[t, t + T_p]$, $\mathbf{U} \in \mathbf{E}^m$ is the set of feasible input values, $\mathbf{X} \in \mathbf{E}^n$ is the set of feasible state values.

Denote by $\tilde{\mathbf{u}}^*(\tau)$ the solution of the optimization problem (10), (11). In order to implement feedback loop, the obtained optimal programmed control $\tilde{\mathbf{u}}^*(\tau)$ is used as the input only on the time interval $[t, t+\delta]$, where $\delta << T_p$. So, only a small part of $\tilde{\mathbf{u}}^*(\tau)$ is implemented. At time $t+\delta$ the whole procedure—prediction and optimization—is repeated again to find new optimal programmed control over time interval $[t+\delta,\, t+\delta+T_p]$. Summarizing, the basic MPC scheme works as follows:

(i) Obtain the state estimation $\hat{\mathbf{x}}$ on the base of measurements $\mathbf{y}$.
(ii) Solve the optimization problem (10), (11) subject to prediction model (8) with initial conditions $\tilde{\mathbf{x}}|_{\tau=t} = \hat{\mathbf{x}}(t)$ and cost functional (9).
(iii) Implement obtained optimal control $\tilde{\mathbf{u}}^*(\tau)$ over time interval $[t, t+\delta]$.
(iv) Repeat the whole procedure 1–3 at time $t+\delta$.

From the previous discussion, the most significant MPC features can be noted:

- Both linear and nonlinear model of the plant can be used as a prediction model.
- MPC allows taking into account constraints imposed both on the input and output variables.
- MPC is the feedback control with the discrete entering of the measurement information at each sampling instant 0, δ, 2δ, ...
- MPC control algorithms imply the repeated (at each sampling instant with interval δ) on-line solution of the optimization problems. It is especially important from the real-time implementation point of view, because fast calculations are needed.

3.2. *MPC real-time implementation*

In order for real-time implementation, piece-wise constant functions are used as a programmed control over the prediction horizon. That is, the programmed control $\tilde{\mathbf{u}}(\tau)$ is presented by the sequence$\{\tilde{\mathbf{u}}_k, \tilde{\mathbf{u}}_{k+1}, ..., \tilde{\mathbf{u}}_{k+P-1}\}$, where $\tilde{\mathbf{u}}_i \in \mathbf{E}^m$ is the control input at the time interval $[i\delta, (i+1)\delta]$, δ is the sampling interval. Note that, P is a number of sampling intervals over the prediction horizon, that is $T_p = P\delta$. Likewise, general MPC formulation presented above consider nonlinear prediction model in the discrete form

$$\begin{aligned} &\tilde{\mathbf{x}}_{i+1} = \mathbf{f}(\tilde{\mathbf{x}}_i, \tilde{\mathbf{u}}_i), \quad i = k+j, \quad j = 0, 1, 2, ..., \quad \tilde{\mathbf{x}}_k = \mathbf{x}_k, \\ &\tilde{\mathbf{y}}_i = \mathbf{C}\tilde{\mathbf{x}}_i. \end{aligned} \tag{12}$$

Here $\tilde{\mathbf{y}}_i \in \mathbf{E}^r$ is the vector of output variables, $\mathbf{x}_k \in \mathbf{E}^n$ is the actual state of the plant at time instant k or its estimation on the base of measurement output. We shall say that the sequence of vectors $\{\tilde{\mathbf{y}}_{k+1}, \tilde{\mathbf{y}}_{k+2}, ..., \tilde{\mathbf{y}}_{k+P}\}$ represents the prediction of future plant behavior.
Similar to the cost functional (9), consider also its discrete analog given by

$$\begin{aligned} J_k = J_k(\bar{\mathbf{y}}, \bar{\mathbf{u}}) = \sum_{j=1}^{P} \big[&(\tilde{\mathbf{y}}_{k+j} - \mathbf{r}^y_{k+j})^T \mathbf{R}_{k+j} (\tilde{\mathbf{y}}_{k+j} - \mathbf{r}^y_{k+j}) \\ &+ (\tilde{\mathbf{u}}_{k+j-1} - \mathbf{r}^u_{k+j-1})^T \mathbf{Q}_{k+j} (\tilde{\mathbf{u}}_{k+j-1} - \mathbf{r}^u_{k+j-1}) \big], \end{aligned} \tag{13}$$

where $\mathbf{R}_{k+j}$ and $\mathbf{Q}_{k+j}$ are the weight matrices as in the functional (9), $\mathbf{r}_i^y$ and $\mathbf{r}_i^u$ are the output and input reference signals,

$$\bar{\mathbf{y}} = \left(\tilde{\mathbf{y}}_{k+1}\ \tilde{\mathbf{y}}_{k+2}\ ...\ \tilde{\mathbf{y}}_{k+P} \right)^T \in \mathbf{E}^{rP},$$
$$\bar{\mathbf{u}} = \left(\tilde{\mathbf{u}}_k\ \tilde{\mathbf{u}}_{k+1}\ ...\ \tilde{\mathbf{u}}_{k+P-1} \right)^T \in \mathbf{E}^{mP}$$

are the auxiliary vectors.

The optimization problem (10), (11) can now be stated as follows

$$J_k(\mathbf{x}_k, \tilde{\mathbf{u}}_k, \tilde{\mathbf{u}}_{k+1}, ...\tilde{\mathbf{u}}_{k+P-1}) \to \min_{\{\tilde{\mathbf{u}}_k, \tilde{\mathbf{u}}_{k+1}, ..., \tilde{\mathbf{u}}_{k+P-1}\} \in \Omega \in \mathbf{E}^{mP}}, \tag{14}$$

where $\Omega = \{\bar{\mathbf{u}} \in \mathbf{E}^{mP} : \tilde{\mathbf{u}}_{k+j-1} \in \mathbf{U},\ \tilde{\mathbf{x}}_{k+j} \in \mathbf{X},\ j = 1, 2, ..., P\}$ is the admissible set.

Generally, the function $J(\mathbf{x}_k, \tilde{\mathbf{u}}_k, \tilde{\mathbf{u}}_{k+1}, ...\tilde{\mathbf{u}}_{k+P-1})$ is a nonlinear function of mP variables and Ω is a non-convex set. Therefore, the optimization task (14) is a nonlinear programming problem.

Now real-time MPC algorithm can be presented as follows:

(i) Obtain the state estimation $\hat{\mathbf{x}}_k$ based on measurements $\mathbf{y}_k$ using the observer.

(ii) Solve the nonlinear programming problem (14) subject to prediction model (12) with initial conditions $\tilde{\mathbf{x}}_k = \hat{\mathbf{x}}_k$ and cost functional (13). It should be noted, that the value of the function $J_k(\mathbf{x}_k, \tilde{\mathbf{u}}_k, \tilde{\mathbf{u}}_{k+1}, ...\tilde{\mathbf{u}}_{k+P-1})$ is obtained by numerically integrating the prediction model (12) and then substituting the predicted behavior $\bar{\mathbf{x}} \in \mathbf{E}^{nP}$ into the cost function (13) given the programmed control $\{\tilde{\mathbf{u}}_k, \tilde{\mathbf{u}}_{k+1}, ..., \tilde{\mathbf{u}}_{k+P-1}\}$ over the prediction horizon and initial conditions $\hat{\mathbf{x}}_k$.

(iii) Let $\{\tilde{\mathbf{u}}_k^*, \tilde{\mathbf{u}}_{k+1}^*, ..., \tilde{\mathbf{u}}_{k+P-1}^*\}$ be the solution of the problem (14). Implement only the first component $\tilde{\mathbf{u}}_k^*$ of the obtained optimal sequence over time interval $[k\delta, (k+1)\delta]$.

(iv) Repeat the whole procedure 1–3 at next time instant $(k+1)\delta$.

Note, that the algorithm stated above implies real-time solution of the nonlinear programming problem at each sampling instant. The complexity of such a problem is determined by the number of sampling intervals P.

The simplest way to reduce the optimization problem order is to decrease the prediction horizon. But, it is necessary to keep in mind that the performance of the closed-loop system depends strongly on the number P of samples. The quality of the processes is decreased if the prediction horizon is reduced. Moreover, the system can lose stability if the quantity P is sufficiently small.

So, the following approaches to reduce computational load can be proposed:

1. Using the **control horizon**. The positive integer number $M < P$ is called the **control horizon** if the following condition hold:

$$\tilde{\mathbf{u}}_{k+M-1} = \tilde{\mathbf{u}}_{k+M} = ... = \tilde{\mathbf{u}}_{k+P-1}.$$

Thus, the number of independent variables is decreased from mP to mM. This approach allows to essentially reduce the optimization problem order. However, if the control horizon M is too small, the closed-loop stability can be compromised and the quality of the processes can decrease.

2. Increasing the sampling interval δ and reducing the number P of samples over the prediction horizon. This also allows to decrease the optimization problem order while preserving the value of the prediction horizon.
3. The computational consumption also depends on the prediction model used. So, one needs to use as simple models as possible. But the prediction model should adequately reflect the dynamics of the plant considered. The simplest case is using the linear prediction model.

3.3. *Linear MPC*

In this particular case, MPC is based on the linear prediction model. These algorithms are computationally efficient which is especially important from the real-time implementation point of view.
Generally, linear prediction model is presented by

$$\begin{aligned} &\tilde{\mathbf{x}}_{i+1} = \mathbf{A}\tilde{\mathbf{x}}_i + \mathbf{B}\tilde{\mathbf{u}}_i, \quad i = k+j, \quad j = 0,1,2,..., \quad \tilde{\mathbf{x}}_k = \mathbf{x}_k, \\ &\tilde{\mathbf{y}}_i = \mathbf{C}\tilde{\mathbf{x}}_i. \end{aligned} \tag{15}$$

Suppose $\bar{\mathbf{u}} = \left(\tilde{\mathbf{u}}_k\ \tilde{\mathbf{u}}_{k+1}\ ...\ \tilde{\mathbf{u}}_{k+P-1}\right)^T$ is the programmed control over the prediction horizon. Then, integrating (15) we obtain future outputs of the plant in the form

$$\bar{\mathbf{y}} = \mathbf{L}\mathbf{x}_k + \mathbf{M}\bar{\mathbf{u}}, \tag{16}$$

where

$$\mathbf{L} = \begin{bmatrix} \mathbf{CA} \\ \mathbf{CA}^2 \\ \vdots \\ \mathbf{CA}^P \end{bmatrix}, \quad \mathbf{M} = \begin{bmatrix} \mathbf{CB} & \mathbf{0} & \dots & \mathbf{0} \\ \mathbf{CAB} & \ddots & & \\ \vdots & & \ddots & \\ \mathbf{CA}^{P-1}\mathbf{B} & \dots & \mathbf{CAB} & \mathbf{CB} \end{bmatrix}.$$

Substituting (16) into (13) we get

$$J_k = J_k(\mathbf{x}_k, \bar{\mathbf{u}}) = \bar{\mathbf{u}}^T\mathbf{H}\bar{\mathbf{u}} + 2\mathbf{f}^T\bar{\mathbf{u}} + g. \tag{17}$$

Here we assumed that all weight matrices are equal, that is

$$\begin{aligned} \mathbf{R}_{k+1} = \mathbf{R}_{k+2} = ... = \mathbf{R}_{k+P} = \mathbf{R}, \\ \mathbf{Q}_{k+1} = \mathbf{Q}_{k+2} = ... = \mathbf{Q}_{k+P} = \mathbf{Q}. \end{aligned}$$

The matrix $\mathbf{H}$ and vector $\mathbf{f}$ in (17) are as follows

$$\mathbf{H} = \mathbf{M}'\mathbf{R}\mathbf{M} + \mathbf{Q}, \quad \mathbf{f} = \mathbf{M}'\mathbf{R}\mathbf{L}\mathbf{x}_k. \tag{18}$$

It can easily be shown that in this case the optimization problem (14) is reduced to the quadratic programming problem of the form

$$J_k(\mathbf{x}_k, \tilde{\mathbf{u}}_k, \tilde{\mathbf{u}}_{k+1}, ..., \tilde{\mathbf{u}}_{k+P-1}) = \bar{\mathbf{u}}^T\mathbf{H}\bar{\mathbf{u}} + 2\mathbf{f}^T\bar{\mathbf{u}} + g \to \min_{\bar{\mathbf{u}} \in \Omega \subset \mathbf{E}^{mP}}. \tag{19}$$

Here $\mathbf{H}$ is a positive definite matrix and Ω is a convex set defined by the system of linear constraints. On-line solution of the optimization problem (19) at each sampling instant generally leads to nonlinear feedback control law.

Note that the optimization problem (19) can be solved analytically for the unconstrained case. The result is the linear controller

$$\tilde{\mathbf{u}}_k = \mathbf{K}\tilde{\mathbf{x}}_k, \tag{20}$$

which converges to the LQR-optimal one as P is increased. This convergence is obvious, because the discrete LQR controller minimizes the functional (13) with infinity prediction horizon for linear model (15).

4. Plasma Vertical Stabilization Based on the Model Predictive Control

Let us remember that SISO model (5) represents plasma dynamics in the vertical stabilization process and limits (6) are imposed on the power supply system. It is necessary to transform the system (5) to the state-space form for MPC algorithms implementation. Besides that, in order to take into account the constraint imposed on the current, one more equation should be added to the model (5). Finally, the linear model of the stabilization process is given by

$$\begin{aligned} \dot{\mathbf{x}} &= \mathbf{A}\mathbf{x} + \mathbf{b}u, \\ \mathbf{y} &= \mathbf{c}\mathbf{x} + \mathbf{d}u, \end{aligned} \tag{21}$$

where $\mathbf{x} \in \mathbf{E}^4$ and the last component of $\mathbf{x}$ corresponds to current, $\mathbf{y} = (y_1, y_2) \in \mathbf{E}^2$, y_1 is the vertical velocity and y_2 is the current in the VS-converter. We shall assume that the model (21) describes the process accurately.

We can obtain a linear prediction model in the form (15) by the system (21) discretization. As a result, we get

$$\begin{aligned} &\tilde{\mathbf{x}}_{i+1} = \mathbf{A}_d\tilde{\mathbf{x}}_i + \mathbf{b}_d\tilde{u}_i, \qquad \tilde{\mathbf{x}}_k = \mathbf{x}_k, \\ &\tilde{\mathbf{y}}_i = \mathbf{C}_d\tilde{\mathbf{x}}_i. \end{aligned} \tag{22}$$

The constraints (6) form the system of linear inequalities given by

$$\begin{aligned} &\tilde{u}_i \le V_{max}^{VS}, \quad i = k, ..., k+P-1 \\ &\tilde{y}_{i2} \le I_{max}^{VS}, \quad i = k+1, ..., k+P \end{aligned} \tag{23}$$

These constraints define the admissible convex set Ω. The discrete analog of the cost functional (7) with $\lambda = 1$ is given by

$$J_k = J_k(\bar{\mathbf{y}}, \bar{\mathbf{u}}) = \sum_{j=1}^{P} \left(\tilde{y}_{k+j,1}^2 + \tilde{u}_{k+j-1}^2\right). \tag{24}$$

So, in this case MPC algorithm leads to real-time solution of the quadratic programming problem (19) with respect to the prediction model (22), constraints (23) and the cost functional (24).

From the experiments the following values for the sampling time and number of sampling intervals over the horizon were obtained

$$\delta = 0.004 \text{ sec}, \quad P = 250.$$

Hence, we have the following prediction horizon

$$T_p = P\delta = 1 \text{ sec}\,.$$

Let us consider the MPC controller synthesis without taking into account the constraints imposed. Remember that in this case we obtain a linear controller (20) that is practically the same as the LQR-optimal one. The transient response of the system closed by the controller is presented in Fig. 2. The initial state vector $\mathbf{x}(0) = \mathbf{h}$ is used, where $\mathbf{h}$ is a scaled eigenvector of the matrix $\mathbf{A}$ corresponding to the only unstable eigenvalue. The eigenvector $\mathbf{h}$ is scaled to provide the initial vertical velocity $y_1 = 0.03$ m/sec. It can be seen from the figure that the constraints (6) imposed on the voltage and current are violated.

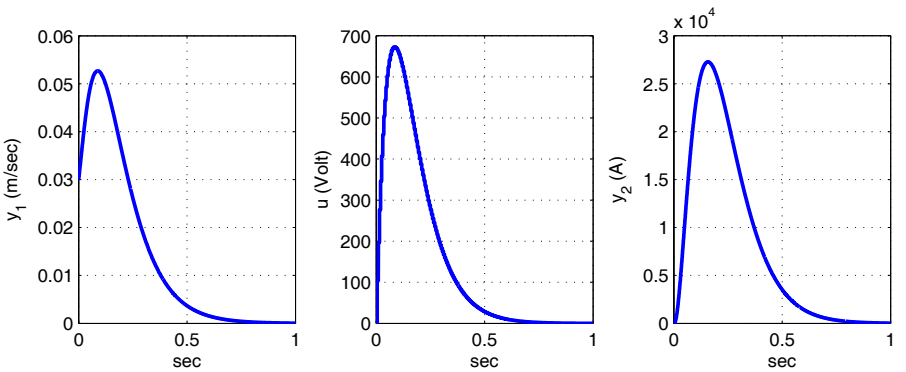

Fig. 2. Transient response of the closed-loop system with unconstrained MPC-controller.

Now consider the MPC algorithm synthesis with constraints. Fig. 3 shows transient response of the closed-loop system with constrained MPC-controller. It is not difficult to see that all constraints imposed are satisfied.

In order to reduce computational load, approaches proposed in Section 3.2 can be used.

1. Experiments with using the control horizon were carried out. This experiments show that the quality of stabilization remains approximately the same with control horizon $M = 50$ and prediction horizon $P = 250$. So, optimization problem order can be significantly reduced.
2. Another approach is to increase the sampling interval up to $\delta = 0.005$ sec and reduce the number of samples down to $P = 200$. Hence, prediction horizon has the same value $T_p = P\delta = 1$ sec. The optimization problem order is also reduced in this case and consequently time consumptions at each sampling instant is decreased. However, further increase of δ tends to compromise closed-loop system stability.

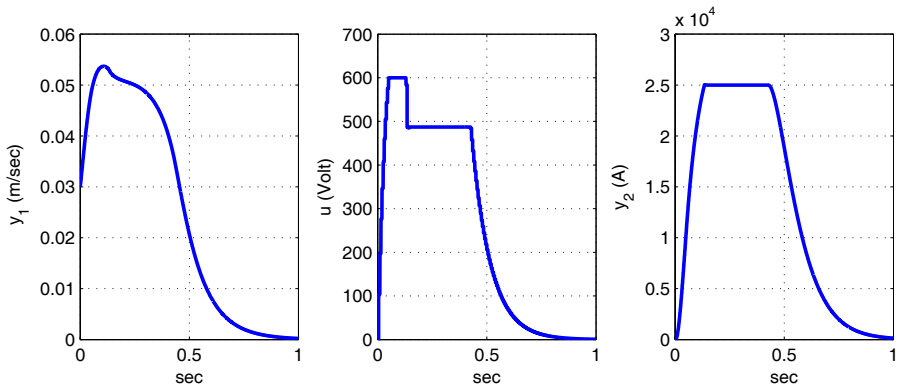

Fig. 3. Transient response of the closed-loop system with constrained MPC-controller.

5. Conclusion

The problem of plasma vertical stabilization based on the model predictive control has been considered. It is shown that MPC algorithms are superior compared to the LQR-optimal controller, because they allow taking constraints into account and provide high-performance control. It is also shown that it is possible to reduce the computational load significantly using relatively small control horizon or by increasing sample interval while preserving the processes quality in the closed-loop system. It allows us to use MPC algorithms to solve plasma vertical stabilization problem.

References

1. Camacho E.F. and Bordons C., *Model Predictive Control.* (Springer-Verlag, London, 1999).
2. Morari M., Garcia C.E., Lee J.H. and Prett D.M., *Model Predictive Control.* (Prentice Hall, New York, 1994).
3. Maciejowski J. M., *Predictive Control with Constraints.* (Prentice Hall, 2002).
4. Ovsyannikov D. A., Veremey E. I., Zhabko A. P., Ovsyannikov A. D., Makeev I. V., Belyakov V. A., Kavin A. A., Gryaznevich M. P., McArdle G. J., Mathematical methods of plasma vertical stabilization in modern tokamaks, in *Nuclear Fusion*, Vol.46, pp. 652-657 (2006).
5. Misenov B.A., Ovsyannikov D.A., Ovsyannikov A.D., Veremey E.I., Zhabko A.P., Analysis and synthesis of plasma stabilization systems in tokamaks, in *Proc. 11th IFAC Workshop. Control Applications of Optimization*, Vol.1 (New York, 2000), pp. 255-260.
6. Gribov Y., Albanese R., Ambrosino G., Ariola M., Bulmer R., Cavinato M., Coccorese E., Fujieda H., Kavin A. et. al., ITER-FEAT scenarios and plasma position/shape control, in *Proc. 18th IAEA Fusion Energy Conference*, (Sorrento, Italy, 2000), ITERP/02.

International Journal of Modern Physics A
Vol. 24, No. 5 (2009) 1009–1018

World Scientific
www.worldscientific.com

SPECTRAL APPROACH TO H-OPTIMIZATION OF PLASMA CONTROL

EVGENY VEREMEY

Applied Mathematics and Control Processes Department, Saint Petersburg State University, 35 Universitetskii prospekt, Petergof, Saint Petersburg, 198504, Russia
veremei@vrm.apmath.spbu.ru

This paper presents a spectral approach to H-optimal linear synthesis with the application for tokamak plasma control systems. Two main problems of a synthesis are discussed: the mean square optimization and the appropriate guaranteeing interpretation. The simple computational technique to solve these problems is proposed. Their implementation is illustrated by the example on the base of one variant of ITER tokamak model for the plasma vertical feedback control.

Keywords: Tokamak; plasma control; optimization.

PACS numbers: 52.55.Fa, 02.30.Yy

1. Introduction

The modern tokamaks represent an extensive and promising field of applied research in modern control theory. The central problem is plasma position, current and shape stabilization.

Various mathematical approaches to the synthesis are widely used as analytical and computational tools for practical problem-solving with the purpose to satisfy *a* priori given conditions, requirements and constraints.[1–3]

In particular, during the last few decades, special attention has been paid to the design methods based on the norms of Hardy spaces H_2 and H_∞. Linear systems optimization in the sense of the mentioned norms is treated now as a basis for a lot of research directions which were formerly considered independent areas of control theory.[4]

Now we have very effective analytical and computational tools to support research and practical design works based on the H-theory. Correspondent review, for example, is presented in [6, 7].

Nevertheless, H-optimization theory continues to develop now both in fundamental and applied directions. Naturally, this is also true with respect to the problems of tokamak plasma control. There exists a variety of theoretical publications reflecting aspects of these problems. However, the practical implementation of H-

optimization results is not too rich. For example, H-theory is not used yet in practice for plasma control in such tokamaks as GLOBUS-M, MAST and other machines. In our opinion, this is because of several reasons, one of which is computational complexity of H-optimization.

This article represents the spectral approach to the mean-square synthesis which is the particular case of H-theory. This approach is quite suitable to simplify the computation of the optimal controller avoiding solving of the Riccati equation for the SISO-situation. In this connection proposed method can be useful for the design of the plasma vertical stabilizers in tokamaks. To illustrate the applicability of the approach, one practical example is considered. This example uses a linear model of plasma stabilization system for ITER machine (one of the mathematical models for ITER-FEAT variant at the technical project stage in 1999–2001).

2. Mathematical Representation of Plasma Control Problem

One of the central problems to be investigated is plasma control in the toroidal magnetic chamber. It is well-known that plasma as an object of control is a mobile non-stable dynamic system with extremely high values of physical parameters, temperatures as high as millions centigrade, first of all. As a result, the requirement for electromagnetic capture system control accuracy is very high. Special attention is paid to the stabilization of the plasma pinch to chamber walls gap at some fixed control points. Therefore, the following high requirements for dynamic characteristics of the control process arise: settling time, overshoot, dispersion, oscillations etc. It is known that plasma position, current and shape are essentially determined by conductor currents and their evolution is dominated by the current dynamics.[2] Conductor current evolution is described by linear circuit equations derived from Faraday's law and presented in the form

$$\begin{aligned} \dot{\mathbf{x}} &= \mathbf{A}\mathbf{x} + \mathbf{B}\mathbf{u}, \\ \mathbf{y} &= \mathbf{C}\mathbf{x}, \end{aligned} \tag{1}$$

where $\mathbf{x} \in R^n$, $\mathbf{u} \in R^m$, $\mathbf{y} \in R^k$ are deviations of currents, voltages and gaps from the nominal values determined by the plasma equilibrium position, correspondingly.

Further we shall limit ourselves by considering only SISO linear models (1) with single input ($m = 1$) and single output ($k = 1$). This particular situation corresponds to the problem of vertical plasma position control in modern tokamaks.

The limitation mentioned above allows presenting the mathematical model (1) in the following input-output form

$$A(p)y = B(p)u + \varphi(t), \tag{2}$$

where $y, u, \varphi \in R^1$ are the controlled value, control and external disturbances, correspondingly, A, B are reciprocally simple polynomials of differential operator $p = d/dt$ with constant coefficients. Suppose that an external disturbance $\varphi(t)$ is a stationary stochastic process with the zero expectation satisfying the ergodic

hypothesis and having given rational spectral density $S_\varphi(\omega)$—a strictly proper even function

$$S_\varphi(\omega) = N_\varphi(\omega)/T_\varphi(\omega) \equiv S_1(j\omega)S_1(-j\omega). \tag{3}$$

Here $S_1(s) \equiv N(s)/T(s)$, $s = j\omega$, N, T—Hurwitz polynomials.

Let us consider the problem

$$I = I(W) \to \min_{W\in\Omega} \tag{4}$$

to find the optimal linear controller

$$u = W(p)y, \quad W(p) = W_1(p)/W_2(p), \tag{5}$$

where W_1, W_2—polynomials,

$$I(W) =< y^2 > +k^2 < u^2 >= \lim_{T\to\infty} \frac{1}{T} \int_0^T \left[x^2(t) + k^2u^2(t)\right] dt \tag{6}$$

—mean square functional, given on the motions of the closed-loop system (2),(5). Here an admissible set Ω is the set of stabilizing controllers (5).

It is also possible to consider another variant of the design problem for plasma stabilizing controllers. This variant is actual if there are some uncertainties concerning the properties of the external disturbance.

Let the controlled plant (2) be given. Consider the controllers (5) and the mean square functional (6). Nevertheless, suppose that a function $S_\varphi(\omega)$ is not given, but we know that it belongs to the set

$$\Re = \left\{ S_\varphi(\omega) : \frac{1}{\pi} \int_0^\infty S_\varphi(\omega)d\omega \leqslant 1 \right\}. \tag{7}$$

It is obvious that the functional (6) depends on the functions W and S_φ. So it is quite suitable to pose the problem of finding the guaranteeing estimation and the appropriate guaranteeing controller for the mean square functional:

$$I_0 = \min_{W\in\Omega} \sup_{S_\varphi\in\Re} I(W, S_\varphi), \quad W_0 = \arg\min_{W\in\Omega} \sup_{S_\varphi\in\Re} I(W, S_\varphi). \tag{8}$$

It is easy to show that the posed problems (4) and (8) can be transformed to corresponding optimization problems in Hardy spaces RH_2 and RH_∞:[7]

$$I_2 = I_2(W) = \left\|\tilde{F}(W)\right\|_2^2 \to \min_{W\in\Omega_2}, \tag{9}$$

$$I_\infty = I_\infty(W) = \left\|\tilde{F}(W)\right\|_\infty^2 \to \min_{W\in\Omega_\infty}. \tag{10}$$

Here $\Omega_2 = \left\{ W \in R_0 : \tilde{F}(W) \in RH_2 \right\}$, $\Omega_\infty = \{ W \in R_0 : F(W) \in RH_\infty \}$. Also the following notation is used

$$\tilde{F}(j\omega) = F(jw)S_1(j\omega), \quad \tilde{F}(s) = F(s)S_1(s), \tag{11}$$

$$|F(j\omega)|^2 = |F_y(j\omega)|^2 + k^2\,|F_u(j\omega)|^2\,, \tag{12}$$

$$F_y = 1/\left[A(s) - B(s)W(s)\right],\; F_u = W(s)/\left[A(s) - B(s)W(s)\right]. \tag{13}$$

It is known that the solutions to the problems (9) and (10) exist on the sets Ω_2 and Ω_∞ correspondingly. These solutions can be obtained based on the special spectral approach which is discussed below.

3. Spectral Algorithms of *H*-Optimal Synthesis

To begin, let us consider the problem (9), where a functional to be minimized can be presented in an explicit dependence on the controller transfer function $F(s)$ as follows

$$I_2(W) = \int\limits_0^\infty \frac{1 + k^2\,|W(j\omega)|^2}{|A(j\omega) - B(j\omega)W(j\omega)|^2} S_\varphi(\omega)\,d\omega. \tag{14}$$

Note that direct search of the minimum $I_2(W)$ (14) is hampered by its nonlinear dependence on the controller transfer function $W(s)$. This difficulty can be overcome using a parameterization of the set Ω with the help of varying functions-parameters $\Phi(s)$:

$$\Phi(s) = \alpha(s)F_x(s) + \beta(s)F_u(s). \tag{15}$$

Here $\alpha(s)$ and $\beta(s)$ are any polynomials not equal to zero at the same time such that

$$Q(s) = A(s)\beta(s) + B(s)\alpha(s) \tag{16}$$

is a Hurvitz polynomial.

Note that the mentioned functions-parameters $\Phi(s)$ and the transfer functions $W(s)$ in (14) are connected by obvious formulas

$$W = W(\Phi) = \frac{A\Phi - \alpha}{B\Phi + \beta}, \quad \Phi = \Phi(W) = \frac{\alpha + \beta W}{A - BW}. \tag{17}$$

Let us introduce the set $\Omega_2^\Phi = \left\{\Phi(s) \in R_0 : \tilde{F}(W(\Phi)) \in RH_2\right\}$ of the rational functions. It is easy to see that the relations (17) determine a biunique correspondence between the sets Ω_2^Φ and Ω_2.

Using formulas (17) we present the functional (14) as an evident dependence on the function-parameter Φ:

$$I_2 = \tilde{I}(\Phi) = \int\limits_0^{j\infty} \left[F_x(\Phi)\bar{F}_x(\Phi) + k^2 F_u(\Phi)\bar{F}_u(\Phi)\right] S_\varphi(s)\,ds. \tag{18}$$

Here and later the sign "$-$" under a rational fraction or polynomial means the change of its argument s to $-s$.

Taking into account the biunique correspondence (17), it is easy to see that the problem (9) is equivalent to the analogous problem

$$\tilde{I}(\Phi) \to \min_{\Phi \in \Omega_2^{\Phi}}, \quad \Phi_0 = \arg\min_{\Phi \in \Omega_2^{\Phi}} \tilde{I}(\Phi). \tag{19}$$

Theorem 3.1. *The function-parameter $\Phi_0(s)$ which is the solution of the problem (19), can be determined by the expressions*

$$\Phi_0(s) = \frac{\left[k^2\alpha(s)A(-s) - \beta B(-s)\right] S_1(s) - R(s)Q(s)}{G(s)G(-s)S_1(s)},$$

where $R(s) = \sum\limits_{i=1}^{n} \frac{G(-s)}{g_i - s} \frac{B(-g_i N(g_i)}{A(g_i)T(g_i)G'(-g_i)}$; g_i are the roots of the polynomial $G(-s)$ (assume that all of them are simple); Hurwitz polynomial $G(s)$ is the result of factorization $k^2 A\bar{A} + B\bar{B} \equiv G\bar{G}$, $G'(-g_i) = \frac{dG(-s)}{ds}\big|_{s=g_i}$.

Proof. Let us transform the integrand expression in (18) the following way

$$F_y(\Phi)\bar{F}_y(\Phi) + k^2 F_u(\Phi)\bar{F}_u(\Phi) = (T_1 - T_2\Phi)(\bar{T}_1 - \bar{T}_2\bar{\Phi}) + T_3, \tag{20}$$

$$T_1 = \frac{k^2\alpha\bar{A} - \beta\bar{B}}{QG}, \quad T_2 = \frac{\bar{G}}{Q}, \quad T_3 = \frac{k^2}{G\bar{G}}.$$

Based on (20), the functional (18) can be represented as

$$\tilde{I}(\Phi) = \int_0^{j\infty} (T_1 - T_2\Phi)(\bar{T}_1 - \bar{T}_2\bar{\Phi}) S_\varphi ds + \int_0^{j\infty} T_3 S_\varphi ds.$$

Since the second item does not depend on the function Φ, the optimal solution Φ_0 of the problem (19) is simultaneously a solution of the problem $I(\Phi) \to \min\limits_{\Phi \in \Omega_2^{\Phi}}$, where

$$I(\Phi) = \frac{1}{2\pi} \int_{-\infty}^{\infty} \left|T_1(\omega) - T_2(\omega)\Phi(\omega)\right|^2 S_\varphi(\omega) d\omega,$$

or $I(\Phi) = \|F(s)S_1(s)\|_2^2 = \|[T_1(s) - T_2(s)\Phi(s)]\, S_1(s)\|_2^2$. After substituting the expressions for T_1 and T_2, we obtain

$$I(\Phi) = \left\| \left(\frac{k^2\alpha\bar{A} - \beta\bar{B}}{QG} - \frac{\bar{G}}{Q}\Phi \right) S_1 \right\|_2^2. \tag{21}$$

This equality can be transformed by dividing both items by $(\bar{G}/G)$. Since $\left\|\bar{G}/G\right\|_2^2 = 1$, we have

$$I(\Phi) = \|(M - L\Phi)\, S_1\|_2^2 = \|MS_1 - L\Phi S_1\|_2^2,$$

$$M = \frac{k^2\alpha\bar{A} - \beta\bar{B}}{Q\bar{G}}, \quad L = \frac{\bar{G}}{Q}.$$

The product MS_1 can be represented as a sum of orthogonal elements using Toeplitz Θ_M and Hankel Γ_M operators:[7]

$$I(\Phi) = \|\Theta_M(S_1) + \Gamma_M(S_1) - L\Phi S_1\|_2^2 =$$

$$= \|\Theta_M(S_1) - L\Phi S_1\|_2^2 + \|\Gamma_M(S_1)\|_2^2,$$

where

$$\Theta_M(S_1) = \frac{M_1(s)}{Q(s)T(s)}, \quad \Gamma_M(S_1) = \frac{R(s)}{G(-s)}. \tag{22}$$

Using the roots g_i $(i = \overline{1,n})$ of the polynomial $G(-s)$, it is possible to find the polynomial $R(s) = \sum\limits_{i=1}^{n} \frac{G(-s)}{g_i - s} \frac{B(-g_i)N(g_i)}{A(g_i)T(g_i)G'(-g_i)}$.

From the obvious condition $\Theta_M(S_1) - L\Phi S = 0$ we find $\Phi_0 = \frac{(k^2\alpha\bar{A} - \beta\bar{B})S_1 - RQ}{G\bar{G}S_1}$. It is easy to see that $\left[(k^2\alpha\bar{A} - \beta\bar{B})S_1 - RQ\right]_{s=g_i} = 0$, $i = \overline{1,n}$, i.e. $\Phi_0 \in \Omega_2^{\Phi}$. □

Note that the given theorem presents only an auxiliary result in the form of optimal varying function-parameter $\Phi_0(s)$. But using the formulas (18) it is possible to find the corresponding expression for the transfer function $W_0(s)$ of the optimal controller to be designed.

In fact, substitution of the optimal parameter $\Phi_0(s)$ into (17) after some algebra taking into account formulas for polynomials $Q(s)$ and $G(s)G(-s)$ gives us the following expression

$$W_0(s) = \frac{\left[A(s)T(s)R(s) + B(-s)N(s)\right]/G(-s)}{\left[B(s)T(s)R(s) - k^2A(-s)N(s)\right]/G(-s)}, \tag{23}$$

It is easy to prove that both the numerator and denominator in the last formula are divisible by the polynomial $G(-s)$.

Let us consider the problem (10) which is equivalent to the problem (8) of the guaranteeing controller synthesis for the particular situation determined by the equality $k = 0$ for mean square functional (6).

Suppose that the polynomial $B(s)$ in (2) can be presented as

$$B(s) \equiv B_h(s)B_n(-s), \tag{24}$$

where $B_h(s)$ is a Hurwitz polynomial and $B_n(-s)$ is a polynomial with the roots β_i, $i = \overline{1,l}$ placed in the half plane $\operatorname{Re} s > 0$.

Let $1 \leqslant l < n$, i.e. polynomial $B(s)$ has at least one root in the open right half plane.

In accordance with (13) and (11) we have $F_x(s) \equiv 1/\left[A(s) - B(s)W(s)\right]$ for the closed-loop system. The functional to be minimized can then be presented based on (10) in the form:

$$I_\infty(W) = \sup_{\omega\in[0,\infty)} \frac{1}{\left|A(j\omega) - B(j\omega)W(j\omega)\right|^2}. \tag{25}$$

As for the previous problem, let us parameterize the set Ω by the functions-paremeters $\Phi(s)$ (15) taking into account (11). We introduce the following set of rational functions:

$$\Omega_\infty^\Phi = \{\Phi(s) \in R_0 : F(W(\Phi)) \in RH_\infty\}.$$

The expressions (19) define a biunique correspondence between the sets Ω_∞^Φ and Ω_∞.

Using the formulas (17), represent the functional (25) as a dependence on the function-parameter Φ:

$$I_\infty = I(\Phi) = \left\| \frac{\beta}{Q} + \frac{B}{Q}\Phi \right\|_\infty^2. \tag{26}$$

So it is easy to see that the problem (10) is equivalent to the search of the optimal function-parameter Φ_∞:

$$I_\infty(\Phi) \to \min_{\Phi \in \Omega_\infty^\Phi}, \quad \Phi_\infty = \arg\min_{\Phi \in \Omega_\infty^\Phi} I(\Phi). \tag{27}$$

Theorem 3.2.

The function-parameter $\Phi_\infty(s)$ which is the solution of the auxiliary problem (27), can be determined by the expression

$$\Phi_\infty(s) = [\gamma_0 Q(s) G_0(s) - \beta(s)] / B(s), \tag{28}$$

where γ_0 is a square root of the maximum eigenvalue of the positive-define Hermitian matrix

$$\Gamma_\infty = \Gamma_m^{-1/2} \Gamma_0 \Gamma_m^{-1/2}, \; \Gamma_m = \left\{ \frac{1}{\beta_i + \bar{\beta}_j} \right\}, \; \Gamma_0 = \left\{ \frac{\beta_i \bar{\beta}_j}{\beta_i + \bar{\beta}_j} \right\}, \tag{29}$$

$G_0(s)$ is the solution of the Nevanlinna-Pick (NP) interpolation problem with initial data $\left\{\beta_i,\ 1/[\gamma_0 A(\beta_i)],\ i = \overline{1,l}\right\}$.

Proof. Let us try to find a function $\Phi \in \Omega_\infty^\Phi$ satisfying the inequality

$$\|(\beta + B\Phi)/Q\|_\infty \leqslant \gamma \tag{30}$$

for some given real number $\gamma > 0$.

This intermediate problem can be transformed to the known equivalent NP-problem. To make this transformation we introduce a rational function of the form

$$G(s) = [\beta(s) + B(s)\Phi(s)] / [\gamma Q(s)]. \tag{31}$$

Note that complex numbers β_i are the roots of the polynomial $B(s)$ and parameters Φ has no poles in the right half plane. So, based on the formula (16) which determines the polynomial $Q(s)$ we have

$$G(\beta_i) = \beta(\beta_i)/[\gamma Q(\beta_i)] = 1/[\gamma A(\beta_i)], \quad i = \overline{1,l}.$$

NP-problem is defined as a search for such a function $G(s) \in RH_\infty$, that satisfies the following two conditions:

$$\|G(s)\|_\infty \leqslant 1; \quad G(\beta_i) = 1/\left[\gamma A(\beta_i)\right], \quad i = \overline{1,l}. \tag{32}$$

The solution of the NP-problem can be obtained with the help of a finite-step algorithm presented in Ref. 6. This solution exists if and only if the Hermitian Pick matrix

$$\Gamma(\gamma) = \left\{ \frac{1 - 1/\left[\gamma^2 A(\beta_i) A(\bar{\beta}_j)\right]}{\beta_i + \bar{\beta}_j} \right\}$$

is nonnegative-definite.

It follows from the Pick's theorem that there exists the a minimal real positive number $\gamma = \gamma_0$, determined by the formulas (29), satisfying the above mentioned condition. It is obvious that this number allows to obtain the corresponding function $G_0(s)$ with the aid of the formula (31) and then to find the optimal parameter $\Phi_\infty(s)$ (28). □

Remark 3.1. It is easy to see that the obtained rational function $G_0(s)$ is all-pass, i.e. $|G_0(j\omega)| = \text{const}, \quad \forall \omega \in [0, \infty)$.

As in the previous case, the last theorem gives an auxiliary result in the form of optimal varying function-parameter $\Phi_\infty(s)$. But the formulas (18) allow to obtain the transfer function $W_\infty(s)$ of the optimal guaranteeing controller.

Indeed, after substitution of the optimal parameter $\Phi_\infty(s)$ to (17) we have

$$W_\infty = W(\Phi_\infty) = \frac{A\Phi_\infty - \alpha}{B\Phi_\infty + \beta} = \frac{(A\gamma_0 Q G_0 - Q)/B_n}{B_h \gamma_0 Q G_0}.$$

Using the notation $G_0(s) \equiv m_1(s)/m_2(s)$, we directly obtain

$$W_\infty(s) = \frac{\left[A(s)m_1(s) - m_2(s)/\gamma_0\right]/B_n(-s)}{B_h(s)m_1(s)}. \tag{33}$$

It is easy to prove divisibility by the polynomial $B_n(-s)$ and all-pass property of the transfer function for the closed-loop system in accordance with the remark 3.1.

Based on spectral theorems presented above, it is possible to construct the effective computational support for optimal controller synthesis in the range of accepted approach. The essence of this support is determined by formulas (23) and (33).

Note that these algorithms do not include operations based on solving Riccati equations. This allows us to use them in real time of the tokamak control processes to adopt control system for actual conditions of the plasma burning.

4. Controller Synthesis Example

To illustrate the practical applicability of the method presented above, let us discuss an example of H_∞-synthesis based on the proposed approach for plasma vertical stabilizer design.

Consider the input-output equation

$$y = P(s)u \tag{34}$$

as a representation of the control plant to be stabilized using the linear controller. In particular, this equation can be used as a mathematical model of plasma vertical dynamics for ITER project. Here y is the rate of the plasma vertical displacement, u is the control voltage of a stabilizer, $P(s)$ is a given plant transfer function.

As for $P(s)$, we shall use the model of ITER-FEAT[5] variant, which was thoroughly investigated on the ITER technical project stage in 1999–2001. This model corresponds to the 15 MA design scenario for the SOF-point without auxiliary heating during the current ramp-up. One of the results obtained at that time was the plant transfer function of the form

$$P(s) = \frac{1.732 \cdot 10^{-6}(s - 121.1)(s + 158.2)(s + 9.641)}{(s + 29.21)(s + 8.348)(s - 12.21)} \tag{35}$$

as a good admissible reduced representation for initial plant of the 58th order. Note that the plant is non-stable and non-minimal-phase that reflects significant features of the vertical plasma dynamics. Thus, it is necessary to design the controller

$$u = W(s)y, \tag{36}$$

stabilizing vertical position of the plasma centroid or the closed-loop system (34), (36).

In accordance with (34) and (35), a differential equation of the controlled plant in the form (2) can be given as follows

$$A(p)y = B(p)u + \varphi(t), \tag{37}$$

$$A(p) = (s + 29.21)(s + 8.348)(s - 12.21),$$

$$B(p) = 1.732 \cdot 10^{-6}(s - 121.1)(s + 158.2)(s + 9.641).$$

Using the formula (33) from the previous section, it is possible to find the transfer function $W = W_\infty(s)$ of the optimal guaranteeing controller (36).

It directly follows from the initial data (37) that $B_n(-s) = s - 121.1$, i.e. we have $l = 1$ and the only root $\beta_1 = 121.1$ is placed in the right half plane.

Then, executing the computations according to the formulas (27), (31) we obtain $\gamma_0 = 12.2$, $G_0(s) = 1$, $m_1(s) = 1$, $m_2(s) = 1$. Accordingly, the transfer function of the optimal controller is

$$W_\infty(s) = \frac{10^7(7.78 \cdot 10^{-5}s^2 + 8.46 \cdot 10^{-3}s + 1.01)}{(0.001s^2 + 0.168s + 1.53)}. \tag{38}$$

Given example allows saying that the proposed spectral approach can be used in principle to design the stabilizing controllers for plasma position control systems. However, the obtained controller is not intended for immediate practical implementation. This is connected with some negative features of the mentioned transfer function such as robust properties, for example. Nevertheless, the result of the above example can be useful for analysis of extreme possibilities of the proposed synthesis. Therefore, studies in the chosen direction applied to plasma control problems should be continued.

In conclusion it is noteworthy that the proposed approach to the vertical stabilizers synthesis has two obvious advantages over the universal methods of H-optimization. Firstly, spectral approach considered in a framework of the mean square synthesis allows to directly take into account the action of external disturbances having a random nature. Secondly, this approach is not based on the solution of the matrix Riccati equations that significantly decreases computational load and makes the analytical investigation of the optimal controller features more convenient. It is probably suitable to discuss a possibility to use proposed algorithms directly in real time of the tokamak control processes to adopt the control system for actual conditions of the plasma burning.

The proposed approach also has certain disadvantages such as mentioned robust features, some problems with the dynamics for low frequency disturbances and some other points to be improved. Nevertheless, in our opinion all the negative features can be overcome in the course of additional research to achieve the best effectiveness for plasma control systems design.

References

1. G. McArdle, V. Belyakov, D. Ovsyannikov and E. Veremey, The MAST plasma control system, in *Proc. 20rd Int. Symp. on Fusion Technology SOFT98*, (Marseille, France, 1998), p. 541.
2. V. Beljakov, A. Kavin, E. Veremey etc. *Fusion Engineering and Design* **45**, 55 (1999).
3. D. Ovsyannikov, E. Veremey, A. Zhabko etc. *Nuclear Fusion* **46**, S652 (2006).
4. E. Veremey, *Vestnik Saint Petersburg University* **10-1**, 48 (2004).
5. Gribov Y., Albanese R., Ambrosino G., Ariola M., Bulmer R., Cavinato M., Coccorese E., Fujieda H., Kavin A. et. al., ITER-FEAT scenarios and plasma position/shape control, in *Proc. 18th IAEA Fusion Energy Conference*, (Sorrento, Italy, 2000), ITERP/02.
6. J. Doile, B. Francis and A. Tannenbaum, *Feedback Control Theory.* (Macmillan Publ., New York, 1992).
7. B. Francis, *A Course in H_∞ Control Theory.* (Springer-Verlag, Berlin, 1987).

International Journal of Modern Physics A
Vol. 24, No. 5 (2009) 1019–1039

World Scientific
www.worldscientific.com

COMPUTATION OF HIGH-ORDER MAPS TO MULTIPLE MACHINE PRECISION

ALEXANDER WITTIG* and MARTIN BERZ†

Department of Physics and Astronomy, Michigan State University,
Biomedical and Physical Sciences Bldg., East Lansing, MI 48824, USA
**wittigal@msu.edu*
†berz@msu.edu

The Beam Dynamics simulation package in COSY INFINITY is built upon a differential algebra data type. With it, it is possible to compute transfer maps or arbitrary systems to arbitrary order. However, this data type is limited by the precision of the underlying floating point number model provided by the computer processor.

We will present a method to extend the effective precision of the calculations based purely on standard floating point operations. Those algorithms are then integrated into the differential algebra data type to efficiently extend the available precision, without unnecessarily affecting overall efficiency. To that effect, the precision of each coefficient is adjusted automatically during the calculation.

We will then proceed to show the effectiveness of our implementation by calculating high precision maps of combinations of homogeneous dipole segments, for which the exact results are known, and comparing the high precision coefficients with the results produced by the traditional COSY beam physics package.

Keywords: High precision; differential algebra; COSY INFINITY; high precision aberrations.

PACS numbers: 41.85.Ja, 41.85.Lc

1. Theory of High Precision Operations

We will begin by introducing some elementary operations on floating point numbers which we will use to build our high precision implementation on.

1.1. *Floating Point Numbers*

To represent calculations on the real numbers on a computer, most modern processors use floating point numbers. The concept behind the representation of a floating point number is essentially the same as the "scientific notation" in terms of relevant digits and a power of ten to represent the order of magnitude. The same is done with floating point numbers. The only difference is that, due to the binary number system, a power of two is used to signify the magnitude.

Definition 1.1. We define the set of all floating point numbers R to be given by

$$R = \{m_z \cdot 2^{e_z} |\ 2^{t-1} \leqslant |m_z| < 2^t;\ \underline{M} < e_z < \overline{M}\},$$

where $t, \underline{M}$ and $\overline{M}$ are positive integer constants.

The constants $t, \underline{M}$ and $\overline{M}$ define the floating point number system. $\underline{M}$ and $\overline{M}$ limit the exponent range and thus the largest and smallest representable numbers. To make the following proofs easier to understand, we will assume that the exponent range is unlimited, i.e. $\underline{M} = -\infty$ and $\overline{M} = \infty$. This is, of course, not true for computer systems, where overflows and underflows of the exponent may happen. In our practical implementation we have to deal with those cases separately. The parameter t is the mantissa length in binary digits and thus defines the relative precision of the floating point system (see below).

In the following we will use floating point systems with different mantissa lengths which we will denote by R_t. Over- and underflows notwithstanding, we clearly have that $R_t \subset R_{t'}$ if $t \leqslant t'$. The lower bound requirement on the mantissa is called the normalization. With this additional requirement, the values represented by floating point numbers become unique. Mantissae with absolute value less than 2^{t-1} can be multiplied by a power of two so that they lie within the allowed range for the mantissa, while the exponent is adjusted accordingly.

Given any real number $r \in \mathbb{R}$ within the range of the floating point representation, we will denote by $\tilde{r} \in R$ the closest floating point number in the given system of floating point numbers. Then it follows readily from Definition 1.1 that

$$\frac{|r - \tilde{r}|}{|r|} < \epsilon_m = 2^{-t}.$$

The value ϵ_m is called the machine precision and is given by the length of the mantissa t.

Every floating point implementation has to provide at least the basic operations addition, subtraction, and multiplication. Clearly the mathematical result of any of those operations on two arbitrary floating point numbers $a, b \in R$ does not necessarily have to be in R. Thus, the floating point operations corresponding to $+, -, \times$ are not the same as their mathematical counterparts on the real numbers. Let $\oplus, \ominus, \otimes$ denote the floating point operations for $+, -, \times$.

Definition 1.2. Let $\odot$ denote one of the floating point operations $\oplus, \ominus, \otimes$ and $\bullet$ the same operation on the real numbers.
The operation $\odot$ is said to be *round-to-nearest* if $\forall a, b \in R$

$$|(a \odot b) - (a \bullet b)| = \min_{x \in R}(x - (a \bullet b)).$$

Note that if a floating point operation is round-to-nearest, the result is the floating point number closest to the mathematically correct result. In case of a toss-up, i.e. if the mathematically correct result is exactly between two floating point numbers, we will accept either one. Another immediate consequence is that if

the result of an operation is representable exactly by a floating point number then we obtain the correct result without roundoff errors.

From the above definition, a bound for rounding errors and a useful condition for the mantissa of the result of a round-to-nearest operation $\odot$ easily follow. Let $z = m_z \cdot 2^{e_z} = a \odot b$. Then

$$|z - (a \bullet b)| < \epsilon_m \cdot z. \tag{1}$$

This is clear since if the error was more than $\epsilon_m \cdot z$ then either the floating point number $(m_z + 1) \cdot 2^{e_z}$ or $(m_z - 1) \cdot 2^{e_z}$ would be closer to the correct result. Furthermore for the mantissa m_z, the following equation holds.

$$m_z = \left[\frac{m_a \cdot 2^{e_a} \bullet m_b \cdot 2^{e_b}}{2^{e_z}} \right], \tag{2}$$

where $[x]$ denotes rounding to the nearest integer.

In most modern computers the constants $t, \underline{M}, \overline{M}$ are defined to follow the IEEE 754 standard.[1] The double precision numbers defined in that standard specify that $t = 53$, $\underline{M} = 1023$, $\overline{M} = -1024$. Thus, for double precision numbers $\epsilon_m = 2^{-53} \approx 10^{-16}$. Therefore in double precision we can represent about 16 valid decimal digits. The standard also defines that the elementary floating point operations $\oplus, \ominus, \otimes$ can be set to be round-to-nearest. Consistent with the notation introduced above, we will denote the set of double precision floating point numbers by R_{53}.

1.2. *Exact operations*

In the following subsections we will state some well-known facts about obtaining exact results for the basic floating point operations. While this may sound surprising at first, it is indeed possible to obtain the roundoff errors of the basic floating point operations exactly from within the floating point arithmetic. The theorems and proofs given here are originally due to Dekker,[2] who showed that the theorems also hold with slightly lesser requirements on the underlying floating point operations than prescribed by the IEEE 754 standard. But since our implementation will build on IEEE 754 double precision floating point numbers, we will restrict ourselves to those. To give the reader an idea of how the proofs of those theorems work, we will prove some of the theorems while referring the reader to [2] for others.

1.2.1. *Two-Sum*

The first theorem will provide us with a way to calculate the exact roundoff error occurring when adding two floating point numbers.

Theorem 1.1. *Let two double precision floating point numbers a and b such that $|a| > |b|$ be given. Let $z = a \oplus b$, $w = z \ominus a$ and $zz = b \ominus w$. Then, neglecting possible over- or underflows during the calculation, we have that $z + zz = a + b$ exactly.*

Proof. Let $a = m_a \cdot 2^{e_a}$ and $b = m_b \cdot 2^{e_b}$. Since $|a| > |b|$ and floating point numbers are normalized, we have that $e_a \geqslant e_b$. It is sufficient to show that $w \in R_{53}$ and $b - w \in R_{53}$, then the result follows readily from optimality of the floating point operations.

Let $z = a \oplus b = m_z \cdot 2^{e_z}$. From Equation 2 we get that

$$m_z = \left[m_a \cdot 2^{e_a - e_z} + m_b \cdot 2^{e_b - e_z} \right].$$

Since $|a + b| < 2|a|$ we have that $e_z \leqslant e_a + 1$. Now we consider the two cases $e_z = e_a + 1$ and $e_z \leqslant e_a$.

- Assume $e_z = e_a + 1$. Then $m_z = \left[m_a \cdot 2^{-1} - m_y \cdot 2^{e_b - e_a - 1} \right]$ and letting $w = m_w \cdot 2^{e_a}$ we find that

$$\begin{aligned} |m_w| &= |m_z \cdot 2^{e_z - e_a} - m_a| \\ &= |m_z \cdot 2^{e_z - e_a} - m_a - m_b \cdot 2^{e_b - e_a} + m_b \cdot 2^{e_b - e_a}| \\ &\leqslant |2m_z - m_a - m_b \cdot 2^{e_b - e_a}| + |m_b \cdot 2^{e_b - e_a}| \\ &< 2|m_z - m_a \cdot 2^{-1} - m_b \cdot 2^{e_b - e_a - 1}| + 2^{53} \\ &< 2\frac{1}{2} + 2^{53}. \end{aligned}$$

  Since m_w is an integer, we therefore have that $m_w \leqslant 2^{53}$ and thus $w \in R_{53}$, i.e. w is a double precision floating point number.
- If $e_z \leqslant e_a$ the exact same proof carries through, the only difference being that we define $w = m_w \cdot 2^{e_z}$.

To prove that $zz \in R_{53}$, we first note that we can write $w = i \cdot 2^{e_b}$ for some integer i since $e_a \geqslant e_b$. Secondly, we have that $|b - w| = |b - z + a| \leqslant |b|$ by optimality. To see this simply let $z = x$, and then apply Definition 1.2. We thus have

$$|zz| = |b - w| = |m_b - i| \cdot 2^{e_b} \leqslant |b| = |m_b| \cdot 2^{e_b} < 2^{53} \cdot 2^{e_b},$$

and therefore $(m_b - i) \cdot 2^{e_b} = zz \in R_{53}$. □

Note that by Definition 1.1 floating point numbers are symmetric, i.e. if $a \in R$ then $-a \in R$. Thus the above theorem automatically provides exact subtraction as well.

It is worth mentioning that there are also other algorithms to calculate the same two values without the condition that $a > b$, but requiring some additional floating point operations. The following algorithm is due to Knuth.[3] The advantage of this method is that due to pipelining on modern processors it is often faster to perform the three additional floating point operations instead of having to evaluate a conditional statement on the absolute values of a and b.

Theorem 1.2. *Let two double precision floating point numbers a and b be given. Let $z = a \oplus b$, $b_v = z \ominus a$, $a_v = z \ominus b_v$ and $zz = (a \ominus a_v) \oplus (b \ominus b_v)$. Then, neglecting*

possible over- or underflows during the calculation, we have that $z + zz = a + b$ *exactly.*

Proof. For a proof see, for example, [3]. □

1.2.2. *Splitting*

Before we can move on to the exact multiplication, we require the concept of the splitting of a double precision number.

Definition 1.3. Let $a \in R_{53}$ be given. We call $a_h, a_t \in R_{26}$ the head and the tail of the splitting of a if

$$a_h = \left[m_a \cdot 2^{-26}\right] \cdot 2^{e_x+26},$$
$$a_t = a - a_h.$$

This definition may sound surprising at first. After all a has 53 mantissa bits, but both a_h and a_t only have 26 bits each yielding a total of 52 bits. The solution to this riddle is the fact that the difference $|[x] - x| \leqslant 1/2$, but depending on x it can have either positive or negative sign. So the missing bit is the sign bit of the tail of the splitting.

The following theorem, also presented by Dekker, allows us to calculate such a splitting of a double precision number.

Theorem 1.3. *Let* $a \in R_{53}$ *be given and let* $p = x \otimes (2^{27} + 1)$. *Then the head of the splitting of* a *is given by* $a_h = p \oplus (x \ominus p)$.

Proof. Since the proof of this theorem is somewhat technical and does not contribute much to the understanding of these operations, we refer the reader to the papers of Dekker[2] or Shewchuk.[4] □

1.2.3. *Multiplication*

With the notion of a splitting, we can formulate the following theorem for exact multiplication of two double precision numbers:

Theorem 1.4. *Given two double precision floating point numbers* a *and* b *let* $a = a_h + a_t$, $b = b_h + b_t$ *be a splitting as defined above. Also let* $p = (a_h \otimes b_h)$, $q = (a_t \otimes b_h) \oplus (a_h \otimes b_t)$ *and* $r = (a_t \otimes b_t)$. *Then, neglecting possible over- or underflows during the calculation,* $z = p \oplus q$ *and* $zz = (p \ominus z) \oplus q \oplus r$ *satisfy* $z + zz = a \cdot b$ *exactly.*

Proof. First note that for any two numbers $x, y \in R_{26}$ their product $x \cdot y \in R_{52} \subset R_{53}$. This is clear since for $x = m_x \cdot 2^{e_x}$ and $y = m_y \cdot 2^{e_y}$ we have that $x \cdot y = m_x \cdot m_y \cdot 2^{e_x+e_y}$ and $|m_x \cdot m_y| < 2^{52}$ since $|m_x| < 2^{26}$ and $|m_y| < 2^{26}$.

We also have that

$$a \cdot b = (a_h + a_t) \cdot (b_h + b_t) = a_h \cdot b_h + a_h \cdot b_t + a_t \cdot b_h + a_t \cdot b_t.$$

Since $a_h, a_t, b_h, b_t \in R_{26}$, each single term in this sum is in R_{52}. Furthermore, the two cross terms $a_h \cdot b_t$ and $a_t \cdot b_h$ have the same exponent and therefore their sum is in R_{53}. Thus p, q, and r, as defined in the statement of the theorem, are exact, and we obtain that $a \cdot b = p + q + r$.

Now we perform an exact addition of p and q as described above, yielding the leading term $z = p \oplus q$ and a remainder term $z_1 = (p \ominus z) \oplus q$. We thus have $a \cdot b = z + z_1 + r$. Close examination of the proof of the exact addition shows that r and z_1 have the same exponent and both are in R_{52}, so their sum can be calculated exactly in R_{53}. This leaves us with the final equation $a \cdot b = z + (z_1 \oplus r) = z + ((p \ominus z) \oplus q \oplus r) = z + zz$, which completes the proof. □

1.3. *High precision numbers*

Based on the exact multiplication and addition, it is now possible to implement high precision numbers. Those numbers are stored as unevaluated sums of double precision floating point numbers. The value represented by that high precision number is given by the exact sum of all terms:

Definition 1.4. A high precision number a is given by a finite sequence of double precision floating point numbers a_i. We call each a_i a limb of the number. The value of a is given by

$$a = \sum_{i=1}^{n} a_i.$$

The sequence a_i is also called a floating point expansion of a.

Note that in this definition we do not specify any requirements as to the relative size of the a_i. In general we would like the a_i to be ordered by magnitude in such a way that $|a_i| \approx \epsilon_m |a_{i-1}|$. If that condition is true for all limbs, we call the number *normalized*.

Depending on the desired accuracy, the maximum length is fixed before calculations commence. Although the machine precision is almost 10^{-16}, we conservatively estimate that each additional limb adds 15 more significant decimal digits to the expansion. Thus for a desired accuracy of n digits the number of limbs necessary is given by $\lceil n/15 \rceil$.

In order to make our high precision numbers rigorous, we add an error bound to the expansion, similarly to the remainder bound of Taylor Models.[5,6]

Definition 1.5. A high precision interval a is given by a high precision number consisting of n limbs a_i and a double precision error term a_{err}. The value of the

interval is then given by

$$a = \left[\sum_{i=1}^{n} a_i - a_{err},\ \sum_{i=1}^{n} a_i + a_{err} \right].$$

For shorter notation we also denote the above interval by $a = \sum_{i=1}^{n} a_i \pm a_{err}$.

This way of storing intervals as only one high precision midpoint and a simple double precision error term has obvious advantages over intervals stored as two high precision endpoints. Only one high precision number is needed, so the memory footprint of the high precision intervals is smaller. Furthermore, the computation time is less since operations only need to operate on one high precision number, whereas the error term can be calculated quickly in double precision arithmetic. Finally, this representation fits in nicely with the general concept of our high precision numbers. As we will see in the next section, verification is almost automatic in our algorithms. Thus our high precision intervals are almost as fast as non-verified high precision numbers would be.

1.3.1. *Accumulator*

The core operation used by our high precision numbers is the addition of a sequence of double precision numbers. The algorithm to perform that operation is called the accumulator. It takes a sequence of n double precision numbers a_i and returns another sequence of double precision numbers b_i of predefined maximum length. If there are roundoff errors or the result does not fit into the requested length, we optionally return an accumulated, outward rounded error term, which contains an upper bound on the error of the result. The input sequence is not required to be in any specific order, but to minimize the roundoff errors and to speed up execution time it is best if the input is sorted by decreasing order of magnitude. The output sequence is not guaranteed to be ordered, yet typically it will even be normalized, depending on the amount of cancellation happening during operations.

The implementation of this accumulator algorithm is not complicated. Let $a_1, \ldots, a_n$ denote the double precision numbers in the input array. Using the exact addition presented in the previous section, we begin by adding a_1 and a_2 exactly resulting in a result sum_1 and an error term b_1. Then we continue to exactly add sum_1 and a_2 into sum_1 and an error term b_2. This process is repeated until we have added all a_n. The resulting term sum_1 then is the first limb of the result. Note that after this procedure we are left with $b_1, \ldots, b_{n-1}$ error terms. To calculate the next limb, we just repeat the same procedure on $b_1, \ldots, b_{n-1}$, and so forth. Once the maximum number of limbs is reached, the absolute values of all remaining error terms are added up and rounded outwards to give a rigorous bound on the error. This algorithm is graphically represented in Fig. 1.

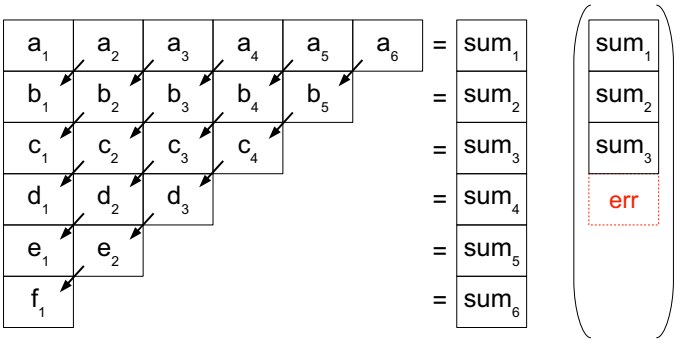

Fig. 1. The accumulator algorithm. In this example we want to add six double precision numbers $a_1 \ldots a_6$. The arrows indicate the error term of the exact addition of the two numbers above them. If only three limbs are desired for the result the summation terminates after three iterations and the left over terms are either discarded or accumulated into an outward rounded error term.

1.3.2. *High precision interval operations*

Utilizing the accumulator as outlined above, we have implemented a rigorous high precision interval arithmetic data type in COSY INFINITY.[7] As in any arithmetic, the two most important operations are addition and multiplication of two such intervals. Using the accumulator, addition is fairly straightforward. All we need to do is copy the limbs of each interval into an array and then send it through the accumulator. Since we get exact values for the leftover roundoff errors in this process, obtaining a remainder bound is trivial. For the multiplication we essentially use the fact that we can multiply each limb of the first argument with each limb of the second argument exactly using Dekker's algorithm. Then all the results of those multiplications are added up using the accumulator. Here, again, the accumulator gives us precise bounds for the left-over errors.

Division and intrinsic functions such as square roots, trigonometric functions, etc. are then implemented based on addition and multiplication. Using argument reduction based on mathematical identities, Taylor expansions, and Taylor remainder formulae for some intrinsics[8] or interval Newton iterations[9] for others, it is possible to calculate rigorous enclosures of the correct results. We will not go into more detail of this implementation, for a full discussion see [6].

At this point it is worth noting some differences between our implementation and other high precision implementations based on floating point expansions, such as the "double double" implementation in the original Dekker paper[2] and the arbitrary precision arithmetic by Shewchuk.[4] In those implementations the authors were very careful to develop algorithms that provide some guaranteed accuracy and derived error estimates for their operations. For floating point expansions, these estimates always lead to a requirement for normalization of the input. Normalization, however, is a rather complicated and computationally expensive operation. We, on the other hand, use an entirely different approach. Instead of making any analytic

estimates for roundoff errors, we have our numbers validate themselves by adding a rigorous remainder bound. The only claim we make is that the interval resulting from an operation rigorously encloses the mathematically correct result. If the input numbers are badly conditioned or if excessive cancellation occurs during the calculation, it is possible that our algorithm produces significant overestimation. The result, however, is rigorous nonetheless. Applying our high precision intervals to real world problems shows that those cases are very rare and that our intervals typically provide sharp enclosures of the correct results.[10] To the best of our knowledge, our implementation is the only rigorous interval implementation based on floating point expansions as of now.

2. Implementation of a High Precision Differential Algebra

Utilizing the same basic algorithms outlined above, we can begin to implement high precision DA vectors. Instead of starting from scratch, we will extend the already existing implementation of a DA vector in COSY. The final goal for this is to extend the existing DA vector type to high precision in such a way that it can act as a drop in replacement for the traditional double precision type. That is, old code should run without any major modification besides adding one command in the beginning of the code to select the desired precision. All subsequent operations should be transparently carried out without any change to the user interface. The full implementation of this is beyond the scope of this paper, but we will present the basic algorithms used.

As with the scalar data type, the two most important operations are addition and multiplication. Once these two have been properly implemented all other operations will follow naturally from those two. But before we can begin with the details of the implementation we shall introduce the way DA vectors are stored in our implementation.

2.1. *Storage*

Currently, DA vectors are stored as a list of double precision coefficients and an associated coding integer denoting the monomial for this coefficient. The method by which these coding integers are calculated is beyond the scope of this paper. For details, see [11]. Our way of representing high precision numbers blends in naturally with this storage format. Instead of only storing one double precision number per monomial, we will simply store several limbs continuously, all with the same coding integer. As with the high precision numbers, the value for each coefficient is the sum of all double precision numbers with the same coding integer.

By thus storing the limbs continuously in memory, we greatly simplify the addition and multiplication process as will be seen later. Also the typical output of such a DA vector is rather easy to interpret. As with the traditional DA vectors we simply print a list of all coefficients. Only this time there will not only be one

coefficient per monomial, but several. In the typical case the coefficients will decrease by orders of ϵ_m, so that the first coefficient printed should be roughly what the traditional DA vectors would produce, while all following coefficients will be corrections to that value. To make the output rigorous, we also print the exact binary representation of the floating point number as given in Definition 1.1.

2.2. *Addition*

The addition of two DA vectors is a fairly straightforward operation. It is a simple merging of the two vectors, where a monomial is copied into the output vector if it only appears in one of the vectors, or is added and then copied if a monomial appears in both vectors. In the high precision implementation we do exactly the same with the only difference that to add up two monomials appearing in both input vectors, we first copy the limbs into a temporary array, alternating between the two vectors. That way, as in the case of the high precision interval addition, we typically obtain an order of the array elements in roughly decreasing order of magnitude.

This array is then sent through the accumulator (see 1.3.1) that accumulates the numbers, starting with the smallest ones at the end of the temporary array, into the output vector. Once the maximum number of limbs has been reached, the absolute values of the left over terms are added up and kept in a separate tallying variable. This is in preparation for the implementation of Taylor Models, where all calculations are made rigorous by keeping an error bound.

This way of adding numbers is essentially the same we used for high precision scalars. Of course we thus get all the benefits that implementation had, including the automatic renormalization in case the input was denormalized and not too much cancellation occurs. Also the addition of a DA vector and a scalar (i.e. in COSY either a real or a high precision number) follows trivially from this. As always, once addition is implemented, by symmetry of the floating point numbers we also automatically have subtraction.

2.3. *Multiplication*

The more complex operation, and thus the core of our DA implementation, is the multiplication of two DA vectors. This is a very important operation that needs to be carried out quickly as it is used often throughout calculations. The performance of all other arithmetic operations depends crucially on this one operation. We therefore have taken great care to make this operation as fast as possible.

Because our way of storing high precision coefficients is quite natural in the current DA implementation, we can use most of the current implementation with only minor changes. A detailed description of the existing DA multiplication is beyond the scope of this paper, the reader is referred to [11] for full details. All we need to know here is that the algorithm walks through each coefficient in the first DA vector and multiplies it with every relevant coefficient in the second DA vector,

adding the result to a location in a temporary array which is determined by the coding integers of the first and the second coefficient. In order to determine which coefficients are "relevant", the algorithm first sorts the second DA vector by the monomial order of the coefficients. Note that this is not the same ordering induced by the coding integers.[11]

To amend this algorithm for efficient high precision operations, several things are necessary. First the temporary array which keeps all the new resulting coefficients needs to be enlarged, so it can keep the maximum number of limbs for each coefficient. Then we need to add the high precision multiplication. The naive way of achieving this would be to first extract all limbs for a given coefficient, and then to utilize the multiplication routine for high precision intervals. That, however, is very time consuming and also does not make use of some intrinsic properties of coefficients of DA vectors, which can be exploited to speed up the operation. So instead, we will rewrite the multiplication from scratch without relying on the high precision interval code here.

First, note that for the exact multiplication we need to split every coefficient into a head and a tail. This operation only has to be done once for each coefficient, and the most natural place to do the splitting is when the second DA vector is sorted by order. The first vector does not need to be pre-split since there every coefficient is only used once. Next, note that, instead of multiplying all limbs of the high precision coefficients at once, we can just multiply each limb separately and add the result to the appropriate resulting coefficient. There are two operations involved in this, a multiplication and then an addition.

One of the intrinsic properties of coefficients in DA vectors is that the magnitude of coefficients typically decrease exponentially with the order. We can use this fact to our advantage. In the COSY implementation of DA vectors, there is a cutoff value that specifies a lower bound on coefficients to be kept in the DA vector. Coefficients that are below that cutoff value are swept out of the calculation. We keep that concept of a cutoff value ϵ for our high precision implementation. Assuming that the high precision coefficients are normalized, we then can say that the last limb of any coefficient is of order ϵ/ϵ_m since all terms of order ϵ or lower are discarded. Now, when multiplying two coefficients, we do not immediately start with an expensive high precision multiplication. Instead, we first multiply the two coefficients in floating point arithmetic and then compare the order of the resulting number. If this product is of order ϵ/ϵ_m then the roundoff error due to floating point precision is of order $(\epsilon/\epsilon_m) \cdot \epsilon_m = \epsilon$ and thus is subject to the cutoff. In this case, there is no need to do any precise operations. We can proceed exactly as in the case of the traditional DA vectors, where the result is just added to the last limb of the correct monomial in the temporary array.

Only when this floating point multiplication yields a result that is of larger order than ϵ/ϵ_m do we perform a precise multiplication of the two coefficients. We still retain the approximate result of the floating point operation, though. This is because, in the next step, we need to add the two double precision numbers we

obtained from the exact multiplication to the resulting high precision coefficient. Naively, one could just copy the two numbers and all limbs in the result into an array and then send that through the accumulator. That, however, is not the most efficient way to perform the addition. Note that if we know the order of magnitude of the numbers we want to add, we can skip all limbs of higher order in the result since during the addition their value will not be affected. This is where the floating point product we calculated as a first step comes in. By estimating the order of magnitude of the approximate product, we can determine at which limb in the result we have to start to add the precise product.

The addition then also is carried out in an especially fast way. Assuming that the result is normalized, it is not necessary to add all numbers using the accumulator algorithm. Instead, we can do the following. Assume a_1 and a_2 are the two parts of the precise multiplication, and c_k is the limb of the result we determined to start our addition at. Then we perform an exact addition of a_1 and a_2 yielding $\tilde{a}$ and an error term a_{11}. Secondly, we exactly add $\tilde{a}$ and c_k to yield the new limb c_k and an error term a_{22}. Now we simply advance to the next limb of the result and repeat the same operations with a_{11}, a_{22} and c_{k+1}. We continue this process until we reach the maximum length of the result or until a_{11} and a_{22} are both zero.

A graphical representation of this algorithm is shown in Fig. 2. It is worth noting that at the end of this procedure, the two error terms left over are the exact roundoff error. Thus it is very easy to turn the DA vectors into rigorous Taylor Models later by simply adding the two left over terms to the correct tallying variable used in the rigorous Taylor Model operations.

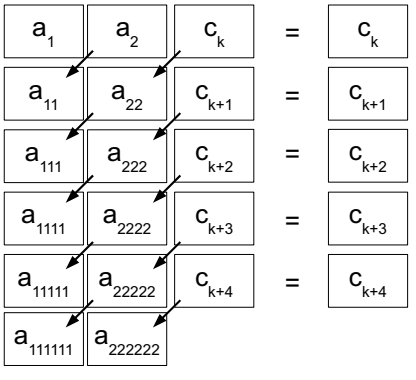

Fig. 2. Addition in the DA multiplication algorithm. a_1 and a_2 are the result of the exact addition, c_k is the limb of the result we start adding to. In this example there are four more limbs after that. The arrows indicate the error term of the exact addition of the two numbers above them.

Last we note that, since the limbs of a coefficient are stored linearly, we can keep the number of lookups in the coding integer tables constant. As in the traditional

DA vector case, only one lookup for each resulting monomial is required. To achieve that, we simply check if the coding integer for each coefficient is that same as that for the preceding one. If so, it is not necessary to perform another lookup since the last calculated address is still valid.

This completes the multiplication algorithm for high precision DA vectors.

To practically implement the algorithm outlined above, we have to have a way to estimate the order of magnitude of a floating point number. Fortunately, the representation of floating point numbers offers an easy way to do that. It is very fast to extract the exponent from a floating point number. But for the exponent e_a of a double precision floating point number a we have that

$$\ln_2(a) \leqslant e < \ln_2(a) + 1,$$

and thus it is a very good measure for the order of magnitude of a.

The efficiency of this implementation can be seen when comparing it to the traditional DA multiplication. Due to the floating point test we introduced, only operations which really need to be carried out in high precision are evaluated in that way. Practically this means that most higher order coefficients, which are typically very small, are treated exactly the same as before. Only the relatively few lower order coefficients are operated on in higher precision, but even here we try to keep the overhead small by only working on the relevant limbs. Thus the overhead is kept at a minimum.

2.4. *Other arithmetic operations*

The implementation of all other arithmetic operations from here on is straightforward. In fact, we can use the almost exact same code that already exists for the double precision DA vectors. The only somewhat non-trivial thing we need are the high precision intrinsic functions for high precision numbers. But as mentioned before, we already did implement a complete data type for high precision intervals based on the same representation used for the coefficients. So we can simply use those functions to calculate the needed high precision intrinsics.

The code for DA intrinsics essentially uses two methods: either a fixed point iteration or a simple Taylor expansion in the DA vector up to the necessary order to calculate the intrinsics. Without going into too much detail about the DA implementation, all intrinsics are reduced to one essential function. The intrinsics split off the constant part of the DA vector, evaluate the intrinsic on it using the corresponding high precision interval operation and then construct a one-dimensional polynomial of the non-constant remaining part of the DA argument. This is then evaluated efficiently by the procedure DAFUN. The original implementation of that function passes coefficients of the polynomial to evaluate as an array of double precision numbers. In the high precision implementation that clearly does not yield the desired result. The coefficients are instead passed as COSY variable numbers referencing high precision intervals. That is an easy and fast way to pass coefficients

to DAFUN while still allowing easy calculation of those coefficients in the calling intrinsic function. It also has the added benefit that repeating coefficients only require one COSY variable, as the same variable can be referenced several times as a coefficient. Those coefficients, of course, have to be calculated in high precision, otherwise the loss of precision there will lead to a loss of precision in the resulting DA vector and neutralize all benefits of high precision DA vectors.

Inside DAFUN we perform exactly the same operations as in the existing double precision implementation. Starting with the argument as the result we successively shift the highest remaining coefficient into the (empty) constant part of the result and multiply it by the argument using the high precision DA multiplication. We continue until all coefficients are used up. This is exactly the approach of the original implementation. The only difference is that we not only have to copy one but several double precision numbers into the result each time, as the coefficients themselves are high precision numbers consisting of several limbs. Since the DA vectors are non-verified, we can discard the high precision interval information and only use the interval's mid point as the coefficient.

With that change to DAFUN and minimal changes to all intrinsic functions to use high precision numbers for the coefficients, we can easily implement all remaining arithmetic operations. This for now completes the implementation of our basic high precision DA vectors. There are other functions in COSY which require further attention to make them work with the high precision DA vectors. Particularly the coefficient extraction operations to extract a certain coefficient from a DA vector need to be adjusted to extract not only one, but all limbs and to return a high precision number instead of just a double precision number.

2.5. *Output*

To output a high precision DA vector, we use essentially the same output format as for the traditional DA vectors. Non-zero coefficients of the expansion are printed, sorted by their order, each in one line. The first number in each line represents a running index of the coefficient, starting with 1. This is followed by a non-rigorous decimal fraction with 16 digits after the decimal point, representing an approximation to the coefficient's value. Note that, due to the nature of floating point numbers, not every floating point value can be represented as a decimal fraction of that length. The third field gives the order of that coefficient, followed by the exponents. Each integer in the exponent field represents a power of the corresponding independent variable.

Thus far, the output follows the traditional format. The last field in the line, however, is new. Here we print a rigorous representation of the floating point number. This is achieved by extracting the exact mantissa and exponent from the representation of the floating point number, as given by Definition 1.1. To assure the representation is compact, yet readable, we followed the representation of decimal fractions. Numbers are output as their mantissa value, the letter "b", followed by

the exponent. Similar to the letter "E" in the decimal fraction notation used in the first field, the "b" represents 2 raised to the power of the following integer.

Consider, for example, the following output line

```
6  -.1250000000000000       2   2 0                          -1b-3
```

This is the 6th line of the output, the decimal representation of the coefficient is given as -0.125. The coefficient has order two, and belongs to the $x^2y^0 = x^2$ term. The exact representation is given by $-1b-3 = -1 \cdot 2^{-3} = -\frac{1}{8}$. Although in this example the exact and decimal representation are the same, this is generally not true due to possible rounding in the conversion to a decimal fraction.

If the DA vector contains high precision coefficients, each limb of the coefficients is printed as a regular coefficient. Since the limbs are stored sequentially, they will also appear in sequence in the output. If the high precision coefficient is normalized, typically each limb will be about 10^{-15} times smaller than the previous limb. An example of this output style is given below.

```
1  0.8660254037844386       1   1 0        3900231685776981b-52
2  0.5017542110903451E-16   1   1 0        8141427543753187b-107
3  -.7479771237866948E-33   1   1 0       -8745358328802511b-163
4  0.2653073781648097E-49   1   1 0         87312899972227b-211
```

Note how each line has the same exponents, $x^1y^0 = x$, thus signaling that these coefficients represent limbs of the same high precision coefficient. The correct value for this coefficient is the exact sum of all limbs. To calculate a decimal representation of the coefficient, one can simply add up the exact representation of each limb using a third party high precision package.

3. Illustrating Example

The DA vectors in COSY INFINITY were initially implemented to derive arbitrary order transfer maps for beam physics applications.[12] This is particularly useful in connection with assessment of long-term stability through symplectic tracking.[13,14] To show how our high precision DA vectors can help to get even better results, we will present transfer maps for several homogeneous dipole magnet segments.

Currently we cannot yet just run the existing COSY INFINITY code with high precision DA vectors due to the missing implementation of some essential functions used in the COSY beam physics package. Instead, we have manually derived an algebraic equation to calculate the final coordinates x_f and a_f of a beam depending on the initial position x_i and slope a_i in a homogeneous dipole magnet of reference radius r_0 and angle θ based on the geometry of the problem.

Let

$$c_x = r_0 \sin(a_i),$$

$$c_y = x_i + r_0 \left(1 - \cos(a_i)\right),$$

$$A = \tan(\theta)^2 + 1,$$

$$B = 2\left(\tan(\theta) c_x + c_y\right),$$

$$C = c_x^2 + c_y^2 - r_0^2.$$

Then

$$x_f = \frac{-B + \sqrt{B^2 - 4 \cdot A \cdot C}}{2\sqrt{A}} - r_0, \tag{3}$$

$$a_f = \theta - \arctan\left(\frac{r_0 \sin(a_i) - (x_f + r_0)\sin(\theta)}{x_i + r_0(1 - \cos(a_i)) - (x_f + r_0)\cos(\theta)}\right). \tag{4}$$

The corresponding COSY INFINITY function that represents the same beam line element is `MS` r_0 θ `1 0 0 0 0 0;`.

With our high precision DA vector implementation we should, of course, be able to reproduce essentially the same map as the COSY beam code, except for small roundoff errors. Our test case will be a homogeneous dipole segment of angle $\theta = \frac{\pi}{6}$ and reference radius $r_0 = 1$. The expansion for the final position and slope as calculated by the current COSY INFINITY double precision code using the command

```
MS 1 30 1 0 0 0 0 0;
```

is given in Fig. 3. Comparing that to the results of the evaluation of Eq. (3) in high precision DA arithmetic with about 60 digits, given in Fig. 4, shows that, indeed, the leading limb of the result is the same as in the COSY beam physics expansion. All the small roundoff errors of magnitude 10^{-15} encountered in the double precision expansion, however, are not seen in the high precision implementation. We have set the cutoff value, below which coefficients are discarded, to 10^{-60} in the high precision operation. That is why there seem to be no roundoff errors in the high precision map. They were all below the cutoff value.

Note how some of the coefficients actually do not require high precision. At first glance it looks like there is no benefit to high precision calculations. All there is, is the same number as in the double precision case. But actually this result shows how well our implementation works. Those coefficients can be accurately represented by only one double precision number. All digits up to 10^{-60} are actually 0.

To see the full power of the high precision DA vectors, we now combine 12 of those 30 degree segments together to form a full 360 degree bend. Clearly the resulting transfer map has to be the identity. Simply repeating the COSY `MS` command 12 times yields the expected transfer map shown in Fig. 5. The linear coefficients are almost 1 whereas the other coefficients are all of order 10^{-15} or less. On the other hand, iterating Eq. (3) 12 times with high precision DA vectors results in the map shown in Fig. 6. In these calculations, we set the cutoff value to 10^{-70}. That way, the small roundoff error terms become visible in the result. As before the result is the identity map, up to roundoff noise introduced during the calculation. The notable difference is that, since we work with high precision numbers of length 60, the noise is of the order of 10^{-63}.

x_f:

```
 I  COEFFICIENT             ORDER EXPONENTS
 1  0.8660254037844386        1   1 0  0
 2  0.4999999999999999        1   0 1  0
 3  -.1249999999999999        2   2 0  0
 4  0.4330127018922192        2   1 1  0
 5  0.5801270189221930E-01    2   0 2  0
 6  -.1250000000000000        3   1 2  0
 7  0.2165063509461096        3   0 3  0
 8  -.7812499999999993E-02    4   4 0  0
 9  0.5412658773652738E-01    4   3 1  0
10  -.1406249999999999        4   2 2  0
11  0.1623797632095823        4   1 3  0
12  0.6690675473054825E-02    4   0 4  0
13  -.1562499999999999E-01    5   3 2  0
14  0.8118988160479110E-01    5   2 3  0
15  -.1718749999999999        5   1 4  0
16  0.1353164693413186        5   0 5  0
-------------------------------------
```

a_f:

```
 I  COEFFICIENT             ORDER EXPONENTS
 1  -.4999999999999999        1   1 0  0
 2  0.8660254037844386        1   0 1  0
 3  -.2500000000000000        2   0 2  0
 4  -.6250000000000000E-01    4   0 4  0
 5  0.2220446049250313E-15    5   2 3  0
 -------------------------------------
```

Fig. 3. Transfer map for a 30 degree homogeneous dipole with COSY beam package.

x_f:

I	COEFFICIENT	ORDER	EXPONENTS	EXACT REPRESENTATION
1	0.8660254037844386	1	1 0	3900231685776981b-52
2	0.5017542110903451E-16	1	1 0	8141427543753187b-107
3	-.7479771237866948E-33	1	1 0	-8745358328802511b-163
4	0.2653073781648097E-49	1	1 0	87312899972227b-211
5	0.5000000000000000	1	0 1	1b-1
6	-.1250000000000000	2	2 0	-1b-3
7	0.4330127018922193	2	1 1	3900231685776981b-53
8	0.2508771055451726E-16	2	1 1	8141427543753187b-108
9	-.3739885618933474E-33	2	1 1	-8745358328802511b-164
10	0.1326536890824049E-49	2	1 1	87312899972227b-212
11	0.5801270189221933E-01	2	0 2	2090127860996437b-55
12	-.2667865061111657E-17	2	0 2	-6926173687902441b-111
13	0.1119742698409979E-34	2	0 2	4189454815015701b-168
14	-.9845464222053095E-52	2	0 2	-2592120999413b-214
15	-.1250000000000000	3	1 2	-1b-3
16	0.2165063509461096	3	0 3	3900231685776981b-54
17	0.1254385527725863E-16	3	0 3	8141427543753187b-109
18	-.1869942809466737E-33	3	0 3	-8745358328802511b-165
19	0.6632684454120243E-50	3	0 3	87312899972227b-213
20	-.7812500000000000E-02	4	4 0	-1b-7
21	0.5412658773652741E-01	4	3 1	3900231685776981b-56
22	0.3135963819314657E-17	4	3 1	8141427543753187b-111
23	-.4674857023666842E-34	4	3 1	-8745358328802511b-167
24	0.1658171113530080E-50	4	3 1	21828224993057b-213
25	-.1406250000000000	4	2 2	-9b-6
26	0.1623797632095823	4	1 3	45705840067699b-48
27	-.4469896349870486E-17	4	1 3	-1450564298463051b-108
28	0.2449402781674419E-33	4	1 3	2863844940720025b-163
29	0.2101110160114334E-49	4	1 3	138295453756081b-212
30	0.6690675473054831E-02	4	0 4	7713823633230503b-60
31	0.2003954727104893E-18	4	0 4	2081025566838551b-113
32	0.2799356746024948E-35	4	0 4	4189454815015701b-170
33	-.2461366055511375E-52	4	0 4	-2592120999411b-216
34	-.1562500000000000E-01	5	3 2	-1b-6
35	0.8118988160479113E-01	5	2 3	45705840067699b-49
36	-.2234948174935243E-17	5	2 3	-1450564298463051b-109
37	0.1224701390837209E-33	5	2 3	2863844940720025b-164
38	0.1050555080057157E-49	5	2 3	553181815024319b-215
39	-.1718750000000000	5	1 4	-11b-6
40	0.1353164693413186	5	0 5	4875289607221227b-55
41	-.1297677216343504E-16	5	0 5	-4211203333632873b-108
42	-.3094644200303947E-33	5	0 5	-7236524105121281b-164
43	0.1750925133428610E-49	5	0 5	3687878766828823b-217

Fig. 4. Transfer map for a 30 degree homogeneous dipole with high precision DA vectors (normalized).

a_f:

I	COEFFICIENT	ORDER	EXPONENTS	EXACT REPRESENTATION
1	-.5000000000000000	1	1 0	-1b-1
2	0.8660254037844386	1	0 1	3900231685776981b-52
3	0.5017542110903451E-16	1	0 1	8141427543753187b-107
4	-.7479771237866948E-33	1	0 1	-8745358328802511b-163
5	0.2653073781648059E-49	1	0 1	349251599888903b-213
6	-.2500000000000000	2	0 2	-1b-2
7	-.6250000000000000E-01	4	0 4	-1b-4

Fig. 4. (*Continued*)

x_f:

I	COEFFICIENT	ORDER	EXPONENTS
1	0.9999999999999993	1	1 0 0
2	-.1665334536937735E-15	1	0 1 0
3	-.1665334536937734E-15	2	1 1 0
4	0.3330669073875470E-15	2	0 2 0
5	0.5499073418846478E-15	4	2 2 0
6	0.3348016308635238E-15	4	1 3 0
7	0.1942890293094024E-15	4	0 4 0
8	-.1387778780781446E-15	5	4 1 0
9	-.1110223024625157E-15	5	3 2 0
10	0.1110223024625157E-15	5	2 3 0
11	0.1082467449009528E-14	5	1 4 0

a_f:

I	COEFFICIENT	ORDER	EXPONENTS
1	0.1665334536937735E-15	1	1 0 0
2	0.9999999999999993	1	0 1 0
3	-.2220446049250313E-15	4	1 3 0
4	-.7359851755371739E-15	5	4 1 0
5	0.9601694439531627E-15	5	3 2 0
6	0.1214306433183765E-14	5	2 3 0
7	0.5273559366969494E-15	5	1 4 0

Fig. 5. Transfer map for 12 30 degree homogeneous dipoles with COSY beam package.

x_f:

I	COEFFICIENT	ORDER	EXPONENTS	EXACT REPRESENTATION
1	1.000000000000000	1	1 0	1b0
2	0.1001967514747971E-62	1	0 1	3712637180178849b-261
3	-.8517491040037048E-63	2	2 0	-3156025864275235b-261
4	0.8502528978208232E-63	2	1 1	6300963802800349b-262
5	-.8058934833360440E-63	2	0 2	-5972229768846003b-262
6	-.1421155290465671E-62	3	3 0	-164558540213685b-256
7	-.1914009193660878E-62	3	2 1	-7092067947309569b-261
8	-.3175427147967325E-62	3	1 2	-367689343684029b-256
9	0.1793778628155982E-62	3	0 3	3323285999734849b-260
10	0.3216870906455098E-62	4	4 0	372488203065175b-256
11	-.7424413638917452E-63	4	3 1	-5502005546318573b-262
12	-.2598190020076057E-62	4	2 2	-4813597610562419b-260
13	0.2515338308647966E-62	4	1 3	4660100446352085b-260
14	0.1805036934614915E-62	4	0 4	6688287929906621b-261
15	0.8011932350143374E-63	5	5 0	5937397668167309b-262
16	-.7490211353162293E-62	5	4 1	-6938457771293817b-259
17	-.7799594535945731E-62	5	3 2	-7225050772168895b-259
18	0.4235531564115624E-62	5	2 3	7847056781432733b-260
19	-.1500571371277421E-62	5	1 4	-5560137412157345b-261
20	0.1584098366644266E-63	5	0 5	4695707121437689b-264

a_f:

I	COEFFICIENT	ORDER	EXPONENTS	EXACT REPRESENTATION
1	0.3560837904659925E-63	0	0 0	75b-217
2	-.2278936258982352E-63	1	1 0	-3b-213
3	1.000000000000000	1	0 1	1b0
4	0.1367361755389411E-62	1	0 1	9b-212
5	0.7976276906438231E-63	2	2 0	21b-214
6	0.1583069429958924E-63	2	1 1	2346328533794189b-263
7	-.6077163357286271E-63	2	0 2	-1b-210
8	-.1367361755389411E-62	3	3 0	-9b-212
9	0.1411139791891778E-62	3	2 1	2614381195344969b-260
10	-.2765903754149412E-62	3	1 2	-5124316389156745b-260
11	-.2051042633084117E-62	3	0 3	-27b-213
12	-.1139468129491176E-63	4	4 0	-3b-214
13	0.2033073242981725E-62	4	3 1	941655193509359b-258
14	0.2449856478406028E-62	4	2 2	129b-215
15	0.9779722569634157E-63	4	1 3	7247452854395351b-262
16	0.1185759022251755E-62	4	0 4	8787296929185793b-262
17	-.4329978892066468E-62	5	5 0	-57b-213
18	0.7659812972263426E-62	5	4 1	7095565977803831b-259
19	0.5849269731388036E-62	5	3 2	77b-213
20	0.1000543052127116E-61	5	2 3	4634198815107191b-258
21	-.5147305191874726E-62	5	1 4	-2384068888437037b-258
22	0.2468847613897548E-62	5	0 5	65b-214

Fig. 6. Transfer map for 12 30 degree homogeneous dipoles with high precision DA vectors (normalized).

References

1. IEEE standard for binary floating-point arithmetic. Technical Report IEEE Std 754-1985, The Institute of Electrical and Electronics Engineers, 1985.
2. T.J. Dekker. A floating-point technique for extending the available precision. *Numerische Mathematik*, 18:224–242, 1971/72.
3. D. E. Knuth. *The Art of Computer Programming*, volume I-III. Addison Wesley, Reading, MA, 1973.
4. J. R. Shewchuk. Adaptive precision floating-point arithmetic and fast robust geometric predicates. *Discrete & Computational Geometry*, 18:305–363, 1997.
5. K. Makino. *Rigorous Analysis of Nonlinear Motion in Particle Accelerators*. PhD thesis, Michigan State University, East Lansing, Michigan, USA, 1998. Also MSUCL-1093.
6. A. Wittig and M. Berz. Design and implementation of a high precision arithmetic with rigorous error bounds. Technical Report MSUHEP 081126, Michigan State University, 2008.
7. K. Makino and M. Berz. COSY INFINITY version 9. *Nuclear Instruments and Methods*, 558:346–350, 2005.
8. K. Braune and W. Kramer. High-accuracy standard functions for intervals. In Manfred Ruschitzka, editor, *Computer Systems: Performance and Simulation*, volume 2, pages 341–347. Elsevier Science Publishers B.V., 1986.
9. R. E. Moore. *Interval Analysis*. Prentice-Hall, Englewood Cliffs, NJ, 1966.
10. A. Wittig, M. Berz, and S. Newhouse. Computer assisted proof of the existence of high order fixed points. In *Proceedings, Fifth Int. Workshop on Taylor Model Methods, Toronto, Canada*, 2008.
11. M. Berz. Forward algorithms for high orders and many variables. *Automatic Differentiation of Algorithms: Theory, Implementation and Application*, SIAM, 1991.
12. M. Berz. *Modern Map Methods in Particle Beam Physics*. Academic Press, San Diego, 1999. Also available at http://bt.pa.msu.edu/pub.
13. B. Erdlyi and M. Berz. Optimal symplectic approximation of Hamiltonian flows. *Physical Review Letters*, 87,11:114302, 2001.
14. B. Erdlyi and M. Berz. Local theory and applications of extended generating functions. *International Journal of Pure and Applied Mathematics*, 11,3:241–282, 2004.

International Journal of Modern Physics A
Vol. 24, No. 5 (2009) 1040–1047

World Scientific
www.worldscientific.com

PARAMETRIC OPTIMIZATION METHODS FOR THE TOKAMAK PLASMA CONTROL PROBLEM

SERGEY V. ZAVADSKY* and DMITRI A. OVSYANNIKOV†

Faculty of Applied Mathematics and Control Processes,
Saint Petersburg State University, Saint Petersburg, Russia
** sergzav@pochtamt.ru*
† dovs45@mail.ru

SHENG-LUEN CHUNG

Electrical Engineering Department,
National Taiwan University of Science and Technology, Taipei, Taiwan
schlung@mail.ntust.edu.tw

Mathematical models of the structural parametric optimization of plasma dynamics are discussed. Optimization approach to plasma dynamic is based on the consideration of trajectory ensemble. This ensemble describes transient process in tokamak subject to the initial data and external disturbances. In the framework of this approach the optimization of dynamics of the trajectory ensemble in ITER tokamak is given. The trajectories of this ensemble are perturbed at the initial point set and the set of external disturbances.

Keywords: Tokamak; ITER; plasma control; optimization; transient process optimization.

PACS numbers: 52.55.Fa, 02.30.Yy

1. Introduction

Problems of analysis and synthesis of stabilizing regulators of current, position and plasma shape in tokamak are of great importance. Linear systems are widely used in design problems of control systems for complex objects. The synthesis of the regulator that stabilizes plasma shape in tokamak is done based on the linearization of differential equations that define plasma behavior. The procedure of reduction and LQG-algorithms of analytical regulator construction are applied to the LTI-object, see [1–7, 10] for more details. The control object in the state space can be described by the following equations:

$$\begin{aligned} \dot{x} &= Ax + Bu + Gf(t), \\ e &= Lx + Mu, \\ y &= Cx + Du + Ff(t), \end{aligned} \tag{1}$$

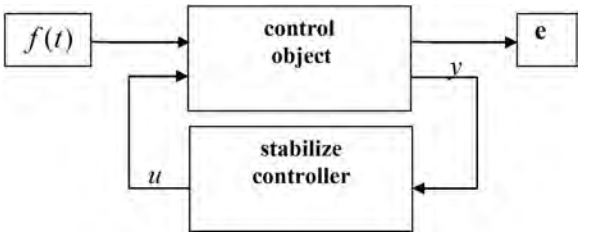

Fig. 1. The control object closure by the obtained regulator.

where $x \in E^n$ is the state space vector, $u \in E^r$ is the control voltages vector, $y \in E^k$ is the diagnostic signals vector, $e \in E^d$ is the measurement variables vector, all the matrices in the model are known, with constant components, $f(t)$ is the vector function of external disturbances, which is called l_i, β – *drops* disturbance and is defined in the following form

$$f(t) = f_{\text{drop}}(t) = \begin{pmatrix} w_1(t) \\ w_2(t) \end{pmatrix}, \quad w_1(t) = d_\beta e^{-(t/t_\beta)}, \quad w_1(t) = d_l e^{-(t/t_l)}, \tag{2}$$

where d_β, d_l, t_β, t_l are known real numbers. The control object is closed with a regulator of a decreased dimension with the following structure:

$$\begin{aligned} \dot{z} &= A_c z + B_c y, \\ u &= C_c z, \end{aligned} \tag{3}$$

where vectors y and u are the output and input of the object (1) respectively, matrices A_c, B_c, C_c are the constant component matrices of the controller, which can be obtained, for example, using the reduction procedure and the LQG-optimal synthesis.[4] The control object closure by the obtained regulator is done in accordance with the scheme in Fig. 1.

By the "regulator synthesis" we mean such a choice of parameters of the regulator of the LTI component that gives us a closed object that is stable. On the trajectory of the closed system we define the following quadratic quality functional and consider the problem of its minimization

$$J(W) = \int_0^T \big(e^*(t)Re(t) + u^*(t)Qu(t)\big)dt \to \min,$$

where R and Q are positively defined, symmetrical weight matrices.

Also, we need to take into account the nonlinear amplitude constraints on control voltage signals. For example, the ITER tokamak has 11 control coils with constraints on voltage amplitudes. These constraints have different numerical values and can be represented in the following form

$$u_i = \begin{cases} c_i, & u_i > c_i \\ u_i, & |u_i| \le c_i, \quad i = 1, \ldots, 11, \\ -c_i, & u_i < -c_i \end{cases}$$

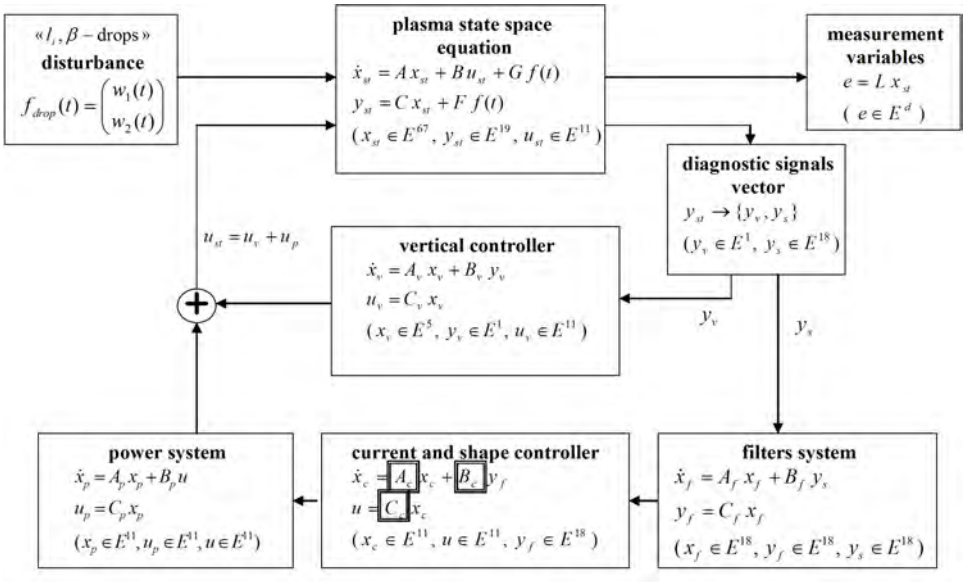

Fig. 2. Structural model of ITER plazma control system.

where i is the index of a coil, c_i is the amplitude maximum for the i-th coil. It complicates the design of the controller and allows no simple raise in the magnitude of control voltage signals.

Note, that the controller design is analyzed by means of the linear model, however this controller is tested on the nonlinear model, and has to possess appropriate characteristics.

2. The Structural Model of ITER Plasma Control System

The mathematical model of ITER plasma control system can be represented using the structural diagram (Fig. 2) which links LTI-blocks of various subsystems. Matrices of these subsystems are known with constant components.

Further, the elements of matrices A_c, B_c, C_c of the dynamic shape controller will be taken as parameters that are to be optimized and combined into a vector of parameters

$$p = \{p_k\} \leftrightarrow \{A_c, B_c, C_c\}.$$

A mathematical model of the structural parametric optimization of dynamics of a set of trajectories that are perturbed at the initial point set and the set of external disturbances is suggested. In the framework of this approach, the optimization of transient processes of the full-sized control object that is closed by a regulator of a decreased dimension is conducted. It is suggested to use an integral performance criterion as a functional that allows optimizing the transient process, perturbed at the initial point set and the set of external disturbances.

3. Parametric Optimization Method

Let us investigate the equation of the control object (1) with constantly applied perturbation (2), which is closed by the regulator of decreased dimension (3) and the subsystem objects of the structural diagram presented in Fig. 2. We combine the structural diagram of control system into a system of linear differential equations with perturbation. To do that, let us introduce the following vectors and matrices: extended state-space vector $x = \{x_{st}, x_\nu, x_p, x_f, x_c\}$ that includes plasma states, vertical controller states, power system states, filter system states and shape controller states; matrices P and N with constant components such what P is a matrix of the linear part of the system mentioned above, and N is the coefficient of the non-linear part; these matrices can be easily identified in Fig. 2; the matrices L and K for linear combinations with extended state- space vector. So, by using the newly introduced variables, we represent the structural diagram of the control system shown in Fig. 2 in the following form:

$$\begin{aligned} &\dot{x} = P(p)x + N(p)f(t), \\ &x(0) = x_0, \\ &f(t) = f(d_\beta, t_\beta, d_l, t_l, t), \\ &e = Lx(t, x_0, p), \\ &u = K(p)x(t, x_0, p), \end{aligned} \tag{4}$$

where $x \in E^{112}$ is the extended state space vector, $e \in E^d$ is the measurement variables vector, $u \in E^{11}$ is the control voltages vector, P, N, L, K are the above introduced constant component matrices, $f(t)$ is the l_i, β–*drops* disturbance, $p = \{p_k\}$ is a vector of parameters. Note, that the matrices A_c, B_c, C_c of a designed regulator (3) will be taken as parameters that are to be optimized. We combine the elements of these matrices into a vector of parameters , where each parameter has its own index. By labeling it $P(p)$ and $N(p)$ we emphasize that it depends on the parameters that are being optimized. Based on this differential system (4) we have measurement variables vector e and control voltages vector u.

Further, we will describe transient process by an ensemble of trajectories. Let $x_0, f(t)$ be arbitrary disturbance vectors that satisfy the following equation at the instant t (disturbance ensemble)[8]

$$\begin{gathered} (x_0, f(t)) \in \Psi \equiv \Psi(G_1, G_2(t), \mu^2), \\ \Psi = \{(x_0, f(t)) : x_0^* G_1 x_0 + \int\limits_{t_0}^{t} f^*(\tau) G_2(\tau) f(\tau) d\tau \le \mu^2\}, \end{gathered} \tag{5}$$

where $G_1, G_2(t)$ are the positively defined matrices and μ is the real positive constant. This disturbance ensemble includes modeling drops and vertical shift of plasma.

Let us consider matrix D as a solution of the matrix differential equation

$$\begin{aligned} &\dot{D} = P(p)D + DP^*(p) + N(p)G_2(t)^{-1}N^*(p), \\ &D(0) = G_1^{-1}, \\ &D(t) \equiv D(t, p, G_1, G_2(t)). \end{aligned} \tag{6}$$

Note that the proposed approach employing the D matrix allows us to estimate the ensemble of trajectories as a whole, compared to the previously developed methods that allowed to estimate just one trajectory. So, using the D matrix we obtain the following dynamic estimations for trajectories ensemble that allow us to control whole set of trajectories:

$$\begin{aligned} s_{e_i}(t) &= \sup_{(x_0, f(t)) \in \Psi} |e_i(t)^2| = \mu^2 l_i D(t) l_i^*, \\ s_{u_i}(t) &= \sup_{(x_0, f(t)) \in \Psi} |u_i(t)^2| = \mu^2 k_i D(t) k_i^*, \end{aligned} \tag{7}$$

where $s_{e_i}(t)$ and $s_{u_i}(t)$ are the estimates for the measurement variables vector and the control voltages vector respectively, l_i, k_i are rows of the matrices L and K. Based on the estimates (7) it is suggested to use the following integral performance criterion that allows optimizing the set of transient processes perturbed by the sets of initial points and external disturbances:

$$I(p) = \int_0^T \left\{ \sum_{i=1}^{p} s_{e_i}(t) + \sum_{i=1}^{r} s_{u_i}(t) \right\} dt + \sum_{i=1}^{p} s_{e_i}(T) =$$

$$= \int_0^T \left\{ \sum_{i=1}^{p} \sup_{(x_0, f(t)) \in \Psi} |e_i(t)|^2 + \sum_{i=1}^{r} \sup_{(x_0, f(t)) \in \Psi} |u_i(t)^2| \right\} dt + \sum_{i=1}^{p} \sup_{(x_0, f(t)) \in \Psi} |e_i(T)|^2.$$

Functional $I(p)$ can be represented in the following form:

$$\begin{aligned} I(p) = \mu^2 \Bigg(\int_0^T \big\{ &\mathrm{tr}[W_1 L D(t) L^*] + \mathrm{tr}[W_2 K(p) D(t) K(p)^*] \big\} dt + \\ &+ \mathrm{tr}[W_3 L D(t) L^*] \Bigg) \to \min, \end{aligned} \tag{8}$$

where $\mathrm{tr}[A]$ is the trace of the matrix A, W_1, W_2, W_3 are symmetrical weight matrices. Let us study the performance functional (8) for the system (4) that is to be optimized, where $p = \{p_k\}$ is a vector of parameters. The algorithms for the optimization of this functional are suggested below.

After transforming the functional using the parametric optimization approach,[9] we obtain a representation for the gradient of the functional with respect to the parameters $p = \{p_k\}$

$$\frac{\partial I}{\partial p_k} = -\mu^2 \int_0^T 2\mathrm{tr} \left(\Theta(t) D(t) \frac{\partial P^*}{\partial p_k} + \Theta(t) N G_2(t)^{-1} \frac{\partial N^*}{\partial p_k} - \frac{\partial K^*}{\partial p_k} W_2 K D(t) \right) dt, \tag{9}$$

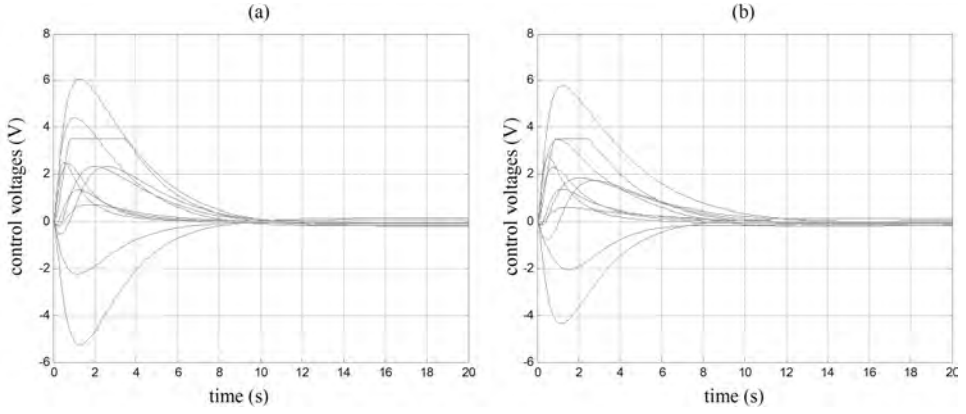

Fig. 3. Control voltage signals $u_1, \ldots, u_{11}$ corresponding to a) initial controller and b) optimized controller.

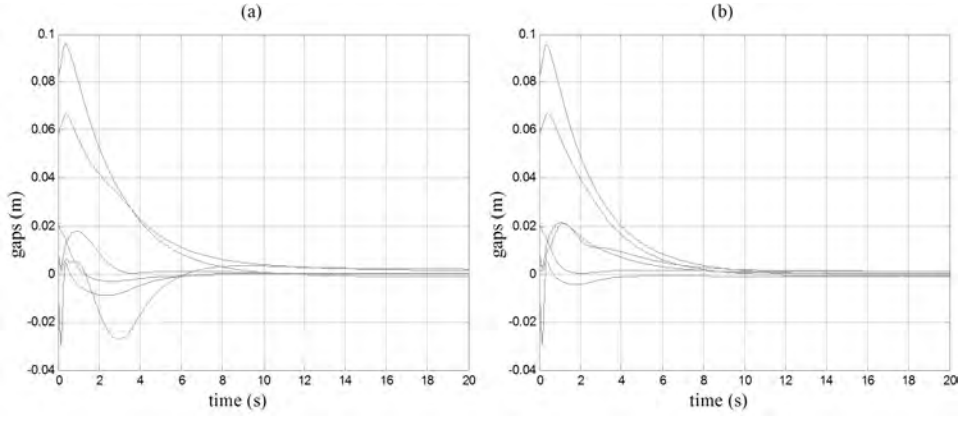

Fig. 4. Transient processes of gaps $g_1, \ldots, g_6$ corresponding to a) initial controller and b) optimized controller.

where matrix D is the solution of Eq.(6), matrix Θ is the solution of the following equation

$$\dot{\Theta} = -\Theta P - P^*\Theta + L^*W_1L + K^*W_2K, \quad \Theta(T) = -L^*W_3L. \tag{10}$$

Based on the analytical expressions (9)–(10) a gradient optimization method for the functional (8) with respect to the parameters $p = \{p_k\}$ is implemented for C++ and Matlab environments.

4. Optimization Results

The optimization results are considered based on transient processes of checked clearances—*gaps*, which are the members of the measurement variables vector for the control object (4). The modeling of transient processes of the control object

closed with the optimized and initial controller is shown. This initial controller is obtained using the approaches described in [4, 10] and already possesses proper characteristics. The graphical results of optimization are presented in Figs. 3–4. Fig. 3 shows control voltage signals $u_1, \ldots, u_{11}$ for control object closed with initial and optimized controllers and Fig. 4 shows transient processes of gaps $g_1, \ldots, g_6$ for control object closed with initial and optimized controllers of the nonlinear model with voltage limitations.

Fig. 3 shows that by using envelope estimation for u_i we can choose maximums of control voltages according to their limitations, then raise them and obtain better performance for measurement variables e_i. This is illustrated in Fig. 4. Also, we consider optimization performance base on the numerical characteristics such as the integral of squared gaps

$$I_{\text{gaps}} = \int_0^T \sum_{i=1\ldots6} g_i^2(t)dt$$

and the settling time

$$t_{\text{settling}} = \min_{\widetilde{t}}\{\widetilde{t} : \max_{i=1\ldots6} |g_i(t)| \leq 0.01, \quad \forall t \geq \widetilde{t}\},$$

which are presented in Table 1.

Table 1. Settling time and integral of squared gaps for control object closed with initial and optimized controllers.

Control object closed with initial controller	Control object closed with optimized controller
$I_{\text{gaps}} = 0.027$ $t_{\text{settling}} = 6.373\,\text{sec.}$	$I_{\text{gaps}} = 0.024$ $t_{\text{settling}} = 5.634\,\text{sec.}$

5. Conclusion

This work is dedicated to questions concerning synthesis and optimization of tokamak plasma control system. The structural model of ITER plasma control system (Fig. 2) is discussed and the structural parametric optimization method is suggested. We combine the structural diagram of control system into differential equations system (4) with disturbances defined by Eq.(5). The estimate (7) for the transient process ensemble dynamics is proposed. Based on the analytical expressions (8)–(10) a gradient method of optimization is implemented for C++ and Matlab environments. Results of the computations are obtained and discussed. Numerical characteristics such as the integral of squared gaps and the settling time are presented for the both initial and the optimized controllers. For the optimized controller the squared gaps and settling time are noticeably lower.

Acknowledgments

The work is done under support of the National Taiwan University of Science and Technology and Saint-Petersburg State University Joint Research Project No. RP07-05.

References

1. D. A. Ovsyannikov, E. I. Veremey, A. P. Zhabko et al. Mathematical methods of plasma vertical stabilization in modern tokamaks // Nuclear Fusion. 2006. Vol 46. P. 652-657.
2. G. J. McArdle, V. A. Belyakov, D. A. Ovsyannikov, E. I. Veremey. The MAST plasma control system // Proc. 20^{th} Intern. Symp. on Fusion Tecnology SOFT'98. Marseille, France. 1998. P. 541–544.
3. D. A. Ovsyannikov, A. P. Zhabko, E. I. Veremey et al. Plasma current and shape stabilization with control power reducing // Proc. of the 5th Intern. workshop: "Beam Dynamics & Optimization". St.Petersburg, 1998. P. 103–111.
4. D. A. Ovsyannikov, E. I. Veremey, A. P. Zhabko et al. Mathematical methods of tokamak plasma shape control // Proc. of the 3th Intern. workshop: "Beam Dynamics & Optimization". St.Petersburg, 1996. P. 218–229.
5. B. A. Misenov, D. A. Ovsyannikov, A. D. Ovsyannikov et al. Analysis and Synthesis of Plasma Stabilization Systems in Tokamaks // Control Application of Optimization: Preprints of the Eleventh IFAC Intern. Workshop. St.Petersburg, 2000. P. 249–254.
6. B. A. Misenov, A. D. Ovsyannikov, D. A. Ovsyannikov et al. Non-linear model of tokamak plasma shape stabilization // Intern. conf. on Informatics and Control (ICI&C'97). St.Petersburg, 1997. P. 382–388.
7. B. Misenov. Computational aspects of plasma shape control synthesis problem // Proc. of 2nd Intern. Workshop "Beam Dynamics and Optimization". St.Petersburg, 1995. P. 138–145.
8. N. F. Kirichenko. Introduction to the motion stabilization theory. Kiev, 1978, in Russian.
9. D. A. Ovsaynnikov. Modeling and optimization of charged particle beam dynamics. St.Petersburg, 1990, in Russian.
10. E. I. Veremey, N. A. Zhabko. Plasma current and shape controllers design for ITER-FEAT tokamak // Book of abstracts of Workshop on Computational Physics Dedicated to the Memory of Stanislav Merkuriev. St.Petersburg, 2003. P. 52.

International Journal of Modern Physics A
Vol. 24, No. 5 (2009) 1048–1056

World Scientific
www.worldscientific.com

SOME H-OPTIMIZATION PROBLEMS FOR THE ITER PLASMA CONTROL SYSTEM

NATALIA A. ZHABKO

Faculty of Applied Mathematics and Control Processes, Saint-Petersburg State University, 35 Universitetskii pr., 198504, Saint-Petersburg, Russia
ztasha@mail.ru

Some ideas concerning the application of methods of H-optimization theory in practice are discussed in this work. The problem of plasma current and shape stabilization system synthesis in tokamak ITER is considered as an application of discussed ideas.

PACS numbers: 11.25.Hf, 123.1K

1. The Problem of Plasma Current and Shape Controller Synthesis

Currently, investigations in the field of nuclear fusion and construction of tokamaks draw considerable interest. There are three problems that can be regarded as the base problems of control system in many tokamaks. The first one is the problem of programmed control design. The second is the problem of vertical displacement stabilization that arises for most of the models of tokamaks. The last is the problem of plasma current and shape stabilization, consisting of providing given requirements and constraints produced for dynamical processes, particularly, for changes of some values, characterizing plasma shape. To set the requirements for stabilization processes dynamics some dynamical test mode is usually considered that is defined by the system motion under the influence of disturbances of the type "l_i, β-drops". Such disturbances are caused by the intermittent changes of plasma density and regarded to be the worst case for plasma current and shape stabilization system. Taking into account the disturbances of "l_i, β-drops" type for adjustment of stabilization system, we can get sufficient assurance of suitable dynamics quality for more propitious external disturbances. But the optimal stabilizing controller synthesis with direct use of information about the above mentioned disturbances is rather difficult. Applying standard algorithms for control design is not reasonable in this case, and therefore some adaptation of standard algorithms and their application techniques specifically for plasma control become the topical problem. Such adaptation, for instance, should be carried out for plasma current and shape stabilization system design in test mode by solving H_2- and H_∞-optimization problems. Some

aspects of application of standard methods for solving H_2- and H_∞-optimization problems in designing plasma current and shape stabilization system are discussed in this work.

2. Regularization of Computing Methods for H_2 and H_∞-Optimization

Implementation of H_2- and H_∞-optimization methods in practice is often embarrassed by different peculiarities of tasks arising in various applications. Particularly, the optimization problems appearing in applications can be singular. It means that the considered mathematical models of plants do not satisfy some conditions of the H_2 and H_∞ problem statement. Such conditions can be determined as regularity conditions. Using standard mathematical instruments, including widely used package MATLAB, is essentially complicated for singular optimization problems. It leads to necessity of regularization methods development in H_2 and H_∞-optimization problems in order to satisfy all given regularity conditions. The linear mathematical models of plasma dynamics in ITER for current and shape stabilization system design in test mode do not satisfy all regularity conditions. Therefore, the regularization should be performed in order to carry out H_2- and H_∞-optimization for control design.

Let us formulate H_2- and H_∞-optimization problems and the above mentioned regularity conditions.

Consider state-space control system models of the standard form

$$\begin{aligned} \dot{\mathbf{x}} &= \mathbf{A}\mathbf{x} + \mathbf{B}\mathbf{u} + \mathbf{G}\mathbf{d}, \\ \mathbf{e} &= \mathbf{L}\mathbf{x} + \mathbf{M}\mathbf{u}, \\ \mathbf{y} &= \mathbf{C}\mathbf{x} + \mathbf{D}\mathbf{u} + \mathbf{F}\mathbf{d}, \end{aligned} \tag{1}$$

where $\mathbf{x} \in \mathbf{E}^n$—vector of states, $\mathbf{u} \in \mathbf{E}^m$—vector of controls, $\mathbf{d} \in \mathbf{E}^{m_d}$—vector of external disturbances, $\mathbf{e} \in \mathbf{E}^p$—vector of regulated variables, $\mathbf{y} \in \mathbf{E}^k$—vector of measurements, matrices $\mathbf{A}$, $\mathbf{B}$, $\mathbf{G}$, $\mathbf{L}$, $\mathbf{M}$, $\mathbf{C}$, $\mathbf{D}$ and $\mathbf{F}$ have constant components.

Another representation of such models is given in frequency area by

$$\begin{pmatrix} \mathbf{e} \\ \mathbf{y} \end{pmatrix} = \mathbf{T}(s) \begin{pmatrix} \mathbf{d} \\ \mathbf{u} \end{pmatrix}, \tag{2}$$

where the transfer matrix is $\mathbf{T}(s) = \begin{pmatrix} \mathbf{L} \\ \mathbf{C} \end{pmatrix} (\mathbf{E}s - \mathbf{A})^{-1} \begin{pmatrix} \mathbf{G} & \mathbf{B} \end{pmatrix} + \begin{pmatrix} 0 & \mathbf{M} \\ \mathbf{F} & \mathbf{D} \end{pmatrix}$

Considering the plant model Eq. (2) together with the mathematical model of controller

$$\mathbf{u} = \mathbf{W}(s)\mathbf{y}, \tag{3}$$

we get a closed-loop system

$$\mathbf{e} = \mathbf{H}(s,\mathbf{W})\mathbf{d}, \tag{4}$$

where $\mathbf{H}(s, \mathbf{W})$ is a transfer matrix from $\mathbf{d}$ to $\mathbf{e}$. This matrix depends on the choice of controller transfer matrix $\mathbf{W}(s)$.

To characterize the optimization process quality let us consider the following functional criterion

$$I = I(\mathbf{W}) = \|\mathbf{H}(\mathrm{s},\mathbf{W})\|, \tag{5}$$

on the set Ω of transfer functions $\mathbf{W}(s)$ with fractional-rational components. A characteristic polynomial for each matrix $\mathbf{W} \in \Omega$ of the closed-loop system Eq. (4) is Hurwitz. Assume that for all matrices $\mathbf{H}(s)$ it follows that the expression $\mathrm{tr}\left[\mathbf{H}^{\mathrm{T}}(-s)\mathbf{H}(s)\right]$ is strictly proper. Hence, the norms H_2 and H_∞ can be used.[1] The optimization problem is formulated in the following way

$$I = I(\mathbf{W}) = \|\mathbf{H}(\mathrm{s},\mathbf{W})\| \to \inf_{\mathbf{W}\in\Omega}, \tag{6}$$

for the mentioned norms on Hardy spaces.

As mentioned above, some regularity conditions must hold for existence of optimization problem Eq. (6) solutions on H_2 and H_∞. Such conditions are given, for example, in Ref. 1:

(i) Pair $(\mathbf{A}, \mathbf{B})$ is stabilizable, and pair $(\mathbf{A}, \mathbf{C})$ is detectable.

(ii) Matrices $\mathbf{M}$ and $\mathbf{F}^{\mathrm{T}}$ have full column rank. It means that the dimension of vector of regulated variables is not less than the dimension of vector of controls, the dimension of vector of disturbances is not less than the dimension of vector of measurements, and columns of these matrices are linearly independent.

(iii) Matrices $\begin{pmatrix} j\omega\mathbf{E} - \mathbf{A} & \mathbf{B} \\ \mathbf{L} & \mathbf{M} \end{pmatrix}$ and $\begin{pmatrix} j\omega\mathbf{E} - \mathbf{A} & \mathbf{G} \\ \mathbf{C} & \mathbf{F} \end{pmatrix}^{\mathrm{T}}$ have full column rank for all $\omega \in [0, \infty)$.

There are widely known results[1] that allow to find solutions of H_2- and H_∞-optimization problems in the case the regularity conditions are met.

If regularity conditions do not hold, we can use the regularization approach, consisting of transformation of the nominal plants by means of introducing some additives. This procedure must lead to the keeping of regularity conditions. Modified in such a way, mathematical models of the plants can be considered as the base models for applying the well-known algorithms of searching solutions in H_2- and H_∞-optimization problems. These additives should be included in the nominal plant to fulfill regularity conditions, but not to deform the nominal plant and its dynamics.

Let us consider this situation, when $m_d < k$, in other words the dimension of the vector of disturbances is less than the dimension of the vector of measurements. This partially breaks regularity conditions. Hence, H_2- and H_∞-optimization problems are singular in this case and the nominal plant Eq. (1) should be modified by introducing of some small regularization additives.

The additives can be formed based on the vector of fictitious disturbances $\mathbf{d}_1(t)$ with dimension $m_1 = \dim \mathbf{d}_1 = k - m_d$ and included in the nominal linear model Eq. (1)

$$\begin{aligned} \dot{\mathbf{x}} &= \mathbf{A}\mathbf{x} + \mathbf{B}\mathbf{u} + \mathbf{G}\mathbf{d} + \gamma \mathbf{G}_d \mathbf{d}_1, \\ \mathbf{e} &= \mathbf{L}\mathbf{x} + \mathbf{M}\mathbf{u}, \\ \mathbf{y} &= \mathbf{C}\mathbf{x} + \mathbf{D}\mathbf{u} + \mathbf{F}\mathbf{d} + \gamma \mathbf{F}_d \mathbf{d}_1, \end{aligned} \tag{7}$$

here $\gamma \in E^1$—small real parameter, matrices $\mathbf{G}_d$ and $\mathbf{F}_d$ are auxiliary.

Theorem 2.1. *If the matrix* $\mathbf{F}$ *has* m_d *linearly independent rows, then the constant matrix* $\mathbf{F}_d$ *exists such that the regularity conditions in H-optimization problems are satisfied for all* $\gamma \neq 0$.

Proof. For a new vector of disturbances $\mathbf{d}_n = \left(\mathbf{d}\ \mathbf{d}_1\right)^{\mathrm{T}} \in E^k$ the model Eq. (7) is represented by

$$\begin{aligned} \dot{\mathbf{x}} &= \mathbf{A}\mathbf{x} + \mathbf{B}\mathbf{u} + \mathbf{G}_n(\gamma)\mathbf{d}_n, \\ \mathbf{e} &= \mathbf{L}\mathbf{x} + \mathbf{M}\mathbf{u}, \\ \mathbf{y} &= \mathbf{C}\mathbf{x} + \mathbf{D}\mathbf{u} + \mathbf{F}_n(\gamma)\mathbf{d}_n, \end{aligned} \tag{8}$$

where $\mathbf{G}_n(\gamma) = \left(\mathbf{G}\ \gamma\mathbf{G}_d\right)$, $\mathbf{F}_n(\gamma) = \left(\mathbf{F}\ \gamma\mathbf{F}_d\right)$. According to regularity conditions, the matrix $\mathbf{F}_n(\gamma)$ of dimension $k \times k$ must be nonsingular. Splitting into blocks of matrices $\mathbf{F}$ and $\mathbf{F}_d$ gives

$$\mathbf{F}_n(\gamma) = \left(\mathbf{F}\ \gamma\mathbf{F}_d\right) = \begin{pmatrix} \mathbf{F}_1\ \gamma\mathbf{F}_{d1} \\ \mathbf{F}_2\ \gamma\mathbf{F}_{d2} \end{pmatrix},$$

where matrix $\mathbf{F}_1$ has dimensions $m_d \times m_d$, $\mathbf{F}_2$ has dimensions $(k - m_d) \times m_d$, $\mathbf{F}_{d1}$ has dimensions $m_d \times (k - m_d)$ and $\mathbf{F}_{d2}$ has dimensions $(k - m_d) \times (k - m_d)$.

Assume now that the condition of the theorem holds, and let the first m_d rows of the matrix $\mathbf{F}_2$ be linearly independent. Then the quadratic matrix $\mathbf{F}_{21}$ is nonsingular. Using a well-known formula for the determinant of block matrix gives

$$\det \mathbf{F}_n(\gamma) = \det \begin{pmatrix} \mathbf{F}_1\ \gamma\mathbf{F}_{d1} \\ \mathbf{F}_2\ \gamma\mathbf{F}_{d2} \end{pmatrix} = \det \mathbf{F}_1 \cdot \det\left(\gamma\mathbf{F}_{d2} - \mathbf{F}_2\mathbf{F}_1^{-1}\gamma\mathbf{F}_{d1}\right).$$

Since $\det \mathbf{F}_1 \neq 0$, the condition of nonsingularity takes the form $\det\left(\gamma\mathbf{F}_{d2} - \mathbf{F}_2\mathbf{F}_1^{-1}\gamma\mathbf{F}_{d1}\right) \neq 0$ for each $\gamma \neq 0$, if it is assumed that $\mathbf{F}_{d1} = 0$, $\mathbf{F}_{d2} = \mathbf{E}_{k-m_d}$(unitary matrix). So, the matrix in the formulation of the theorem takes the form $\mathbf{F}_d = \begin{pmatrix} \mathbf{0}_{m_d \times (k-m_d)} \\ \mathbf{E}_{k-m_d} \end{pmatrix}$, and regularity conditions for such matrix $\mathbf{F}_d$ in system Eq. (8) are fulfilled for each $\gamma \neq 0$. □

Thus, one can form the model Eq. (8), and for each $\gamma \neq 0$ compute controller of the form Eq. (4) for the modified model Eq. (8), providing minimum of one of two norms $\|H_2\|$ and $\|H_\infty\|$ and then solve H_2- or H_∞-optimization problem for

the plant Eq. (8). However, the designed controllers should be used to stabilize the nominal plant Eq. (1) for which the value of the functional $I(\mathbf{W}) = \|\mathbf{H}_n(\mathrm{s},\mathbf{W})\|$, where $\mathbf{H}_n$ is transfer matrix from $\mathbf{d}_n$ to $\mathbf{e}$ of the closed-loop system Eq. (8), Eq. (3), is the function of parameter γ: $I^* = I^*(\gamma) = I(\mathbf{W}) = \|\mathbf{H}_n(\mathrm{s},\mathbf{W})\|$. The smaller the value of $|\gamma|$ is the more precisely the obtained result corresponds to the initial problem.

3. Regularization of the Algorithms for Plasma Current and Shape Controller Synthesis

The common regularization approach considered above can be applied for plasma current and shape stabilization system design in tokamak ITER-FEAT.

The controlled plant for the problem of current and shape controller synthesis in ITER tokamak is described by the LTI model

$$\begin{aligned} \dot{\mathbf{x}} &= \mathbf{A}\mathbf{x} + \mathbf{B}\mathbf{u} + \mathbf{G}\mathbf{d}, \\ \mathbf{e} &= \mathbf{L}\mathbf{x}, \\ \mathbf{y} &= \mathbf{C}\mathbf{x}, \end{aligned} \tag{9}$$

where $\mathbf{x} \in \mathbf{E}^n$ is a state vector, $\mathbf{u} \in \mathbf{E}^m$ is a control vector, $\mathbf{d} \in \mathbf{E}^{m_d}$ is a vector of disturbances, $\mathbf{e} \in \mathbf{E}^p$ is a vector of regulated variables, $\mathbf{y} \in \mathbf{E}^k$ is a vector of measurements, matrices $\mathbf{A}$, $\mathbf{B}$, $\mathbf{G}$, $\mathbf{L}$ and $\mathbf{C}$ have constant components, $n = 11$, $m = 11$, $m_d = 2$, $p = 11$ and $k = 18$. Vector of regulated variables includes the functions $g_j(t)$, $j = \overline{1,6}$, the gaps (the checked clearances). Vector of controls consists of functions $u_i(t)$, $i = \overline{1,11}$, the voltages.

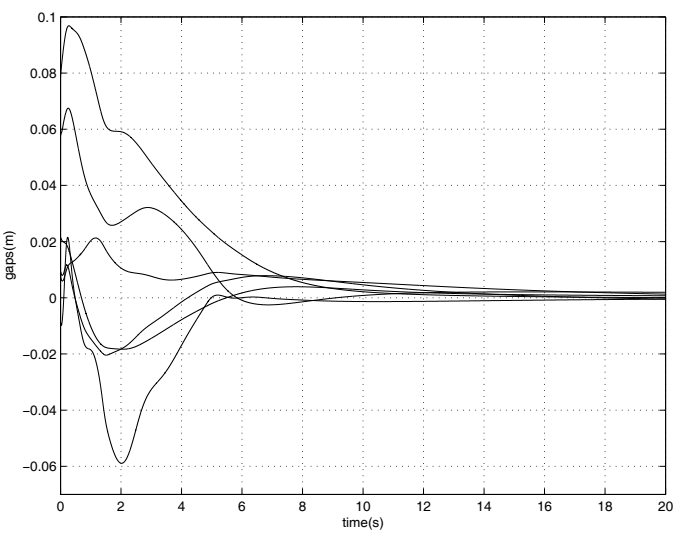

Fig. 1. Regulated variables $g_j(t)$, $j = \overline{1,6}$, corresponding to H_2- optimal controller, designed for modified plant Eq. (10).

It should be noted that the plant Eq. (9) is a reduced model with 79 removed states.[2]

To set the requirements for the dynamics of stabilization processes, let us consider dynamical test mode, defined by the motion of the full system (not reduced), closed with controller of type Eq. (3) under the influence of the "l_i, β-drops" distur-

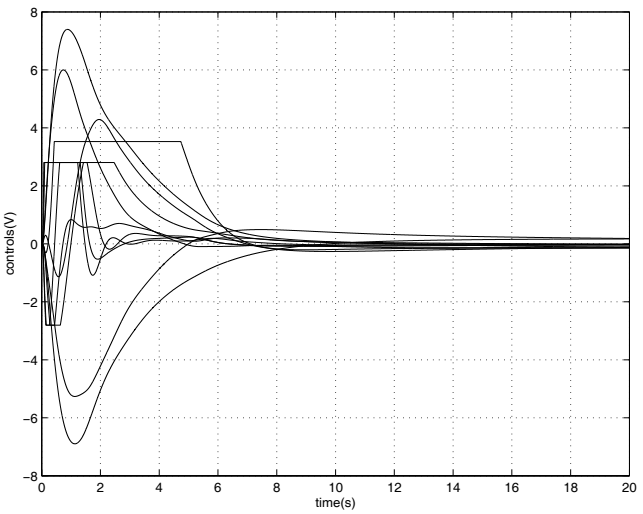

Fig. 2. Control voltages $u_i(t)$, $i = \overline{1,11}$, corresponding to H_2- optimal controller, designed for modified plant Eq. (10).

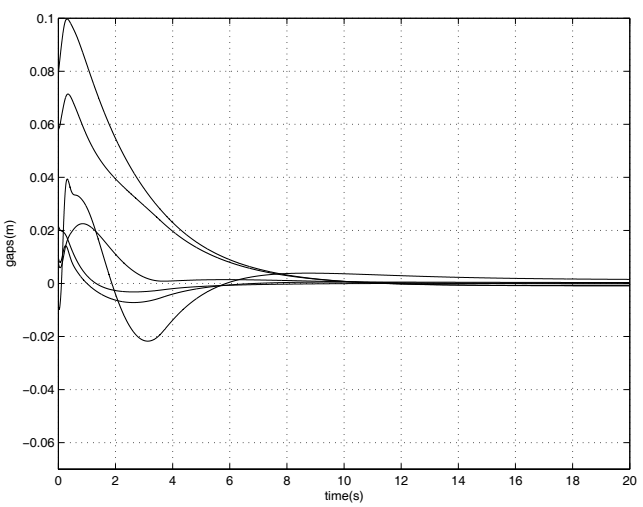

Fig. 3. Regulated variables $g_j(t)$, $j = \overline{1,6}$, corresponding to test controller.

bances. Simulation of dynamical processes for the closed-loop system is performed under constraints of saturation type for the components of control vector $\mathbf{u}$. All figures in the paper show simulated processes under these conditions.

Now the problem of plasma current and shape stabilization system synthesis can be formulated as follows: based on the reduced model Eq. (9), design the control law of the form Eq. (3) such that the characteristic polynomial of the closed-loop system is Hurwitz, and the following constraints are satisfied for simulated processes:

(i) for settling time

$$J_1(\mathbf{W}) = T_p(\mathbf{W}) = \inf\{t_m : \|\mathbf{e}(t, \mathbf{W})\| \in M(0, \Delta), \forall t \geq t_m\} < T_{p0},$$

where $\Delta = 0.05\,\|\mathbf{e}(0)\|$, $M(0, \Delta)$ is the neighborhood of zero of radius Δ, $T_{p0} = 1.0$ sec;

(ii) for overshoots

$$J_{2j}(\mathbf{W}) = P_{pj}(\mathbf{W}) = \max_{t \in [0, T_p]} \left| \frac{e_j(t, \mathbf{W}) - e_j(0)}{e_j(0)} \right| < P_{p0}, \quad j = \overline{1, 6},$$

where P_{p0} is a fixed number;

(iii) for oscillation

$$J_{3j}(\mathbf{W}) = K_{pj}(\mathbf{W}) = K[e_j(t, \mathbf{W})] < K_{p0}, \quad j = \overline{1, 6},$$

where $K[e_j(t, \mathbf{W})]$ is a fixed real number of roots of nonlinear equation $e_j(t, \mathbf{W}) = 0$ on the segment $t \in [0, T_p]$, $K_{p0} = 3$.

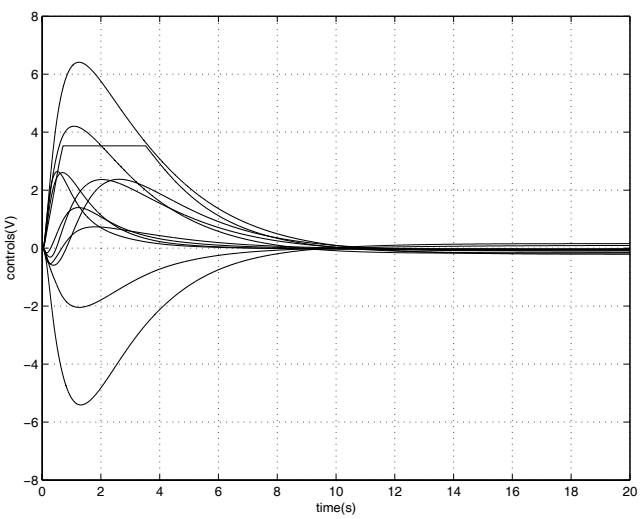

Fig. 4. Control voltages $u_i(t)$, $i = \overline{1, 11}$, corresponding to test controller.

We consider the indicated values of J_1, J_{2j} and J_{3j} for processes $g_j(t)$, $j = \overline{1,6}$ in the closed-loop system, as the values defining the quality of stabilization process.

One of the possible techniques for such plasma current and shape controller design is to modify the nominal plant Eq. (9) by entering some additives as it was described earlier, and to find the H_2- or H_∞-optimal control for the modified plant. For the design problem under consideration we should also enter the matrix $\mathbf{M}$ in Eqs. (9). In addition, we can include explicitly the new vector of disturbances in model (9) instead of the nominal vector $\mathbf{d}$, then we have $\mathbf{d}_n = \mathbf{d}_1$. Specifying the structure of matrices $\mathbf{G}_d$, $\mathbf{F}_d$ and $\mathbf{M}$ and putting their elements together in a vector of variable parameters $\gamma^* \in \mathbf{E}^\beta$, we get that the value of the functional $I(\mathbf{W}) = \|\mathbf{H}_n(\mathrm{s},\mathbf{W})\|$ depends on the vector γ^*: $I^* = I^*(\gamma^*) = I(\mathbf{W}) = \|\mathbf{H}_n(\mathrm{s},\mathbf{W})\|$. Here $\mathbf{H}_n$ is a transfer matrix from $\mathbf{d}_n$ to $\mathbf{e}$ of the closed-loop system Eq. (8), Eq. (3). In this case continuous transformation in the vector of variable parameters results in the continuous change of the value of function $I^* = I^*(\gamma^*)$. Hence, for each vector of variable parameters we obtain the solution of H_2- or H_∞-optimization problem. Transformation must be carried out in such a way that the smaller value of $\|\gamma^*\|$ corresponds to the smaller value of I^*. Minimizing the function of vector γ, we can choose any suboptimal solution of the optimization problem, if that solution satisfies the introduced constraints for simulated processes and controls. Thus, all additives in Eq. (9) modifying nominal plant can be chosen to provide the desirable closed-loop system performance.

One of such choices gives the following system

$$\begin{aligned}
&\dot{\mathbf{x}} = \mathbf{A}\mathbf{x} + \left(\left(\mathbf{B}\mathbf{S}_{\varphi_1}\ \mathbf{0}_{11\times 18}\right)\mathbf{B}\right)\begin{pmatrix}\mathbf{d}_n\\ \mathbf{u}\end{pmatrix},\\
&\begin{pmatrix}\mathbf{e}_n\\ \mathbf{y}\end{pmatrix} = \begin{pmatrix}\begin{pmatrix}\mathbf{R}_1\\ \mathbf{0}_{11\times 11}\end{pmatrix}\\ \mathbf{C}\end{pmatrix}\mathbf{x} + \begin{pmatrix}\mathbf{0}_{22\times 29} & \begin{pmatrix}\mathbf{0}_{11\times 11}\\ \mathbf{Q}_1\end{pmatrix}\\ \left(\mathbf{0}_{18\times 11}\ \mathbf{S}_{\psi_1}\right)\mathbf{0}_{18\times 11}\end{pmatrix}\begin{pmatrix}\mathbf{d}_n\\ \mathbf{u}\end{pmatrix},
\end{aligned} \tag{10}$$

here $\mathbf{x} \in \mathbf{E}^{11}$—state vector, $\mathbf{u} \in \mathbf{E}^{11}$—vector of controls, $\mathbf{d} \in \mathbf{E}^{29}$—vector of new disturbances, $\mathbf{e} \in \mathbf{E}^{22}$—vector of new regulated variables, $\mathbf{y} \in \mathbf{E}^{18}$—vector of measurements. $\mathbf{R}_1$ is a fixed positive definite matrix, $\mathbf{Q}_1$, $\mathbf{S}_{\varphi_1}$, $\mathbf{S}_{\psi_1}$ are fixed positive definite diagonal matrices, $\mathbf{R}_1 = \mathbf{M}$. Note that in the modified model Eq. (10) vector $\mathbf{d}_n$ is used instead of $\mathbf{d}$ and this vector is completely new, i.e. the direct information about the exogenous entries is not used in the modified model.

Solving the H_2-optimization problem for plant Eq. (10), we get the controller of type Eq. (3), and Fig. 1 and Fig. 2 show gaps $g_j(t)$, $j = \overline{1,6}$ and control voltages $u_i(t)$, $i = \overline{1,11}$, correspondingly. Solving the H_∞-optimization problem gives extremely close results. Following the above mentioned requirements for J_1, J_{2j}, J_{3j}, $j = \overline{1,6}$ one can conclude that the closed-loop dynamics is close to acceptable. For comparison, gaps $g_j(t)$, $j = \overline{1,6}$ and control voltages $u_i(t)$, $i = \overline{1,11}$, corresponding to the alternative test control law,[3] are shown in Fig. 3 and Fig. 4.

This test control law does not show significantly better performance compared to the controller found as a solution of the H_2-optimization problem for the modified

plant (10). The test law was formed by another technique and can be considered good for satisfying the requirements for dynamical processes.

4. Conclusion

The lack of information about the exogenous disturbances in applications usually complicates the production of optimal control design. Therefore, the adaptation of standard methods is necessary, specifically for the considered problems. Thus, the approach of adaptation of standard methods for solving H_2- and H_∞-optimization problems considered in this article is efficient and can be used, in particular, to design plasma current and shape stabilization system.

References

1. J. Doyle, B. Francis, A. Tannenbaum. *Feedback control theory* (Macmillan Publ. Co., New York, 1992.).
2. Gribov Y., Albanese R., Ambrosino G., Ariola M., Bulmer R., Cavinato M., Coccorese E., Fujieda H., Kavin A. et.al., ITER-FEAT scenarios and plasma position/shape control, in *Proc. 18th IAEA Fusion Energy Conference*, (Sorrento, Italy, 2000), ITERP/02.
3. E. I. Veremey, N. A. Zhabko. Analysis of Complementary Filters Influence on the Dynamics of the Plasma Stabilization System in Tokamak ITER-FEAT. *Control Applications of Optimization. Prroc. of the Ninth International Workshop: Beam Dynamics and Optimization* (Russia,SPb,2002). p. 361–366.

International Journal of Modern Physics A
Vol. 24, No. 5 (2009) 1057–1067

World Scientific
www.worldscientific.com

EFFECTS OF THE WIGGLER ON THE HEFEI LIGHT SOURCE STORAGE RING

HE ZHANG* and MARTIN BERZ†

Department of Physics and Astronomy, Michigan State University, East Lansing, MI, 48824, USA
**zhanghe@msu.edu*
†berz@msu.edu

The Hefei light source (HLS) is a second generation synchrotron radiation light source, in which a superconducting wiggler is installed and operating. The effects of the wiggler on the beam dynamics on the HLS storage ring are studied, in order to make sure the wiggler can operate properly when the ring is working in the high brilliance mode. We generate a model of the magnetic field in the midplane of the wiggler. The 3D magnetic field model is also builded up by COSY infinity 9.0. Both the linear and nonlinear effects of the wiggler are discussed. The vertical tune is changed from 2.535 to 2.567 and the vertical beta function is heavily distorted, while a symplectic tracking study shows the dynamic aperture is only slightly affected by the wiggler. And the wiggler should be able to run on the high brilliance mode after the linear effects get compensated.

Keywords: Wiggler; nonlinear effects; differential algebra.

1. Introduction

The Hefei light source (HLS) is a second generation dedicated VUV radiation light source. It is composed of a 200 MeV linac and an 800 MeV storage ring. The storage ring consists of four triple bend achromat (TBA) cells and four 3 m long straight sections. The characteristic wavelength of the bending radiation is 2.4 nm. In order to meet the requirement of the hard X-ray synchrotron radiation users, a superconducting wiggler was installed on the storage ring. The characteristic wavelength of the wiggler radiation is 0.485 nm, and its usable wavelength is extended to 0.097 nm, which lies in the hard X-ray range.[1]

HLS runs in general purpose light source (GPLS) operation mode now. The emittance in this mode is 133 nm · rad. A high brilliance light source (HBLS) operation mode was proposed, in which the emittance was reduced to 27 nm · rad. The tunes of HBLS are (5.2073, 2.5351). The β functions and dispersion function of HBLS are shown in Fig. 1. In the following, we are going to discuss the effects of the wiggler when the storage ring runs in HBLS mode.

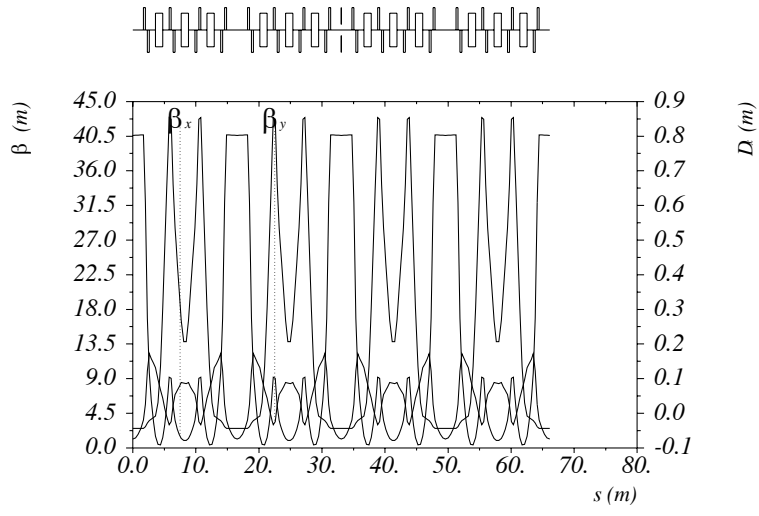

Fig. 1. The β functions and the dispersion function of HLS storage ring in HBLS mode.

2. Magnetic Field Model of the Wiggler

The wiggler that is installed in the HLS storage ring has single period composed of three poles, and the peak magnetic field strength of the central pole and the poles in either side is 6 T and 4.3 T respectively. The magnetic field of the wiggler is shown in Fig. 2, but we do not have the explicit data of the curve. Because of the lack of the wiggler field data, only the linear effects of it were studied by the hard edge model.[1,2] In the following we will build up an analytic magnetic field model similar enough to the real wiggler field, by which we can study both the linear effects and the nonlinear effects. And if our model wiggler can work on the HBLS mode, we can reasonably assume the real wiggler can also work in that mode.

A model of the wiggler's magnetic field can be generated by COSY Infinity 9.0.[3,4] Considering the motion of the electrons in the wiggler, we can reasonably assume the traces of the electrons are close to the axis of the wiggler, so that the electrons can not see the drop of the fringe field in x direction when the wiggler has enough width. Then the midplane field can be described by the following formulas.[3] The periodic field can be described as

$$B_m(x,z) = B_0 \cos\left(\frac{2\pi}{\lambda}\cdot z + k\cdot z^2\right), \tag{1}$$

in which λ is the wavelength of the wiggler, and the item $k\cdot z^2$ is used when the wiggler has a changing wavelength respect to z. The formula for the left fringe field is

$$B_l = K_l \cdot B_m(x,z), \tag{2}$$

$$\text{with } K_l = \frac{1}{1+\exp(a_0 + a_1(-z+z_l)/d + \cdots + a_9((-z+z_l)/d)^9)}. \tag{3}$$

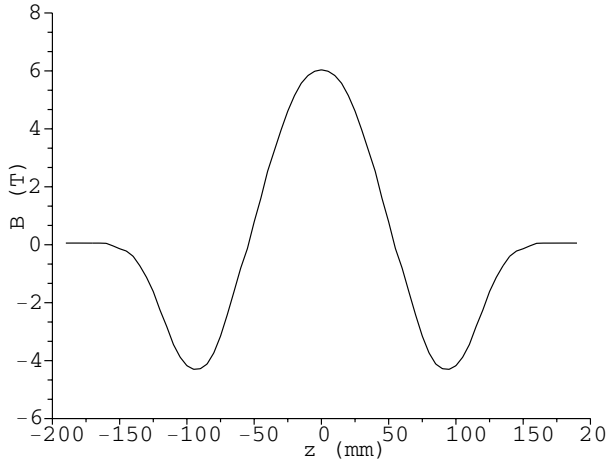

Fig. 2. The midplane magnetic fields of the wiggler.

When z goes to $-\infty$, $B_l(x,z)$ goes to 0, while when z goes to $+\infty$, $B_l(x,z)$ goes to $B_m(x,z)$. So we can get a good model of the fringe field by carefully customizing the coefficients $a_0, a_1, \ldots, a_9$, and d. In a similar way, the right fringe field can be described as

$$B_r = K_r \cdot B_m(x,z), \tag{4}$$

$$\text{with } K_r = \frac{1}{1+\exp(a_0 + a_1(z-z_r)/d + \cdots + a_9((z-z_r)/d)^9)}. \tag{5}$$

So that the whole magnetic field of wiggler can be described as

$$B = K_l \cdot B_m(x,z) \cdot K_r. \tag{6}$$

In our case, we choose $\lambda = 210$ mm, $k = 0$, $B_0 = 6.08$ T, $d = 40$ mm, $l = z_r - z_l = 252$ mm, $a_0 = 0.478959$, $a_1 = 1.911289$, $a_2, a_3, \ldots, a_{10} = 0$. The magnetic field of the model wiggler is shown in Fig. 3, comparing with the magnetic field of the real wiggler. We can see that we have arrived at a good model of the wiggler's magnetic field.

The 3D magnetic field can be generated in the following way.[5] Maxwell's equations of the magnetic field are

$$\overrightarrow{\nabla} \cdot \overrightarrow{D} = \rho, \overrightarrow{\nabla} \times \overrightarrow{E} = -\frac{\partial \overrightarrow{B}}{\partial t}. \tag{7}$$

If we only consider the field without time dependence in the region where there are no sources of the field, Maxwell's equations can be simplified as

$$\overrightarrow{\nabla} \cdot \overrightarrow{D} = 0, \overrightarrow{\nabla} \times \overrightarrow{E} = \overrightarrow{0}. \tag{8}$$

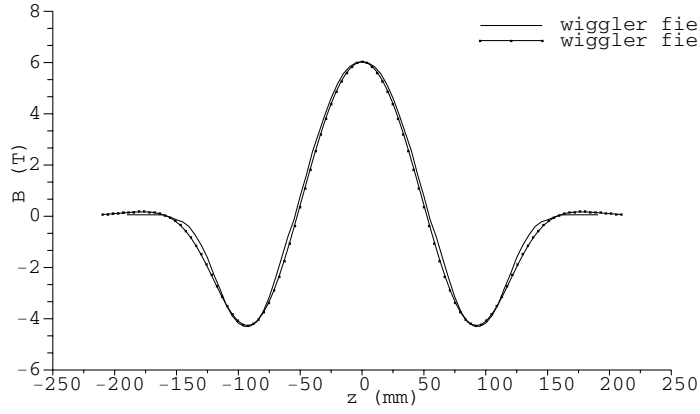

Fig. 3. The midplane magnetic field model of the wiggler.

In this case, $\overrightarrow{B}$ has a scalar potential V, which satisfies the Laplace equation

$$\triangle V = \frac{\partial^2 V}{\partial x^2} + \frac{\partial^2 V}{\partial y^2} + \frac{\partial^2 V}{\partial z^2} = 0, \tag{9}$$

and $\overrightarrow{B} = -\overrightarrow{\nabla} V$. The Eq. (9) can be rewritten in the fixed-point form as

$$V = O(V) = V|_{y=0} + \int_y \left\{ \frac{\partial}{\partial y} V|_{y=0} - \int_y \left(\frac{\partial}{\partial x} \left(\frac{\partial V}{\partial x} \right) + \frac{\partial}{\partial z} \left(\frac{\partial V}{\partial z} \right) \right) \right\} \tag{10}$$

The operator $O(V)$ on ${}_nD_3$ is contracting. And in the differential algebra (DA) picture, Eq. (10) can be easily solved to order n by iteratively applying the operator $O(V)$ on V for at most $n+1$ times, assuming V and $\partial V/\partial y$ are given in the $y = 0$ plane.

In the case of the wiggler, $\partial V/\partial y$ in the $y = 0$ plane is known as the midplane field. As the Eq. (6) shows, the midplane field does not explicitly depend on y, so the potential V in the $y = 0$ plane is simply $y \cdot \partial V/\partial y$. Solving the Eq. (10), we get the potential V, then the field at any point is just the gradient of the potential at the point. COSY Infinity 9.0 can calculate the field of the wiggler automatically.

3. Beam Dynamics Study by COSY Infinity 9.0

The tracking study of the beam dynamic effects of the wiggler was done by the COSY Infinity 9.0 beam physics package, which is based on DA arithmetic. After a storage ring was defined by the user, COSY can calculate the map of each element to arbitrary order, compose all the maps into a one-turn map of the storage ring, find the generating function of the one-turn map, then do the symplectic tracking by various methods.[3,5]

When the field of an element, such as a dipole, a quadruple, or a wiggler etc, is known, it is easy to write the dynamic equations of the electron motion as a group of ODE in the following form,

$$\dot{\vec{z}} = \vec{f}(\vec{z}, t), \tag{11}$$

where $\vec{z}$ is usually a 4D or 6D vector of positions and momenta. COSY has two methods to generate the map to arbitrary order from an given ODE.[5] One method is based on the antiderivation operator. Eq. (11) can be rewritten as

$$\vec{z} = O(\vec{z}) = \vec{z}_i + \int_{t_i}^{t} \vec{f}(\vec{z}, t')dt'. \tag{12}$$

The operator $O(\vec{z})$ on ${}_nD_v$ is contracting, and now we have a fixed-point problem again, which can be easily solved to the order n in the DA picture by iteratively acting the operator $O(\vec{z})$ at most $n+1$ times as we mentioned before. The integral in Eq. (12) can be done by the antiderivation operator in the DA picture. The other method is based on the derivation operator. For a given function $g(\vec{z}, t)$ in phase space, we have

$$\frac{d}{dt}g(\vec{z}, t) = \vec{f} \cdot \vec{\nabla} g + \frac{\partial}{\partial t} g = L_{\vec{f}} g, \tag{13}$$

where $L_{\vec{f}}$ is called Lie derivation operator, and $\dot{\vec{z}} = \vec{f}$ is the ODE we want to solve. The Taylor expansion of the solution of the ODE is

$$\vec{z}_f = \sum_{i=0}^{\infty} \frac{t^i \cdot L_{\vec{f}}^i}{i!} \cdot \vec{I}, \tag{14}$$

where $\vec{I}$ is the identity function. When g and $\vec{f}$ are not explicitly time dependant, the partial derivative respect to t in $L_{\vec{f}}$ disappear. If $\vec{f}(\vec{0}) = \vec{0}$, and letting g be a component of $\vec{z}$, we obtain the map

$$\vec{z}_0 = \vec{z}_i, \quad \vec{z}_j = \frac{t \cdot (\vec{f} \cdot \vec{\nabla})}{i} \cdot \vec{z}_{j-1}, \quad \vec{z}_f = \sum_{j=0}^{\infty} z_j. \tag{15}$$

As to the elements like dipoles, quadrupoles and etc, whose fields do not depend on the time variable, the derivation method works well. While the map of the elements like wigglers and undulators, whose fields change with the time variable, should be calculated by the antiderivation method.

The map of an element or a whole ring generated by COSY is described by an n-th order DA polynomial, so it is not symplectic because of the truncation. Symplectic Tracking is achieved in COSY by using the generating function, which can be easily calculated from a given map by DA method.[5] COSY provides the four basic types of generating functions[6] and the extended Poincare (EXPO) generating function, which in general gives optimal results in the weakly nonlinear case.[7,8] In the following, we will take the second kind of generating function as an example to

show how COSY works on this. Assume an origin preserving map M, we can write it as $M = (M_1, M_2)$, where M_1 is the position part, and M_2 is the momentum part. In the same way, we can write the identity map $I = (I_1, I_2)$. Let

$$N_1 = (I_1, M_2), \tag{16}$$

then

$$(\vec{q}_i, \vec{p}_f) = N_1(\vec{q}_i, \vec{p}_i), \text{ and } (\vec{q}_i, \vec{p}_i) = N_1^{-1}(\vec{q}_i, \vec{p}_f). \tag{17}$$

Let

$$N_2 = (M_1, I_2), \tag{18}$$

then

$$(\vec{q}_f, \vec{p}_i) = N_2(\vec{q}_i, \vec{p}_i) = N_2 \circ N_1^{-1}(\vec{q}_i, \vec{p}_f) = G(\vec{q}_i, \vec{p}_f). \tag{19}$$

The second kind of generating function F_2 satisfies

$$(\vec{q}_f, \vec{p}_i) = (\vec{\nabla}_{\vec{p}_f} F_2, \vec{\nabla}_{\vec{q}_i} F_2). \tag{20}$$

Comparing Eq. (19) with Eq. (20), we can see that F_2 is just a potential for G, which can be obtained by integration along an arbitrary path. The symplectic tracking can be performed in the following way. Firstly $\vec{p}_f$ can be solved from $\vec{p}_i = G_2(\vec{q}_i, \vec{p}_f)$ by some numerical method such as Newton iteration, where G_2 is the momentum part of Eq. (20). Then $\vec{q}_f$ can be calculated directly from $\vec{q}_f = G_1(\vec{q}_i, \vec{p}_f)$, where G_1 is the position part of Eq. (20).

In the above calculation of the generating function, the inverse map of N_1 needs to be calculated. This is also a fixed-point problem in DA picture, which can be easily solved.[5] Assuming A is a origin preserving map, it can be write as $A = A_1 + A_2$, where A_1 is the linear part of A, and A_2 is the nonlinear part of A. Then

$$A \circ A^{-1} = (A_1 + A_2) \circ A^{-1} = I \tag{21}$$

$$A^{-1} = O(A^{-1}) = A_1^{-1} \circ (I - A_2 \circ A^{-1}). \tag{22}$$

The Eq. (22) now has the fixed-point form and A_1^{-1} can be easily calculated since the Jacobian of the linear map A_1 is just a square matrix.

4. Linear Effects of the Wiggler

With the above model of the wiggler's magnetic field, we can calculate both the linear and the nonlinear map of it by COSY Infinity 9.0. The linear map of the wiggler is found to be

$$M_x = \begin{pmatrix} 0.9997516 & 0.2532518 \\ 0 & 1.000248 \end{pmatrix}, \; M_y = \begin{pmatrix} 0.9409307 & 0.2462244 \\ -0.4852251 & 0.9358029 \end{pmatrix}. \tag{23}$$

Under the effects of the wiggler, the tunes change from (5.2073,2.5351) into (5.2072, 2.5674). The horizontal tune almost remains the same value, while the vertical tune increases a little bit. This result is reasonable because the horizontal map is very similar to a drift map, but the vertical map shows the focusing effect of the wiggler. The positions of the tunes and the 3rd, 4th, 5th, and 6th order resonance lines nearby are shown in Fig. 4. Fortunately one observes that the position change of the tunes does not cross any third order resonance lines, because the third order resonance is dangerous and the beam will get lost if the resonance is strong enough.

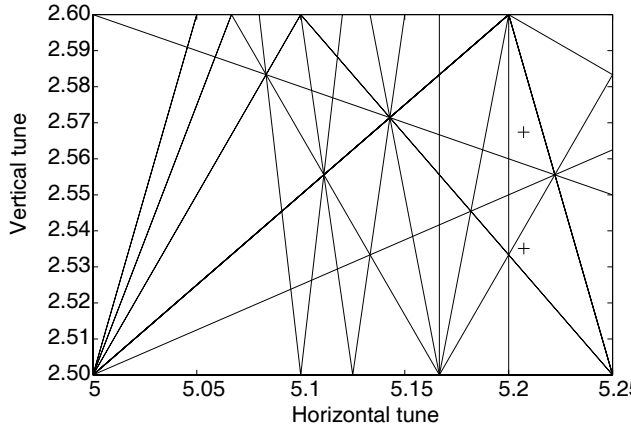

Fig. 4. The position change of the tunes and the 3rd, 4th, 5th, and 6th order resonance lines nearby.

The β functions with the wiggler are shown in Fig. 5. Comparing with Fig. 1, we can see the vertical β function is heavily disturbed, and the highest value increases from 11 m to 23 m. The changes of the vertical β functions are shown in Fig. 6. The increase of vertical β function will enlarge the close orbit distortion. It will also decrease the physical acceptance of the storage ring, and result in the decrease of the beam lifetime. So it is important to compensate the change of the β functions, and keep the tunes in a proper position at the same time. Generally it can be done by changing the strength of the quadrupoles in the storage ring, or adding extra quadrupoles on it.[1]

5. Effects of the Wiggler on Dynamic Apertures

To study the nonlinear effects of the wiggler, we concentrate on the change of the dynamic apertures with and without the wiggler. For each case, the one-turn map up to the 10th order was generated, and then the EXPO generating function was calculated from the map and was used for the symplectic tracking up to 5000 turns by COSY Infinity 9.0. The tunes were compensated back to the original values by

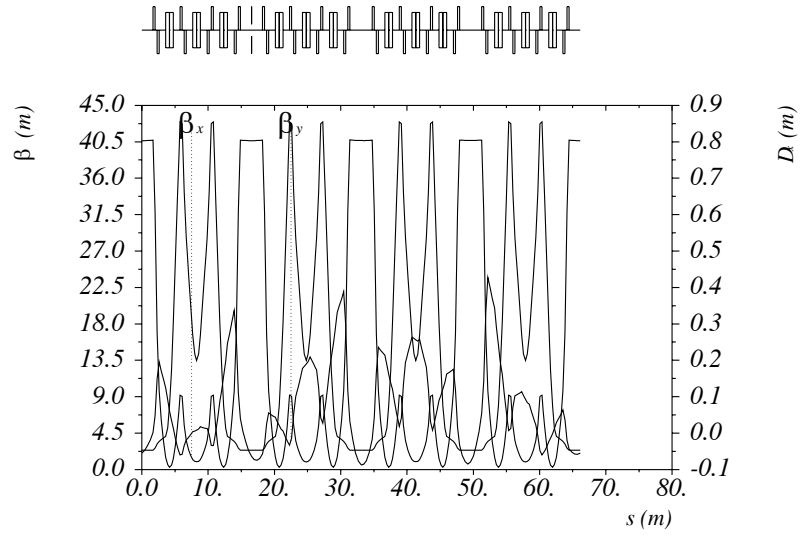

Fig. 5. The β functions and the dispersion function of HLS storage ring in HBLS mode with wiggler.

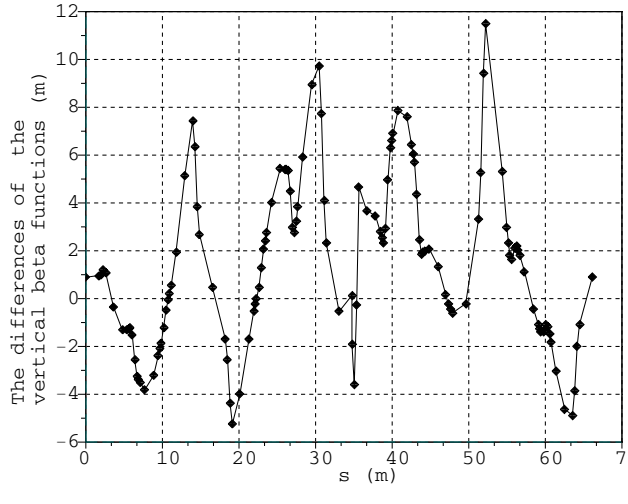

Fig. 6. The difference of the vertical β functions of HLS storage ring in HBLS mode with and without wiggler.

appropriately adjusting the strength of the quadrupoles before the tracking study in the case in which the wiggler is present, in order to avoid the change of the dynamic apertures due to the change of the global tunes. The tracking results of on-energy

particles in both x and y axis in bare lattice without the wiggler are shown in Fig. 7. The same tracking are made with the wiggler, and the results are shown in Fig. 8. In order to access the effects of the fringe field, we also trace the particles without the fringe field. In this case, the wiggler was treated as a periodic cosine magnetic field. The results are shown in Fig. 9. The traces in $x - a$ phase plane are almost the same. The dynamic aperture in horizontal direction is up to 26 mm.

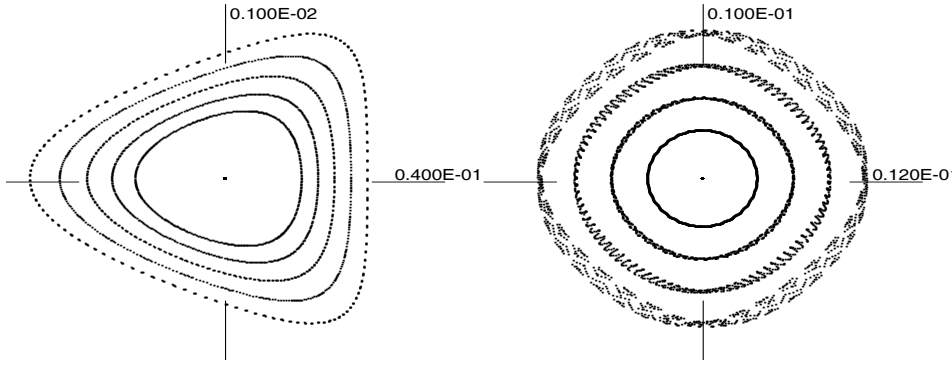

Fig. 7. Tracking pictures of on-energy particles launched along x axis and y axis without the wiggler.

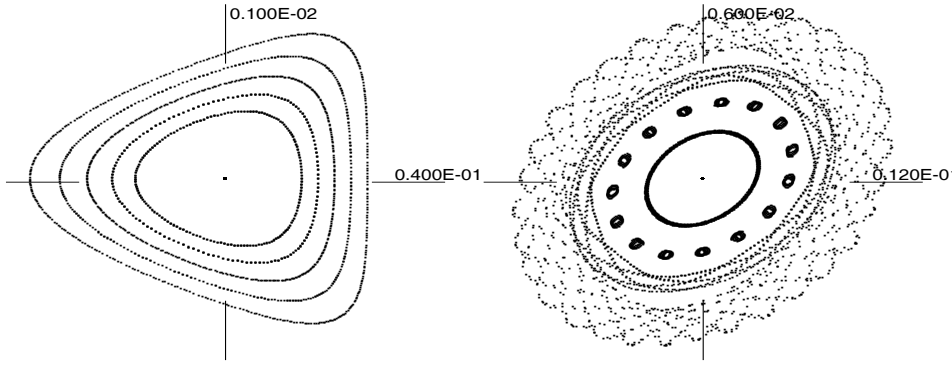

Fig. 8. Tracking pictures of on-energy particles launched along x axis and y axis with the wiggler.

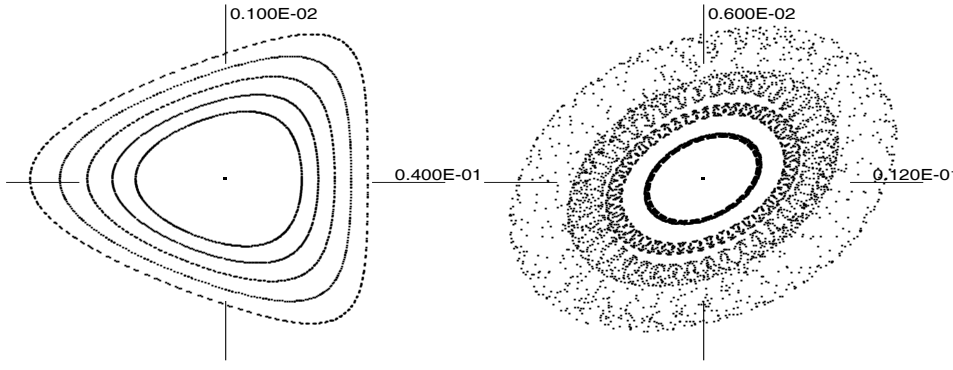

Fig. 9. Tracking pictures of on-energy particles launched along x axis and y axis with the wiggler but without considering the fringe field.

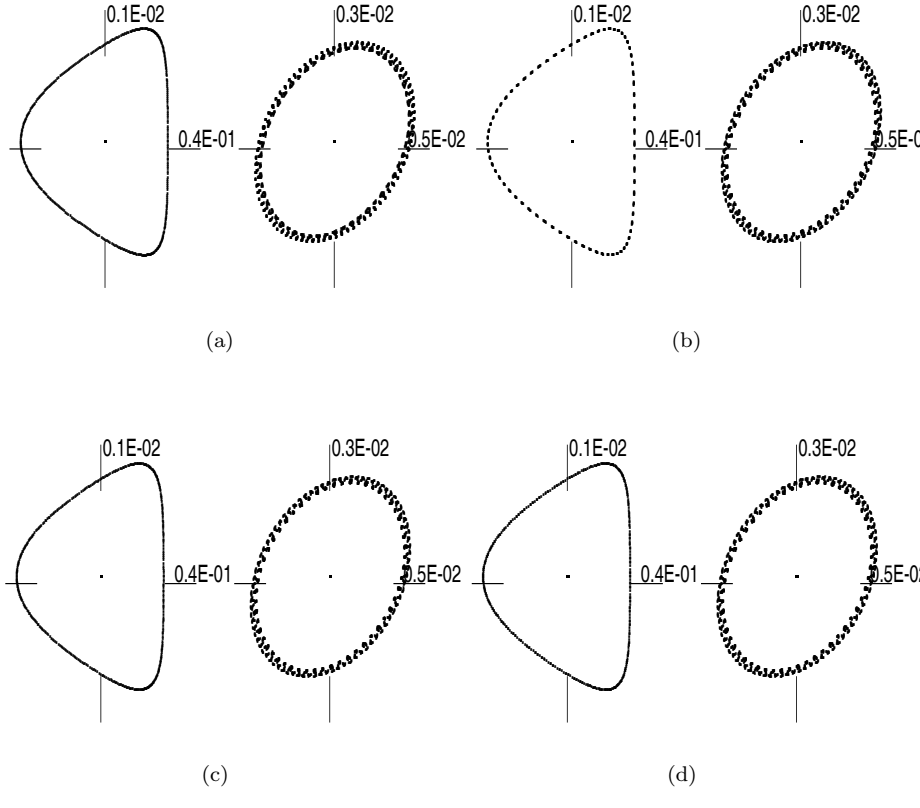

Fig. 10. Tracking pictures of on-energy particles launched at $x = 0.026$m, $y = 0$m (left) and $x = 0$m,$y = 0.004$m (right) with the wiggler up to the (a) 8th, (b) 9th, (c) 10th, (d) 11th order.

The traces in $y - b$ phase plane are different. Without the wiggler, the vertical dynamic aperture reaches 9 mm. With the wiggler, the particles might get lost at the island area in Fig. 8, which means the dynamic aperture decreases to about 4 mm. But it is still about 50 times of the vertical beam size at the middle point in the straight section, where the vertical beta function is only 2.03 m and the vertical beam size is only 0.07 mm.[9] In order to verify the dynamic apertures, we provide tracking pictures of the on-energy particles at $x = 0.026$ m, $y = 0$ m and $x = 0$ m, $y = 0.004$ m, with the EXPO generating functions of the 8th to the 11th order maps, which are shown in Fig. 10. And we can see these pictures agree with each other.

6. Conclusion

Considering the above results, we can draw the conclusion that the nonlinear affects of the wiggler will not seriously affect the performance of the storage ring, since the dynamic apertures with the wiggler are still large enough. But the vertical β function is distorted heavily because of the linear effects of the wiggler, which will decrease the physical acceptance and beam lifetime of the storage ring. The linear effects can be compensated by appropriately adjusting the strength of the quadruples. More work on the compensation should be done in the future.

References

1. L. Wang, H. Xu, G. Feng, and et al., Linear optics compensation of the superconducting wiggler in HLS, in *Proc. 2005 Particle Accelerator Conf.*, eds. B.Siemann (Knoxville, Tennessee, USA, 2005), p. 3037.
2. N. Liu, Y. Jin, H. Yan, and et al., Beam dynamic effects of 6 T superconducting wiggler on the Hefei light source storage ring, in *Development report of 6 T superconducting wiggler in NSRL*, (1999).
3. M. Berz, and K. Makino, COSY Infinity 9.0 beam physics manual, (2006), p. 17.
4. http://www.bt.pa.msu.edu/index_cosy.htm.
5. M. Berz, *Modern Map Methods in Particle Beam Physics*, 1st edn. (Academic Press, London, 1999).
6. H. Goldstein, C. Poole, and J. Safko, *Classical Mechanics*, 3rd edn. (Higher Education Press, Beijing, 2005), p. 373.
7. B. Erdelyi and and M. Berz, *Physical Review Letters* **87**, 11 (2001).
8. M.L. Shashikant, M. Berz, and B. Erdelyi, *Institute of Physics CS* **175** (2004).
9. H. Zhang, Study on the HLS high brilliance operation mode, Ph.D thesis, University of science and technology of China, (2006), p. 47.